APPLICATIONS OF LIGHT SCATTERING AND REFRACTION BY ATMOSPHERIC GASES

Ashokabose MOORGAWA

Submitted in partial fulfillment of the
Requirements for the degree of
Doctor of Philosophy,
in the
School of Pure and Applied Physics,
University of Natal.

Durban
South Africa
June 2002

Preface

The experimental work described in this thesis was carried out in the School of Pure and Applied Physics, University of Natal, Durban, from July 1997 to October 2001, under the supervision of Professor Max M. Michaelis.

These studies represent original work by the author and have not otherwise been submitted in any form for any degree or diploma to any tertiary institution. Where use has been made of the work of others it is duly acknowledged in the text.

Acknowledgements

Many people have contributed towards the completion of this work. To give due credit to everyone involved would not be possible. For those persons whom I fail to mention here under I extend my sincerest thanks.

I would firstly like to thank my supervisor Professor Max Michaelis, for his hard work and initiative, his invaluable guidance, encouragement, generosity and sense of humour during the preparation and compilation of this thesis. Thanks Max for helping me financially to survive and letting me stay in your flat (when you were away) during times when I was running the LIDAR late night.

I would also like to thank Dr Arnold Prause for teaching me most of what I know concerning the operation of the old LIDAR.

I would also like to thank my co-supervisor Dr Hassan Bencherif at the Laboratoire de Physique de l'Atmosphère (Université de la Reunion) for his invaluable guidance and hard work over the past three years. Hassan has been a very dynamic and motivated person not only on a personal level but also on a scientific level as well and for this I am grateful.

A special thanks go to Prof Roseanne Diab at the School of Life and Environmental Sciences for her invaluable discussions, encouragement and advice during the preparation of this thesis. Thanks Roseanne for also helping me financially.

I would also like to thank Prof Manfred Hellberg for his efficient administration and interest.

A special thanks go to Prof Terry Doyle for his keen interest and efficient administration prior to the installation of the new LIDAR .

I would also like to thank Mr Jacques Porteneuve, the French LIDAR engineer at the CNRS-SA for teaching me most of the optics and operation of the new LIDAR, and Mr Guy Bain for running the new LIDAR late at night.

A special thanks go to Miss B. Morel, Mr D. Faduilhe and all visiting honours students from Université de la Reunion for their invaluable help during the preparation of this thesis.

I would also like to thank Mr Willem de Beer, Mr Derek Dixon and all other members of the Physics workshop for their assistance and maintenance of the LIDAR equipment during the course of this study.

Robert Piasecki and the staff of the electronics workshop for their support and prompt solutions to electronic problems.

The University of Natal for the financial support of a Graduate Assistantship.

Finally, a very special word of thanks must go out to my family, Jàynand, Sunmuttee, Ravi, Vishal, Neetoo, Valerie and Prem for their love, support and belief in me. Without their support, this work would not have been possible.

Abstract

LIDAR, an acronym for LIght Detection And Ranging, is a system used for studying the scattering of laser light incident on a parcel of air. This thesis investigates the atmosphere above the Durban region using two atmospheric LIDARs, referred to, in this study, as the "old LIDAR" and the "new LIDAR".

The old LIDAR was used in a campaign of observation from July to October 1997 in a study of aerosol concentrations over Durban. This thesis will focus on, among other things, the local aerosol profiles for low altitude (0 to 10 km) and high altitude (10 to 35 km). In particular, the focus will shift on any long persistence in this region (it was found that the aerosol layer observed by M. Kuppen (1996) on June 1994 at 25 km may have moved to the higher altitude of 28 km in October 1997. This may be explained by stratospheric upwelling, carrying the layer to higher altitude. These aerosols are known to influence the local climate). This investigation will give some useful insight into the local atmospheric dynamics.

The new LIDAR system (Rayleigh-Mie LIDAR) has been used to measure atmospheric temperatures from 20 to 60 km as well as aerosol extinction coefficients from 15 to 40 km. Height profiles of temperature have been measured by assuming that the LIDAR returns are solely due to Rayleigh scattering by molecular species and that the atmosphere obeys the perfect gas law and is in hydrostatic equilibrium (Hauchecorne and Chanin 1980).

Since its installation in April 1999, the new LIDAR has been used to monitor stratospheric temperatures and aerosol concentrations from 10 to 40 km. In this study, we discuss in chapter 7 the results of a validation campaign conducted during the period of April 1999 to December 2000. Average monthly LIDAR temperatures are computed from April 1999 to December 1999 and compared with radiosonde temperatures obtained from the South African Weather Service (SAWS) at Durban. The monthly LIDAR temperature profiles over two years (1999 and 2000) were also computed and compared with the climatological model Cospar International

Reference Atmosphere (CIRA)-1986 and with the average monthly European Centre for Medium Range Weather Forecast (ECMWF) temperatures. The results show that there is good agreement between LIDAR and SAWS radiosonde temperatures in the 20 and 30 km altitude range. Between 20 and 40 km, the monthly LIDAR temperatures agree closely with the CIRA-86 and ECMWF profiles. However, during winter, in the altitude range 40 to 60 km, LIDAR temperatures are warmer than CIRA-1986 and ECMWF temperatures, and they show large variability. These variations could be due to relatively fast transient phenomena like gravity waves or planetary waves propagating vertically in the stratosphere. As part of the validation process, the aerosol extinction coefficients retrieved from the LIDAR data have also been compared with the extinction coefficients measured by Stratospheric Aerosol and Gas Experiment (SAGE) II close to the LIDAR location and on coincident days.

Appendix E of this thesis also investigates the concept of refraction by atmospheric gases as applied to gas lenses. A simple spinning pipe gas lens (SPGL) has been used as the objective lens of a camera to take pictures of the moon and sun spots. The SPGL is a varifocal length lens which depends on the temperature of the pipe and the angular velocity at which it spins. For our purpose a focal length of 8 m has been used. The moon pictures are compared with a lunar map so as to identify the maria.

Contents

List of Figures

List of Tables

List of Acronyms and Symbols

$CIRA$	:	Cospar International Reference Atmosphere
$CNRS$	:	Centre National de la Recherche Scientifique
$ECMWF$	:	European Centre for Medium Range Weather Forecast
$ENVISAT$	:	ENVIronment SATellite
$ERBS$	:	Earth Radiation Budget Satellite
ESA	:	European Space Agency
$GOMOS$	:	Global Ozone Monitoring by Occultation of the Stars
$HRDL$	:	High Resolution Doppler Lidar
ICF	:	Inertial Confinement Fusion
$LARC$	:	LAngley Research Centre
$LIDAR$	:	LIght Detection And Ranging
$LITE$	:	Lidar In space Technology Experiment
LPA	:	Laboratoire de Physique de l'Atmosphere
$MISR$	:	Multi-angle Imaging SpectroRadiometer
$NASA$	:	National Aeronautics and Space Administration
PTU	:	Pressure Temperature hUmidity
SA	:	Service d'Aéronomie
$SAFARI$	:	Southern Africa Fire-Atmosphere Research Initiative
$SAGE$	:	Stratospheric Aerosol and Gas Experiment
$SAOZ$	:	Système d'Analyse par Observation Zénithale
$SAWS$	:	South African Weather Service
$TRACAS$	:	TRAnsport of Chemical species Across the Subtropical tropopause
$UARS$	:	Upper Atmosphere Research Satellite
UND	:	University of Natal Durban
UR	:	Université de la Reunion
UT	:	Universal Time
WMO	:	World Meteorological Organisation
A	:	Area of receiver
ALR	:	Adiabatic lapse rate
B	:	Rotational constant
b	:	Receiver spectral bandwidth
C	:	Current amplification

CSL	:	Colliding Shock Lens
Cv	:	Specific heat capacity at constant volume
d	:	Diameter of laser beam at emission
D	:	Diameter of laser beam after being expanded
e	:	Electronic charge
Eo	:	Magnitude of electric field of incident wave
f	:	Focal length of receiver telescope
Fb	:	Body force responsible for natural convection
$FWHW$	:	Full Width Half Maximum
$F\,\lambda$	:	the extraterrestrial solar radiance for wavelength λ
g	:	Rms noise voltage factor
G	:	Number of molecules per unit volume
h	:	Planck's constant
Hs	:	Scale height
$H\,\lambda$	:	Solar irradiance
I	:	Intensity of light
ia	:	Anode current
Ig	:	Intensity of light scattered at the ground
$Igtot$	:	Total intensity of light scattered at the ground
Io	:	Intensity of incident radiation
Jd	:	Momentum flux density
Jo	:	Laser output power
K	:	Sky radiance
k	:	Boltzmann's constant
l	:	Resolution length
L	:	Length of SPGL tube
M	:	Temperature
Md	:	Momentum density
$N(z)$	:	Brunt-Väisälä frequency
ns	:	Total number of power spectra
P	:	Number of photons
Pc	:	Number of photons collected
PCS	:	Pulse Counting System
PE	:	Potential Energy per unit mass
PMT	:	Photomultiplier Tube
p	:	Induced polarisation

pr : Pressure

q : Amplification factor

Q : Overall efficiency of the observing system

r : Radial distance

R : Scattering ratio

rp : Radius of pipe

$S(z)$: Instantaneous energy received at time t from altitude z

So : Transmitted laser energy

$SPGL$: Spinning Pipe Gas Lens

$s(z)$: Logarithmic range-adjusted power

T : Attenuation of light

$TGGL$: Thermal Gradient Gas Lens

u : Round trip travel time of light

U : Accelerating voltage

UR : Universal gas constant

v : Speed

vw : wind speed

V : Scattering volume

W : White noise

Wm : Mean molecular weight of air

$w(z)$: Half width of laser beam at distance z

wo : Half width of laser beam at emission

X : Load resistor

Xt : Thermal conductivity

y : Number of dynodes

Y : Filter transmission

z : Altitude

α : polarisability

$\alpha 1$: Weak modulation

β : Volume backscattering coefficient of the atmosphere

βa : Volume backscattering coefficient arising from aerosols

βm : Volume backscattering coefficient arising from air molecules

χ : Extinction cross-section for a particle

$\Delta\vartheta$: Change in frequency of rms voltage

δ : Quality of optics and atmospheric turbulence

δz : height resolution

Δ : Axial separation

Δb : Spectral bandwidth

ϵ : Intrinsic frequency of the wave

ϵo : Permittivity of free space

γ : Attenuation coefficient

Γ : Diameter of scattering volume

ι : Apparent frequency of the wave

κ : Optical frequency of return signal

λ : Wavelength

Λ : Defocussing

μ : Refractive index

ν : Frequency of incident wave field

Ω : Solid angle subtended at ground

$\phi mirror$: Diameter of mirror

$\phi fibre$: Diameter of optical fibre

$\phi tube$: Diameter of tube

$\Pi\lambda$: Radiometer field function at wavelength λ

Ψ : Amplitude of gravity wave

ρs : Scattering cross-section

ρr : Rayleigh scattering cross-section

ρR : Rayleigh scattering function for backscatter

ρL : LIDAR cross-section

σ : Volume extinction coefficient of the atmosphere

σa : Volume extinction coefficient arising from aerosols

σm : Volume extinction coefficient arising from air molecules

τ : Duration of the laser pulse

θ : Angular displacement

Θ : Atmospheric transmission

υ : Angular velocity

Υ : rms voltage factor

φ : Parallax error

ϖ : Backscatter phase function

ϱ : Density of atmosphere

ς : Duration of pulse

ϑ : Azimuthal angle

ξ : Divergence of laser beam

ζ : Vertical displacement of an atmospheric fluid

Chapter 1

LIDAR Review

1.1 Historical Background

Probing the atmosphere with light beams is by no means a new technique. As early as 1869, Tyndall used an electric lamp to study the polarisation of light scattered from smoke in his laboratory. In 1930 Synge proposed that a vertically directed searchlight beam could be utilised to measure density and temperature profiles of the upper atmosphere. Hulburt (1937) studied atmospheric turbidity and molecular scattering to a height of 28 km. This was accomplished by photographing a searchlight beam over an observing station 18,4 km away. In 1939 Johnson *et al.* used a modulated light beam and a photoelectric detector to make quantitative measurements of the scattered intensity up to 30 km.

Eltermann (1951) used a rotating shutter to modulate a searchlight beam, which he used as the transmitter and a parabolic reflector with a photomultiplier at the focus as the receiver. The transmitter and receiver were spatially separated in an arrangement called a bistatic LIDAR (which will be

discussed later) and with this set up Eltermann was able to obtain density and temperature profiles up to 60 km which agreed well with profiles from other meteorological techniques. Since the scatter altitude was determined by triangulation, a single profile took an entire evening.

Friedland (1956) recognised that there was little scientific value in obtaining profiles over such long time periods since atmospheric changes could take place between the first and last observations. Also weather changes may force the cessation of observations before a complete profile was obtained. There was therefore a need for a system that could sample faster. Friedland used a pulsed light source as the transmitter, and the receiver was separated by a distance of 0,17 km. With this system he was able to obtain density profiles up to 40 km in height in a time extremely short (500 μs) compared to Eltermann's sampling time of one night.

The invention of the laser by Maiman (1960) meant that a high intensity monochromatic collimated beam of light was now available as the transmitter for the LIDAR systems. The laser was an obvious replacement for the searchlights used previously. The invention of the Q-switch by McClung and Hellwarth (1962) made the generation of very short high energy single laser pulses possible. This development meant that range resolved measurements could now be carried out. This revolutionised optical probing of the atmosphere.

Fiocco and Smullin (1963) were the first to use the laser for atmospheric studies. They utilised a Q-switched pulsed ruby laser at 694,3 nm with a

pulselength of 50 ns to obtain backscattered echoes up to an altitude of 25 km. With these echoes Fiocco and Smullin were able to detect the presence of atmospheric aerosols.

In the very early days of LIDAR development, the return signal was measured as an intensity and displayed on an oscilloscope as a plot of voltage versus time. The current out of the photomultiplier was passed through a resistor and the voltage change was measured as the light was scattered back into the detector. The oscilloscope was triggered the moment the laser was fired, hence the time axis represented the distance from which the light was scattered.

LIDAR systems have now become more sophisticated: different and shorter wavelength lasers are used and better detection techniques, e.g. pulse counting, are employed. Not only do we have ground based LIDAR but there are also airborne LIDARs (Spinburne 1982) as well as space-borne LIDAR systems. Mobile LIDARs are also present in this field of study (Fredriksson *et al.* 1981).

LIDAR systems are used in the study of various atmospheric constituents and properties which include aerosols, sodium, calcium, lithium, ozone, wind, temperature, and humidity. The studies of atmospheric aerosols, density and temperature are essentially meteorological.

In situ measurements were initially carried out by instruments mounted on giant kites. Today lightweight instruments are borne on free balloons and telemeter their measurements back to earth. These systems are called

Figure 1.1: A typical radiosonde launch in the early hours of the morning at the Aerological Station Payerne (a regional office of the Swiss Meteorological Institute).

radiosondes. Fig.(1.1) shows a typical launching of a radiosonde in the early hours of the morning at the Aerological Station, Payerne in Switzerland (which is a regional office of the Swiss Meteorological Institute). The method consists of launching a balloon filled with helium in the atmosphere. The balloon carries a radiosonde which is capable of measuring almost vertically (the balloon drifts with wind) the pressure, temperature and relative humidity for a PTU (Pressure, Temperature and hUmidity) sonde. Some sondes can also measure ozone concentration. During the ascent of the balloon, the measurements are telemetered to a receiving station on the ground every 10 secs until the balloon bursts. Fig.(1.2) shows a commonly used sonde in most meteorological offices around the world for upper air measurements (here shown in the UK).

The ground station receives, records and processes the measurements of

Figure 1.2: A commonly used sonde RS80 in the world (here shown in the UK). The antenna which sends the signal to the ground can be seen on top.

pressure, temperature and relative humidity taken by the radiosonde. From these measurements, the dew point temperature, the wind speed and direction are calculated. These measurements are important to meteorology for two reasons:

(i) weather conditions can be reported at certain pressure levels, and

(ii) the data collected can be used in the analysis of charts and numerical weather prediction models.

Dust-sondes (balloon borne) are also used to measure aerosol concentrations. Radiosondes and dust-sondes are capable of producing profiles with vertical resolutions of up to 100 m. Altitudes of 28 km are attainable at which point the balloons usually burst. This is a good direct measurement technique. However, there are two disadvantages:

(1) Winds tend to carry the balloons away from the point of release, up

to 30 km away (Northam 1974). Hence the profile is not strictly vertical.

(2) An entire profile (0-30 km) can take up to 2 hours during which atmospheric changes could take place.

For sounding in the upper stratosphere and mesosphere (25-70 km range), beyond the reach of balloons, rocket systems have been used. During the 1960's, rockets were developed with specific meteorological applications, capable of carrying the scientific payload up to 75 km or higher. Equipment consisting of a specially adapted and more sophisticated radiosonde systems are released with a parachute at high altitude. However, the parachute is affected by wind and drifts horizontally as well as vertically. Hence the profile is quasivertical at best.

LIDAR profiles are however very localised and vertical. The time taken to obtain a single profile can be short compared to radiosondes. It is limited only by the pulse length and repetition rate of the laser. A single laser pulse can produce an entire profile up to an altitude of (typically) 100 km. For better results, many laser shots are done which are integrated to give a single temperature profile for the night. The profile is usually integrated over 4 to 5 hours acquisition.

Even with the limitations that balloon-borne detectors have, Northam *et al.* (1974) have shown good correlation between aerosol concentrations measured using a balloon borne dust-sonde and a ground-based LIDAR system.

Satellites have also been used extensively to remotely measure vertical temperature profiles and atmospheric densities. In short, satellites have ex-

tended our measurement of atmospheric temperature in three main ways (Barnett 1980):

(i) Daily radiosonde analyses are available up to 30 km for both hemispheres. In the past, weekly analyses up to 70 km could be obtained, although the latter depended upon a network of rocket stations which is very sparse. Satellites now offer complete daily analyses throughout the middle atmosphere.

(ii) Satellites offer complete coverage of the middle atmosphere of the Southern and Northern Hemispheres, where up to now radiosonde observations cover relatively few places over land.

(iii) Satellites provide homogeneous data from the same instrument and allow the study of planetary waves of amplitude as small as 0.3 K can be detected. Most studies with satellite data have dealt with winter disturbed stratosphere and mesosphere (Harwood 1975; Leovy and Webster 1976; Hirota 1978), which are dominated by planetary waves and stratospheric warmings.

1.2 Deployment of LIDARs in Space

The applications of ground-based and airborne LIDAR systems have validated the measurement capabilities and reliability of the technique. The incorporation of such systems in spacecraft for providing global data on a number of atmospheric parameters is expected to make significant contributions to meteorology and climatology, and has consequently been the subject of considerable research by both ESA and NASA since 1974. However, de-

velopments in laser technology and the access to greater weight, volume and power facilities on large space platforms deployed since the mid-1990s have inspired renewed attention to the concept of space-borne LIDARs and specific missions have already been planned in the USA (Winker *et al.* 1996) and USSR (Balin *et al.* 1990).

The particular advantage of a LIDAR system in space is its good vertical resolution which is demonstrated in ground-based and airborne LIDARs. The minimum footprint is determined by the diffraction limit of the transmitting telescope, which can be as small as a few mrad. These capabilities will be particularly suited to studies of the height of the planetary boundary layer, cloud-top heights, vertical profiles of aerosols, and sub-visible clouds. The LIDAR In space Technology Experiment (LITE) conducted by the NASA on board the US shuttle flight in 1993 was used to measure the above-mentioned parameters and also atmospheric temperatures with a reasonable height resolution. LITE incorporates a Neodymium-YAG laser, with frequency-doubling and tripling crystals, and a 1 m diameter receiving mirror. The doubling and tripling crystals are used to provide 0.46 J at 532 nm and 0.20 J at 355 nm. The primary goals of LITE are to demonstrate the maturity of space-based LIDAR technology, to provide some unique measurements, and to provide a platform for future development of technology for space-based systems (Winker *et al.* 1996). A corresponding development took place in the USSR where a system incorporating a frequency-doubled Neodymium-YAG laser and a 27 cm diameter receiving mirror was mounted on the manned orbital station MIR for measurements of the upper boundary of clouds and their optical properties (Balin *et al.* 1990). The European Space Agency

(ESA) is planning to launch ENVIronment SATellite (ENVISAT) in March 2002 which has the instrument Global Ozone Monitoring by Occultation of the Stars (GOMOS) on board (ESA 2001). The primary aim of GOMOS is to measure stratospheric ozone globally using the stellar occultation technique. The Service-d'Aéronomie of the CNRS, Verrières-le-Buisson, France will assume the conception and validation of the GOMOS measurements. Ground-based LIDAR data will be used to validate the satellite measurements.

Differential absorption LIDAR systems were developed from these simple backscatter systems, and the measurements of particular value to meteorological and climate studies are profiles of water-vapour and temperature, and also of pressure down to the Earth's surface.

The traditional method of global wind measurements from space is based on the observation of cloud movements using geostationary imaging radiometers. The provision of improved cloud heights determined by LIDAR will assist in obtaining wind vectors at different atmospheric levels, provided the LIDAR measurements and the information from the satellite sensor images can be correlated. However, serious consideration is also being given to the measurement of the three dimensional wind field throughout the troposphere and lower stratosphere using a Doppler LIDAR system (NASA 1987). Fig.(1.3) shows a range-time display of vertical profiles of the vertical wind acquired by the High Resolution Doppler LIDAR (HRDL) in Boulder, USA, during system tests. Positive velocities indicate rising air parcels. The column of high negative velocity between 19:10 and 19:12 is a shaft of light rain. The simultaneous 30 m range resolution and 0.05 m/s velocity resolu-

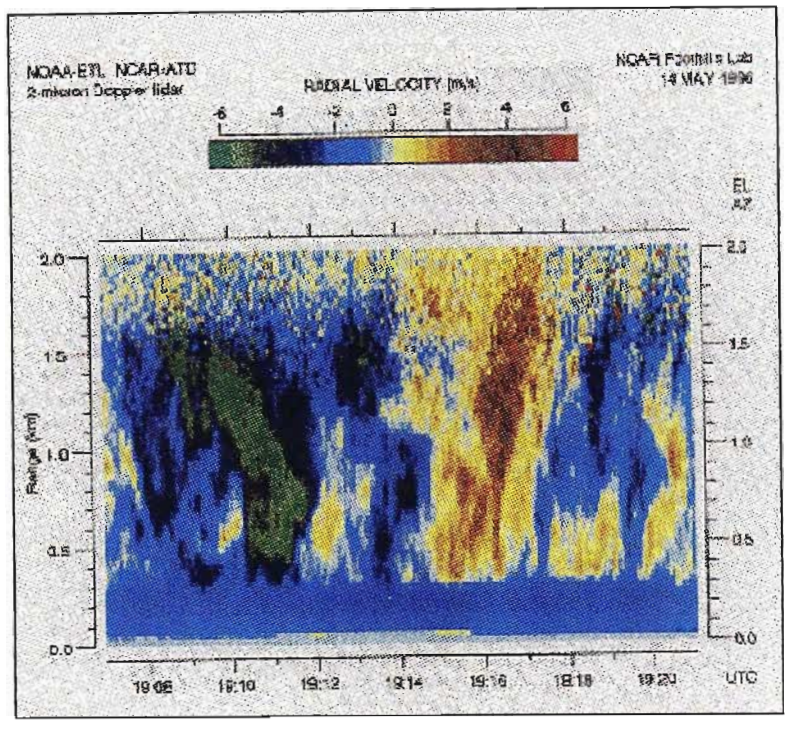

Figure 1.3: A range-time display of vertical profiles of the vertical wind acquired by the High Resolution Doppler LIDAR (HRDL) in Boulder (Wulfmeyer et al. 1998). The image was taken on May 14 1996, between 19:08 and 19:20 UTC.

tion are unprecedented for a high repetition rate coherent Doppler LIDAR. The system is based on a diode pumped Ti:Nu YAG laser with an emission wavelength of 2.02 μm and average power of 2 W.

A major consideration of each of the two types of application (backscatter and Doppler wind) is the choice of the laser. The life time and reliability will be particularly relevant because of the need to ensure a minimum operational time of 2-3 years for meteorological-type applications. Fortunately, progress in new laser material and advances in diode laser pumping arrangements promise improvements in performance and reliability of solid-state lasers, and improved lifetimes and stability have been achieved with CO_2 lasers. The Neodymium-YAG laser could also find applications in the types

of measurement: differential absorption and Doppler measurements. In the former, the YAG laser is used as a source for backscatter. In the Doppler measurements, the YAG laser is used to pump a Ti-Sapphire laser to produce the 710-950 nm wavelength range for differential absorption measurements of molecular oxygen and water-vapour. Considerable attention has also been paid to the Alexandrite laser operating between 720-780 nm (Pelon 1985) and it seems likely that it will find application in space-borne measurements.

1.3 Franco-South African Cooperation and the Durban LIDAR

Since 1992 the Laboratoire de Physique de l'atmosphère, University of La Réunion (LPA-UR), Réunion, and the Service d'Aéronomie-Centre Nationale du Recherche Scientifique (SA-CNRS), Verrières, France have been collaborating with the University of Natal, Durban (UND) and other institutions such as the South African Weather Service (SAWS) in different projects and campaigns as summarised below:

- Collaboration in the campaign South African Fire/Atmosphere Research Initiative(SAFARI) 1992 (LPA-UR/UND),
- Comparison of radiosonde measurements of Pressure Temperature hUmidity (PTU)-O_3 between Irene (25 ^{0}S) and Reunion (21 ^{0}S), 1995 (LPA-UR/UND),
- Communication of the results obtained from comparison Irene/Reunion radiosonde ozone measurements at the XVIII Quadrennial Ozone Sym-

posium, 1996 (LPA-UR/UND),

- Re-installation of the SAOZ system at UND as an honours project by Laurent Robert under the supervision of T. Portafaix, 1997(LPA-UR),

- Establishment of the TRansport of Chemical species Across the Subtropical tropopause (TRACAS) campaign, project funded by the European Program for Research and Technological Development, 1998 (SA-CNRS/LPA-UR/UND),

- Installation of a Rayleigh-Mie LIDAR at UND, 1999 (LPA-UR/UND)

.

The installation in April 1999 of a Rayleigh-Mie LIDAR at UND is the first of its kind in South Africa as indeed there is no other such LIDAR system found in the country. This bilateral research programme is aimed at un erstanding the contribution of dynamic processes to the phenomena that drive meridional exchanges through the southern subtropical barrier. It has also contributed to the transfer of technology and exchange of scientists with regard to LIDAR instrumentation and data analysis.

Reunion Isla5nd (21^0S,55^0S) is in a tropical zone, north of the southern subtropical barrier (SSB). Durban (30 ^{0}S, 31^0E) is on the other side of the SSB. Simultaneous LIDAR measurements at these two sites will help to understand the transfer of energy and mass across the SSB. Other measurements such as SAOZ, radiosonde and satellite data obtained from the experiments of the Upper Atmosphere Research Satellite (UARS) and the Earth Radiation Budget Satellite (ERBS) together with data related to dynamical parameters

(zonal wind and potential vorticity from ECMWF data) will help to further our understanding in the mechanisms involved in the transfer.

The LIDAR measurements obtained will also help to understand the climatology and variability of aerosols above South Africa. Aerosol studies are important as they give an indication of the loading of the atmosphere in relation to anthropogenic sources, biomass burning (burning of forest, sugarcane, etc), smoke and other gases emitted by factories. These studies can also help to identify dynamic tracers in the upper troposphere and the lower stratosphere. LIDAR measurements can also help calculate parameters of radiative transfer.

A joint collaboration between UR-LPA-CNRS and the School of Geography and Environmental Sciences, University of Natal has existed since 1992. Research in the evolution of tropospheric ozone has been undertaken by both institutions during the SAFARI 1992 campaign. A second collaboration recently occurred with two intensive campaigns in 1998 and 1999 during the period of biomass burning in the Southern subcontinent.

During July and August 2000, the LIDAR was part of the SAFARI-2000 campaign which aims, among others, at understanding the dispersal and transport of aerosols.

To conclude this short review, one could note that thanks to the Franco-South African atmospheric collaboration, South African meteorology has the opportunity of keeping pace with the major remote sensing techniques (LIDAR, SAOZ, etc) used in the Northern Hemisphere. In the future, the University of Natal could position itself to become a centre of excellence for atmospheric studies on the African continent.

Chapter 2

Scattering Theory

2.1 Introduction

This chapter describes the different scattering processes involved when a monochromatic light source is incident into the atmosphere. The main scattering processes are Rayleigh scattering, Mie scattering, particulate scattering, Raman scattering, resonance and fluorescent scattering.

2.2 Rayleigh Scattering

The scattering caused by air molecules the size of which are smaller than the wavelength of the incident radiation is termed Rayleigh scattering. The theory of molecular scattering was first developed by Lord Rayleigh and is discussed in the context of general scattering theory by Van de Hulst (1957). The results of the theory, as applied to backscatter, may be summarised as follows.

Let a wave of intensity I_o be incident on a gas containing G molecules per unit volume and having polarisability α. It may be shown (Kent *et al.* 1967)

that the intensity of the light scattered back in the direction of the incident beam, at a distance z from the scattering volume, is given by

$$I = I_0 \cdot \frac{\pi^2 \cdot \alpha^2}{\varepsilon_o^2 \cdot \lambda^4 \cdot z^2} \cdot V \cdot G \tag{2.1}$$

where λ is the wavelength used and V the scattering volume. G is the number of molecules per unit volume. α is the polarisability and is equal to $2 \cdot (\mu - 1) \cdot \frac{\varepsilon_o}{G}$, where μ is the refractive index, ε_o is the permittivity of free space.

For light in the visible region of the spectrum, $\frac{\alpha}{\varepsilon_o}$ has the numerical value $2.17 \times 10^{-29}\ m^{-3}$, provided no dissociation occurs.

Two important conclusions that can be drawn from equation (2.1):

(i) the intensity and the power of the scattered wave are proportional to λ^{-4}.

(ii) the backscattered intensity varies as $\frac{1}{z^2}$, for a purely molecular atmosphere.

Rayleigh scattering is frequently described in terms of various scattering cross-sections. The most commonly used terms are:

(a) The Rayleigh scattering cross-section

$$\rho_r = \frac{8 \cdot \pi^3 \cdot \alpha^2}{3 \cdot \lambda^4 \cdot \varepsilon_o^2} \tag{2.2}$$

This formula may be obtained by integrating the general formula for Rayleigh scattering (Van De Hulst (1957)), over a complete sphere. The Rayleigh scattering cross-section is very small. For our systems, the wavelengths used are 589 nm and 532 nm, $\frac{\alpha}{\varepsilon_o} = 2.17 \times 10^{-29} m^3$ (provided no dissociation occurs) then ρ_r will approximate the value $10^{-31}\ m^2 sr^{-1}$.

The total fraction of light scattered per unit path length from a beam traversing a region with G molecules per unit volume is $\rho_r.G$ (ρ_r will change very little with altitude as it depends mostly on λ and provided there is no dissociation of the air molecules).

The concentration of molecules in the atmosphere varies from 2×10^{25} molecules per cubic metre at the ground level and 10^{19} molecules per cubic meter at 100 km altitude (Kent *et al.* 1967). The following calculation estimates the value of $\rho_r.G$ at a height of 100 km where we assume the atmosphere is purely molecular.

Typical value of G near the ground is 2.7×10^{25} molecules per cubic metre. Hence $\rho_r.G$ has magnitude $\sim 10^{-6} m^{-1} sr^{-1}$. We can estimate the fraction of light backscattered from a height of 100 km to a height of 6 km by using a "half height" approximation:

$$\frac{100 \text{ km}}{6 \text{ km}} = 16.67$$

We assume that the backscattered signal due to air molecules (Rayleigh scattering) follows an inverse-squared law of the distance of the scatterers from the point of emission of the radiation.

This corresponds to a backscattered signal of intensity $\left(\frac{1}{2}\right)^{16.67} \approx 10^{-5} m^{-1} sr^{-1}$.

Similarly, the fraction of light backscattered from a height of 100 km to a height of 6.5 km is $\left(\frac{1}{2}\right)^{\frac{100}{6.5}} = 2 \times 10^{-5}\ m^{-1} sr^{-1}$.

The fraction of light backscattered from a height of 100 km to a height of 5.5 km will be $\left(\frac{1}{2}\right)^{\frac{100}{5.5}} = 3.3 \times 10^{-6} m^{-1} sr^{-1}$, which is approaching the value of $\rho_r.G$. This "half height" approximation method is an alternative method of estimating the value of $\rho_r.G$. These three values of the parameter $\rho_r.G$ show that the fraction of light backscattered from a height of 100 km decreases by a factor of 10 for a 1 km difference in height from 6.5 to 5.5 km.

(b) The Rayleigh scattering function for backscatter ρ_R (Kent *et al.* 1967) can be written in terms of Rayleigh scattering cross-section ρ_r as follows:

$$\begin{aligned} \rho_R &= \frac{\pi^2 \cdot \alpha^2}{\lambda^4 \cdot \varepsilon_o^2} \\ &= \frac{3}{8 \cdot \pi} \cdot \rho_r \end{aligned} \tag{2.3}$$

Using the above value for ρ_r, ρ_R will have magnitude $\sim 10^{-32} m^2 sr^{-1}$.
The fraction of light backscattered, per unit path length, per unit solid angle, from an incident beam is, as shown by the formula given earlier as $\rho_R.G$. With the same value of G as above, $\rho_R.G$ will have magnitude $\sim 10^{-7} m^{-1} sr^{-1}$.

(c) The LIDAR cross-section

$$\begin{aligned} \rho_L &= \frac{4 \cdot \pi^3 \cdot \alpha^2}{\lambda^4 \cdot \varepsilon_0^2} \\ &= 4 \cdot \pi \cdot \rho_R \\ &= \frac{3}{2} \cdot \rho_r \end{aligned} \tag{2.4}$$

Hence ρ_L will have the same magnitude as ρ_r, viz. $10^{-31} m^2 sr^{-1}$.

The fraction of light that would be scattered per unit length, if the amount of scatter in all directions were the same as that for backscatter is

$\rho.G$ and has magnitude $\sim 10^{-6} m^{-1} sr^{-1}$.

When discussing back-scatter theory, either ρ_R or ρ is normally used and we may rewrite the formula for I as

$$I = \frac{\rho_R \cdot V \cdot G \cdot I_o}{z^2} \tag{2.5}$$

where

V : is the scattering volume,

G : is the number of molecules per unit volume,

I_o: is the intensity of incident radiation,

z : is the distance of the scattering volume to the source of the radiation.

ρ_R will take different values depending on the wavelength of the incident radiation. Typical value of ρ_R at a wavelength of 532 nm is 5.74×10^{-32}

$m^2 sr^{-1}$. At a distance of 10 km, with $G \sim 10^{25}$ molecules per cubic metre, $V \sim 10^{-5}\ m^3$ then $\frac{I}{I_o} = \frac{\rho_R \cdot V \cdot G}{z^2} \sim \frac{10^{-32} \cdot 10^{-5} \cdot 10^{25}}{10^4} = 10^{-16}$.

This is a reasonable estimate of the fraction of the intensity of light scattered back by a pure molecular atmosphere in the direction of the incident beam.

Consider a pulse of length t sec, containing P photons which is directed upwards through the lower atmosphere. Let the attenuation in passing once through the lower atmosphere be T, then the intensity I at a height z is

$$I = \frac{P \cdot T}{t \cdot z^2 \cdot \Omega} \text{ photons / unit area / unit time} \tag{2.6}$$

where Ω is the angular beamwidth or solid angle subtended by the laser beam at the ground (see fig. (2.1)). If we consider light scattered from a thin slice of height δz, as shown in fig.(2.1), then the scattering volume V is given by

$$V = z^2 \cdot \Omega \cdot \delta z \tag{2.7}$$

and the scattered intensity at the ground is

$$I_g = \frac{\rho_R \cdot P \cdot T^2 \cdot G \cdot \delta z}{t \cdot z^2} \text{ photons / unit area / unit time} \tag{2.8}$$

where T^2 is the total attenuation for the round trip.

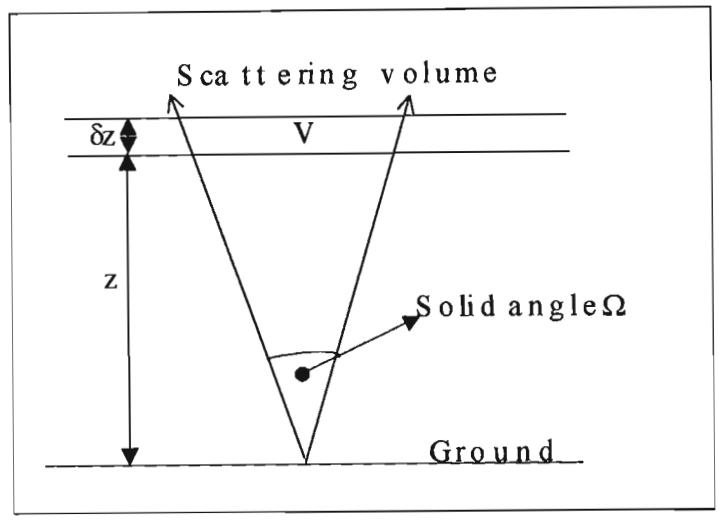

Figure 2.1: The scattering geometry.

Light will be received simultaneously from a height range $\frac{c \cdot t}{2}$, where c is the velocity of light and t is the length of the transmitted pulse. The total intensity on the ground is therefore

$$I_{gtot} = \frac{\rho_R \cdot P \cdot T^2 \cdot G \cdot c}{2 \cdot z^2} \text{ photons / unit area / unit time} \qquad (2.9)$$

provided $\frac{c \cdot t}{2}$ is small compared with the variation of G. A rough estimate of the total intensity of light backscattered on the ground is of the order 10^{11} photons / unit area / unit time as shown by the following calculation. The values of ρ_R, P, T, and G have been obtained from Kent *et al.* 1967.

At a height of 10 km, $\rho_R \sim 10^{-32}$ m^{2}sr^{-1}, $P \sim 10^{19}$ photons, $T = 0.7$, $G \sim 10^{25}$, $c = 3 \times 10^8$ m/s and $z = 10$ km,

$$I_{gtot} = \frac{10^{-32} \cdot 10^{19} \cdot (0.70)^2 \cdot 10^{25} \cdot 3 \times 10^8}{2 \cdot (10^4)^2} \sim 10^{11} \text{ photons / unit area / unit time}$$

If we integrate the amount of light falling on an area A for a time τ, then the number of collected photons is

$$\begin{aligned} P_c &= \frac{A \cdot \rho_R \cdot P \cdot T^2 \cdot G \cdot c \cdot \tau}{2 \cdot z^2} \\ &= \frac{A \cdot \rho_R \cdot P \cdot T^2 \cdot G \cdot \delta z}{z^2} \end{aligned} \tag{2.10}$$

where δz is the height range over which the integration is carried out. P_c depends linearly upon δz and so may be increased simply by increasing δz. However, since in the lower atmosphere, the density changes by a factor of $\frac{1}{e}$ for a height change of about 7 km, a value rather less than this has to be used in practice if the results are to be useful. If we put in a factor Q representing the overall efficiency of the observing system and assume no atmospheric dissociation, then the number of photons actually recorded is

$$P_r = \left(\frac{G \cdot \rho_R}{z^2}\right) \cdot \left(A \cdot \delta z \cdot P \cdot Q \cdot T^2\right). \tag{2.11}$$

This expression consists of two parts: the first term relates to the atmosphere, of which N is the parameter to be determined, and the second term describes the receiving system and associated losses (including those in the lower atmosphere).

The factor $\left(\frac{G \cdot \rho_R}{z^2}\right)$ decreases rapidly with increasing height; using the standard atmosphere data for 15^0N obtained from Kent *et al.* (1967), a short list of expected values is shown in Table (2.1). It shows the variation of $\left(\frac{G \cdot \rho_R}{z^2}\right)$ with height.

Height z/ km	$\frac{G \cdot \rho_R}{z^2}$/m^{-3}sr^{-1}
10	1.70×10^{-15}
30	8.3×10^{-18}
50	1.90×10^{-19}
70	7.5×10^{-21}
90	1.78×10^{-22}

Table 2.1: Variation of the fraction of light that would be scattered per unit volume with height.

2.3 Mie Scattering

Expressed in simple terms: the scattering caused by a particle the size of which is comparable to or larger than the wavelength, can be envisaged as an interference of partial waves which pass around, and in the case of dielectric media, through the particle. The size of the particles is usually less than 0.1 μm in media such as dust, aerosols and water droplets. The scattering cross-section in this case is larger than Rayleigh scattering cross-section and is of the order 10^{-14} m^2 in the visible region.

For the simplest case of a metallic sphere of infinite conductivity, fig.(2.2) shows the normalised cross-section $\frac{\rho_s}{\pi \cdot a^2}$ as a function of the ratio $\frac{2 \cdot \pi \cdot a}{\lambda}$

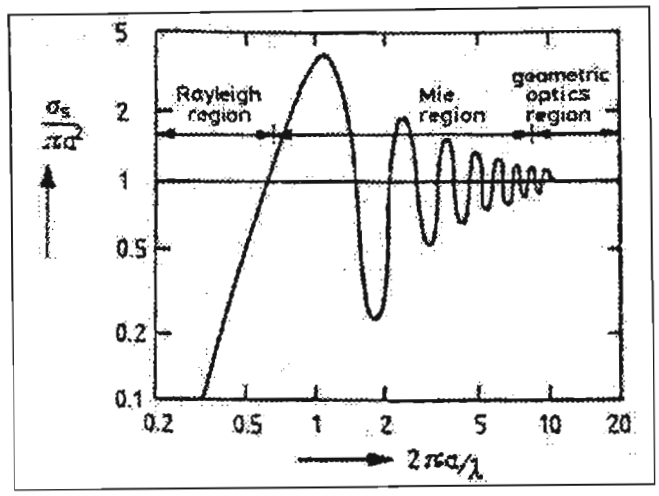

Figure 2.2: Normalised scattering cross-section as a function of the normalised circumference of a sphere (Siegert et al. 1963).

for a metallic sphere, where ρ_s is the scattering cross-section of the sphere and a is the radius of the sphere.

From fig.(2.2) we can distinguish three regions: for $\frac{2 \cdot \pi \cdot a}{\lambda} < 0.5$, the curve obeys the Rayleigh approximation i.e. $\frac{\rho_R}{\pi \cdot a^2} \propto \left(\frac{a}{\lambda}\right)^4$.

At about $2 \cdot \pi \cdot a \approx \lambda$ the maximum scatter cross-section occurs due to Mie (or "resonant") scattering.

For larger ratios of circumference to wavelength up to about 10, constructive and destructive interferences of the partial waves due again to Mie scattering add up vectorially, so that ρ_s shows an oscillatory behaviour slowly damped out as higher modes become involved at higher $\frac{a}{\lambda}$ values. Finally, for $\frac{2 \cdot \pi \cdot a}{\lambda} > 10$ we reach the asymptotic property of Mie scattering, the

simple geometrical optics solution $\rho_s = \pi \cdot a^2$.

To a very good approximation, Mie scattering varies as $\lambda^{-1.5}$.

2.4 Particulate scatter

The lower atmosphere contains large numbers of suspended solid and liquid particles (aerosols) that vary in size from about one hundredth of a micron to a micron (Junge 1963). The main characteristics of their variation with height are fairly well known up to a height of about 30 km (Junge and Manson 1961; Junge *et al.* 1961; Rosen 1961).

An outline of this variation, as shown by balloon borne particle counters, is shown in fig.(2.3). It can be seen that there is a maximum near the ground level followed by a further maximum near the tropopause. Observations of optical scattering from the layer have been made (Fiocco and Grams 1964; Kent *et al.* 1967) showing an enhancement over the Rayleigh scattered signal by a factor of approximately two. The height of the tropopause varies considerably with latitude and it might be expected that the aerosol layer would show similar variation, as yet however there is little evidence on this.

Deirmendjian (1965) has estimated the intensity of the scattered signal using the known aerosol concentrations. These are necessarily subject to considerable uncertainty but agree approximately with the experimental values.

At heights above 30 km the importance of particulate scattering is uncertain. Fiocco and Smullin (1963) and Fiocco and Colombo (1964) have reported the existence of dust layers between 60 and 140 km. Presence of

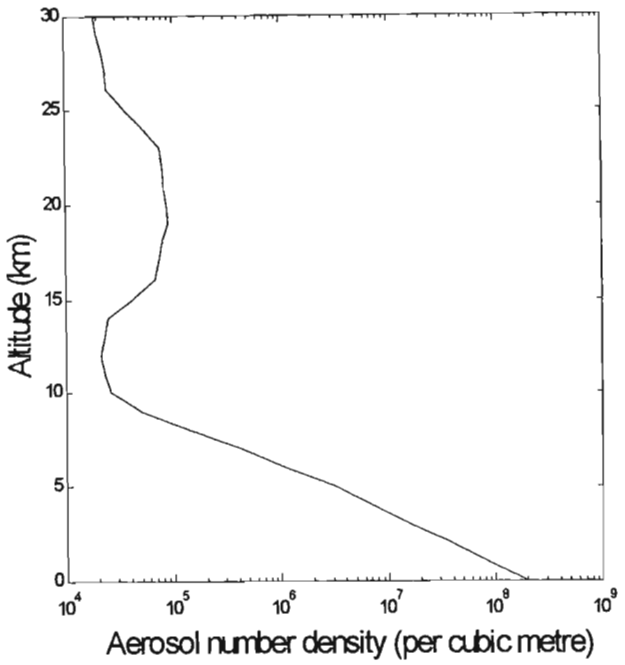

Figure 2.3: Approximate variation of aerosol number density with height.

these layers can influence greatly laser propulsion of rockets into outer space as much of the beam will be attenuated.

2.5 Raman scattering

Raman scattering occurs due to vibrational or rotational transitions within molecules. The Raman spectrum consists of several peaks, shifted with respect to the excitation wavelength by an amount which is characteristic of the studied molecule. One of the advantages of this process is that it enables us to detect simultaneously several constituents using the same laser beam. It also enables one to measure accurately the concentrations of constituents in the atmosphere with respect to an abundant species in the atmosphere,

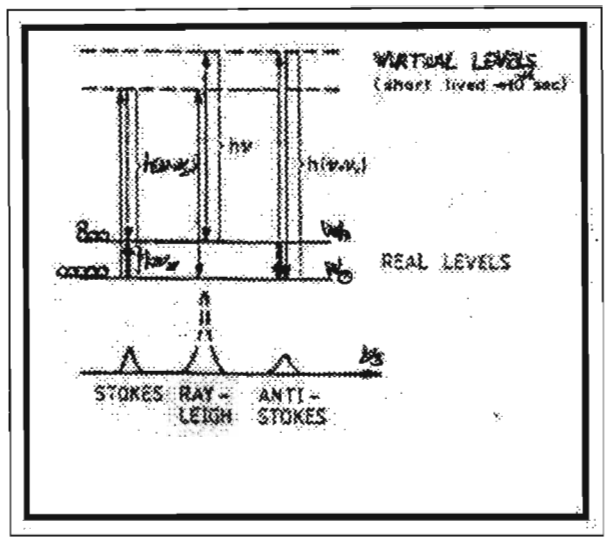

Figure 2.4: Energy level diagram for Raman scattering.

for example nitrogen.

If a molecule is vibrating at its proper vibration frequency ν_ν, then the ability of the molecule to become polarised, the polarizability α, is oscillating with the vibration frequency about its mean value α_0.

Assuming a weak modulation ($\alpha_1 \ll \alpha_0$), the resulting polarisability

$$\alpha = \alpha_0 + \alpha_1 \sin \nu_\nu \cdot t \tag{2.12}$$

will cause the polarization induced p, by the incident wave field at frequency ν to be modulated by the vibration as

$$p = \alpha_0 \cdot E_0 \cdot \sin \nu \cdot t + \frac{1}{2}\alpha_1 \cdot E_0 \left[\cos(\nu - \nu_\nu)t - \cos(\nu + \nu_\nu) \cdot t\right] \tag{2.13}$$

where E_0 is the magnitude of the electric field of the incident wave and ν is the frequency of the incident wave field. The first term in equation (2.13)

is the Rayleigh (elastic) term. The second and third terms represent the Stokes and Anti-Stokes lines of the Raman scattering respectively; they are the inelastic side bands of the Rayleigh scattering (fig.(2.4)). In fig.(2.4), ν_ν is the frequency of the scattered radiation.

Due to the quantum-mechanical selection rules for vibrations $\Delta\nu = \pm 1$ and for rotations $\Delta J = 0, \pm 2$, in vibrational-rotational Raman scattering the spectrum is given by

$$\nu = \nu_\nu \begin{pmatrix} +\frac{4B}{h}(J+\frac{3}{2}) \text{ for } J \rightarrow J+2 \\ 0 \text{ for } J \rightarrow J \\ -\frac{4B}{h}(J-\frac{1}{2}) \text{ for } J \rightarrow J-2 \end{pmatrix} \tag{2.14}$$

where $B = \dfrac{h}{8\pi^2} \cdot I$ is the rotational constant, i.e. a factor characterizing each molecule because of its moment of inertia I for polyatomic non-linear molecules B assumes different values in the different directions of orthogonal coordinates. h is the Planck's constant.

The scattering cross-section for Raman scattering is two to three orders of magnitude smaller than that of Rayleigh scattering and is of the order 10^{-34} m^2.

Raman scattering is important in that the scattered light is frequency shifted by an amount that is characteristic of the scattering molecule. The Raman spectrum can thus be used to identify the scatterer, measure its number density, and measure its energy state by means of the population of the different energy levels.

2.6 Resonance and Fluorescent Scattering

Resonance scattering occurs when the emission wavelength of the atom or molecule is the same as the excitation wavelength. The interaction time is of the order 10^{-8} s to 10^{-9} s and this corresponds to the lifetime of the excited level. The scattering cross-sections in this case vary from 10^{-16} m^2 for atoms and 10^{-21} m^2 for molecules. Resonance scattering occurs without substantial energy or wavelength change, but the scattering cross-section is order of magnitude larger than the Rayleigh cross-section for incident wavelengths matching an absorbing (and reemitting) transition in the molecule or atom. Resonant elastic scattering has been used to detect atomic sodium layer which is located around 80 km, as reported by Hake *et al.* 1972. They found that an atomic sodium layer could be used as a ground-accessible tracer to monitor the position and strength of transition from water cluster ions to diatomic ions.

Fluorescent scattering consists of a spontaneous emission of photons at a wavelength shifted towards the red of the visible spectrum with respect to the excitation wavelength. The scattering cross-sections are of the order 10^{-22} m^2 and the lifetimes of the excited levels vary from 1 μs to 1 s. Fluorescent scattering and resonance scattering are similar in that a match between the transmitting laser wavelength and an absorbing transition is required, but the fluorescent scattering is at a longer wavelength than the incident and is characteristic of the scattering material. Fluorescent scattering from dye particles in the aerosol is possible in the planetary boundary layer and can be used to differentiate LIDAR return from tracer particles and

LIDAR return from ambient aerosol particles and molecules. The planetary boundary layer is the layer of the atmosphere where most of the aerosols are concentrated and is located about 6 km above the ground.

2.7 Multiple Scattering

In multiple scattering, received photons have been scattered more than once. The theory of multiple scattering is complex and could be the subject of post-doctoral studies. However, interested readers should consult Carswell (1983) for a more detailed explanation.

For LIDAR design purposes it is sufficient to note that multiple scattering delays parts of the return signal, so that range resolution of a LIDAR in a multiple-scattering situation is generally degraded. The problem can be overcome by making the receiver field of view as small as possible. In fact, Weinman (1976) showed that a study of LIDAR signal strength as a function of receiver field of view is one way of determining the contribution of multiple scattering to a LIDAR return. Another way to estimate the amount of multiple scattering is to reduce the backscatter coefficient by increasing the incident wavelength ($\propto \lambda^{-4}$).

Light can also undergo multiple scattering and produce a signal in the receiver from low altitudes at a time when the principal signal is entering from higher altitudes. As a first approximation, we have not considered the effect of multiple scattering on the LIDAR returns.

2.8 The LIDAR equation

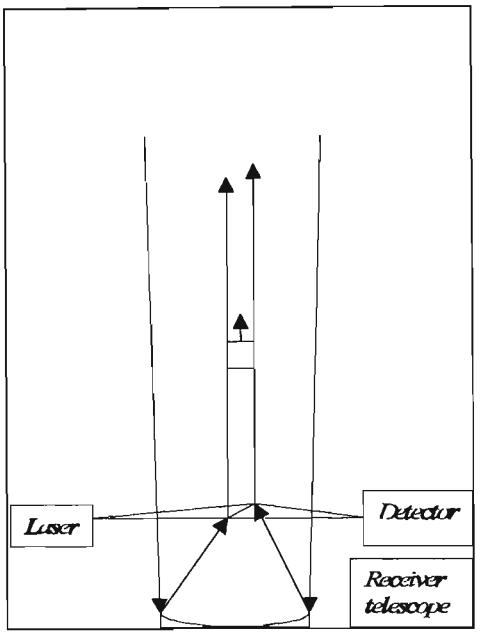

Figure 2.5: General configuration of a monostatic LIDAR.

The light of a laser pulse sent vertically into the atmosphere is backscattered by the air molecules and by the aerosols. For a monostatic LIDAR configuration (fig.(2.5)), where the pulsed laser output is transmitted in a narrow beam with a co-aligned receiver telescope arranged to collect the radiation scattered in the backward direction, the backscattered signal can be described very conveniently in terms of the so-called LIDAR equation (Carswell 1983):

$$S(z) = S_o \cdot Q \cdot \frac{A}{(z - z_L)^2} \cdot \left(\frac{c \cdot \tau}{2}\right) \cdot \beta(z) \cdot \exp\left[-2 \int_{z_L}^{z} \sigma(z')\, dz'\right] \qquad (2.15)$$

where

$S(z)$: the instantaneous energy received at time t from the atmospheric scatterers at altitude z,

S_o : the transmitted energy,

Q : the instrument parameter including the efficiencies of receiver optics and detector,

A : the collecting area of the receiver telescope,

$\frac{A}{(z-z_L)^2}$: the solid angle subtended by the receiver at the altitude $z - z_L$,

β : the volume backscattering coefficient of the atmosphere,

σ : the volume extinction coefficient of the atmosphere,

τ : the duration of the laser pulse, and

z_L : the altitude of the LIDAR station above sea level.

This equation assumes that only a single scattering event takes place to redirect photons from the source back to the receiver.

β is defined as the fractional amount of incident energy scattered per steradian in the backward direction per unit atmospheric path length. β has the dimensions of $\mathrm{m}^{-1}\mathrm{sr}^{-1}$.

σ is defined as the extinction cross-section per unit volume. It is expressed as $\frac{\mathrm{m}^2}{\mathrm{m}^3} = \mathrm{m}^{-1}$ and is numerically equal to the standard linear extinction coefficient.

In the LIDAR equation, the information on the atmospheric properties are contained in the coefficients σ and β.

β is a superposition of scattering contributions from all atmospheric constituents: gas molecules, aerosol particles, dust, water droplets, etc. β can

be written as

$$\beta = \sum_i \beta_i = \sum_i N_i \, d \sum_i \frac{(\pi)_i}{d\Phi} \tag{2.16}$$

where the summation is taken over all species i of number density N_i and backscattering cross-section $\frac{d\sum(\pi)_i}{d\Phi}$.

The cross sections for the various scattering processes range from values as high as $10^{-12}\text{cm}^2\text{sr}^{-1}$ for larger aerosol particles, down to values below $10^{-32}\text{cm}^2\text{sr}^{-1}$ for Raman scattering. These scattering cross-sections are also wavelength dependent.

The number densities N_i depend on the species concentration in the atmosphere. For aerosols and dusts in the lower atmosphere the N_i values vary widely in the range from about 10^8 to 10^{11} m^{-3}. Thus the range of β values encountered can extend from 10^{-3} $\text{m}^{-1}\text{sr}^{-1}$ for larger particle Mie scattering in clouds to less than 10^{-12} $\text{m}^{-1}\text{sr}^{-1}$ for Rayleigh scattering in molecular species (Collis *et al.* 1976).

The extinction coefficient σ includes all of the attenuation processes in the atmosphere. The laser beam energy is lost through both scattering and absorption.

Thus σ can be written as a summation of the following terms (McClatchey *et al.* 1971):

$$\sigma = \sigma_a + \sigma_m \tag{2.17}$$

where σ_a : volume extinction coefficient arising from aerosols

σ_m : volume extinction coefficient arising from air molecules

2.9 The Scattering Ratio

In much of the LIDAR research involving elastic backscattering from aerosols it is necessary to find a way of separating the Mie scattering component from the total return signal. This is often done by introducing the scattering ratio (Measures, 1984):

$$R(\lambda, z) = 1 + \frac{\beta_a(\lambda, z)}{\beta_m(\lambda, z)} \tag{2.18}$$

where

$\beta_a(\lambda, z)$: Mie volume backscattering coefficient arising from aerosols,

$\beta_m(\lambda, z)$: Rayleigh volume backscattering coefficient arising from air molecules,

λ : wavelength of the incident radiation,

z : altitude.

Northam *et al.* 1974 suggested that better accuracy is achieved if pressure and temperature profiles are measured by balloon-borne in situ sensors. For a detailed treatment of the scattering ratio the reader should refer to Measures (1984).

Scattering ratios are very important tools for analysing LIDAR returns. However, they have one disadvantage. They are based on the assumption that the atmosphere is purely molecular (no aerosols) at some altitude. The value of $R(\lambda, z)$ at this altitude is then taken to be 1. However, determination of this "pinned altitude" may pose some problems especially when the atmosphere is loaded with aerosols.

We therefore need some other technique so that the density of the aerosol layer may be determined absolutely. The Klett inversion method has been chosen in this study. A brief description of the method is given in the next chapter. For a detailed treatment of the derivation the reader is referred to Klett (1981).

2.10 Signal-to-noise Ratio

The primary sources of noise in a LIDAR system are shot noise on the photon arrival rate, detector noise (dark current), and sky background noise. The shot noise is due to the large LIDAR return due to backscattering from the lower atmosphere.

The number of photons detected are random and can be approximated by a Poisson statistics. If P is the number of photons detected then the error induced on the LIDAR signal is $\frac{1}{\sqrt{P}}$ (Hauchecorne and Chanin 1980).

The detector noise can be made smaller than signal noise by using a photomultiplier with photon-counting electronics (as in the author's study).

The LIDAR equation given by equation (2.15), can be simplified and written as the detected signal energy from a transmitted light pulse of energy S_o as a function of range z. The return LIDAR signal energy can therefore be written as:

$$S(z) = S_o \cdot \beta \cdot G(z) \cdot l \cdot A \cdot Y \cdot Q \cdot \exp(-2.\gamma(z).z)/z^2 \qquad (2.19)$$

where

β : the volume backscattering coefficient of the atmosphere,

$G(z)$: number of scatterers per unit volume at range z,

l : resolution length,

A : effective area of receiver telescope,

Y : filter transmission,

Q : overall optical efficiency,

$\gamma(z)$: attenuation coefficient.

Both equations (2.15) and (2.19) are identical in nature. The resolution length is equal to $\frac{c.t}{2}$ compare with equation (2.15).

The sky background energy in the receiver (Schwiesow and Lading 1981) is given by

$$S_b = 2 \cdot K \cdot l \cdot A \cdot Q \cdot b \cdot \Omega \cdot \frac{Y}{c} \tag{2.20}$$

where

K : sky radiance,

l : resolution length,

A : effective telescope area,

Q : optical efficiency,

b : receiver spectral bandwidth,

Ω : solid angle field of view,

Y : filter transmission and,

c : speed of light.

This includes the fact that the time interval the receiver is turned on (i.e. open) for a given resolution length l is

$$\Delta t = \frac{2l}{c} \tag{2.21}$$

For a night time sky, K varies widely around 2.5×10^{-1} W/(m^{2}sr nm) at a wavelength of 0.5 μm (Schwiesow and Lading (1981)).

The most effective way to reduce S_b is to reduce Ω and b because these parameters do not appear in equation (2.19), which assumes that the transmitter and receiver fields are properly matched.

Therefore, the overall signal-to-noise ratio is

$$\frac{\text{Signal}}{\text{Noise}} = \frac{\left[\dfrac{\text{Signal(r)}}{h.b}\right]}{\left\{\left[\dfrac{\text{Signal(r)}}{h.b}\right] + \left[\dfrac{\text{S}_b}{h.b}\right] + \left[\dfrac{\text{S}_d}{h.b}\right]\right\}} \tag{2.22}$$

where S_d is the detector noise energy in time Δt, h is the Planck's constant and b is the receiver spectral bandwidth.

2.11 Use of filters to detect higher altitude aerosols

The old LIDAR uses a wavelength of 589 nm which is obtained by tuning the rhodamine-6G laser with a prism grating. This wavelength is chosen as

it differs from the absorption wavelength due to ozone and water-vapour in the atmosphere. The filters, centred at 589 nm with a bandwidth of 10 nm, show that the backscattered signals are not attenuated severely while the night sky noise is reduced considerably.

The new LIDAR uses a wavelength of 532 nm which is obtained by frequency-doubling the fundamental wavelength of the Nd:YAG laser. The wavelength 532 nm is chosen for the same reason as mentioned above. The filters used for the new LIDAR, are centred at 532 nm with a bandwidth of 1 nm. It should be noted that a smaller bandpass removes most of the background noise from the LIDAR return.

A gain in signal can be expected with the use of an ideal filter which has a band pass wide enough to transmit the peak emission bank of the emitter source with nearly 100 % transmittance and yet narrow enough to eliminate most of the night sky emission.

2.12 Spatial and temporal coherence of a LIDAR system

Both spatial and temporal coherence are important in LIDAR applications. This is to ensure that the receiver and emitter of the LIDAR system are well aligned to receive backscattered signals from different heights of the atmopshere. Some LIDARs are basically spatially incoherent in the sense that the illuminated target volume is much larger than that corresponding to the diffraction limit of the largest telescope in the system, that is, larger than a single spatial mode.

Other LIDARs, particularly those with very high spectral resolution, operate in a single spatial mode.

High resolution LIDARs are temporally coherent in the sense that the spectral width of the return is a very small fraction of the optical frequency. The spectral resolution in a Doppler LIDAR, for example, is of the order of

$$\frac{\kappa}{\Delta\kappa} \cong 10^{10} \tag{2.23}$$

where κ is the optical frequency of the return signal.
No LIDAR can be temporally coherent in the sense that the optical phase of the return signal is in a fixed relationship to the phase of the transmitter. This is because each scatterer of the distributed source in the extended scattering volume will scatter independently, and the phase of the scattered wave will be determined by the exact range on a wavelength scale. Scattering from all the centers adds coherently, resulting in a fluctuating amplitude and phase at the receiver. This vector addition is considered more comprehensively by Hardesty *et al.* 1981 and gives a result known as the Rayleigh phasor.

2.13 Spatial Resolution of a Pulsed LIDAR

Fig.(2.6) shows a schematic view of the $\frac{1}{z^2}$ behaviour of the signal from the equation (2.19) applied to a homogeneous atmosphere, i.e a purely molecular atmosphere (no aerosols present).

The transformation between range and time is simply

$$z = \frac{\mathrm{c} \cdot \mathrm{u}}{2} \tag{2.24}$$

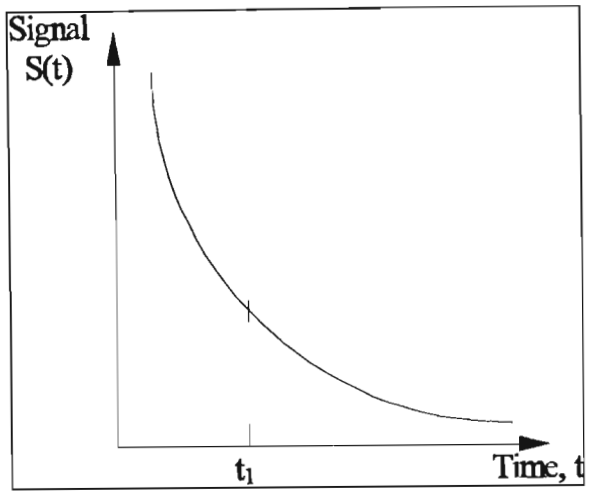

Figure 2.6: LIDAR return versus time.

where u is the round-trip travel time and c is the speed of light, so that these variables may be used interchangeably.

Consider a scatterer at range z and a pulse length p as in fig.(2.7), p is given by

$$p = c \cdot \tau \tag{2.25}$$

where τ being the duration of the pulse.

Assuming that a certain region of the atmosphere contributes to the signal at time u, then from equation (2.24), the range corresponding to a round-trip travel time u_1 is

$$z_1 = \frac{c \cdot u_1}{2} \tag{2.26}$$

Continuously distributed scatterers at a range z_a ($z_a > z_1$) will scatter from the leading edge of the pulse, which departs at a time $-\frac{\tau}{2}$, and will contribute to signal at u_1. This range is

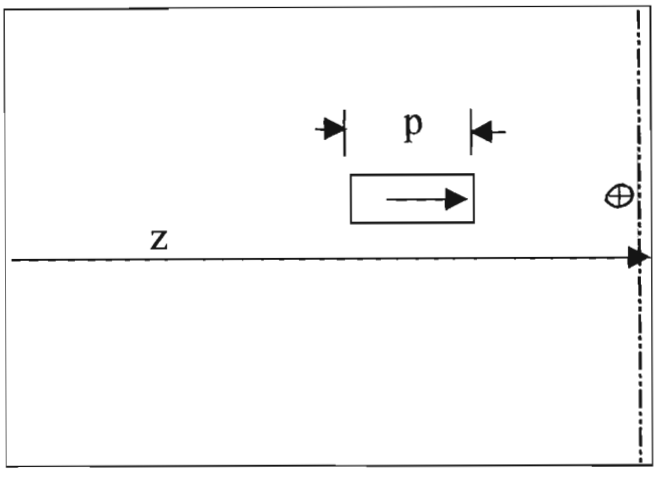

Figure 2.7: LIDAR pulse and scatterer.

$$z_a = \frac{c\left[u_1 + \left(\frac{\tau}{2}\right)\right]}{2} \tag{2.27}$$

Contributions to u_1 can also come from range z_b, where particles scatter from the trailing edge of the pulse at z_b ($z_b < z_1$) given by

$$z_b = \frac{c\left[u_1 - \left(\frac{\tau}{2}\right)\right]}{2} \tag{2.28}$$

Solving for the range resolution Δz between z_a and z_b,

$$\begin{aligned} \Delta z &= z_a - z_b \qquad (2.29) \\ &= \frac{c\left[u_1 + \left(\frac{\tau}{2}\right)\right]}{2} - \frac{c\left[u_1 - \left(\frac{\tau}{2}\right)\right]}{2} \\ &= \frac{c \cdot \tau}{2} \end{aligned}$$

Therefore, the best possible range resolution for a pulsed lidar can be remembered as 150 metres per microsecond, i.e. $\Delta z = 150$ metres for a $\tau = 1\ \mu s$ laser and 0.15 metre for $\tau = 10\ ns$.

If the detector time resolution is longer than τ, then the range resolution is degraded. In this case, a reasonable value $p > c{\cdot}\varsigma$ can be chosen for a range gate by using appropriate time integration at the receiver.

Note that equation (2.29) also applies approximately to any pulse shape provided τ is FWHM of the pulse. The FWHM (Full Width Half Maximum) is twice the 1/e or 86 % criterion for a Gaussian beam diameter where the angular spread of the beam is defined by the width corresponding to the 1/e point for the electric field amplitude at large distance along the axis of the beam.

Chapter 3

Description of the Durban LIDAR systems

3.1 The old Durban LIDAR

The "Old LIDAR system" used in this study was assembled during the period 1991-1992 (M. Kuppen 1992)[1]. The main equipment parameters are listed in table (3.1). Fig.(3.1) shows the receiver and transmitter configuration. PMT is the acronym for the photomultiplier tube.

Model	Phase R
Repetition Rate	0.5 Hz
Energy per pulse at 589 nm	800 mJ
Pulse duration(at FWHM)	0.6 μs
Tuning range	420-760 nm
Divergence of beam	$\approx$ 4mrad
Bandwidth	4nm(FWHM)

Table 3.1: Dye laser specifications.

[1]This LIDAR was originally built at Rhodes University by Dr Richard Grant and installed at the University of Natal by Prof Peter Cunningham and Mr Derek Davies and maintained by Dr A. Prause.

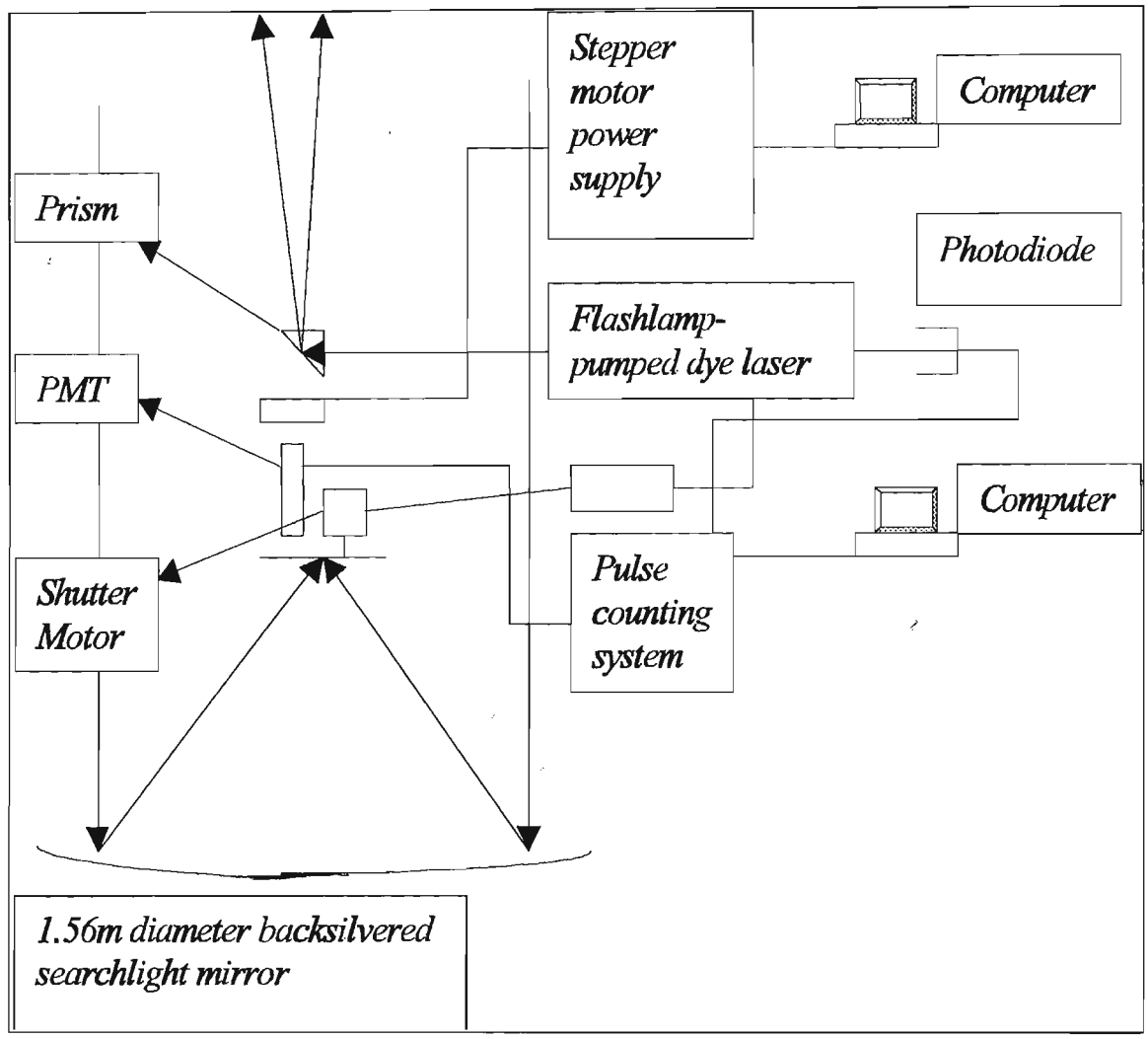

Figure 3.1: Experimental set-up of the old Durban LIDAR system. The acronym PMT stands for PhotoMultiplier Tube.

Two digital computers are used. The first controls the data acquisition and storage, and the second controls the stepper motor for alignment of the 90^0 laser directing prism.

The laser is fired manually in single shot mode every 2 seconds. Each laser shot is detected by a photodiode which is placed at the back of the laser cavity. The photodiode then sends a voltage pulse to the pulse counting system (PCS). This triggers the counters in the PCS and it is at this stage that data collection starts.

The laser beam travels along a plastic tube and strikes the directing prism where it is deflected vertically up in the sky. This is shown in fig.(3.2) which is a three dimensional reconstructed image of the old LIDAR. As the laser beam interacts with air molecules and aerosols it is backscattered. Since the telescope points vertically upwards, only laser radiation scattered vertically down is collected by the mirror and focused onto the aperture.

Two stacked interference filters centred on 589 nm (dye laser is tuned with a prism grating to 589 nm) and 10 nm bandwidth are placed in front of the aperture to discriminate against background radiation. The light is finally collimated and falls on the photocathode of the photomultiplier tube (PMT). The collimating optics have a 79^0 field of view and use only 1.05 m of the mirror surface (Ideally one would like to have a larger collimating system with a greater field of view which would utilise the entire mirror surface).

The light incident on the photocathode consists of large numbers of photons. A large fraction of these photons causes electrons to be emitted from

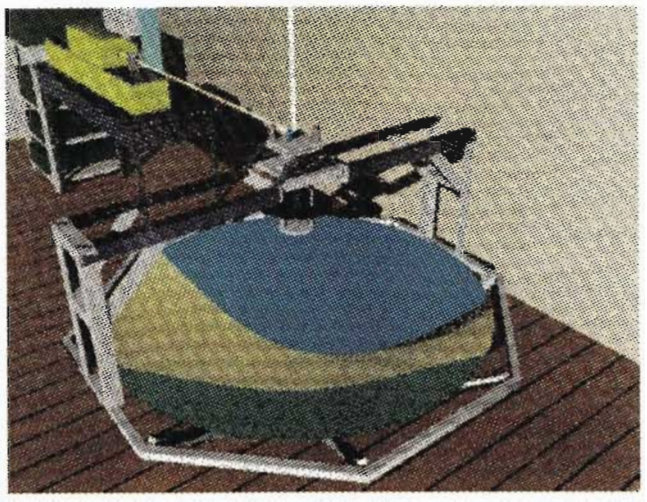

Figure 3.2: Three dimensional reconstruction of the old Durban LIDAR. The rhodamine-6G laser (rectangular green box) can be seen in the back. The thick white line is the emitted laser beam after 90^0 deflection by a prism.

the photocathode of the photomultiplier. These photoelectrons emitted are accelerated by the anode voltage where each electron incident on the dynode releases secondary electrons. Each electron incident on the anode gives rise to a single pulse. These pulses are amplified and fed into the PCS via a long 50 Ω cable where they are counted. The PCS is located in the transmitter chamber while the pulse amplifier is situated close to the PMT. The PCS is shielded from the laser power supply by a Faraday cage.

The moment the laser is fired the PCS starts the counting process and integrates the discrete counts for every microsecond. As calculated in section 2.14, each microsecond corresponds to an altitude range of 150 m. The PCS is designed to store counts for every microsecond for 667 microseconds corresponding to a total altitude of 100 km and hence a profile is built up for each laser shot. On average 150 laser shots are taken and the counts are added to produce a single profile.

3.1.1 LIDAR Specifications

The transmitter

The transmitter consists of a flashlamp-pumped dye laser manufactured by "Phase R". The laser dye is Rhodamine 6G in a concentration of 0.5×10^{-4} moles/litre of methanol. When the dye is optically pumped by the flashlamp, lasing action occurs and a series of pulses of wavelength 589 nm with a total energy of 0.8 J are obtained. Care must be taken not to allow any air bubbles to get in the circulation of the dye as lasing action may be hampered. The windows at the end are cleaned to allow easy transmission of the laser beam along the dye laser. The laser pulselength is 0.6 μs (FWHM) at 589 nm.

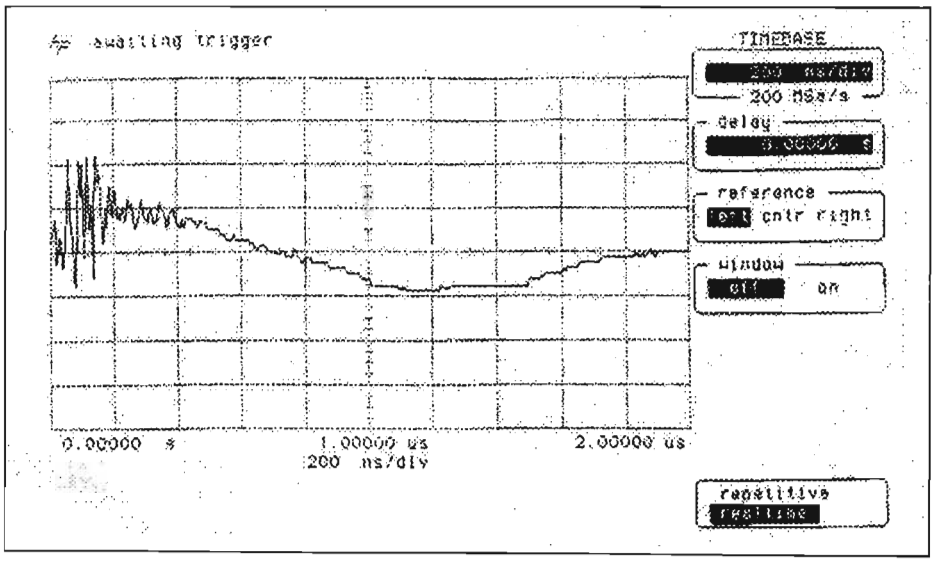

Figure 3.3: Decay time of the laser.

Fig.(3.3) shows a plot of the decay time of the laser. The flashlamp was fired at 11 kV and the signal was measured using a Rogowski coil connected to an oscilloscope. The wild fluctuation in the signal in the beginning is due

to noise in the flashlamp. The decay time was found to be 800 ns.

The homogeneous broadening of dyes means that large energies can be obtained in very narrow line widths and the technology for obtaining controllable narrow-band tunable outputs is well advanced. Flashlamp pumped dyes are attractive because of their high energy output and relative simplicity of construction. They are excellent sources for some applications requiring tunability, high energy, and narrow spectral width (Allain 1979). Harmonic generation using the dye laser outputs is also used to generate additional short wavelength LIDAR sources with tunability.

3.1.2 The receiver

The receiver consists of a 1.56 m backsilvered parabolic searchlight mirror with a focal length of 654 mm. Collimating optics are positioned at the focus of the mirror. These consist of a microscope objective with a field of view of 79^0 followed by a variable aperture (1 mm-10 mm). The aperture is set to 5 mm paying particular attention to the attenuation of the returned signal. Two stacked 589 nm interference filters each with a bandwidth of 10 nm and 50 % transmission are placed in front of the collimating optics. These filters absorb a large proportion of the background light. The photomultiplier tube (EMI 9558B) is mounted immediately after the collimating optics.

3.1.3 The dynamic range of the receiver

The operation of the receiver as well as the transmitter is based entirely on pulse techniques. High voltage is applied to the photomultiplier only when it is to receive reflected signal from the upper atmosphere. This method of

operation has several advantages:

(i) The removal of photomultiplier fatigue due to the passing of stray intense light.

(ii) The possibility of turning the receiver on only after the laser has been fired. This reduces internal noise to be detected by the photomultiplier.

3.1.4 Photomultiplier

The 9558B photomultiplier was chosen because it has a large spectral range covering the wavelength bandwidth of the laser. Photomultipliers are mainly used in photon counting, spectrophometry and film scanning.

The photomultiplier tube (PMT) used in the old Durban LIDAR experiment has no cooling system and is mounted immediately after the collimating optics.

Theory of photomultipliers

When light is incident on a photomultiplier, photoelctrons are emitted from the cathode. These are then accelerated by a voltage of a few hundred volts and are focused onto the metal surface (e.g. Cu-Be) of the first "dynode" where each impinging electron releases on the average q secondary electrons. These electrons are further accelerated to a second dynode where each secondary electron again produces about q tertiary electrons, and so on. The amplification factor q depends on the accelerating voltage U, on the incidence angle α, and on the dynode material. Typical figures for U= $200V$ are q= $3-5$. A photomultiplier with 10 dynodes therefore has a total current

amplification of C $= q^{10} \approx 10^5 - 10^7$.

In general a photomultiplier of y dynodes will produce a charge avalanche at the anode of C $= q^d e$ and corresponding voltage pulse of

$$B = \frac{C}{W} = \frac{q^d e}{W} = \frac{Ce}{W} \tag{3.1}$$

where W is the capacitance of the anode (including connections).

Sources of noise in photomultipliers

There are three main sources of noise in photomultipliers:

(i) Photomultiplier dark current

(ii) Noise of the incoming radiation

(iii) Shot noise and Johnson noise of the load resistor.

(a) Photomultiplier dark current

When a photomultiplier is operated in complete darkness, electrons are still emitted from the cathode. This dark current is mainly due to thermal agitation of electrons and is strongly dependent on the ambient temperature. It is also partly caused by cosmic rays or by radioactive decay of spurious radioactive isotopes in the multiplier material. In order to decrease the dark current, the temperature of the cathode must be reduced. However, excessive cooling can cause undesirable effects such as reduction of signal photocurrent or voltage drops across the cathode because the resistance of the cathode film increases with decreasing temperature.

The PMT (9558B) used in the old LIDAR is not cooled as a water-cooled or liquid nitrogen-cooled PMT was not available.

(b) Amplification noise in the photomultiplier The noise due to photocurrent is amplified in the photomultiplier by the gain factor C. The r.m.s. noise voltage Υ across the anode load resistor X is therefore

$$< \Upsilon >= X \cdot (2 \cdot C \cdot e \cdot i_a \cdot \Delta\vartheta)^{\frac{1}{2}} \tag{3.2}$$

where i_a is the anode current, e is the electronic charge of the electron and $\Delta\vartheta$ is the change in frequency of the r.m.s. voltage.

The gain factor C itself is not constant but shows fluctuations due to random variation of the secondary emission coefficient q which is a small integer. This contributes to the total noise and multiplies the r.m.s. noise voltage by a factor $g > 1$ which depends on the mean value of q. Typical values of the gain factor C are 10^5-10^6.

(c) Shot noise and Johnson noise When radiation is incident on the cathodes of the photomultiplier tube, photoelectrons are emitted from the cathodes. The photoelectron current associated with the emitted photoelectrons has a noise called the shot noise of the photoelectron current. For a detection system of bandwidth Δb, the photocurrent has a r.m.s. value of

$$< i >_{Shot} = (2 \cdot e \cdot i \cdot \Delta b)^{\frac{1}{2}} \tag{3.3}$$

where i is the actual photoelectron current.

When the photoelectron current flows through a load resistor X at a temperature M, it generates a noise in the resistor called the Johnson noise. Using the Nyquist formula, the magnitude of the Johnson r.m.s. noise current of the load resistor X at a temperature M is given by

$$< i >_{Johnson} = \left(\frac{4 \cdot k \cdot M \cdot \Delta b}{X}\right)^{\frac{1}{2}} \tag{3.4}$$

where k is the Boltzmann constant, Δb is the frequency bandwidth of the detection system.

The total r.m.s. noise voltage is therefore

$$< \Gamma_{Total} >= X \left(< i >^2_{Shot} + < i >^2_{Johnson}\right)^{\frac{1}{2}} = \left[e \cdot X \cdot \Delta b \cdot \left(2X \cdot i + \frac{4 \cdot k \cdot M}{e}\right)\right]^{\frac{1}{2}} \tag{3.5}$$

From equations (3.2) and (3.5), the sum of shot noise and Johnson noise across the anode load resistor R at room temperature where $\frac{4 \cdot k \cdot M}{e} \approx 0.1$ V is

$$< \Gamma >_{Johnson+Shot} = e \cdot X \cdot \Delta b \cdot \left(2 \cdot C \cdot g^2 \cdot X \cdot i_a + 0.1\right)^{\frac{1}{2}} \tag{3.6}$$

For $C \cdot g^2 \cdot X \cdot i_a \gg 0.05$ V, the Johnson noise can be neglected. With a gain factor $C = 10^6$ and a load resistor of $X = 10^5$ Ω this implies that the anode current i_a should be larger than $5 \times 10^{-13} A$. The photomultiplier dark current dark current is already much larger than this limit, the Johnson noise does not contribute to the total noise of photomultipliers but it cannot be neglected.

3.2 The new Durban LIDAR

Figure 3.4: The new Durban LIDAR set-up.

The new LIDAR, installed in April 1999, is a much more sophisticated system than the old. Fig.(3.4) shows the configuration of the new LIDAR system. Like the old LIDAR, it consists of a transmitter (a pulsed laser), a receiver (biaxial telescopes), a photodetector (a photomultiplier tube) and an electronic acquisition system controlled by a computer.

3.3 Location of the LIDAR systems

The two LIDAR systems (the old and the new) are situated on the roof of the Desmond Clarence building at the University of Natal. The building is

five storeys high. This location was chosen to avoid stray lights from the surrounding city lights and the Durban harbour from interfering with the return LIDAR signal. All the equipments of the old LIDAR, viz. receiver and transmitter, are housed in a container which has a one metre diameter circular lid opening on the receiver side. The transmitter chamber is well air-conditioned. The new LIDAR system is found in a Wendy house which is attached to the container of the old LIDAR. Fig.(3.5) shows a schematic view of the set-up of the new LIDAR system inside the Wendy house.

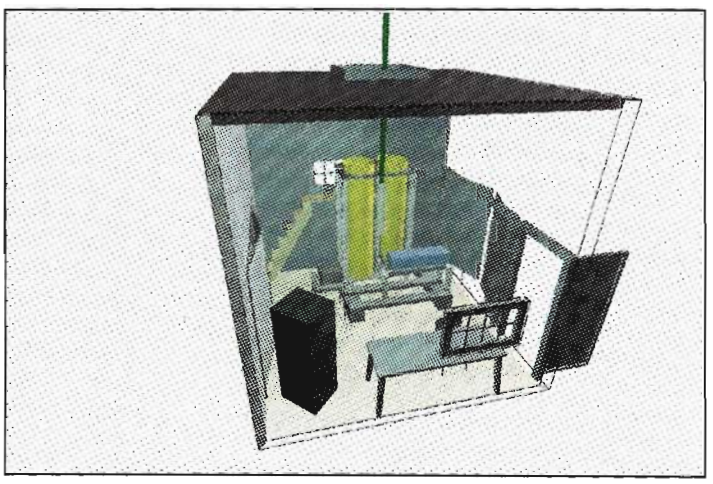

Figure 3.5: Schematic view of the interior of the wendy house showing the set-up of the new LIDAR. The vertical green box on the left is the electronic acquisition system; the laser beam can be seen projected vertically into the atmosphere after passing through the Galilean telescope.

3.3.1 The transmitter

The transmitter consists of a pulsed Nd:YAG (Neodymium:Yttrium Aluminium Garnet) laser. The fundamental wavelength $\lambda_0 = 1064$ nm is frequency-doubled using a potassium dihydrogen phosphate (KDP) crystal to produce the emission wavelength $\lambda_e = 532$ nm. The main characteristics of the laser

are summarised in table (3.2).

Model	GCR-150 (Spectra Physics)
Repetition rate	10 Hz
Energy per pulse (Q-switch mode)	650 mJ for $\lambda_0 = 1064$ nm
	300 mJ for $\lambda_e = 532$ nm
Pulse width	$\approx$ 6-7 ns for $\lambda_e = 532$ nm
	$\approx$ 8-9 ns for $\lambda_0 = 1064$ nm
Beam divergence (FWHM) before beam expansion	$\approx$ 0.7 mrad
Beam divergence after beam expansion	$\approx$ 0.07 mrad
Diameter of beam before expansion	$\approx$ 8 mm
Diameter of beam after expansion	$\approx$ 80 mm

Table 3.2: Characteristics of the laser for the new LIDAR.

The emission wavelength λ_e has been selected so that it does not correspond to any transition characteristic of any constituent of the atmosphere (absorption or resonance). Two pairs of dichroic mirrors are used at emission to separate the second harmonic from the fundamental wavelength. The dichroic mirrors have coatings which have refractive indices lower for λ_0 but higher for λ_e. The mirrors allow 96 % reflection of λ_e. λ_0 is absorbed by a beam trap after the frequency doubling by the KDP crystal.

3.3.2 The emitter

The new LIDAR system at Durban operates with two acquisition channels, referred to channel A and channel B. Channel A allows vertical temperature and relative density profiles to be measured in the stratosphere and lower mesosphere (from 10 km to 60 km). Channel B allows measurement in the

troposphere and lower stratosphere (from 10 km to 45 km) of aerosol profiles. A correction has been done on the temperature and relative density profiles on the altitude overlap of the two channels.

The laser pulses are transmitted vertically into the atmosphere after passing through a system of mirrors and a Galilean telescope.

Let ξ be the divergence of the laser beam (diameter d) before entering the Galilean telescope and ξ' be the divergence of the beam (diameter D) at the exit of the telescope.

ξ and $\xi'$are related to D and d by Lagrange invariance:

$$D \cdot \xi' = d \cdot \xi, \quad \therefore \frac{D}{d} = \frac{\xi}{\xi'} \tag{3.7}$$

Using the values for ξ and ξ' from table (3.2), $\frac{D}{d} = \frac{0.70}{0.07} = 10.$

This factor 10 beam-expansion reduces the divergence of the emitted beam by the same amount and also increases the laser-atmosphere surface interaction. Typically, for the new LIDAR $\xi' = 0.070$ mrad.

3.3.3 The receivers

Channel A

In the field of view of the mirrors of channel A, the backscattered photons from different heights of the atmosphere are received by two parabolic mirrors (diameter $\phi_{mirror} = 445$ mm). The mirrors are held inside two long tubes, as shown in fig.(3.6), which shield them from luminous interference. Channel A allows backscattered photons to be received from 12 km to 60 km. After collection by the telescope the photons are transmitted by optical

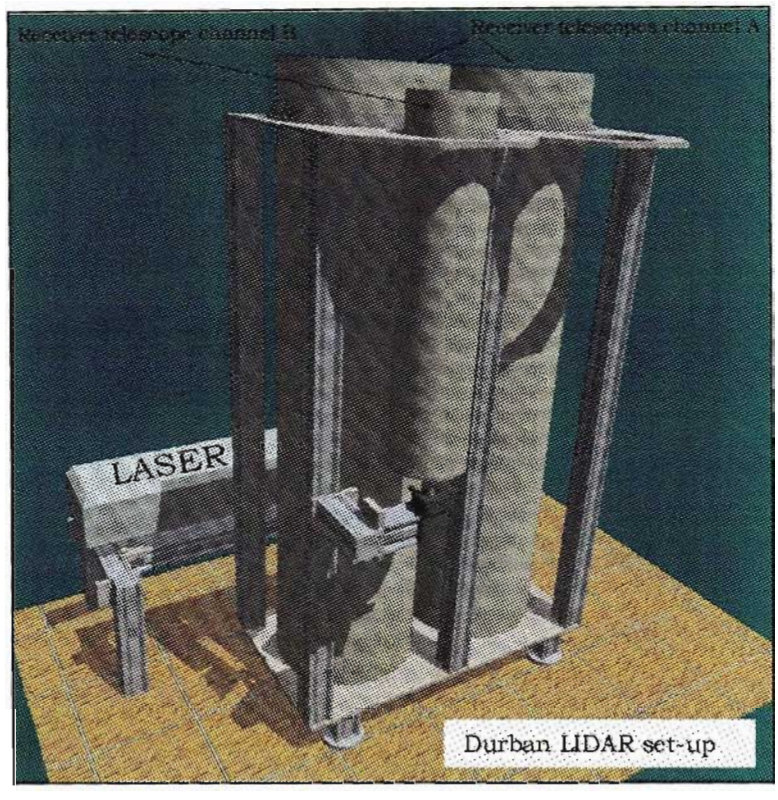

Figure 3.6: Schematic view of the receivers of channel A and B.

fibres (diameter $\phi_{fibre} = 1$ mm) placed at the focal point of each mirror, to the detection box which contains a collimator, an interference filter and a photomultiplier tube (PMT). The interference filter centred on $\lambda_e = 532$ nm and bandwidth $\Delta\lambda = 1$ nm is placed between the arrival point of the fibre and the PMT.

Channel B

As shown in fig.(3.6), channel B consists of a smaller mirror ($\phi_{mirror} = 200$ mm) used to receive backscattered photons from the lower layers of the atmosphere. Mounted bistatically, the mirror can receive signals from 10 km to 45 km. As with channel A, the mirror of channel B is held inside a

tube which shields it from luminous interference. Table (3.3) summarises the characteristics of the receiver systems.

Receivers	Channel	Specifications
Telescope (×2)	A	Parabolic mirrors: $\phi_{mirror} = 445$ mm
		Focal length, $f_A = 2000$ mm
Telescope (×1)	B	Parabolic mirror: $\phi_{mirror} = 200$ mm
		Focal length, $f_B = 1000$ mm
Optical fibres (×2)	A	$\phi_{fibre} = 1$ mm
Optical fibre (×1)	B	$\phi_{fibre} = 1$ mm
Interference filter (×1)	A	Centred on $\lambda_e = 532$ nm
		Bandwidth $\Delta b = 1$ nm
Interference filter (×1)	B	Centred on $\lambda_e = 532$ nm
		Bandwidth $\Delta b = 1$ nm

Table 3.3: Characteristics of the receiver system.

3.3.4 The Detector and Data acquisition system

Type	Hamamatsu R 1477
Maximum Voltage	900 V
Gain	10^7
Quantum efficiency at 532 nm	17 %
Cathode sensitivity	72.9 μA/W
Rising time	2.2 ns
Transit time	22 ns
Anode dark current	typical 2 nA
	max 5 nA

Table 3.4: Specifications of the photomultiplier of the new LIDAR.

The main characteristics of the R 1477 PMT are summarised in table (3.4). The PMT (Hamamatsu R 1477) of the new LIDAR system is a photodetector of high sensitivity. The R 1477 is equipped with a multialkaline

photocathode (Na, K, Sb, Cs) of high sensitivity and has 9 dynodes. The spectral response covers the range from 185 nm to 900 nm with a maximum at 450 nm wavelength. The R 1477 has a high gain and a low dark current.

The new LIDAR system uses a PMT which is contained in a Peltier effect cooling system (model C659-S) which reduces the dark current by lowering the cathode temperature and maintaining it between -15 ^{0}C and -20 ^{0}C. The Peltier cooling system has a built-in water cooling system.

The signals detected by the PMTs are amplified by pre-amplifiers which are mounted directly above the PMTs. The signal is reconstructed for each channel in terms of the number of photon counts per μs. Each electronic bin of the acquisition system corresponds to an integration time of 1 μs. Hence the vertical resolution of the LIDAR is 150 m. The acquisition system stores the data in counts every microsecond for a duration of 1024 μs (1024 electronic bins). Each bin corresponds to a vertical resolution of 150 m. The maximum theoretical height attainable by the LIDAR is 153.6 km. The vertical resolution can be degraded by grouping the bins.

An electronic shutter is applied on the PMT of channel A which prevents saturation due to strong returns from the lower layers of the atmosphere. The electronic shutter operates as follows: a reverse voltage is applied to the second dynode or simultaneously to all the dynodes of the PMT for a time Δt which prevents acceleration of the photoelectrons. A certain amount of time is necessary before the PMT stabilises to its normal working state (100 μs which correspond to a vertical height of 15 km). Recent improvements in shutter function have reduced this transition period from 100 μs (15 km) to 10 μs (1.5 km) by simultaneously applying a weaker reverse voltage on

several dynodes of the PMT. By using an electronic shutter, the LIDAR signal is improved. The saturation of the photomultiplier for LIDAR returns from the lower atmosphere is reduced.

The electronic shutter for channel A was set to $\Delta t = 60$ μs, which corresponds to a vertical resolution of 9.0 km. Backscattered photons of the lower atmosphere ($0 \leq z \leq 9$ km) are not received by the PMT. Figs. (3.7)-(3.8) show this effect where the curves represent two acquisitions, one done without electronic shutter (June 2 1999) and the other with electronic shutter set at $\Delta t = 60$ μs (June 8 1999).

3.4 Sources of error in the LIDAR measurements

In any measurement, the study of errors is a critical step which cannot be avoided. The exploitation of the LIDAR data for the study of the thermal structure of the middle atmosphere is becoming increasingly important and it is necessary to identify all possible errors that affect the LIDAR measurements. The errors can be classified into three categories:

(i) Instrumentation errors,

(ii) Errors associated with the optics,

(iii) Errors induced on the temperature profiles due to aerosols.

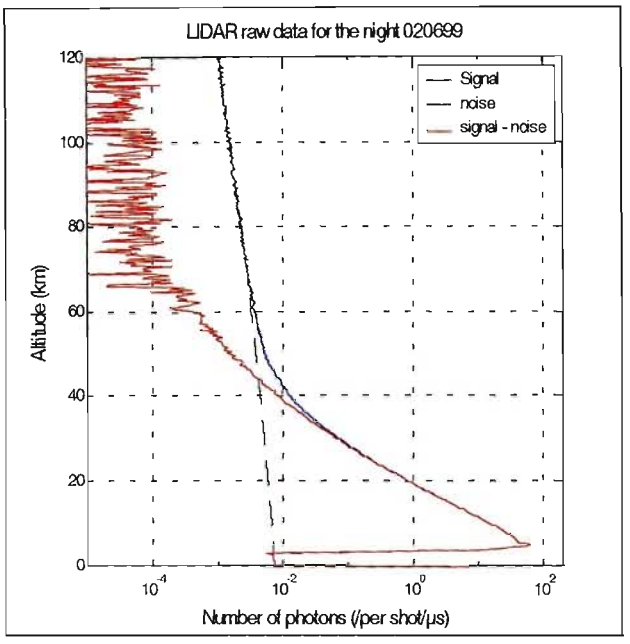

Figure 3.7: Plot of LIDAR raw data for June 2 1999 where no electronic shutter has been used.

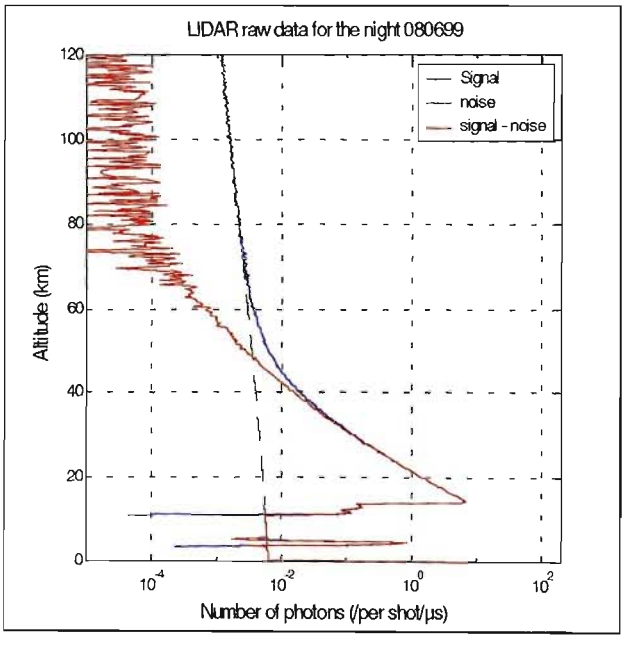

Figure 3.8: Plot of LIDAR raw data for June 8 1999 where electronic shutter has been used at $\Delta t = 60\ \mu s$.

3.4.1 Instrument errors

Dynamic range of the signal

One of the difficulties encountered with the measurement of the atmospheric density on a large vertical scale is the large dynamic range of the signal. The density of the atmosphere, from 30 to 90 km, decreases exponentially by an order greater than 4; in addition to this, the solid angle $\propto \frac{1}{(z-z_0)^2}$ varies by an order of 10 for the same height range. It is therefore necessary to look for a detection system that is capable to take precise measurements on a scale $\geqslant 5$ orders of magnitude. Up to now there is no detector available on the market which can take measurements with a precision of order $\geqslant 5$. In order to resolve this problem, two acquisition channels are used. Channel A allows the sounding of the upper atmosphere (from 20 km to 60 km) and channel B the lower atmosphere (from 12 km to 40 km). By having large telescopes (channel A) and a small telescope (channel B), the large dynamic range of the LIDAR return signal can be resolved into two altitude ranges.

Saturation of the detector

With the availability of more powerful lasers of high repetition rate and larger receiver telescopes, the number of backscattered photons received above 50 km is still low, and represents on average a few photons per thousands of shots (Keckhut et al., 1993). The detection of backscattered signals at higher altitudes ($\geqslant$ 50 km) is possible with a photomultiplier working in photon-count mode only. However for the low altitude, the number of backscattered photons increases considerably so that the photomultiplier tube (PMT) cannot

count all the photons received on the photocathode. The PMT reaches a state of saturation after receiving more photons than it can count. Also the band pass (100 MHz) of the acquisition system sets a limit to the counting rate of the photons. Furthermore, if the PMT is not protected, the large scattering from the low altitudes causes an induced current on its photocathode, which adds a spurious signal to the backscattered signal over the entire altitude range.

To overcome the saturation effect of the PMT, three methods are often employed:

(i) using a geometrical shutter by adjusting the alignment of the receiver and emitter, and increasing the distance between the receiver and emitter axes.

(ii) protecting the photocathode of the PMT by a mechanical rotating shutter whose speed can be adjusted to select the appropriate range of height for a set of laser firings.

(iii) inhibiting the functioning of the PMT for a certain time, Δt, by applying an electronic shutter.

The first method is no longer in use because it indroduces parallax error on the backscattered signal. Electronic shutters are used more often than the mechanical rotary shutters. This is because of their great flexibility in adjusting the shutter opening time Δt according to the altitude range for which sounding is required. Electronic shutters are applied to channel A as described above. No electronic shutter is applied to the signal of channel B. This is because in the inversion programme to obtain aerosol profile from channel B, the profile starts from 9 km which is well above saturation effects

of the PMT. Saturation effect can also be reduced by using a laser of higher repetition rate for example, 50 Hz or 60 Hz.

In most cases not all the light actually hits the optical fibres of channel A and B, which are placed in the focal planes of the receiver optics for optimum collecting efficiency from infinity. Light power is normally lost by 2 mechanisms:

(i) the overlap of the transmitted beam with the receiver field of view is often incomplete as in noncoaxial systems.

(ii) light backscattered from small and medium distances is not focused in the focal plane, but forms there a diffuse intensity pattern only part of which is sensed by the optical fibre.

Both effects give rise to a deviation of the detector power from the $\frac{1}{z^2}$ dependence as given by the LIDAR equation. In order to reduce the saturation effects of the PMT, the new LIDAR employs an electronic shutter on the PMT which opens and closes according to the time Δt set on the electronic shutters.

Linearity of the PMT

In practice, the photons arrive randomly on the photocathode and if the events are indistinguishable, several events may be counted as one event. The use of electronic shutters allows one to choose an optimum altitude z_0 where the backscattered photons are not received by the PMT for the time Δt set on the PMT. However, due to strong returns from low altitudes, the saturation effect of the PMT is not completely eliminated.

The arrival of backscattered photons on the photocathode are random

and can be assumed to follow a Poisson distribution. The non-linear response of the PMT in the low altitudes can be represented by an exponential law (Pelon 1985) with an accuracy of approximately 5 %.

Let P_c be the number of backscattered photons counted by the PMT and P_r the number of photons received by the photocathode. Then P_c and P_r are functionally related by:

$$P_c = P_r \exp(-\frac{P_r}{P_{\max}}) \tag{3.8}$$

where P_{max} is the maximum number of photons that the PMT can count.

For a first approximation, $P_{max} = \frac{t}{\tau}$, where t is the integration time of the PMT at the acquisition system (1 μs), and τ is the amount of time required before the PMT returns to its stable operating conditions.

Finally, the photons received are not all counted by the electronic counting system in the acquisition. This can be explained by the fact that the photons arrive simultaneously so that two or more photons are counted as one.

Errors associated with the optics

The density of the atmosphere is deduced directly from the number of backscattered photons. It is therefore necessary to collect most of the photons scattered in the receiver telescopes. This requires that the field of view of the receiver telescopes overlaps that of the laser. In other words, the scattering volume must lie within the field of view of the telescopes. The latter criterion is affected by four factors:

(i) Divergence of the laser,

(ii) Parallax effect,

(iii) Defocussing effect and

(iv) Quality of the optics and turbulence of the atmosphere.

Fig.(3.9) shows a schematic diagram of the factors affecting the scattering volume entering the field of view of the receiver telescope.

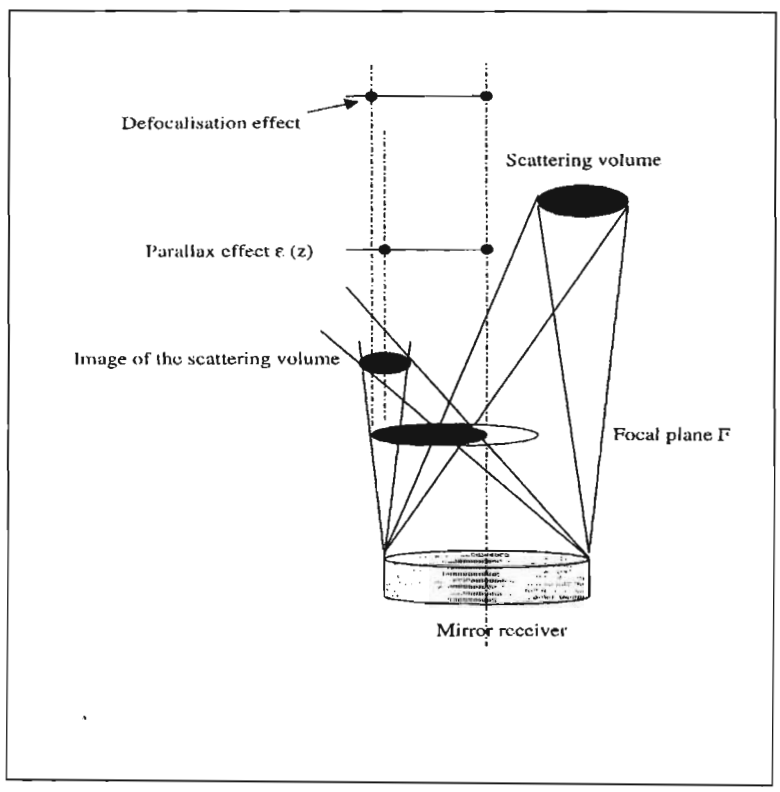

Figure 3.9: Schematic diagram showing the geometry due to parallax and focal aperture obstruction effect that arise in the focal plane of the receiver (Keckhut et al. 1993).

Divergence of the laser

If the laser emission could be considered to be of a purely TEM_{00} mode, the light intensity I, at a fixed altitude z would display a Gaussian profile

(Gaubau 1963, Kogelnik and Li 1966):

$$I(r,z) = \frac{J_0}{\pi \cdot \omega^2(z)} \exp\left[\frac{-z^2}{\omega^2(z)}\right] \tag{3.9}$$

where J_0 is the laser output power and $\omega(z)$ is the halfwidth of the laser beam.

The halfwidth increases with z as :

$$\omega^2(z) = \omega_0^2\left[1 + \left(\frac{\lambda \cdot z}{\pi \cdot \omega_0^2}\right)^2\right] \tag{3.10}$$

where ω_0 is half the width of the laser at emission i.e, the z = 0 plane. In the case of Rayleigh-Mie LIDAR, for large distances from the width of the beam, $z \gg \frac{\pi \cdot \omega_0^2}{\lambda}$, the beam diverges linearly with z, and the corresponding diffraction-limited far-field Gaussian-beam divergence half angle is

$$\theta = \frac{\omega(z)}{z} = \frac{\lambda}{\pi \cdot \omega_0} \tag{3.11}$$

which is in fact the minimum that can be achieved.

By minimising the divergence of the laser, the size of the scattering volume is reduced. This is achieved by using a Galilean telescope as emitter, where the focal lengths of the diverging and converging lenses inside the telescope have been chosen to give a reduction in divergence of the beam by a factor of 10.

The divergence ξ of the laser beam before entering the Galilean telescope is taken as the sum of the divergence of the laser specified in the manual of the laser (0.50 mrad at FWHM) and the uncertainties in the beam (0.20 mrad) due to its axial direction.

Thus ξ = 0.70 mrad.

Parallax effect

The new LIDAR system has a non-coaxial configuration in which the receivers and the transmitter are separated. This configuration leads to a parallax error of the image of the scattering volume at the focus of the receiver telescope. The parallax error ($\varphi(z)$) can be deduced by the following simplified equation:

$$\varphi(z) = \frac{f \cdot \Delta}{z} \tag{3.12}$$

where f is the focal length of the receiver telescope, Δ is the axial separation of the emitter and receiver telescopes, and z is the altitude studied.

For the high altitude channel (channel A), $f_A = 2.00$ m, $\Delta_A = 0.50$ m. Therefore, the parallax error φ_A at an altitude z is

$$\begin{aligned} \varphi_A &= \frac{2.00 \times 0.50}{z} \\ &= \frac{1}{z} \end{aligned}$$

For channel B, $f_B = 1.00$ m, $\Delta_B = 1.00$ m. Therefore, the parallax error φ_B at the same altitude z is

$$\begin{aligned} \varphi_B &= \frac{1.00 \times 1.00}{z} \\ &= \frac{1}{z} \end{aligned}$$

At any given altitude z, this shows that the parallax error is the same for both channels.

It should be noted that at the focus of each receiver, an optical fibre is placed. The diameter ϕ of the optical fibre determines the field of view of the telescope at infinity. Both channels have the same optical fibres, with ϕ = 1 mm.

Defocussing effect

The soundings from different layers of the atmosphere are not all found at infinity. Their images are therefore not formed at the same distance in the focal plane of the receiver. Hence these images are much larger in the plane of the optical fibre and are therefore defocussed. The image of the scattering volume is observed with a small telescope installed at the top of the receiver mirror (fig.(3.10)). The small telescope is adjusted so that it receives light from a distant object, for example the moon. The small telescope is then directed towards the centre of the receiver and its position adjusted until the backscattered laser light from the scattering volume can be seen through it.

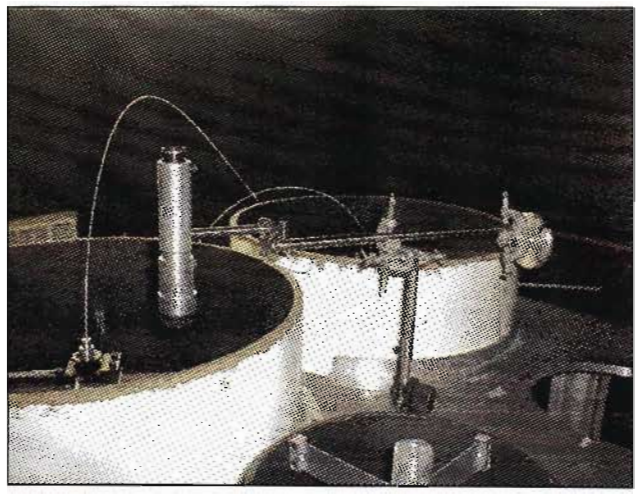

Figure 3.10: The small telescope shown next to the tube is used to view the backscattered laser light from the scattering volume.

The defocussing Λ of the image of the scattering volume at a given altitude z can be expressed by the following equation:

$$\Lambda = \frac{f \cdot \phi}{z} \tag{3.13}$$

where f is the focal length of the mirror and ϕ is the diameter of the receiver.

For the Durban LIDAR, the mirror of channel A has a diameter $\phi = 0.445$ m and focal length $f = 2.00$ m. The defocussing of the image of the scattering volume as observed from a height of 10 km is

$$\begin{aligned} \Lambda &= \frac{2.00 \times 0.445}{10000} \\ &= 8.90 \times 10^{-5} \text{ m} \\ &= 0.089 \text{ mm} \end{aligned}$$

The defocussing effect is assumed to be negligible compared to the other factors affecting the scattering volume.

Quality of the optics and turbulence of the atmosphere

The scattering volume is also affected by the quality of the optics (lenses are free from aberrations, the aluminium coating on the receiver mirrors are free from distortions, etc) used in the LIDAR experiment. This parameter is estimated to be 0.03 mrad. Atmospheric turbulence can also affect the size of the scattering volume and is estimated to be 0.02 mrad.

In the case of Rayleigh-Mie LIDAR, to a good approximation the total size of the scattering volume V is a linear combination of all the four factors discussed above and is given by

$$V \approx \xi + \varphi + \Lambda + \delta \tag{3.14}$$

where ξ = divergence of the laser,

φ = parallax,

Λ = defocussing,

δ = quality of the optics and atmospheric turbulence.

The effects of aperture and obstruction of the receiver telescope has been derived mathematically in Appendix D.

3.4.2 Errors induced on the temperature profiles due to aerosols

Generally speaking, the term coming from the Mie scattering due to aerosols $\beta_a(z)$ is added to the Rayleigh term $\beta_m(z)$ in the LIDAR equation. The number of photons received is multiplied by a factor R(z), known as the scattering ratio, and defined as:

$$R(z) = 1 + \frac{\beta_a(z)}{\beta_m(z)} \tag{3.15}$$

In the presence of aerosols, the determination of the density of the atmosphere by the measurement of backscattered photons is overestimated and is a function of R:

$$\frac{\Delta M(z)}{M(z)} = \frac{\Delta G(z)}{G(z)} = R(z) - 1 \tag{3.16}$$

where $G(z)$ is the concentration of air molecules and $M(z)$ is the LIDAR temperture profile derived from the density profile.

During periods of major volcanic eruptions, Mie scattering due to particles in suspension can contribute to the backscattered signal up to altitudes

of 38 km (Lefrère *et al.* 1981; Thomas *et al.* 1987). This represents a major limiting factor for the downward extension of the temperature measurements. In order to resolve this problem, we make use of the vibrational (Keckhut *et al.* 1990) or rotational (Hauchecorne *et al.* 1992) Raman scattering of the nitrogen molecule. Unfortunately, the new LIDAR is not equipped with a Raman channel to enable us to take temperature measurements in the troposphere.

Another problem which often arises in the determination of R (equation (3.15)) is the determination of the altitude at which the atmosphere is 'clean' (no aerosols). Russell et al. (1979) determine R with an accuracy of less than 0.3 %. One solution will be to compare simultaneous Rayleigh and Raman backscatter. Unfortunately, even if this solution is not based on any hypothesis on the nature and characteristics of the aerosols, it does not provide the necessary accuracy. In the case of Durban, the lower limit at which we consider the atmosphere to be absolutely free of aerosols is 38 km.

To summarise, we can posit that the errors on the temperature profiles are localised at two distinct height ranges:

(1) At the top of the temperature profile, the extraction of the background noise, the initialisation of the pressure profile and the photon noise may affect the temperature measurements,

(2) Errors associated with the lower part of the temperature profile are due to presence of aerosols, the nonlinear correction of the PMT, and the alignment of the emission and reception telescopes.

Chapter 4

Alignment Procedure

4.1 Introduction

Rough alignment of the old and the new LIDARs is usually done during the day. The fine alignment of the receivers of the new LIDAR is best done at night on the basis of the LIDAR return signal. The alignment of the transmitter of the old LIDAR is done with the LIDAR return signal. Both LIDARs are operated only at night under clear skies.

4.2 Alignment of the old LIDAR

Before any measurements can be taken, the receiver and transmitter (laser) must be aligned properly otherwise the measurements may be erroneous. This is usually done twice a day in the absence of wind as the latter tends to move the prism mounting. If there is reason to believe that the alignment is off axis due to strong winds then care is taken to realign the system again.

4.2.1 Alignment of the old LIDAR receiver

The receiver was already aligned (Kuppen 1992) and was used in that state without further manoeuvring. Two important conditions must be met during the alignment procedure of the receiver:

(i) The mirror must point vertically upwards.

(ii) Vertical rays of light reflected off the mirror must pass into the aperture of the PMT. Therefore collection optics must be situated precisely at the focus of the mirror.

4.2.2 Alignment of the mirror and photomultiplier

Both the mirror and photomultiplier were already aligned (Kuppen 1992) and were used in this state. Nevertheless the alignment of the mirror is previously checked to make sure that it was not tilted off the vertical position. Fig.(4.1) shows the large searchlight mirror with collimating optics and two stacked 589 nm interference filters at the focus of the mirror.

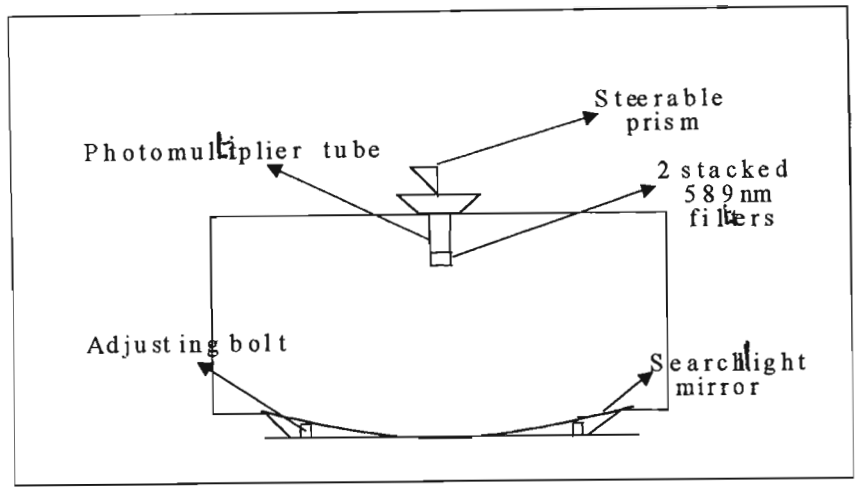

Figure 4.1: Alignment of the mirror.

The mirror is then adjusted by means of adjustment bolts at the base of the mount. Assuming that there is no imperfection in the mirror and that the rims are horizontal with respect to the base of the mirror, we can safely conclude that the mirror is now pointing vertically upward.

The author assumes that the alignment of the photomultiplier has not changed and is at the focus of the mirror.

4.3 Alignment of the laser

Fig.(4.2) shows the method used to align the laser. A dish of oil is placed on top of the system directing prism. Viscous oil is used to avoid vibration. A plane mirror inclined at 45^0 is clamped over the dish. A He-Ne laser is directed to the mirror. The light gets reflected on the mirror and falls onto the oil surface where it again gets reflected back onto itself. The mirror and the He-Ne are adjusted so that the reflected laser beam (He-Ne) falls exactly

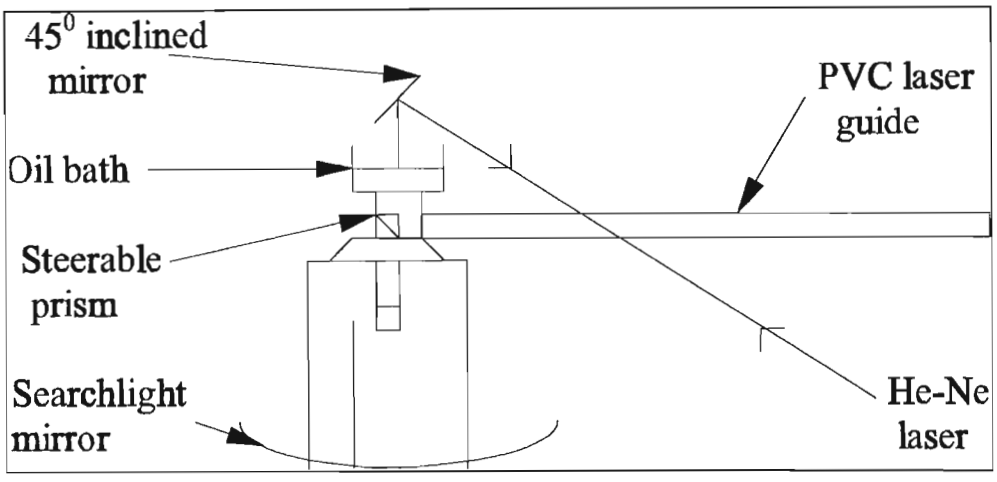

Figure 4.2: Alignment of the laser.

on the aperture of the He-Ne.

The oil dish is then removed and the He-Ne laser beam is allowed to strike the prism after reflection off the mirror. The beam undergoes multiple reflections before falling back onto itself, that is, on the aperture of the He-Ne laser.

In order to bring the reflected He-Ne laser beam as close as possible to the aperture, the shafts of the steerable table on which the directing prism rests are tweaked manually.

The He-Ne laser is then allowed to pass back into the transmitting system, that is, through the dye laser. The dye laser is then adjusted so that the He-Ne laser passes centrally through the tube and falls on the centre of the mirror. The front and back mirrors are then tweaked to ensure that the back reflections due to the laser beam pass back to the aperture of the He-Ne laser.

When the alignment is completed, interference "fringes" are seen on the

aperture of the He-Ne . Before dismantling the alignment system, the 100% reflector mirror is removed and the He-Ne laser is allowed to strike the photodiode. The latter is adjusted such that the laser beam falls on the centre of the diode. This is important so that the photodiode will pick up only laser light and not flashlamp light. The diode is used to trigger the Pulse Counting System (PCS).

4.3.1 Suggested method to align the prism using the stepper motor

During operation of the laser, the beam is fired onto a 90^0 prism which in turn directs the beam vertically up into the sky. It is therefore imperative that the prism should be aligned with a high degree of precision. This is done by a system of two stepper motors incorporated in the design of the prism table (Kuppen 1992). The stepper motors are computer driven. For convenience only one stepper motor is used.

The following calculation shows the resolution attained when the stepper motor is turned through a single step.

Consider data being sampled at an altitude of 30 km.

The stepper motors work in conjunction with shafts having a thread similar to optical micrometers.

1 revolution on the shaft corresponds to a vertical shaft displacement of 0.6×10^{-3}m.

The stepper motors used give 200 steps per revolution.

The motor was driven at 1 step interval.

200 steps correspond to a vertical distance of 0.6×10^{-3}m.

Therefore, 1 step corresponds to a vertical distance of $\frac{1}{200} \times 0.6 \times 10^{-3} = 3 \times 10^{-6}$m.

Thus the maximum vertical resolution that can be obtained when the stepper motor is moved one step is 3×10^{-6}m.

Another interesting calculation that can be done is to determine the distance the laser beam would move horizontally at 30 km altitude if the motor is moved one step.

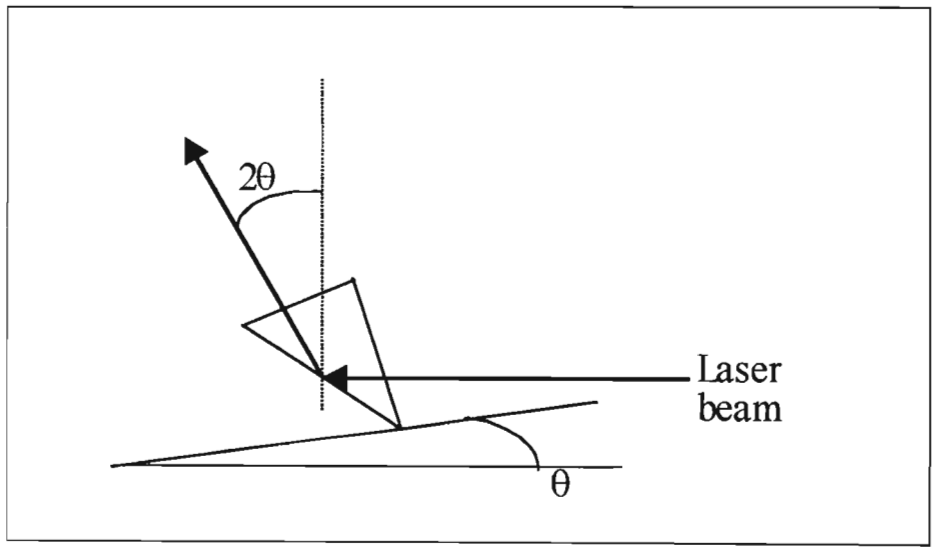

Figure 4.3: Diagram showing deviation of the laser beam when stepper motor is turned by 1 step.

From the geometry of fig.(4.3), it is clear that when the prism table is inclined by an angle θ, the laser beam is deviated by 2θ.

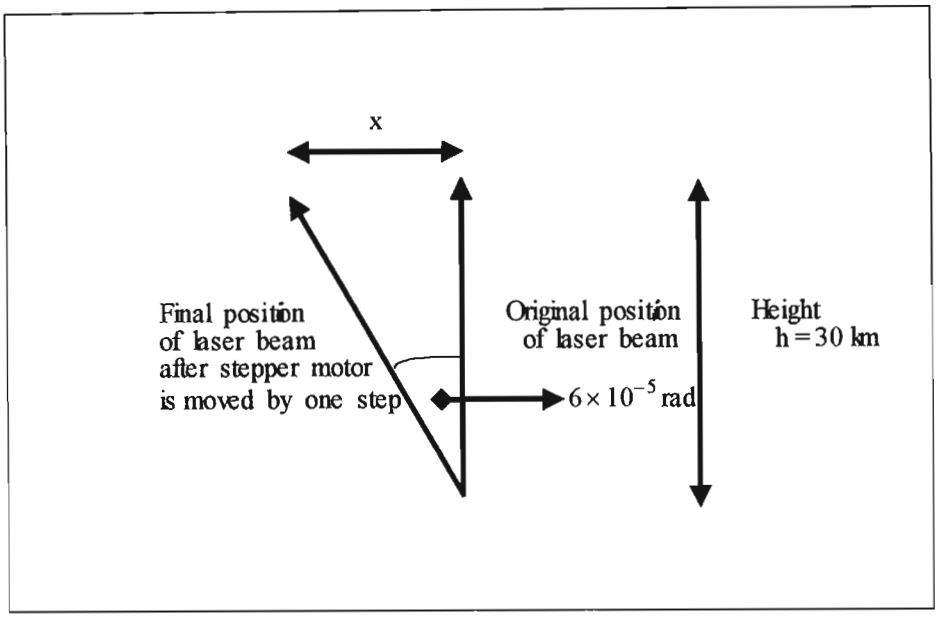

Figure 4.4: Diagram showing horizontal movement of the laser beam when the stepper motor is moved one step.

The angular displacement θ of the base plate of the prism is given by (fig.(4.3))

$\tan\theta = \dfrac{3 \times 10^{-6}}{0.10} \Longrightarrow \theta = 3 \times 10^{-5}$rad, where 0.10m is the length of the plate.

Therefore, the angular shift of the laser beam= $2\theta = 2 \times 3 \times 10^{-5} = 6 \times 10^{-5}$rad.

Hence at an altitude of 30 km, when the stepper motor is moved 1 step, the laser beam will move horizontally in the sky by (fig.(4.4))

$x = (\tan 2\theta) \times 30 \times 10^3$

$= \tan(6 \times 10^{-5}) \times 30 \times 10^3$

$= 1.8$ m.

It is felt that with a better alignment procedure, including concrete mounting platforms for the transmitter and receiver, still higher altitudes can be attained without any additional modification to the equipment.

4.4 Alignment of the new LIDAR

The alignment of the new LIDAR requires a different procedure. Both the receivers and the emitter are aligned in such a way that higher atmospheric layers are reached and at the same time sky background noise is eliminated by reducing the field of view of the receiving telescope. However, this improvement makes it more difficult to match the divergence of the laser with the receiver field of view. The following simplified equation demonstrates this effect on the diameter $\Gamma(z)$ of the image of the scattering volume:

$$\frac{\Delta\Gamma(z)}{\Gamma(z)} = \frac{\phi}{z \cdot \xi} \tag{4.1}$$

where ϕ is the diameter of the collecting surface, z is the height and ξ is the divergence of the laser. The inverse dependency of the alignment of the receiver telescope (equation (4.1)) as a function of altitude makes the lower altitude signal more sensitive to this effect.

4.4.1 Alignment of the receivers

The receivers of channels A and B are aligned using the autocollimation technique. We will describe the method of alignment used for channel A. The mirrors of channel A and B must have their axes parallel with the emitter axis. They are aligned to receive backscattered photons from infinity.

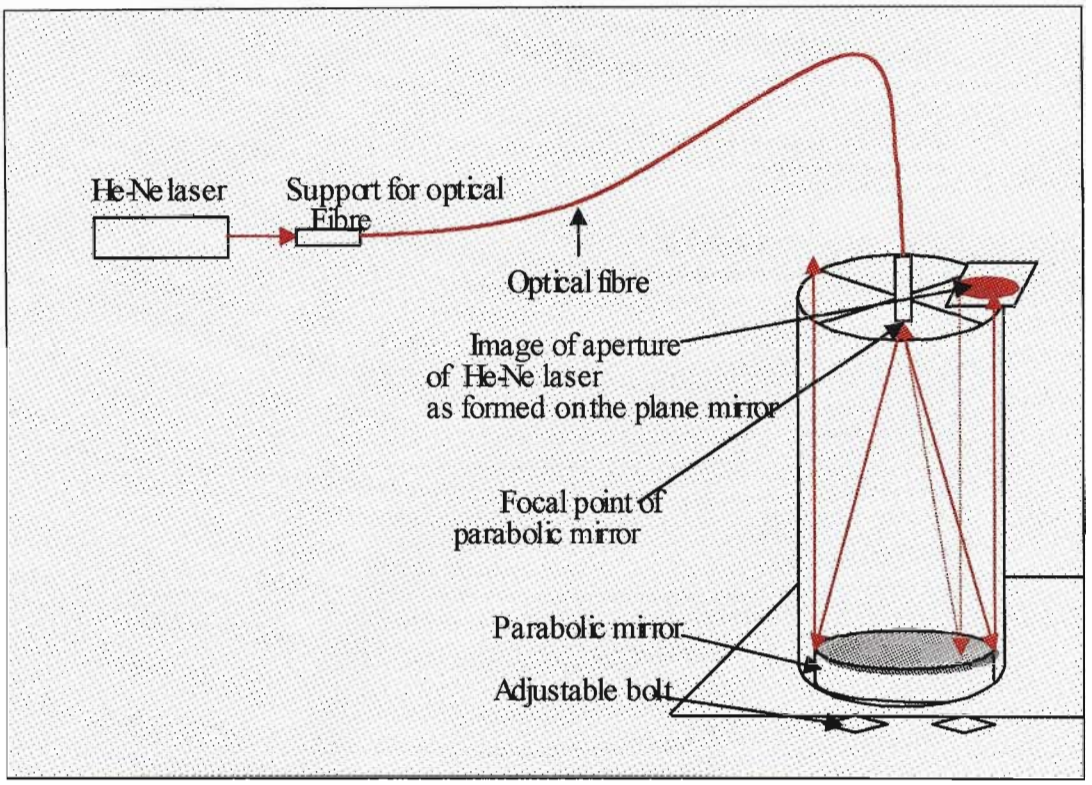

Figure 4.5: Alignment of the mirror of channel A.

A He-Ne laser is incident on one end of the optical fibre as shown in fig.(4.5). The laser beam after coming out of the optical fibre falls on the parabolic mirror and is reflected vertically upwards. The parabolic mirror rests on three adjustable bolts. By moving one of the bolts the laser beam is directed to a horizontal plane mirror placed at the top of the tube. An image of the aperture of the He-Ne laser is formed on the plane mirror. By carefully adjusting the bolts underneath the parabolic mirror, the reflection of the laser beam from the plane mirror is made to enter the optical fibre and passes back to the He-Ne laser (fig.(4.5)). This method is the same as having the parabolic mirror receiving light from a source at infinity. Fine adjustment of the receiver mirror is made at night time using the LIDAR return signal which is displayed on the oscilloscope.

Channel B which receives backscattered photons from the lower altitude is less affected by sky background noise. It also has a larger field of view and does not require a rigorous alignment. On the other hand, channel A which receives backscattered photons from high altitude has a smaller field of view and its alignment with the laser is more difficult. These operations for aligning channel A and B are often difficult, as the atmospheric transmission, the laser energy and the detection efficiency vary from one laser shot to the other. Also, it becomes extremely difficult to detect small variations of the backscattered LIDAR signal with the eye.

4.4.2 Optimisation of the signal

To ensure proper alignment of the receiver mirrors in order to receive signals from high altitude (40-60 km), the most commonly used method is to opti-

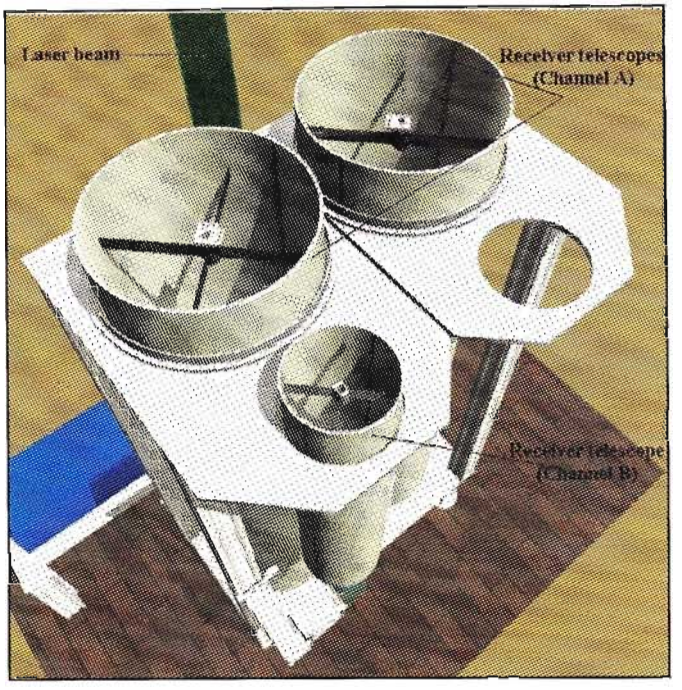

Figure 4.6: Top view of the receiver telescopes for channels A and B.

mise the backscattering signal using an oscilloscope. Fig.(4.6) shows a top view of the receiver telescopes of channels A and B.

At the top of the tube of channel A, there are two rotating knobs which can be used to optimise the signal on the oscilloscope. By moving one of the knobs at a time, the backscattered signal is shifted to higher altitude. Fig.(4.7) shows a magnified view of the rotating knobs. The knob on the left hand side moves the optical fibre diagonally towards the right whereas the right hand side knob moves the fibre diagonally towards the left.

Fig.(4.8) shows a low altitude reception signal on the oscilloscope when the LIDAR signal is not properly optimised. The signal displayed on the oscilloscope is in real time. By carefully rotating the knobs shown in fig.(4.7),

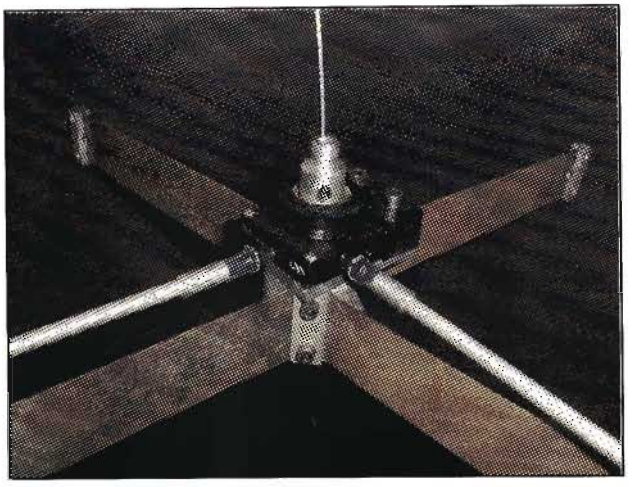

Figure 4.7: Magnified view of the two rotating knobs use to optimise the LIDAR signal.

the LIDAR signal for channel A is greatly improved (fig.(4.9)).

As shown in fig.(4.9), a strong LIDAR return has been detected at about 12 km. This could be due to a cirrus cloud and serves as a good reference for the optimisation of the LIDAR signal. The alignment prodecure is usually done under clear sky.

Fig.(4.10) shows the signal for channel B when the LIDAR return is not optimised. In this case the optimisation is done by slowly moving the receiver mirror of channel B using two rotating knobs. The optical fibre found at the top of the tube is kept fixed.

Fig.(4.11) shows a properly optimised LIDAR return from channel B. Comparing fig.(4.10) with fig.(4.11), the latter has the signal shifted towards the right, i.e., to higher altitude. Note that the small peaks on the far left of the signal are due to the saturation of the photomultiplier for the first 900 m height.

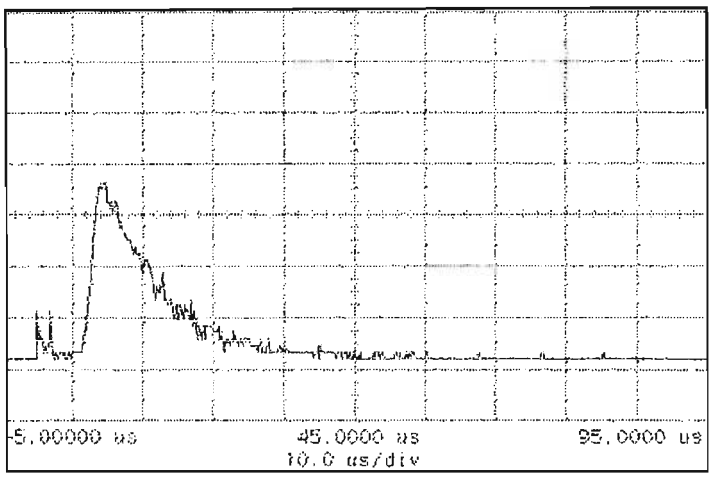

Figure 4.8: Backscattered signal as displayed on the oscilloscope for channel A. The y-axis is the analogue output from the photomultiplier and the x-axis is the time in microsecond per shot of the laser.

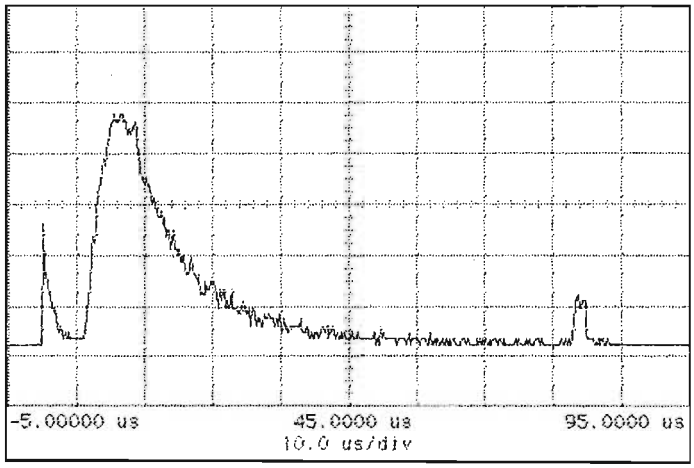

Figure 4.9: The same backscattered signal after optimising the LIDAR return. The small peak on the right could be due to return from a cirrus cloud. The peak is at 80 μs which corresponds to a vertical height of 12.0 km.

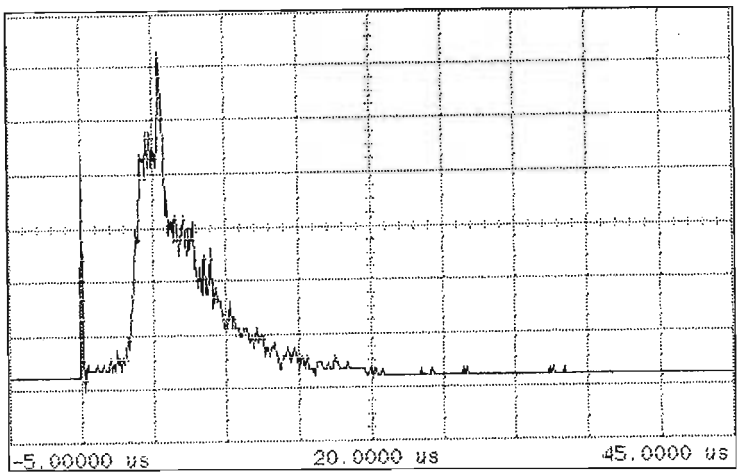

Figure 4.10: The backscattered signal from channel B.

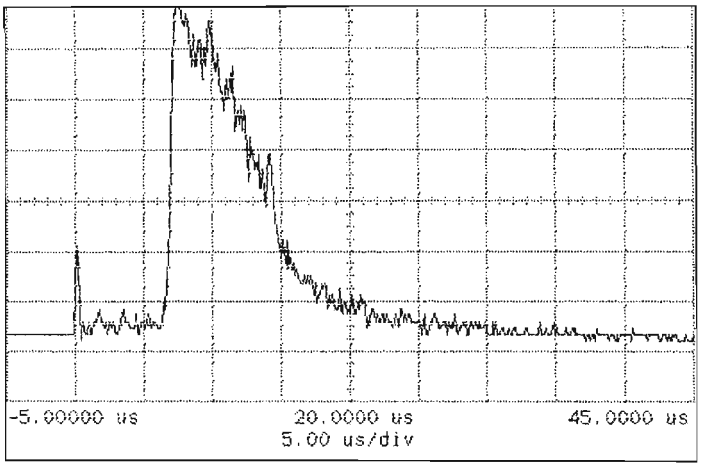

Figure 4.11: The same backscattered signal from channel B after optimisation.

4.5 Operation of the old LIDAR

If the sky is clear and sufficiently dark, the receiver lid is opened. The light tight door of the receiver chamber is closed. The dye circulation and the water pump are switched on. Cold water circulates around the dye to cool it. The dye requires some time to stabilise in temperature. The power supply of the laser and the PMT are switched on. Once power to the PMT is switched on, the receiver chamber cannot be entered anymore unless a problem arises with the receiver in which case the whole system is shut down.

The background count is measured and recorded. Before any measurements are taken, a blank check is done as follows. The aperture through the partition is blocked with non reflective paper and 20 shots are fired onto it. The results obtained are stored for later comparison with LIDAR profiles. This will serve as a guide to determine whether the system is detecting aerosols or just reflections of laser light inside the receiver chamber.

The system is then ready for measurements to be taken. The data obtained is stored on disk and later processed to obtain the profiles. The old LIDAR is usually run for 45 mins to 1 hour since the power supply is quite old and easily breaks down during long runs.

4.6 Operation of the new LIDAR

The new LIDAR is operated only at night under clear skies with no strong wind. Two hours prior to operating the LIDAR, the Durban International Airport is contacted to inform the air-traffic officer of the starting and finish-

ing times of the LIDAR operation over the Durban skies. This is important to ensure no aircraft is allowed to fly over the zone above and surrounding the LIDAR when the latter is operating.

The water-cooling system of the PMT is switched on at least 2 hours before operating of the LIDAR. The receiver mirrors for channel A and B are uncovered. The openings at the bottom of the tubes of channel A (which allow access to the mirrors for cleaning purpose) are closed with lids.

The pre-amplifiers for channels A and B vertically above the PMTs are switched on. The acquisition system including the computer and the power supplies for the PMs are switched on. If we require to use the electronic shutter, especially for channel A, it is important to set the control box for the Nd:YAG laser on 'external' which prompts the laser to wait from an incoming signal from the computer. When the acquisition programme is run from the computer, the latter triggers the laser and the acquisition of LIDAR data starts. The LIDAR return signals are recorded in terms of photon counts. The photon counts are integrated after every 2000 shots and are saved automatically in files. Each file therefore corresponds to an integration time of 3 mins 20 secs. Usually, before the acquisition pogramme is run, an alignment programme is run for 50 laser shots which displays the signals in a shorter integration time (5 secs). If the signals received during that time are not of good quality, an optimisation of LIDAR signal is done on each channel, as described above.

4.7 Summary

Fine alignment of the transmitter (90^0 prism) of the old LIDAR is done with the stepper motor which is located below the prism table. By carefully moving the prism table to 1 step clockwise or counter-clockwise higher altitude can be attained with the old LIDAR.

The optimisation of the LIDAR return signal of the new LIDAR is usually done once a week when the LIDAR is running at night with the sky visibly free of haze. The acquisition of data is done for at least 4 to 5 hours. Once set into operation, the LIDAR system becomes autonomous. The data are saved automatically by the computer which controls the acquisition. The raw LIDAR data are processed to yield temperature, Mie ratio, relative density, and aerosol extinction profiles.

Chapter 5

Results and discussion of the old LIDAR observations

5.1 Introduction

In this chapter, profiles of the raw data from the old LIDAR are shown for the low and high altitudes. The old LIDAR data was compiled during a campaign carried out from April to November 1997. Given the temporal quality of the old LIDAR and the saturation effects encountered by the photomultiplier, these results have been questioned by the French authorities in the field. I suggest that I am incorporating the results of the old LIDAR in the thesis in case they are valid and in view of the doubt of these authorities, I suggest that these results should be corroborated with the new LIDAR results. However this may be problematic as the wavelength of the old LIDAR (589 nm) which corresponds to the sodium resonance line is different from the wavelength used for the new LIDAR (532 nm). It should be noted that Dr Kuppen (1996) observed a high altitude aerosol layer around 60 km using the old LIDAR in June 1994.

5.2 The old LIDAR results

Due to unfavourable weather conditions in Durban (lack of clear skies) and technical problems associated with the LIDAR (being quite old), it was not possible to run the LIDAR on a day-to-day basis. I will report results obtained for the months of July, August, September and October. This coincides with the time of sugar cane burning along the Natal coast. The LIDAR profile was taken on the following nights:

(i) July 3rd 1997,

(ii) July 23rd 1997,

(iii) August 21st 1997,

(iv) September 26th 1997,

(v) October 20th 1997,

(vi) October 21st 1997.

The sky was visibly clear with no low or high altitude clouds. Low level haze which is usually present during the day was also absent.

It should be noted that the LIDAR system can be used to measure low altitude (0 to 10 km) aerosols as well as high altitude (10 to 90 km) aerosols. This yields profiles spanning the entire altitude range for the nights during which the system was operated.

The data collection campaign was done in the following way:

(i) The system was operated on clear nights only. It is important that

the moon and clouds should not be present during data acquisition. The moon light will saturate the photomultiplier so that LIDAR returns from low altitudes will not be detected. The high water vapour concentration in clouds result in beam attenuation from higher altitudes and hence the signals will not be detected.

(ii) Between 150 and 230 laser shots were integrated to obtain each LIDAR profile. During some nights, depending on the operating parameters, up to 225 shots were used. This allows us to measure higher altitude aerosols. The laser was fired at a repetiton rate of 0.5 Hz. It was found that 150 shots were sufficient to smooth out random fluctuations in the returned signal. Also, since the integration time corresponding to 150 laser shots is short, no appreciable atmospheric changes occurred in the laser shots.

(iii) Profiles of 150 shots were taken at intervals of 15 mins. This would give some indication of the short time behaviour of the aerosol layers.

(iv) To detect low altitude aerosols, the photomultiplier voltage was increased in steps of 50 V until counts were obtained on the screen. This technique prevents saturation of the photomultiplier due to strong returns from low altitude aerosols.

For high altitude aerosols, the photomultiplier was operated at its normal operating voltage of 9 kV. For detecting low and high altitudes aerosols, the laser was fired at 12 kV.

5.3 Low Altitude Aerosols

5.3.1 Raw Data

The earliest LIDAR profiles were taken on July 3rd 1997 when interesting behaviour of the low altitude aerosol was seen. Fig.(5.1) shows a time evolution with profiles taken from 18:15 to 19:00 at intervals of 15 mins.

The x-axis represents altitude in km and the y-axis photon counts from the photomultiplier. These profiles are raw as they are recorded by the data capturing system.

Three layers of aerosols are clearly evident from the plot. The first layer is at 1.2 km. The second and third layer are more prominent and are found at 2.4 km and 4 km respectively. In all five profiles the photomultiplier is saturated for the first 400 m.

In order to see whether these results persist for the rest of the month, a set of profiles were taken three weeks later on July 23rd 1997 (fig.(5.2)). Each profile was taken in intervals of 15 mins as before. The three layers (1.2 km, 2.4 km and 4 km) which appeared on July 3rd 1997 seem to reinforce and appear at greater heights on July 23rd 1997. The estimated thickness of the each layer is 800 m.

From the profiles of figs.(5.1) - (5.2), the following conclusions can be drawn:

(i) The 1.2 km layer seems to be enhanced from July 3rd to July 23rd.

(ii) The 2.4 km and 4 km layers remain fixed in altitude.

(iii) These two layers seem to behave independently of each other.

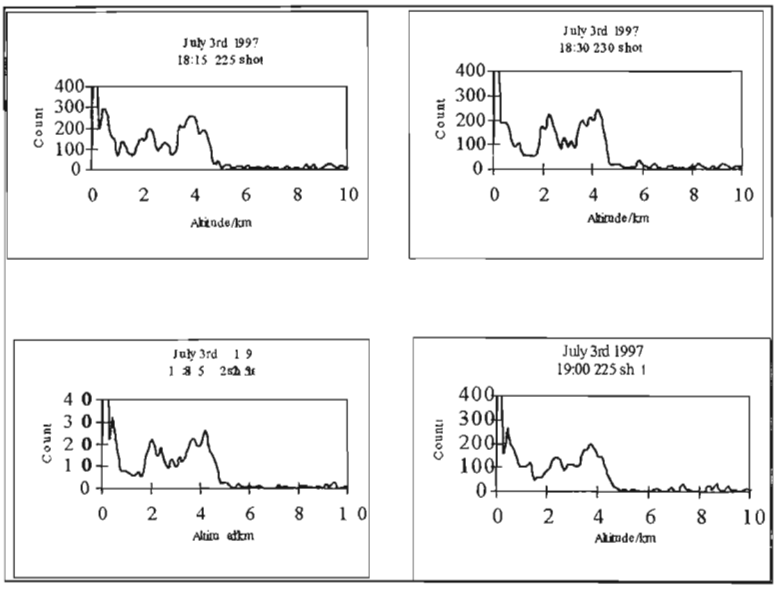

Figure 5.1: Low altitude LIDAR profiles taken on July 3 1997 from 18:15 to 19:00.

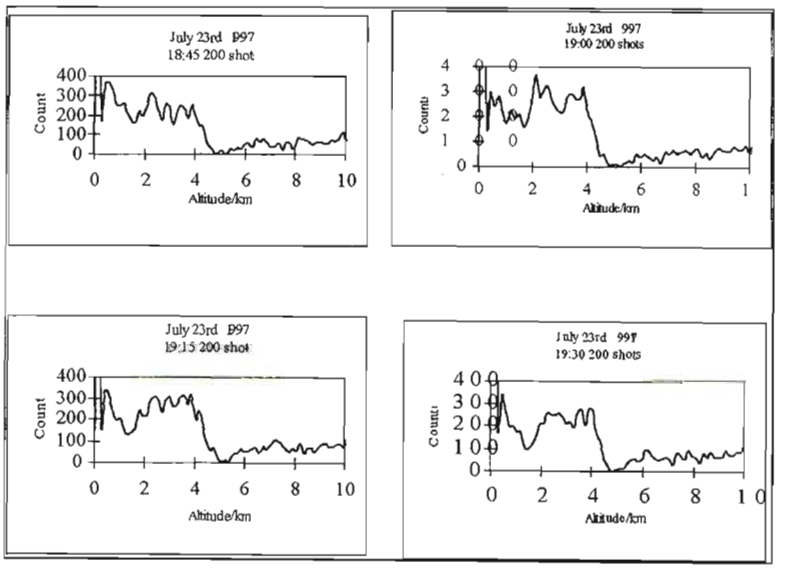

Figure 5.2: Low altitude LIDAR profiles taken on July 23 1997 from 18:45 to 19:30.

Another set of profiles were taken more than four weeks later on August 21st 1997 (fig.(5.3)) in order to see whether the aerosol layers detected on July 3rd and July 23rd persist.

We can therefore conclude that the three aerosol layers seem to persist for most of July. The layers disappear towards the end of the month. This is clearly seen in the profiles of August 21st 1997 (figs.(5.3)) where all the three peaks have disappeared.

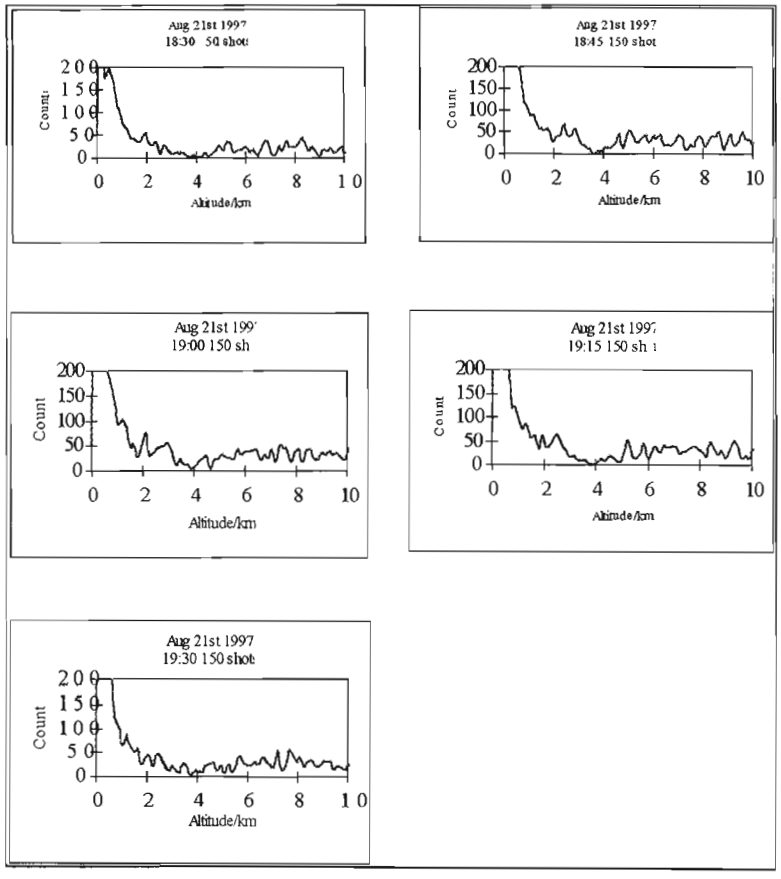

Figure 5.3: Low altitude LIDAR profiles taken on August 21 1997 from 18:30 to 19:30.

Low altitude LIDAR raw data profiles are plotted for the dates September

26th to October 21st 1997 (figs.(5.4) - (5.6)) in order to see whether the trend in August persists.

From the September 26th results (fig.(5.4)), it appears there has been some developments at 2.8 km and 3.6 km. The layers seem to be so close that they appear as two broad peaks in the LIDAR profiles. Comparing with the July 3rd results, it seems that the 2.4 km layer has moved to higher altitude (2.8 km) and the 4 km layer to lower altitude (3.6 km). The two layers at 2.8 km and 3.6 km seem to be stable for the whole of September and October (figs.(5.5) - (5.6)). The persistence of these layers suggest that they are unaffected by circulation changes in the atmosphere.

Three possible explanations which could account for this erratic behaviour of the aerosols are:

(i) As shown in fig.(5.7), over most of Southern Africa, layers of absolutely stable air occur preferentially at around 700 hPa ($\sim$ 3 km), 500 hPa ($\sim$ 5 km) and 300 hPa ($\sim$ 9 km) (Cosijn and Tyson 1996). A fourth layer also occurs over coastal areas around 850 hPa ($\sim$ 1.5 km). All four layers have the effect of inhibiting vertical transfer of aerosols and trace gases and of trapping them in the intervening layers (Cosijn and Tyson 1996). The solid line refers to the height of the escarpment above sea level.

(ii) Biomass burning occurs frequently in South Africa, either in the form of prescribed burns or wild fires (Pillay *et al.* 1995). The extent of these burns on the east coast of South Africa reaches its maximum in the winter season (Pillay *et al.* 1995). Thus the loading of the atmosphere will be higher in winter.

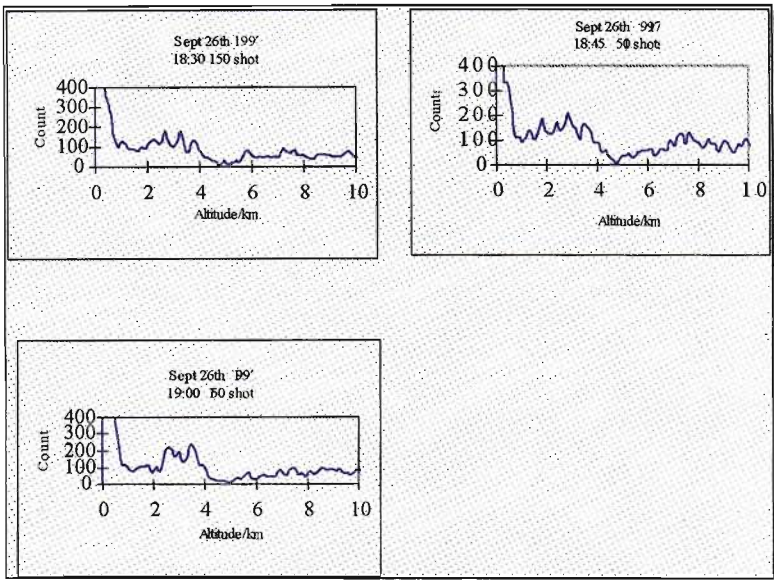

Figure 5.4: Low altitude LIDAR profiles taken on September 26 1997 from 18:30 to 19:00.

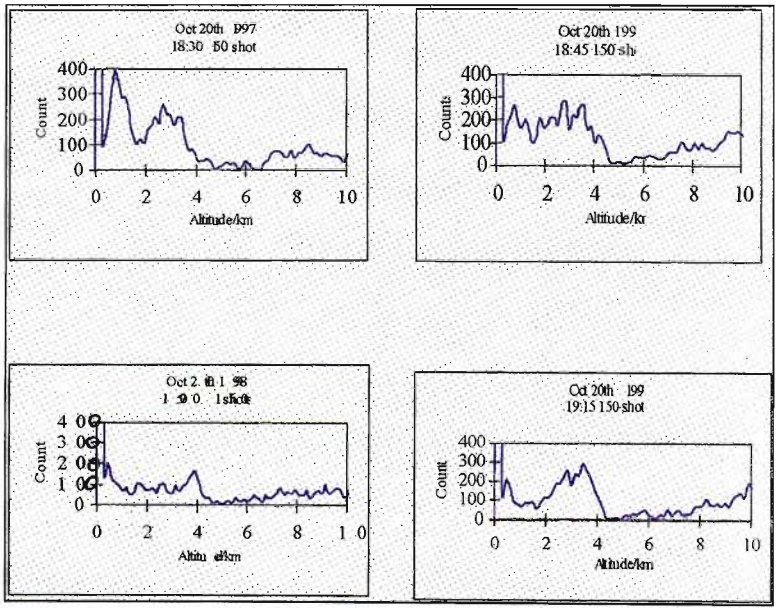

Figure 5.5: Low altitude LIDAR profiles taken on October 20 1997 from 18:30 to 19:15.

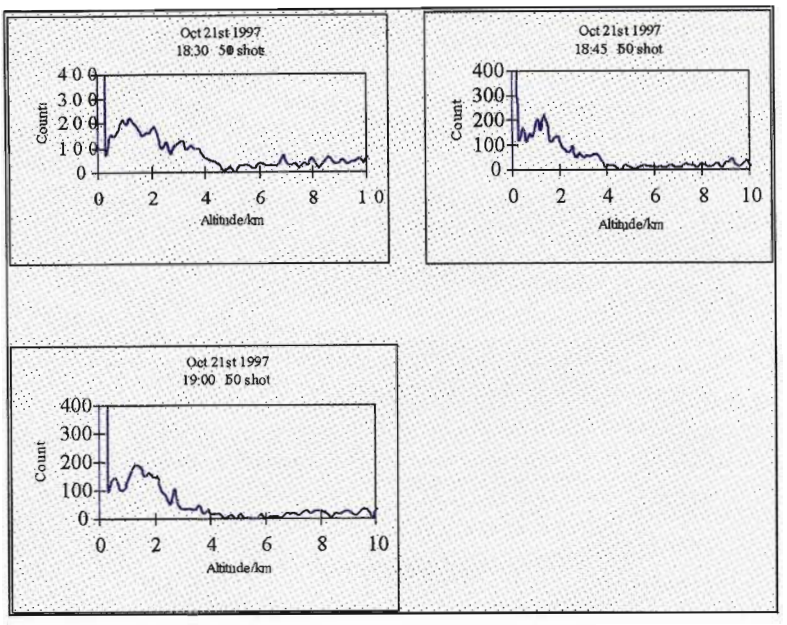

Figure 5.6: Low altitude LIDAR profiles taken on October 21 1997 from 18:30 to 19:00.

(iii) The loading of the atmosphere when sugar cane burning began in June is different in July and October.

The September 26th and October 20th results show a higher concentration of aerosols at 2.8 km and 3.6 km. This observation can be accounted for by the fact that the burning of sugar cane has reached its end in September and also the largest number of active fires detected in South Africa occurred between July and September (Justice *et al.* 1996). Therefore the aerosol loading of the atmosphere would be higher in September than in June. Indeed this is what can be seen from the LIDAR profiles (fig.(5.4)). The stable discontinuities (point (i) above) which are present during most of the year (Cosijn and Tyson 1996) serve to trap the aerosols produced during the burning of sugar cane and biomass burning. Towards the end of September and

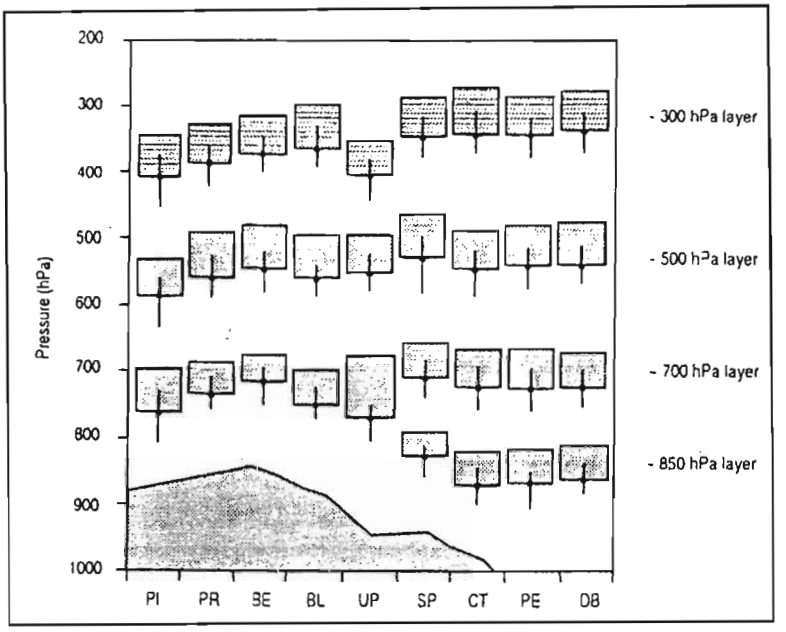

Figure 5.7: Mean annual spatial variation of absolutely stable layers at 850, 700, 500 and 300 hPa over South Africa. PI denotes Pietersburg, PR Pretoria, BE Bethlehem, BL Bloemfontein, UP Upington, SP Spingbok, CT Cape Town, PE Port Elizabeth and DB Durban (Cosijn and Tyson (1996)).

October, although mixing is taking place, continuous loading of the atmosphere has resulted in a higher concentration of aerosols. Fig.(5.5) shows a strong return between 8 km and 10 km on October 20th 1997 at 18:30. This may be due to the stable discontinuity at 300 hPa ($\sim$ 9 km) (see fig.(5.7)).

5.4 High Altitude Aerosols

5.4.1 Raw Data

The first LIDAR profile was taken on the night of July 3rd 1997 at 18:30. The sky was visibly clear with no low or high altitude clouds. Profiles were taken every 15 mins interval. Fig. (5.8) shows a time evolution of five profiles taken from 18:30 to 19:30. The y-axis represents photon counts from the

photomultiplier and the x-axis represents the altitude in km.

There are three interesting points to note in these plots.

First, consider the aerosol layer at 14 km. There is evidence to support that this increased aerosols concentration originates from sugar cane burning. The upward tropospheric circulation has transported this layer to higher altitude. The estimated thickness of this layer is 1 km.

The second feature of interest is the partial saturation and recovery of the photomultiplier between 20 km and 30 km. The mechanical shutter was not in operation at the time which could have solved the saturation problem.

Thirdly, the erratic behaviour of the LIDAR signal after 30 km. This is due to internal noise from the equipment.

In order to see whether this aerosol layer persists for the whole of July, profiles were taken three weeks later, more specifically on July 23rd 1997 and the results are shown in fig. (5.9). The time was taken in intervals of 15 mins as before. The 14 km aerosol layer which appeared on July 3rd 1997 seems to reinforce and appears at greater height. The estimated thickness of the layer is 1 km.

The peaks appearing after 20 km are background noise mixed with shot noise when the laser is fired. We can therefore safely conclude that the 14 km aerosol layer persists for the whole of July and seems to increase in concentration towards the end of July. This is obvious because of the continuous loading of the atmosphere with sugar cane burning which started in the beginning of June. At the same time mixing is also taking place but

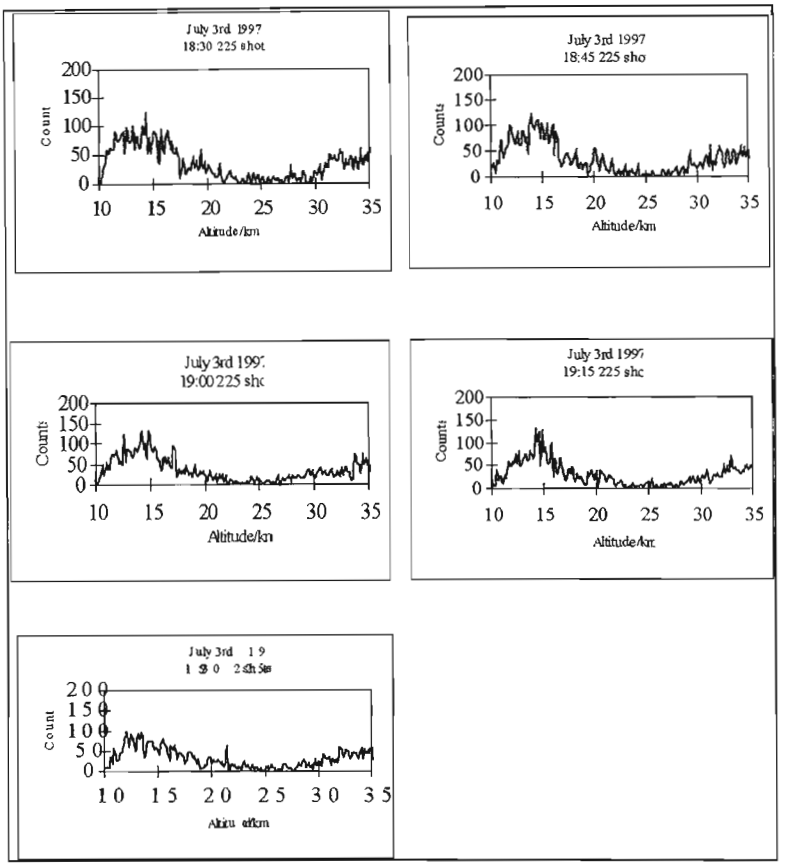

Figure 5.8: High altitude LIDAR profiles taken on July 3 1997 from 18:30 to 19:30.

probably at a slower rate.

In order to understand the behaviour of the aerosol layer, five other profiles were taken in August. Unfortunately, unfavourable weather conditions in the beginning of August has prompted us to take profiles on the third week of August. Fig.(5.10) shows the results obtained on August 21st.

From the profiles of August 21st 1997 we can conclude that the aerosol layer at 14 km has disappeared. At this point we can say that mixing of the atmosphere has contributed to this disappearence.

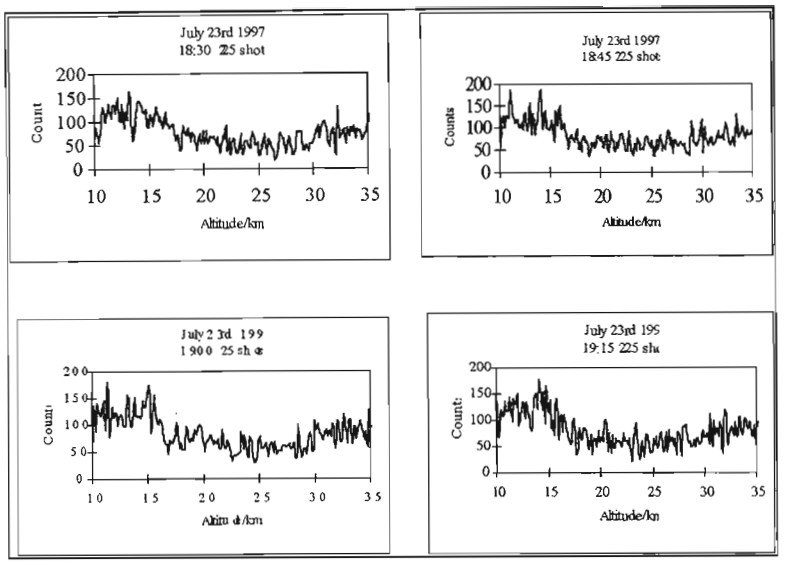

Figure 5.9: High altitude LIDAR profiles taken on July 23 1997 from 18:30 to 19:15.

In order to obtain a clear understanding of the aerosol behaviour, we plotted profiles for the months of September and October. Figs.(5.11) - (5.13) show the results obtained on the nights of September 26th, October 20th and 21st.

From the profiles of September 26th, it is clear that the peaks that appear at 12 km depict some aerosol concentration at this altitude. The appearence of the 12 km aerosols layer can be explained by the fact that some tropospheric upwelling has transported the low altitude aerosols (from sugar cane burning) to higher altitude.

Perhaps a more interesting feature that can be seen from the October 20th and October 21st profiles (figs.(5.12) - (5.13)) is the dramatic increase in the lidar return at 28 km. Kuppen (1996) previously detected an aerosol layer at 25 km. This might be the same layer with the exception that over

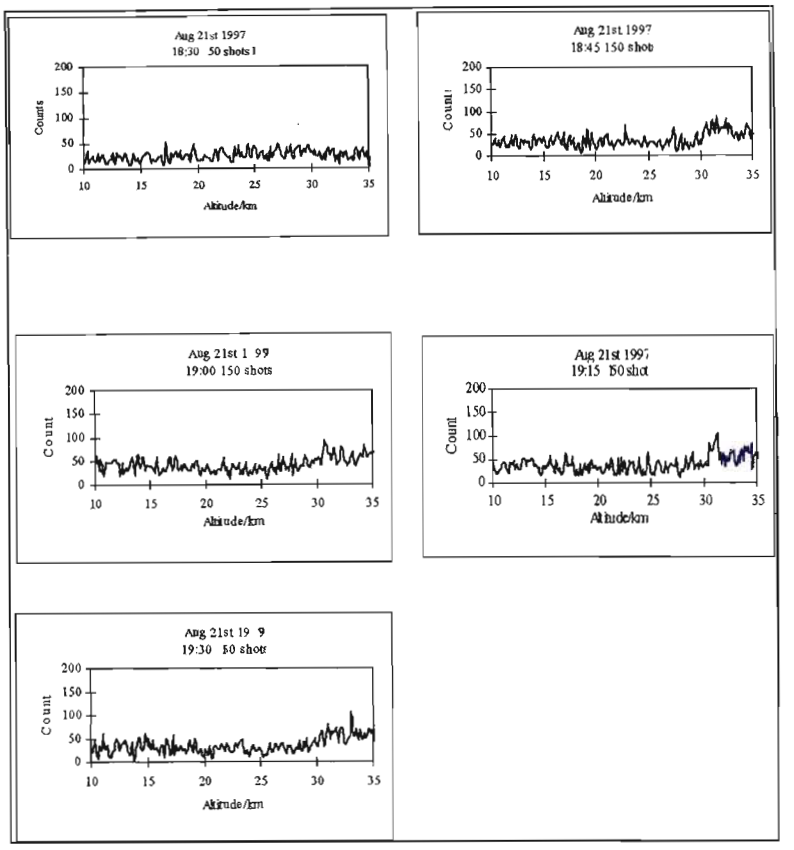

Figure 5.10: High altitude LIDAR profiles taken on August 21 1997 from 18:30 to 19:30.

the space of 1 year some stratospheric upwelling has taken place which has carried the layer to 28 km.

The "28 km layer" (as we shall henceforth call it) was detected only for the month of October 1997 (fig.(5.13)). This may be due to the fact that weather conditions might have been ideal in October, that is low water vapour concentrations have resulted in strong return from higher altitudes. This 28 km layer was rather intriguing.

Personal correspondence via e-mail with the LIDAR group in Reunion (H.

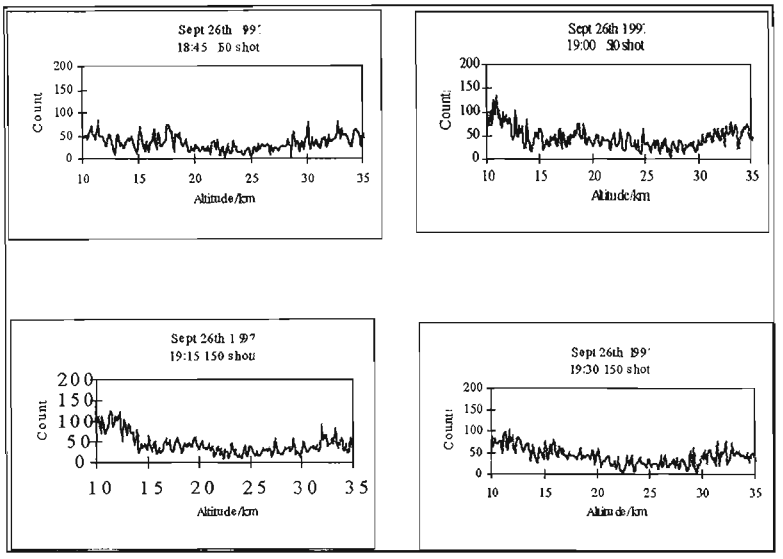

Figure 5.11: High altitude LIDAR profiles taken on September 26 1997 from 18:45 to 19:30.

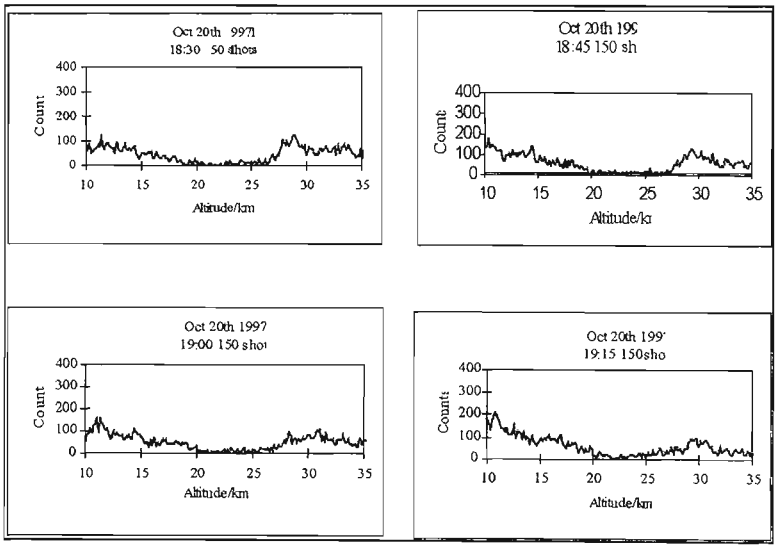

Figure 5.12: High altitude LIDAR profiles taken on October 20 1997 from 18:30 to 19:15.

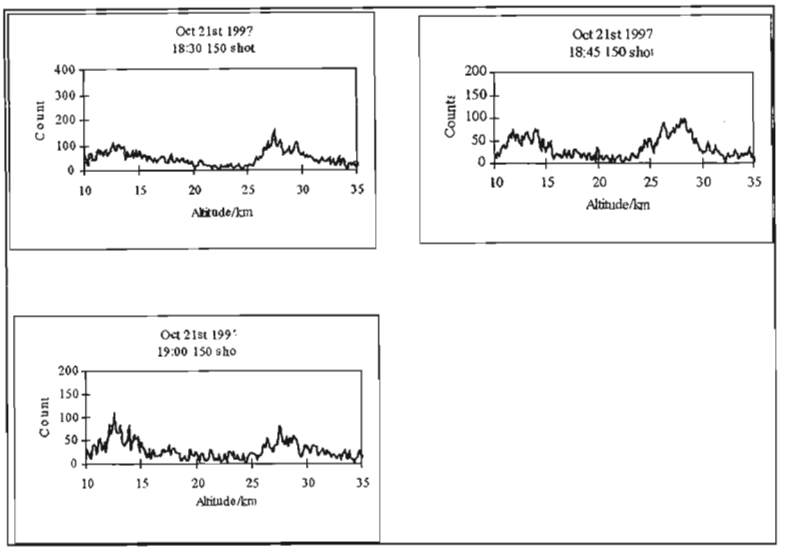

Figure 5.13: High altitude LIDAR profiles taken on October 21 1997 from 18:30 to 19:00.

Bencherif, 1997, pers. comm.[1]) and in New Zealand (G. Bodeker, 1998, pers. comm.[2]) indicated that they did not detect aerosols at such high altitude. In order to compare the Durban old LIDAR system with that used in Reunion Island, we describe briefly in the next section the LIDAR system used in Reunion Island.

The LIDAR system in Reunion consists of a Nd-YAG laser as transmitter, operating at a wavelength of 532 nm (frequency doubled) with a repetition rate of 10 Hz, and the energy per pulse is 300 mJ.

There are two channels for data acquisition:

(i) Channel A. This is used for measurement of vertical temperature profiles and relative density in the altitude range 30 to 80 km.

(ii) Channel B. This is an extension of channel A towards lower altitude

[1]Dr Hassan Bencherif, Department of Physics, University of Reunion, 15 av R. Cassin, BP 7151, 97715, St-Denis cedex, Reunion, France.

[2]Dr Greg Bodeker, National Institute of Water and Atmospheric Research, P.O. Box 50061, Omakau, Central Otago, New Zealand.

and allows measurement of temperature and density to be done in the range 10 to 45 km. It also corrects for overlap with the altitude range of channel A.

The receiver is a Cassegrain telescope type with a system of photomultipliers (PMTs) as detector. Each PMT has an interference filter centred on 532 nm with a bandwidth $\Delta\lambda = 1$ nm and is equipped with electronic shutters. The latter prevent saturation of the PMTs during LIDAR returns from low altitude. The PMTs are also cooled by thermo-elements ("Peltier effect") which are themselves cooled by water. This reduces considerably the dark current in the PMTs.

The laser system and the acquisition channels used in Reunion Island have been installed recently at Durban and form part of the new LIDAR system.

The wavelength (589 nm) of the old LIDAR system of Durban is marginally different from that of Reunion Island (532 nm) but both are equally capable of detecting the 28 km layer. We now make a deeper analysis of our results by computing the extinction coefficients due to aerosols.

As will be pointed out later (Chapter 6) the Klett inversion method is a more accurate method to retrieve aerosol extinctions from the LIDAR data. Due to the strong laser returns from low altitude (0 - 10 km), saturation of the photomultiplier swamped most of the relevant features. We therefore opted to apply Klett inversion method to analyse features above 10 km. Figs.(5.14)-(5.15) show plots of the extinction coefficient versus altitude in the 10 km to 35 km range for July 23rd 1997 and August 21st 1997 lidar profiles re-

spectively. Figs.(5.16) and (5.17) show plots of the extinction coefficients in the altitude range 10-15 km and 20-32 km for the same date October 20th 1997. Plots of extinction coefficients were also made for October 21st 1997 in the altitude range 10 to 15 km and 20 to 30 km and these are shown in figs (5.18) and (5.19) respectively. The programme Klett_Inv.for was used to calculate the extinction coefficients using the Klett inversion method. A listing of the source code is given in Appendix A.

The programme requires 3 inputs:

(i) the raw data file,

(ii) the lower altitude limit for the integration (z_0),

(iii) the upper altitude limit for the integration (z_m).

The values z_0 and z_m are chosen according to the range the integration is carried out.

Returning to figs.(5.12) - (5.13) there are two features of interest:

(i) the aerosol layer between 14 km and 15 km,

(ii) the aerosol layer between 28 km and 30 km.

We plotted the extinction coefficients for the altitude range 10 km to 15 km using the raw data from fig.(5.12) for October 20th and fig.(5.13) for October 21st. These are shown in fig. (5.16) and fig.(5.18) for the two consecutive days (October 20th and 21st). In fig. (5.12), the large LIDAR return ($\sim$ 100 counts) between 14 km and 15 km shows an extinction coefficient of

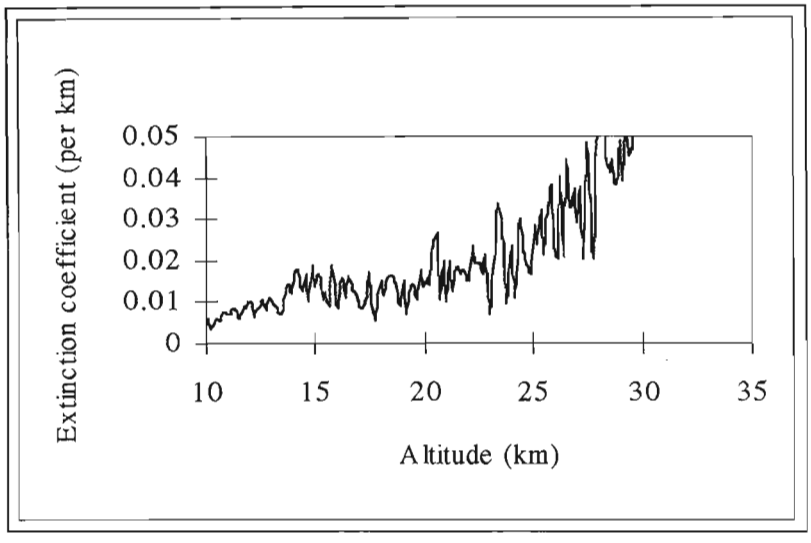

Figure 5.14: Extinction coefficient versus altitude in the 10 km to 35 km range- July 23 1997.

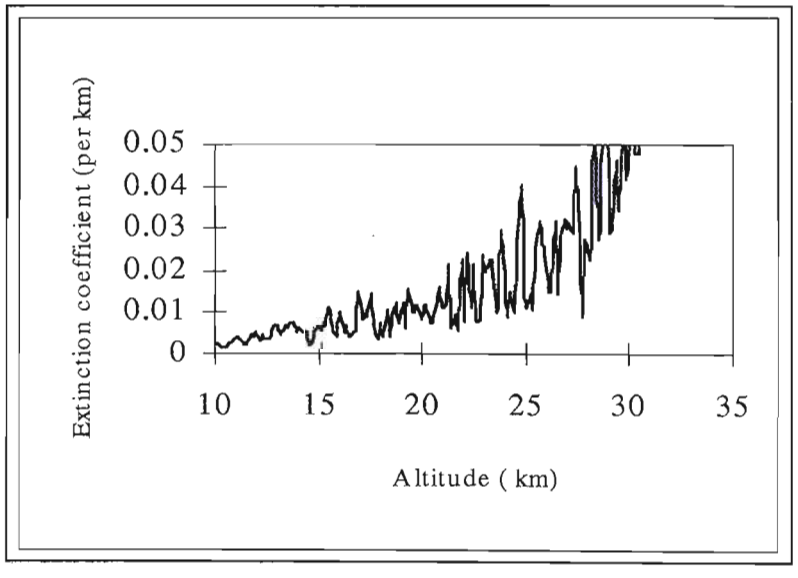

Figure 5.15: Extinction coefficient versus altitude in the 10 km to 35 km range- August 21 1997.

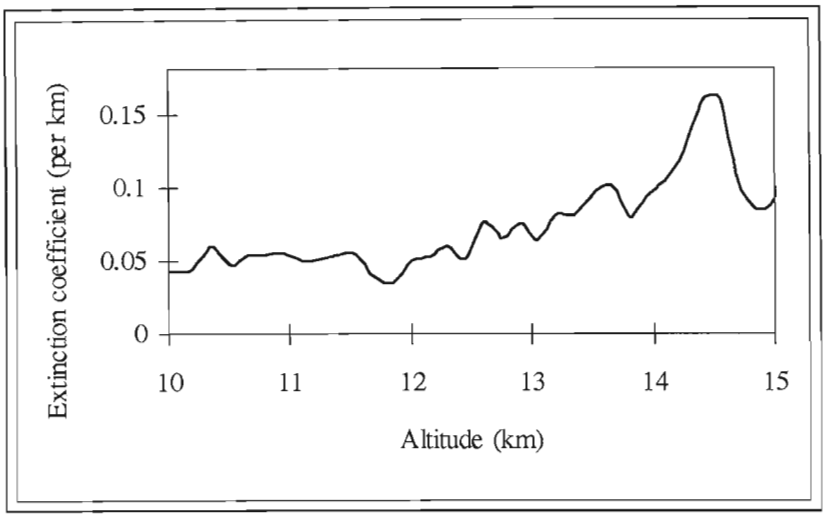

Figure 5.16: Extinction coefficient versus altitude in the 10 km to 15 km range- October 20 1997.

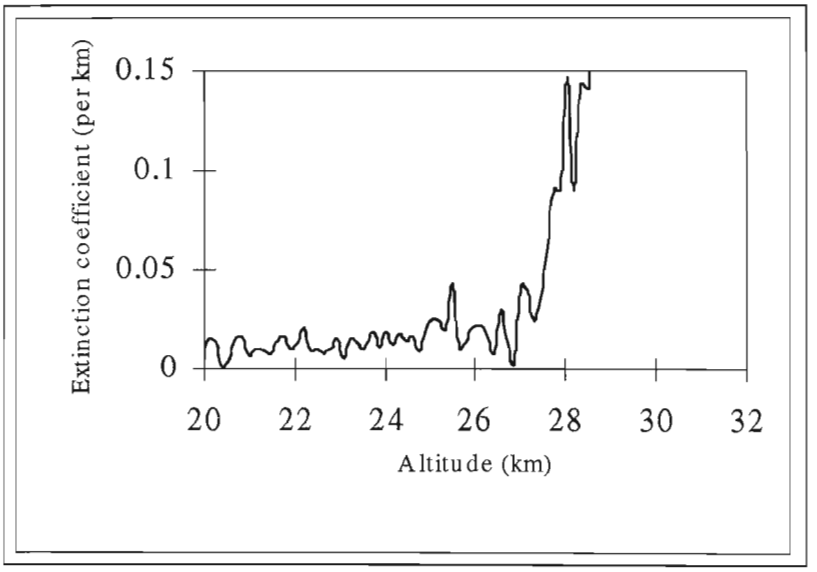

Figure 5.17: Extinction coefficient versus altitude in the 20 km to 32 km range- October 20 1997.

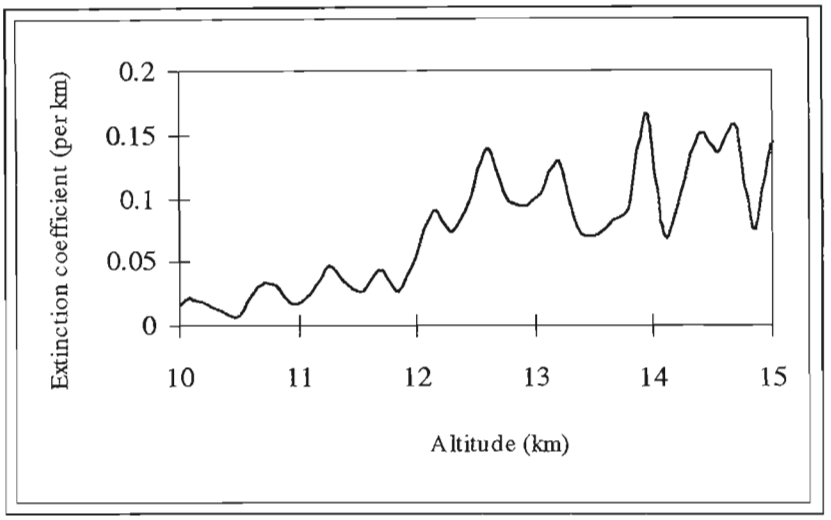

Figure 5.18: Extinction coefficient versus altitude in the 10 km to 15 km range- October 21 1997.

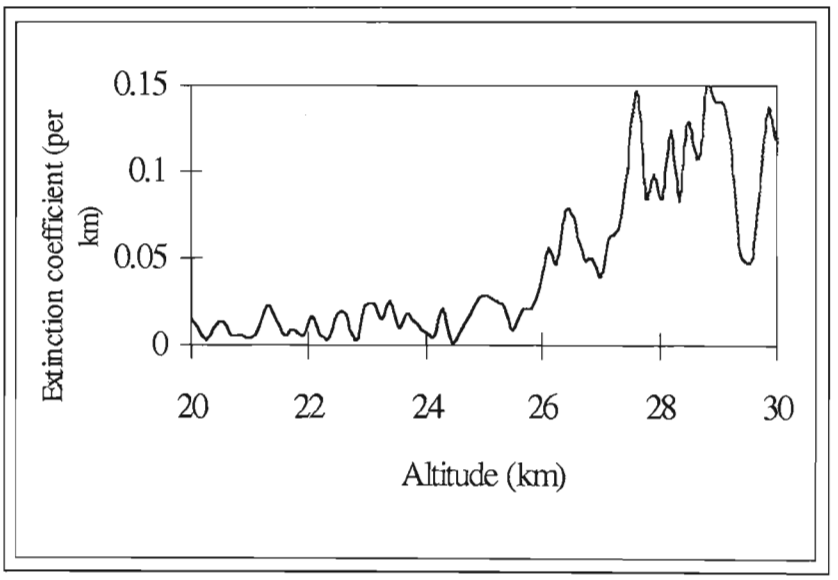

Figure 5.19: Extinction coefficient versus altitude in the 20 km to 30 km range- October 21 1997.

≈ 0.15 km^{-1}. Therefore on the basis of this observation (October 20th 1997) we can deduce that there is an aerosol layer between 14 km and 15 km. This layer can also be seen from the raw data of fig.(5.13) when compared with fig.(5.10) (no aerosol signal). There are two possible reasons for this:

(i) The contribution of sugar cane burning towards the loading of the atmosphere has reached its peak in October rather as was initially expected to July and August.

(ii) In addition to sugar-cane burning, biomass burning either in the form of prescribed burns or wild fires reaches its peak towards the end of the winter season (Rutherford and Westfall 1986). Thus the atmosphere will be richer in aerosols in October than it will be in July and August.

For the higher altitude between 27 km and 30 km, fig.(5.19) shows a remarkable increase in the extinction coefficient of ≈ 0.15 km^{-1} between 28 km and 30 km. From this value, it is evident that there is an aerosol layer between 28 km and 30 km of thickness ≈ 2 km.

This layer is rather intriguing as aerosols have rarely been detected at such high altitude. In the past, Hirono *et al.* (1974) observed aerosol layers above 25 km during 1972 and 1973 which are reported to be rather variable. Iwasaka and Isono (1977) reported a dust layer above 24 km with a peak intensity at 27 km which has been observed in April 1976 with a two-frequency LIDAR.

5.5 Comparison of Durban old lidar results with SAGE II

SAGE II (Stratospheric Aerosol and Gas Experiment II) is an instrument which was launched into a 57^0 inclination orbit aboard the Earth Radiation Budget Satellite (ERBS). During each sunrise and sunset encountered by the orbiting spacecraft, the instrument uses the solar occultation technique to measure attenuated solar radiation through the Earth's limb in seven channels centred at wavelengths ranging from 385 nm to 1020 nm. These measurements are then inverted to yield 1 km vertical resolution profiles of aerosol extinction(at 385 nm, 453 nm, 525 nm, and 1020 nm), ozone, nitrogen dioxide and water vapour. The focus of the measurements is on the lower and middle stratosphere.

The SAGE II instrument consists of a seven-channel Sun photometer, a Cassegrainian-configured telescope, a grating spectrometer and a 12-bit data acquisition system. The instrument's instantaneous field of view produces a vertical resolution at the tangent point on the Earth's horizon of about 0.50 km.

In order to verify our results, we compared our extinction coefficient with that obtained by SAGE II. The data have been obtained by courtesy of NASA Langley Research Centre. The data have been extracted within a 1200 km radius of the geographical location 20.0 S and 28.0 E which is not far from the location of Durban. The closest wavelength to our lidar system was 525 nm. The seven SAGE II profiles were extracted on:

(i) July 13th 1997 at coordinates 32.7 S and 29.7 E,

(ii) July 31st 1997 at coordinates 28.0 S and 29.2 E,

(iii) August 29th 1997 at coordinates 27.8 S and 34.1 E,

(iv) September 26th 1997 at coordinates 29.4 S and 34.4 E,

(v) September 27th 1997 at coordinates 24.3 S and 32.9 E,

(vi) October 13th 1997 at coordinates 23.8 S and 30.2 E,

(vii) October 14th 1997 at coordinates 28.7 S and 27.6 E.

The data were selected on the basis that the latitude lies 2^0 and the longitude lies 3^0 within the location of Durban. Unfortunately there was 10 days difference in the time at which SAGE II data were obtained except for the September data where the date exactly matched the lidar data.

In order to make a direct comparison with figs. (5.14) - fig. (5.19) we plotted SAGE II profiles for the altitude range 10 km to 35 km. These are shown in figs. (5.20) - (5.26).

In all these plots we can conclude the following:

(i) At 28 km altitude the SAGE II extinction coefficient on October 14th is 1.00E-04 km^{-1} whereas our calculated extinction coefficients on October 20th is 0.20 km^{-1}.

(ii) At 14 km altitude the SAGE II extinction coefficient on October 14th is above 5.00E-04 whereas our calculated coefficient on October 21st is between 0.10 km^{-1} and 0.15 km^{-1}.

(iii) The increase in extinction coefficient at 20 km.

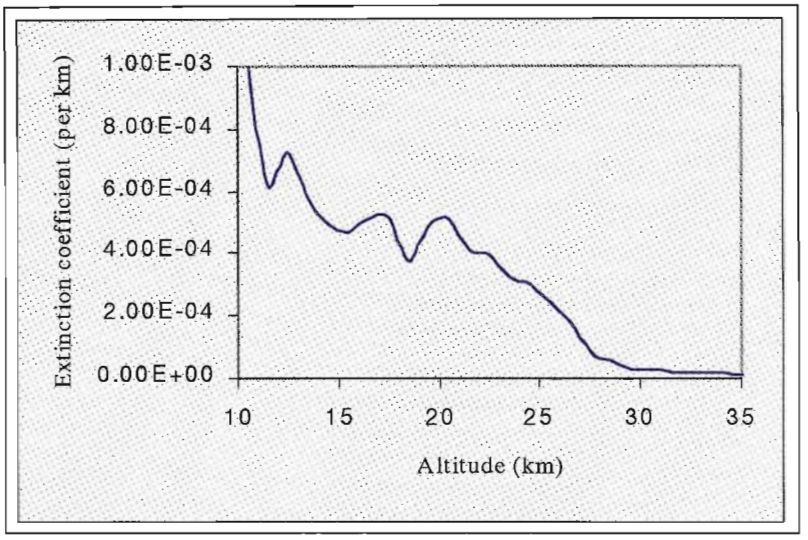

Figure 5.20: SAGE II profile taken on July 13 1997 at 32.7 S and 29.7 E.

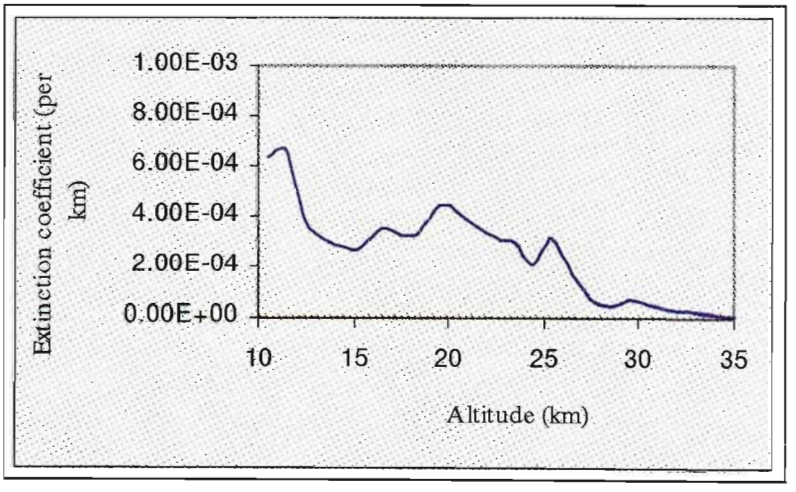

Figure 5.21: SAGE II profile taken on July 31 1997 at 21.6 S and 28.3 E.

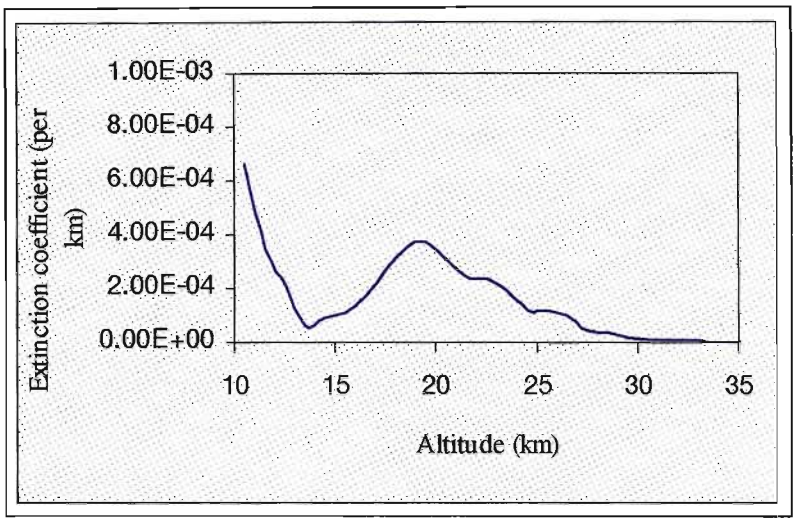

Figure 5.22: SAGE II profile taken on August 29 1997 at 27.8 S and 34.1 E.

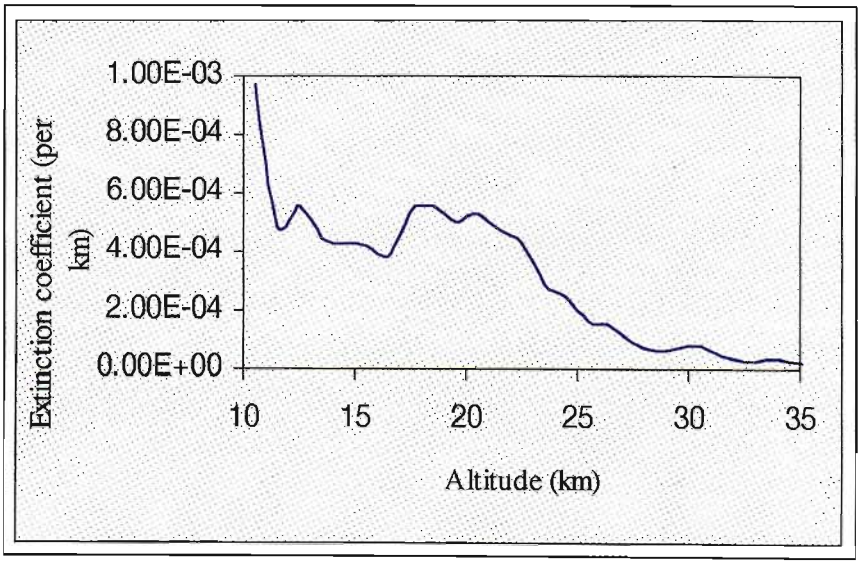

Figure 5.23: SAGE II profile taken on September 26 1997 at 29.4 S and 34.4 E.

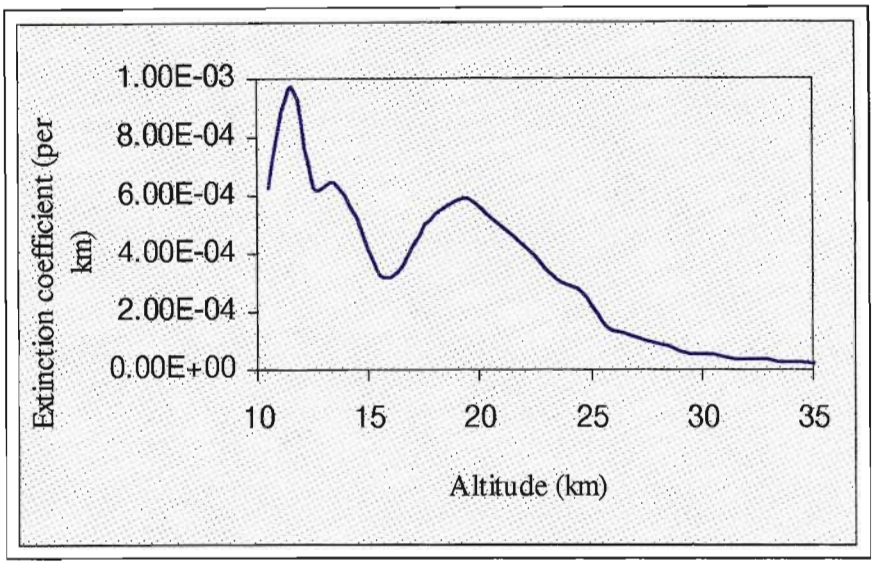

Figure 5.24: SAGE II profile taken on September 27 1997 at 24.3 S and 32.9 E.

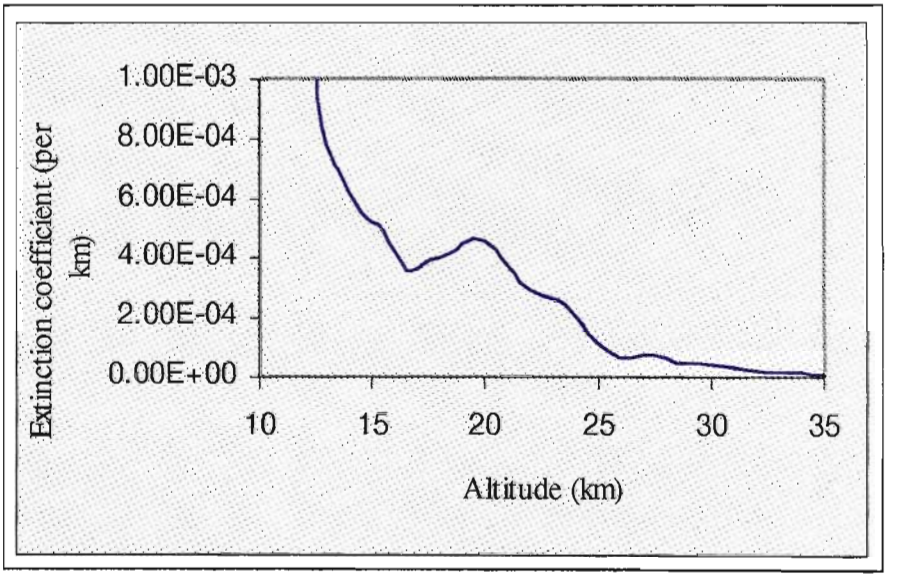

Figure 5.25: SAGE II profile taken on October 13 1997 at 23.8 S and 30.2 E.

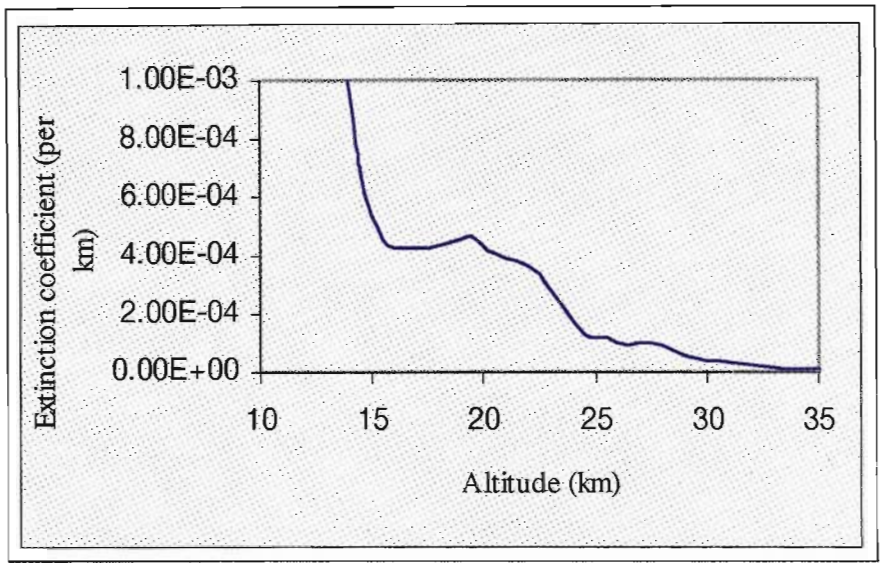

Figure 5.26: SAGE II profile taken on October 14 1997 at 28.7 S and 27.6 E.

These discrepancies between our calculated extinction coefficients profiles and the SAGE II extinction coefficient profiles are due to the different dates and locations the SAGE II data were extracted. Also LIDAR technique involves scanning one region of the atmosphere with a vertical resolution of 150 m, for a short time interval (several hours) whereas SAGE II has a vertical resolution of 1 km and measures the attenuated solar radiation horizontally during both sunrise and sunset while in orbit around the earth.

The broad peak depicted at 20 km in all the SAGE II profiles (figs.(5.20) - (5.26)) is sometimes referred to as the "Junge layer" (Junge and Manson 1961) and is mainly due to background aerosols. There is a time lag of 8 days for the SAGE II data compared to the LIDAR data. Unfortunately, we could not obtain SAGE II data for the date and time of operation of the LIDAR.

5.6 Conclusion

The old LIDAR system detected three aerosol layers in the lower troposphere during the month of July. They occurred at 1.2 km, 2.4 km and 4.0 km respectively. Each has an estimated thickness of 800 m. The layers seemed to disappear during the month of August.

During the months of September and October the old LIDAR detected higher concentration of aerosols occuring at 2.8 km and 3.6 km. The high concentration of aerosols is attributed to the burning of sugar-cane which reached its peak in October, and also during the months of September and October, when we have the largest number of active fires detected in South Africa (Justice *et al.* 1996).

The old LIDAR also detected for the month of July an aerosol layer in the upper troposphere at a height of 14 km. This layer is believed to originate from sugar cane burning. The upward troposheric circulation has transported it to higher altitude. For the month of October, a high altitude aerosol layer was detected at 28 km. Previously, Kuppen (1996) using the same LIDAR system detected an aerosol layer at a height of 25 km. This might be the same layer with the exception that over the space of one year some stratospheric upwelling has carried the layer to 28 km.

In chapter 7, we discuss the results obtained using the new LIDAR.

Chapter 6

Inversion method used to retrieve aerosol, relative density and temperature profiles for the new LIDAR

6.1 Introduction

This chapter deals with the different inversion methods employed to retrieve aerosol and temperature profiles from the data of the Rayleigh-Mie LIDAR. We will illustrate each method as applied to the LIDAR return signal. The uncertainties on the aerosol and temperature profiles are also discussed.

6.2 Klett Inversion Method

This is a widely used technique for extracting extinction coefficients of LIDAR returns. The method yields absolute values for extinction coefficients as opposed to the scattering ratio calculation which gives relative values.

Consider the LIDAR equation (2.15) as defined in section (2.8) of Chapter

2 where each term has already been defined on page 31:

$$S(z) = S_o \cdot Q \cdot \frac{A}{(z - z_L)^2} \cdot \left(\frac{c \cdot \tau}{2}\right) \cdot \beta(z) \cdot \exp\left\{-2 \int_{z_L}^{z} \sigma(z')\, dz'\right\} \qquad (6.1)$$

The aim is to solve this equation to obtain values of the extinction coefficients σ. We will illustrate this method as applied to the return signal of the new LIDAR. Fig.(6.1) shows the LIDAR return signal for the high altitude channel for 8 Jul 1999. After the signal has been corrected for background noise, the Klett inversion method is applied to the corrected signal shown in black in fig.(6.1). $S(z)$ is proportional to the corrected signal.

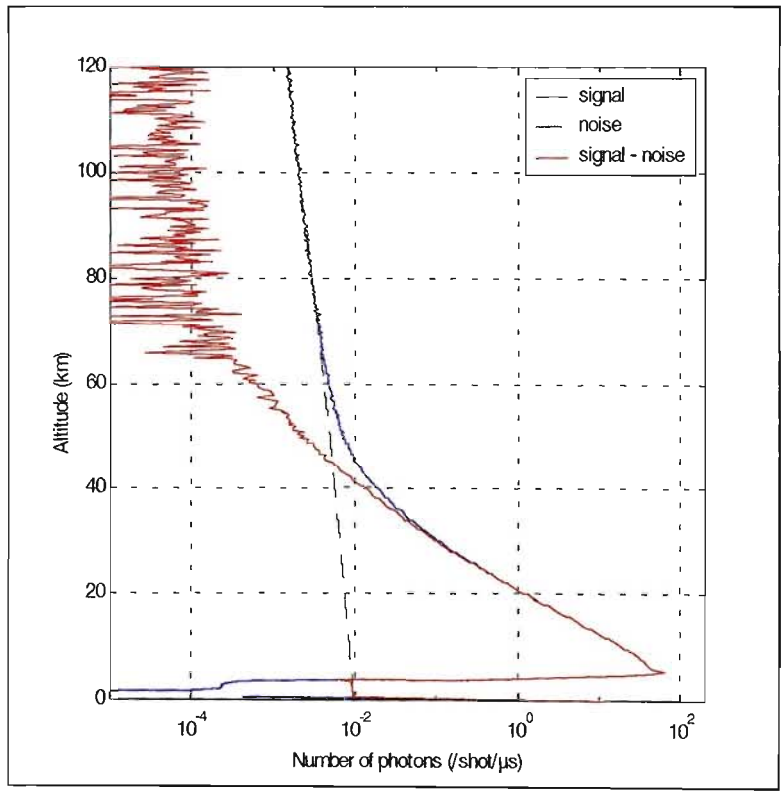

Figure 6.1: LIDAR return signal from high altitude for July 8 1999.

The method consists of the following steps:

(i) Converting the signal variable $S(z)$ to a logarithmic range-adjusted power, defined by

$$s(z) = \ln\left[z^2 \cdot S(z)\right]. \tag{6.2}$$

Using equation (2.15), equation (6.2) can now be written as in a logarithmic form as:

$$s(z) = \ln\left\{(z - z_L)^2 \cdot S_o \cdot Q \cdot \frac{A}{(z - z_L)^2} \cdot \left(\frac{c \cdot \tau}{2}\right) \cdot \beta(z) \cdot \exp\left[-2\int_0^z \sigma(z')\, dz'\right]\right\},$$

which simplifies to

$$s(z) = \ln\left\{S_o \cdot Q \cdot A \cdot \left(\frac{c \cdot \tau}{2}\right) \cdot \beta(z) \cdot \exp\left[-2\int_0^z \sigma(z')\, dz'\right]\right\}. \tag{6.3}$$

S_o, Q, A and $\left(\frac{c \cdot \tau}{2}\right)$ are all constants for a given LIDAR system. Consider LIDAR return from a constant reference altitude z_o. The LIDAR signal $s(z_o)$ will have a similar form as equation (6.3) and the difference between $s(z)$ and $s(z_o)$ eliminates the above four constants to give a simplified differential equation:

$$s - s_0 = \ln\left(\frac{\beta}{\beta_0}\right) - 2\int_{z_0}^{z} \sigma dz' \tag{6.4}$$

where $s = s(z)$, $s_0 = s(z_0)$ and β_0=$\beta(z_0)$.

(ii) Solving the differential equation corresponding to equation (6.4). This is of the form

$$\frac{ds}{dz} = \frac{1}{\beta}\frac{d\beta}{dz} - 2\sigma \tag{6.5}$$

If the atmosphere is homogeneous, $\frac{d\beta}{dz} = 0$ and the attenuation coefficient can be expressed directly in terms of the signal slope:

$$\sigma_{\text{hom}} = -\frac{1}{2}\frac{ds}{dz} \tag{6.6}$$

This is the basis of the slope method where the extinction coefficient is calculated directly from the slope of the graph of s versus z times -$\frac{1}{2}$. But if the atmosphere is assumed to be homogeneous over small rather than over large altitude ranges, applying the slope method to a succession of small intervals gives a reasonable first approximation to $\sigma = \sigma(z)$ in a notably inhomogeneous atmosphere. Unfortunately, assumptions like this are not well justified for many situations of interest, for example, under conditions of dense cloud, fog, smoke, and dust.

In several observational and theoretical studies it has been shown that under a wide range of circumstances for which particulate backscattering dominates that due to atmospheric gases (i.e., roughly for hazy, cloudy or foggy conditions and generally for IR wavelengths), β and σ can in fact be related approximately according to a power law of the form

$$\beta = \text{const } \sigma^j \tag{6.7}$$

where j depends on the LIDAR wavelength and various properties of the aerosols.

Reported values of j are generally in the interval $0.67 \leq j \leq 1.0$ (Barteneva 1960; Twomey and Howell 1965; Fenn 1966). If such a relationship is assumed, equation (6.5) becomes

$$\frac{ds}{dz} = \frac{j}{\sigma}\frac{d\sigma}{dz} - 2\sigma \tag{6.8}$$

In the case of Durban, it has been found suitable to use $j = 1$ (Dr H Bencherif, 2000, pers. comm.[1]). The ratio $\frac{\beta}{\sigma}$, known as the phase function, varies from the troposphere to the stratosphere. Suggested values have been listed in the work of Chazette *et al.* (1995). For a purely molecular atmosphere, the ratio $\frac{\beta}{\sigma}$ as deduced from Rayleigh's theory on scattering is $\frac{3}{8 \cdot \pi}$ or 0.120 sr^{-1} (Chazette *et al.* 1995). The values of the phase function most suitable for Durban region are 0.018 sr^{-1} for the troposphere, and 0.020 $sr^{-1}$for the stratosphere (Dr H Bencherif, 2000, pers. comm.[1]).

(iii) Equation (6.8) is an ordinary differential equation but non-linear. It nevertheless has an elementary structure, namely that of a Bernoulli equation. Equation of this type may be transformed to a first-order linear form by introducing a new unknown equal to the reciprocal of the original. Using $j = 1$ the general solution of equation (6.8) can therefore be written as (Klett 1981):

$$\sigma^{-1} = \exp\left(-\int^{z} \frac{ds}{dz'} \cdot dz' \left[m - 2\int^{z} \exp\left(-\int^{z'} \exp\left(-\int^{z'} \frac{ds}{dz"} \cdot dz"\right)\right)\right]\right) \tag{6.9}$$

where m is the integration constant. A particular solution for σ is

[1]Dr H Bencherif, Laboratoire de Physique de l'Atmosphère, Université de La Reunion, av. R. Cassin, BP 7151 97715, St-Denis cedex 9, Reunion Island, France.

$$\sigma = \frac{\exp[s - s_0]}{\left\{\sigma_0^{-1} - 2\int_{z_0}^{z} \exp[s - s_0]\, dz'\right\}} \tag{6.10}$$

where σ_0 is the value of σ at the $z = z_0$.

In our calculation we choose the reference altitude z_0 as 40 km where the atmosphere is free of aerosols. Equation (6.10) shows that σ is determined as the ratio of two numbers, which each become progressively smaller with increasing z; furthermore the denominator, which must approach zero at nearly the same rate as the numerator, is expressed as the difference between two relatively large numbers. This produces a strong tendency of instability and suggests that the determination of σ_0 will be inaccurate even for signals that are free of noise.

(iv) A particular solution for equation (6.9) was suggested by Klett (1981) for $z \leq z_0$:

$$\sigma = \frac{\exp[(s - s_0)]}{\left\{\sigma_0^{-1} + 2\int_{z}^{z_0} \exp[s - s_0] \cdot dz'\right\}} \tag{6.11}$$

where $s_0 = s(z_0)$ and $\sigma_0 = \sigma(z_0)$.

This new solution form is stable compared to equation (6.10) and so great accuracy in the choice of k is not needed. Applying equation (6.11) to the LIDAR signal of 8 July 1999 (fig.(6.1)), the extinction coefficients due to aerosol are obtained. Fig.(6.2) shows a plot of altitude versus extinction coefficients of aerosol between the altitudes 14 and 28 km.

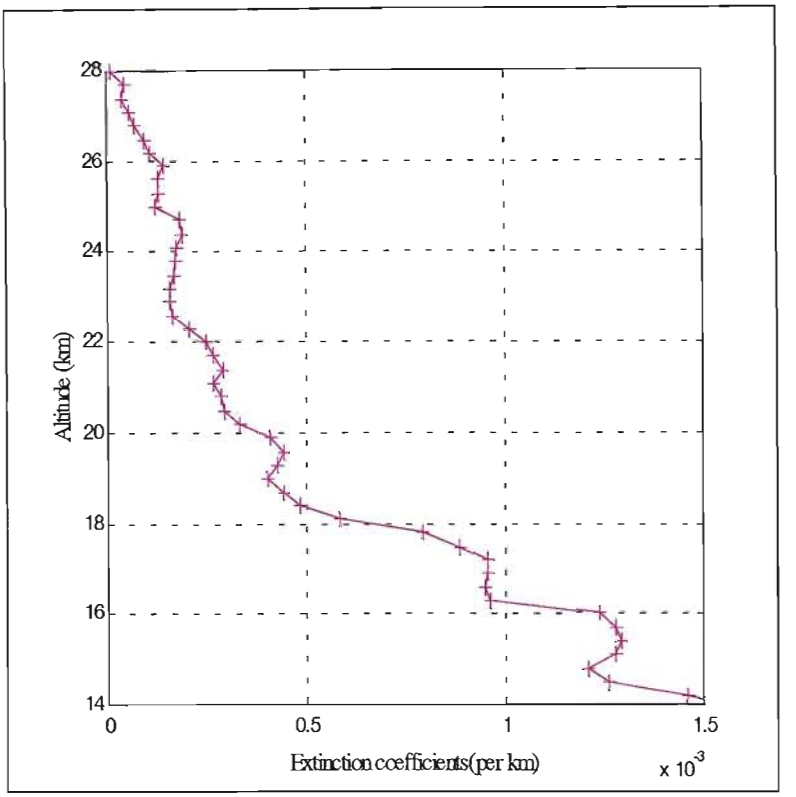

Figure 6.2: Plot of LIDAR extinction coefficients for July 8 1999 obtained using the Klett inversion method.

6.3 Determination of the relative density

The first measurement of density of the atmosphere was carried out using the searchlight technique by Elterman (1951). The result obtained on 19-20 August 1950 is shown in fig.(6.3). The data obtained are for Albuquerque, New Mexico. As shown in fig.(6.3) the density decreases exponentially with height.

The determination of relative density of the atmosphere using any LIDAR is based on the assumption that the atmosphere is purely molecular so that Mie scattering can be ignored.

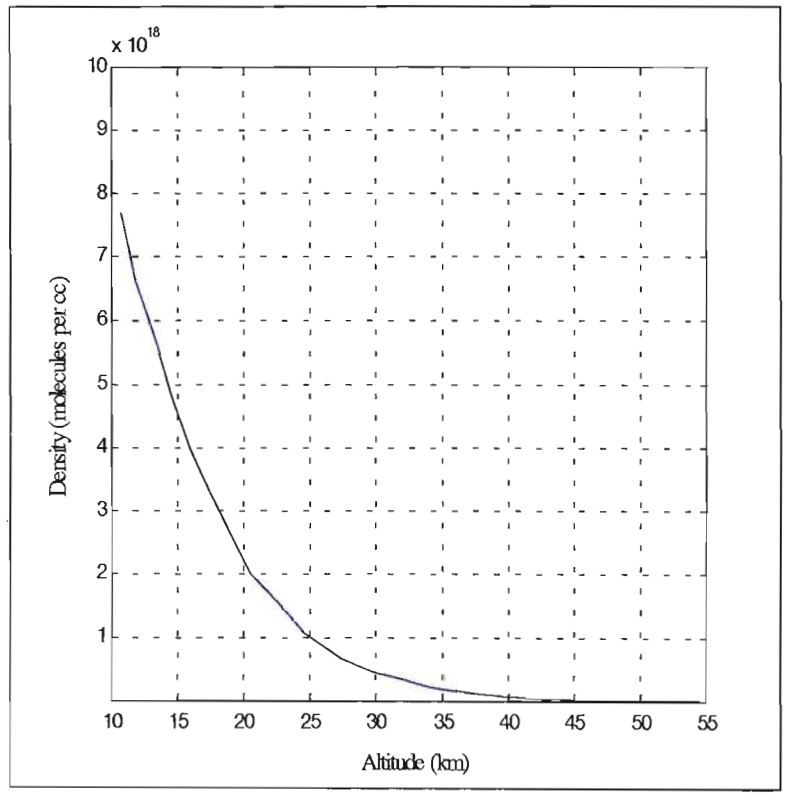

Figure 6.3: Density distribution from searchlight data (Elterman 1951).

In terms of the LIDAR signal S(z) (refer to equation (6.1)), the density of the atmosphere $\varrho_{LIDAR}(z)$ as deduced from the LIDAR signal can be expressed as:

$$\varrho_{LIDAR}(z) = k'[S(z) - K(z)] \cdot \Theta^2(z, z_o) \cdot \frac{(z - z_L)^2}{\left(\frac{c \cdot \tau}{2}\right)} \qquad (6.12)$$

where k' : normalisation constant,

S(z) : LIDAR signal after correcting for the non-linearity and saturation effects of the PMT,

K(z) : sky background noise which has been estimated using a quadratic equation of the form $Az^2 + Bz + C$ where A, B, C are constants

and z is the altitude,

$\Theta(z)$: atmospheric transmission between the altitude z and the top of the atmosphere z_o,

z_L : the altitude of the LIDAR station above sea level,

τ : the duration of the laser pulse.

The atmospheric transmission is determined from a standard climatological model after correcting the signal for the attenuation due to ozone and Rayleigh scattering at the emission wavelength of the laser (λ_e). It can take values between 0.995 and 1 above 30 km (Handbook of Geophysics and Space Environments 1965). Up to now no different values of the atmospheric transmission have been obtained.

The normalisation constant k cannot be determined experimentally. This is because of the uncertainties in the parameters of the LIDAR equation such as the laser energy, transmission optics, quantum efficiency of the photomultiplier, and also due to uncertainties in the atmospheric transmission of the lower atmosphere. It is determined by assuming that the atmosphere has the same density as that given by the CIRA - 1986 model at 30-35 km for the latitude and month corresponding to the LIDAR measurements.

The relative density profile is obtained from $\frac{\varrho_{LIDAR}}{\varrho_{CIRA}}$ where ϱ_{CIRA} is the density of the atmosphere as obtained from the CIRA-1986 model. The density obtained is not absolute as we are calculating the ratio $\frac{\varrho_{LIDAR}}{\varrho_{CIRA}}$ for each value of z. Fig.(6.4) shows the relative density profile obtained from the LIDAR data of 4 October 2001.

Wave-like structures are seen above 20 km are due to vertical propagation

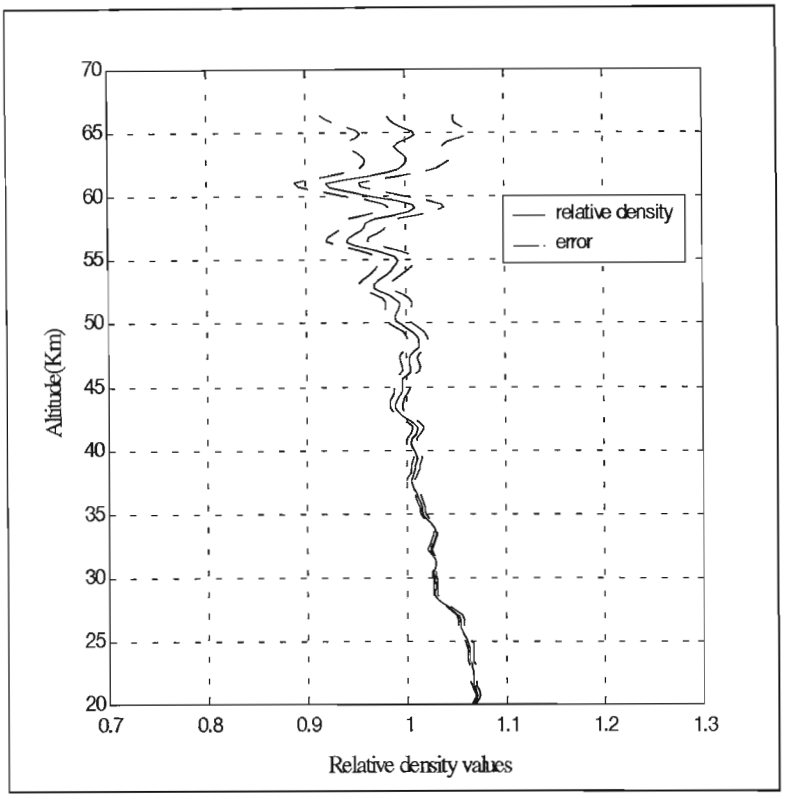

Figure 6.4: The relative density of the atmosphere above Durban as obtained from the LIDAR data of October 4 2001.

of the planetary waves in the atmosphere. The uncertainty in the realtive density profile is also shown in fig.(6.4). The uncertainty increases with altitude because of the increase in the sky background noise with altitude.

The uncertainty of the relative density profile is obtained from

$$\frac{\Delta \varrho_{LIDAR}}{\varrho_{LIDAR}} = \frac{\Delta S(z)}{S(z) - K(z)} \tag{6.13}$$

6.4 Determination of temperature profiles

The temperature profile is computed from the density values ϱ_{LIDAR} by assuming that the LIDAR returns are due to Rayleigh scattering by molecular

species and that the atmosphere is in hydrostatic equilibrium with pressure, density and temperature related through the ideal gas law. It is assumed that atmospheric turbulence does not affect the mean air density, which is indeed the case when considering the temporal and spatial resolutions of the LIDAR data.

The possibility of finding the temperature in this way was demonstrated for the first time using mechanically modulated searchlights by Eltermann (1953, 1954). The temperature profile for 10 October 1952 is shown in fig.(6.5) (Elterman 1953). This clearly shows that the temperature of the atmosphere initially decreases with altitude up to the tropopause ($\approx$ 17 km) and there after the temperature increases with height in the stratosphere followed by the stratopause ($\approx$ 55 km) and then the temperature decreases with height in the mesosphere. Preliminary studies using laser pulses as monochromatic light were obtained by Kent and Wright (1970).

The constant mixing ratio of the major atmospheric constituents (N_2,O_2,etc) and the negligible value of the H_2O mixing ratio justify the choice of a constant value W_m for the air mean molecular weight. This has been proved adequate to altitudes of up to 80 km. Above this altitude, dissociation of O_2 must be taken into account.

In an ideal gas, the air pressure $p_r(z)$, density $\varrho(z)$ and temperature $M(z)$ are related by

$$p_r(z) = \frac{U_R \cdot \varrho(z) \cdot M(z)}{W_m} \tag{6.14}$$

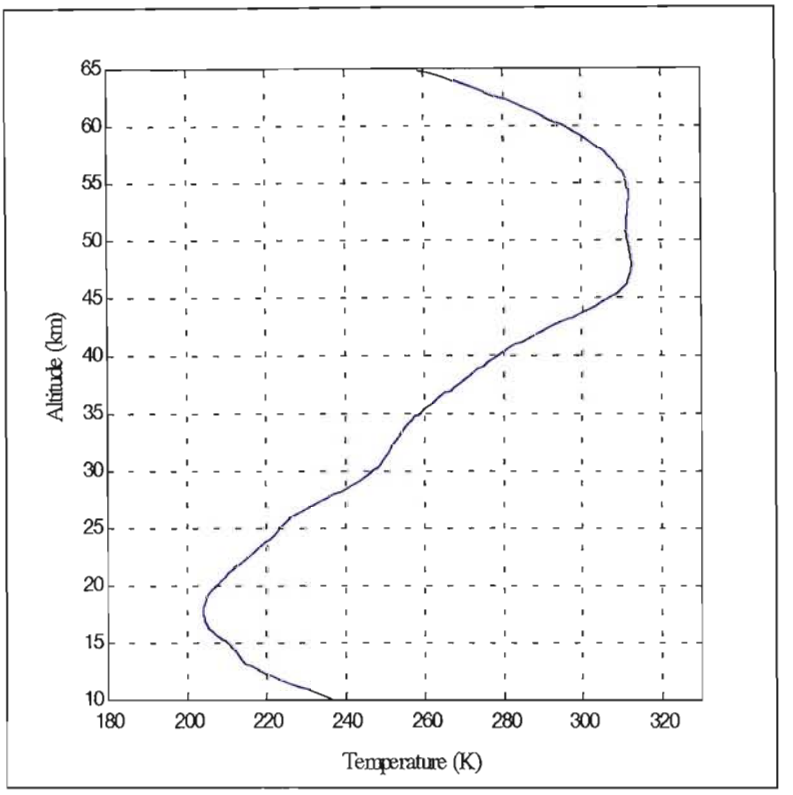

Figure 6.5: Temperature distribution from searchlight data (Elterman 1953).

and hydrostatic equilibrium implies that

$$dp_r(z) = -\varrho(z) \cdot g(z) \cdot dz \tag{6.15}$$

where U_R is the universal gas constant which has value 8.31 J $\text{mol}^{-1}\text{K}^{-1}$ and $g(z)$ is the acceleration due to gravity at altitude z. We assume that g remains constant throughout the altitude range of observation and is equal to 9.81 ms^{-2}.

The combination of equations (6.14) and (6.15) leads to

$$\frac{dp_r(z)}{p_r(z)} = d(Log\ p_r(z)) = -\frac{W_m \cdot g(z)}{U_R \cdot M(z)} dz \tag{6.16}$$

If the acceleration due to gravity and the temperature are assumed to be constant in the i^{th}layer, the pressure at the bottom and top of the layer are related by

$$\frac{p_r(z_i - \frac{\triangle z}{2})}{p_r(z_i + \frac{\triangle z}{2})} = \exp\left(\frac{W_m \cdot g(z_i)}{U_R \cdot M(z_i)}\right) \cdot \Delta z \tag{6.17}$$

Hence the temperature in each layer may be expressed in terms of the log pressure difference between top and bottom as

$$M(z_i) = \frac{W_m \cdot g(z_i) \cdot \triangle z}{U_R \cdot Log\left[\frac{p_r(z_i - \frac{\triangle z}{2})}{p_r(z_i + \frac{\triangle z}{2})}\right]} \tag{6.18}$$

where $M(z_i)$ is the temperature in the i^{th} layer, assumed constant throughout the layer.

The density profile is measured up to the n^{th} layer. The pressure at the top of this layer is fitted with the pressure of the CIRA - 1986 model $p_{rm}(z_n + \frac{\triangle z}{2})$ for the corresponding month and latitude. The top and bottom pressure of the i^{th} layer are then given by

$$p_r(z_i + \frac{\triangle z}{2}) = \sum_{j=i+1}^{n} \varrho(z_j) \cdot g(z_j) \cdot \triangle z + p_{rm}(z_n + \frac{\triangle z}{2}) \tag{6.19}$$

$$p_r(z_i - \frac{\triangle z}{2}) = p_r(z_i + \frac{\triangle z}{2}) + \varrho(z_i) \cdot g(z_i) \cdot \triangle z \tag{6.20}$$

Let $X = \dfrac{\varrho(z_i) \cdot g(z_i) \cdot \triangle z}{p_r(z_i + \dfrac{\triangle z}{2})}$.

Consider $1+X = 1+\dfrac{\varrho(z_i) \cdot g(z_i) \cdot \triangle z}{p_r(z_i + \dfrac{\triangle z}{2})} = \dfrac{p_r(z_i + \dfrac{\triangle z}{2}) + \varrho(z_i) \cdot g(z_i) \cdot \triangle z}{p_r(z_i + \dfrac{\triangle z}{2})}$,where

the numerator is the same as equation (6.20). Therefore the expression $1+X$

can be written as $\dfrac{p_r(z_i - \dfrac{\triangle z}{2})}{p_r(z_i + \dfrac{\triangle z}{2})}$.

Using equation (6.18), the expression for the temperature can be written in terms of X as

$$M(z_i) = \frac{W_m \cdot g(z_i) \cdot \triangle z}{U_R \cdot Log(1+X)} \tag{6.21}$$

The statistical standard error of the temperature is

$$\frac{\delta M(z_i)}{M(z_i)} = \frac{\delta Log\,|1+X|}{Log\,|1+X|} = \frac{\delta X}{(1+X) \cdot Log(1+X)} \tag{6.22}$$

with

$$\left(\frac{\delta X}{X}\right)^2 = \left|\frac{\delta \rho(z_i)}{\rho(z_i)}\right|^2 + \left|\frac{\delta p_r(z_i + \dfrac{\triangle z}{2})}{p_r(z_i + \dfrac{\triangle z}{2})}\right|^2 \tag{6.23}$$

$$\delta p_r(z_i + \frac{\triangle z}{2})^2 = \sum_{j=i+1}^{n} |g(z_j) \cdot \delta\varrho(z_j) \cdot \triangle z|^2 + \left|\delta p_{rm}(z_n + \frac{\triangle z}{2})\right|^2 \tag{6.24}$$

where p_{rm} is the pressure at the top of the n^{th} layer and is fitted with the pressure of the CIRA - 1986 model for the corresponding month and latitude.

Hauchecorne *et al.* (1980) have shown that the contribution of the extrapolated pressure at the n^{th} layer on the local pressure below decreases rapidly with altitude due to the exponential decrease of pressure with altitude, and its influence on the temperature determination is marginal. Then the term X represents a ratio of experimental density values from which absolute temperature can be deduced even though the density measurements are only relative.

The atmospheric transmission at the wavelength used for the new LIDAR (532 nm) is affected by Mie scattering, Rayleigh scattering and absorption by ozone. The attenuation of the LIDAR return due to aerosols, clouds, haze, and fog is difficult to estimate. In the temperature retrieval programme we only consider molecular scattering and absorption by ozone. A listing of the source code is given in Appendix B. Fig.(6.6) shows the LIDAR temperature profile for October 4 2001 obtained using the algorithm as outlined above. The broken line shown in red is the CIRA-1986 model. Again as with the relative density profile, the wave-like structures which appear above 40 km on the temperature profile are due to vertical propagation of planetary waves.

The atmospheric transmission at altitudes between 30 and 100 km is greater than 0.995 (Cole *et al.* 1965). The attenuation is therefore very low and may be determined by an atmospheric model. The resulting error is very small and much less important than other sources such as statistical fluctuations of the signal at high altitude.

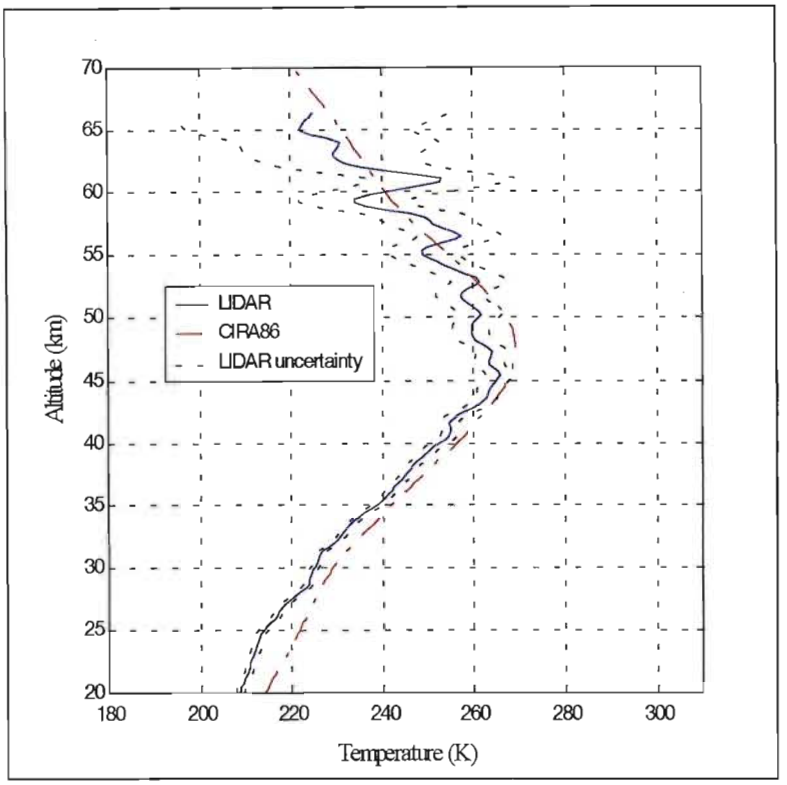

Figure 6.6: LIDAR temperature profile obtained from the density profile for October 4 2001.

6.5 Summary

The Klett inversion, the temperature and the relative density retrieval methods described in this chapter have been applied successfully to the new LIDAR data. As for the old LIDAR data, only the Klett inversion method has been used to retrieve aerosol extinction coefficients.

The wave-like structures seen in the LIDAR temperature profiles have also been observed in rocketsonde temperature measurements of the stratosphere and mesosphere (Labitzke 1980) and also in satellite measurements of the middle atmosphere temperature (Barnett 1980).

Chapter 7

Results and validation of the new LIDAR measurements

7.1 Introduction

A validation campaign of the new LIDAR data was carried out from April 1999 to December 2000. The preliminary LIDAR data first obtained during April 1999 (when the new LIDAR was installed) were used to test the inversion codes for temperature, relative density and extinction coefficients of aerosols, and to adapt them to the local conditions. The LIDAR has since been operational on clear sky nights. Table (7.1) summarises the number of months, nights and hours of LIDAR acquisition done during the years 1999 and 2000.

The validation of the aerosol measurements was done with SAGE II data as described in the next section.

	1999	2000
Total number of months	9	9
Total number of nights	72	65
Total number of hours	284	230
Total number of hours in summer	19	19
Total number of hours in winter	265	211

Table 7.1: Summary of LIDAR measurements in 1999 and 2000.

7.2 Validation of the aerosol measurements by the new LIDAR

Accurate measurements of atmospheric aerosols are of considerable importance to our understanding of the depletion of ozone (World Meteorological Organisation 1991), especially in this part of the world, as well as its influence on the local climate. Fig.(7.1) shows a Multi-angle Imaging SpectroRadiometer (MISR) image of the north-eastern part of South Africa, near Kruger National Park, taken on September 7, 2000 during the Southern Africa Fire-Atmosphere Research Initiative (SAFARI)-2000 campaign. The latter is an international science initiative aimed at developing a better understanding of the Southern African land-atmosphere-human system.

The left image shows the Drakensberg mountains, where east of its range a large burn scar with thin smoke plumes is visible. The right-hand image is a "zoomed-in" view of the upper central part of the left image. These fires are deliberately set to burn off dry vegetation - a common agricultural practice in many parts of Africa. The vertical transport of the smoke is controlled by the stability structure of the atmosphere and the horizontal transport by

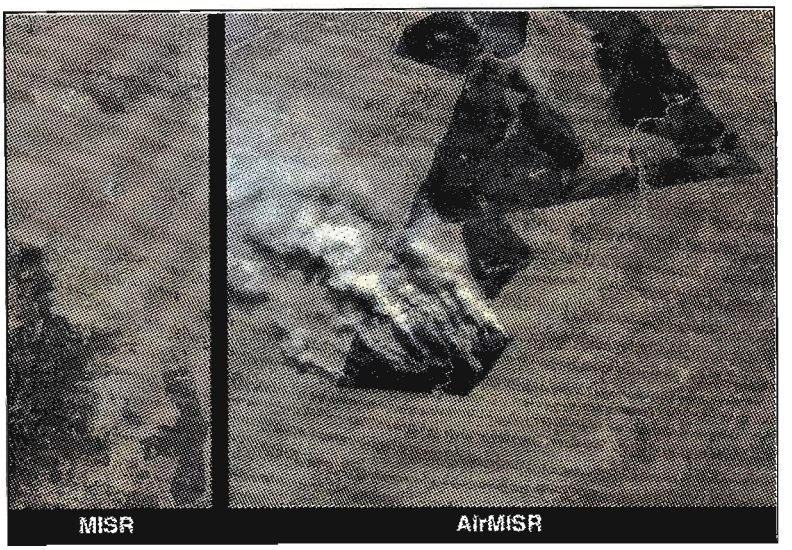

Figure 7.1: MISR and airMISR images of north eastern part of South Africa taken on September 7, 2000 during the SAFARI 2000 campaign.

the local thermo-topographic winds near the surface. Remote measurements of the vertical distribution of aerosol backscattered by LIDAR contribute significantly to an understanding of the vertical transport of aerosols in the troposphere as well as horizontal transport in the stratosphere during major volcanic eruption.

Before we proceed with the validation of the new LIDAR measurements of aerosols, we will give a brief introduction of stratospheric aerosols.

7.2.1 Stratospheric aerosols

Stratospheric aerosols are an important focus of scientific investigation since 1883 when the eruption of Krakatoa attracted the attention of the world with its spectacular optical effects caused by the large outpouring of ashes which blocked out some of the sunlight. The explosion is classed as one of the largest volcanic eruptions in modern times; so great was the outpouring of

lava that new islands were formed and debris was scattered across the Indian Ocean as far as Madagascar.

The aerosols in the stratosphere play also an important role in the ozone cycle. Climatological studies accomplished with balloons, rockets and satellites show that for the last 20 years the quantity of ozone in the middle latitude of the northern winter hemisphere (Stolarski *et al.* 1991) has decreased by 2 to 3 % per decade (WMO 1989). In the middle latitude of the southern winter hemisphere the decrease of ozone is more pronounced and is of the order 2 to 12 % per decade (WMO 1991).

Aerosols (liquid particles and solids) diameter in the range 0.01 to 10 μm are located in the stratosphere around 20 km. This is often referred to the Junge layer and consists mainly of natural background aerosols. They are mainly sulphate particles and sulphuric acid droplets (Junge *et al.* 1961; Junge 1963). They maintain a quasi-constant concentration in the form of a homogeneous layer. Other aerosols such as SO_2 and OCS are injected directly into the stratosphere by volcanic eruptions. Since the average residence time of volcanic aerosols in the stratosphere is of the order of $\approx$ 10 months (Hofmann and Rosen 1981) they do not constitute a major source of the Junge layer. They are also transported vertically from the troposphere into the stratosphere by diffusion and wave activity.

Above Durban (29.8^{0}S, 30^{0}E) the atmosphere is under the influence of subtropical air masses and the jet stream (located around 30^{0}S in winter with a mainstream wind speed exceeding 30 ms^{-1} at an average height of 12 km). Sometimes strong wind gives rise to turbulence and one would expect

variations in the background aerosols.

We will make a comparative study between the aerosol measurements by LIDAR and those made by the Stratospheric Aerosol and Gas Experiment II (SAGE II) which is located on board the Earth Radiation Budget Satellite (ERBS). We will first describe the method used by SAGE II to measure aerosols.

7.3 Aerosol measurements by the SAGE II experiment

SAGE II, launched aboard the ERBS in October 1984, is the latest in a series of satellite-borne stratospheric aerosol and gas monitoring instruments flown by NASA. Fig.(7.2) shows the predicted measurement locations of SAGE II from June 2001 to May 2002. As shown in the plot, there is a global coverage from 80^0S to 80^0N. The objectives of SAGE II are:

(i) to map vertical profiles of stratospheric aerosols, ozone, nitrogen dioxide, and water vapour globally from 80^0S to 80^0N,

(ii) to study the seasonal and global variations of these measurements,

(iii) to utilise stratospheric aerosols and gases as atmospheric tracers to study the circulation, sources, and sinks of these species, and transient phenomena such as volcanic eruptions,

(iv) to investigate atmospheric chemistry involving the gaseous species and to study the optical and physical properties of aerosols, and

(v) to determine high-altitude cloud cover and its variations (McMaster 1986).

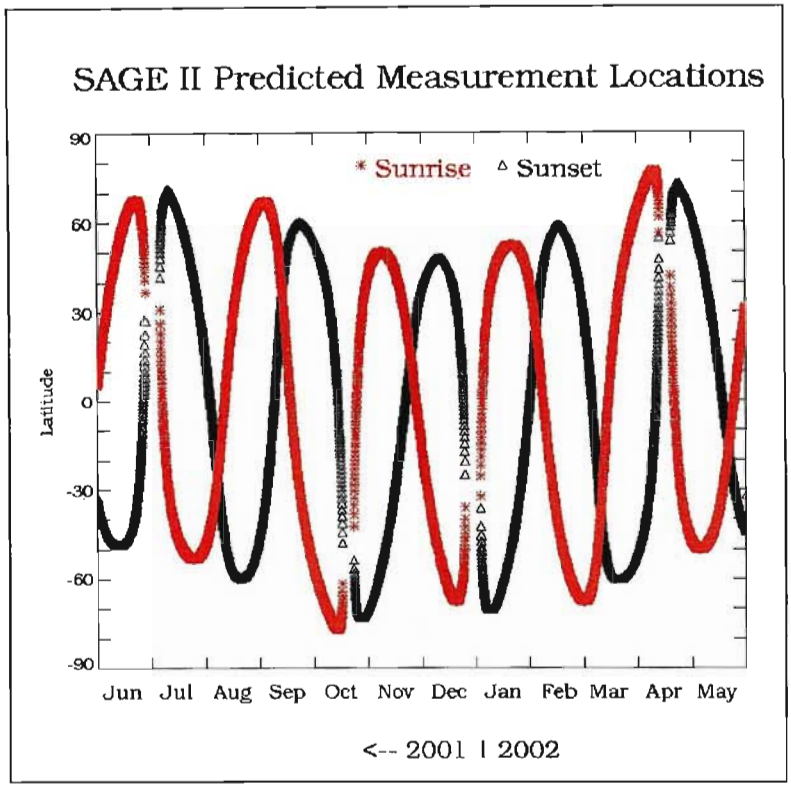

Figure 7.2: SAGE II predicted measurement locations during sunrise and sunset events (NASA, Langley Research Centre (LaRC)).

The SAGE II instrument, designed to accomplish these goals, is a seven-channel Sun photometer, which vertically scans the Sun during both spacecraft sunrise and sunset. Each day, SAGE II measures approximately 15 sunrise and sunset events, equally spaced in longitude along two latitude belts between approximately 80 ^{0}N and 80 ^{0}S. Values of limb path atmospheric extinction are measured from the top of the atmosphere to cloud tops or to the Earth's horizon. These values are combined with spacecraft ephemeris and molecular density data to generate seven slant path transmission versus tangent altitude profiles. The transmission data are then averaged into 1-km vertical increments and inverted to yield profiles of aerosol extinction at the

wavelengths 1.02, 0.525, 0.453, 0.385 μm, as well as O_3, NO_2, and water vapour number density. Each extinction profile describes an average of the extinction coefficient within the spherical atmospheric shells cut by the limb path between SAGE II and the Sun.

Fig.(7.3) shows a map of 1020 nm SAGE II aerosol extinction at an altitude of 6.5 km during a long term-average from 1985-1990 and from 1994-1997 for September-November. The strong extinction enhancement over Brazil is clearly visible, as is the aerosol band extending round the globe in Southern mid-latitudes. The elevated aerosol layers over Brazil could be smoke from biomass burning that has been transported across the Southern oceans (Kent *et al.* 1998). The white band through the equator indicates no measurement by SAGE II.

We now describe briefly the inversion algorithm used by SAGE II. For a detailed treatment, the reader should refer to Chu *et al.* (1989).

7.4 Inversion Algorithm used by SAGE II

Fig. (7.4) shows the experimental geometry of SAGE II for the measurement of the solar extinction. The solar irradiance H_λ passing through the atmosphere between the spacecraft and the sun as measured by the SAGE II instrument at a given time t is given by

$$H_\lambda = \int_{\Delta\lambda} \int_{\Delta b} \Pi_\lambda(\theta, \vartheta) \cdot F_\lambda(\theta, \vartheta, t) \cdot \Theta_\lambda(\theta)\, d\Omega\, d\lambda \qquad (7.1)$$

where Π_λ : radiometer's field of view function at wavelength λ,

ϑ : azimuthal angle,

Ω : solid angle,

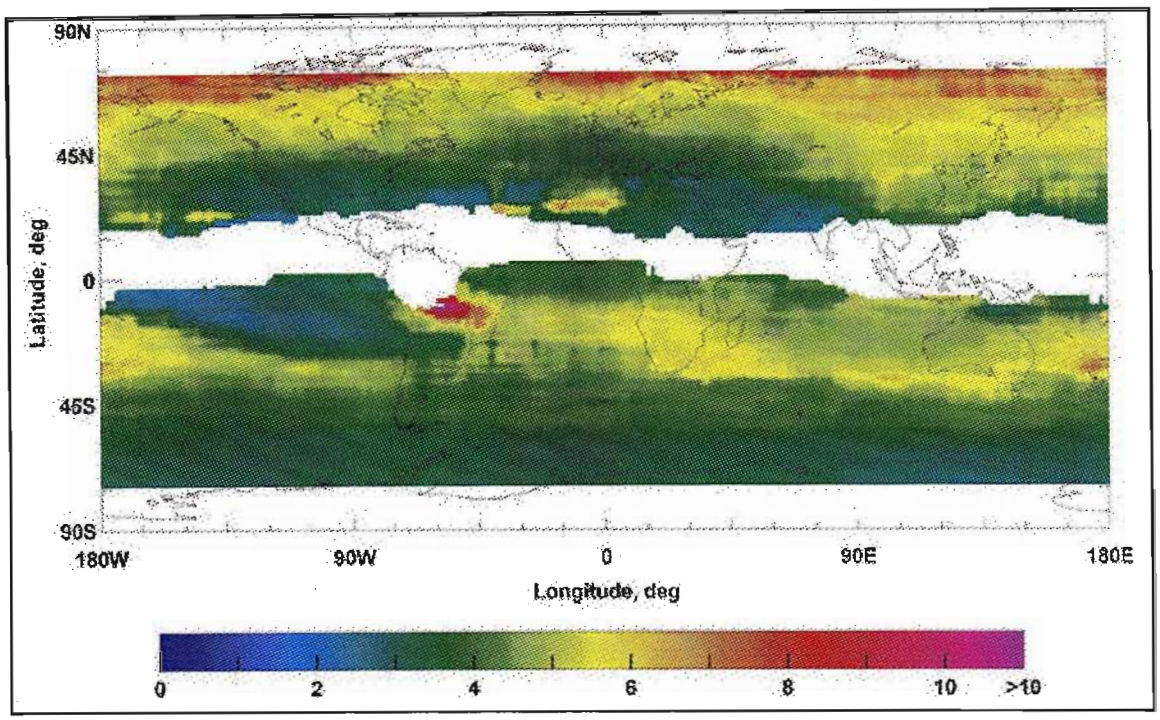

Figure 7.3: Global map of 1020 nm SAGE II aerosol extinction at an altitude of 6.5 km for the months Sep to Nov averaged over the years 1985 - 1990 and 1994 - 1997. The bottom scale is the aerosol extinction in 10^{-3} km^{-1}(from NASA, Langley Research Centre (LaRC)).

Θ_λ : transmission of the atmosphere as a function of view angle θ,

F_λ : the extraterrestrial solar radiance for wavelength λ,

Δb : spectral bandwidth of the radiometer's field of view.

The radiometer is situated on the circularly orbiting satellite with velocity V. Each instantaneous view angle θ measured from V will define a unique tangent altitude h_t for the sun ray.

The transmission Θ of the atmosphere is a unique function of the tangent height h_t (see fig.(7.4)). The mean transmission of the atmosphere over the spectral bandwidth and instrument field of view is calculated by ratioing

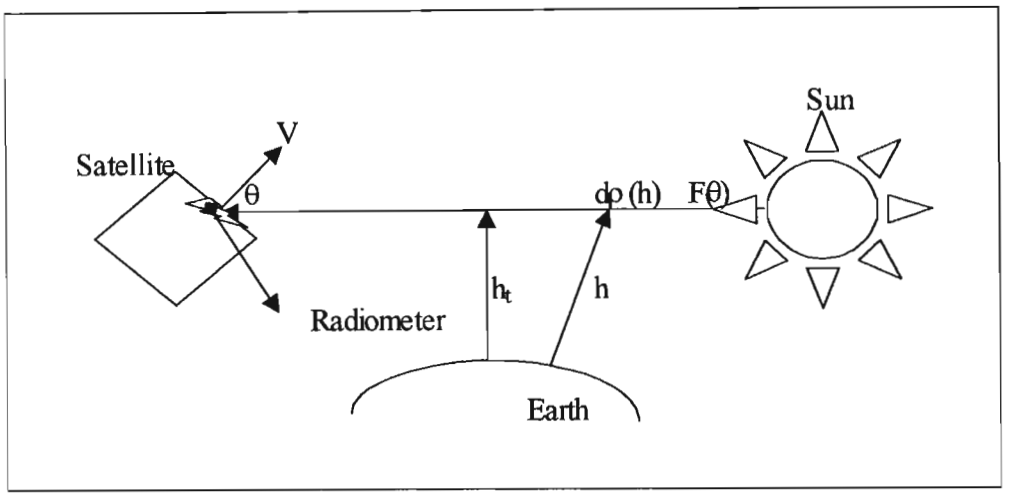

Figure 7.4: Experimental geometry for solar extinction measurement by SAGE II. The distances are exaggerated. h_t is the tangent height, h is the height above the Earth, ρ_λ is the Sun ray optical path length, θ is the view angle of SAGE II and F is the solar irradiance.

the irradiance measured within the atmosphere to that measured outside the atmosphere. The transmission function Θ_λ in terms of the tangent height h_t, according to Bouguer law, is given by

$$\Theta_\lambda(h_t) = \exp\left[-\int \sigma_\lambda(h) \cdot \, d\rho_\lambda(h)\right] \tag{7.2}$$

where $\sigma_\lambda(h)$ is the total extinction coefficient of the atmosphere as a function of altitude h for wavelength λ and $\rho_\lambda(h)$ is the sun ray optical path length corrected for refraction.

The total extinction coefficient σ_λ at each tangent altitude consists of contributions mainly from:

(a) air molecules (Rayleigh),

(b) ozone,

(c) nitrogen dioxide,

(d) aerosols.

This can be expressed as a linear combination of the extinctions of each type, as given by

$$\sigma_\lambda = \sigma^{Ray}(\lambda) + \sigma^{O_3}(\lambda) + \sigma^{NO_2}(\lambda) + \sigma^{aero}(\lambda) \tag{7.3}$$

where $\sigma^{Ray}(\lambda)$ is the extinction coefficient for Rayleigh scattering, and $\sigma^{O_3}(\lambda)$, $\sigma^{NO_2}(\lambda)$ and $\sigma^{aero}(\lambda)$ are the extinction coefficients for O_3, NO_2 and aerosol at wavelength λ respectively. The Rayleigh scattering term is described by the well-known inverse fourth power dependence on wavelength.

For O_3 and NO_2 the extinction coefficients are determined by the product of the species number density and their absorption cross-section at the specific wavelength. The aerosol extinction coefficient is a function of aerosol size distribution, shape, and index of refraction. For homogeneous, spherical aerosol particles, the extinction coefficient is given by the following equation (Deirmendjian 1965):

$$\sigma^{aero}(\lambda) = \int_0^\infty \chi(n, r, \lambda) \cdot \ w(r)\ dr \tag{7.4}$$

where $w(r)$ is the size distribution function, and $\chi(n, r, \lambda)$ is the extinction cross section for a particle with refractive index n and radius r. The extinction coefficient $\chi(n, r, \lambda)$ for homogeneous spherical particles can be computed from Mie theory (Van de Hulst 1957).

The SAGE II data are processed by reducing the solar radiance measurements at the seven spectral channels into transmission functions of the atmosphere at the seven wavelength regions. The transmission data are then inverted using equations (7.2), (7.3) and (7.4) to obtain the vertical extinction profiles for each of the species. Fig.(7.5) shows the tangent altitude versus

computed atmospheric transmission profiles at four SAGE II wavelengths: 1.0 μm, 0.6 μm, 0.45 μm and 0.385 μm.

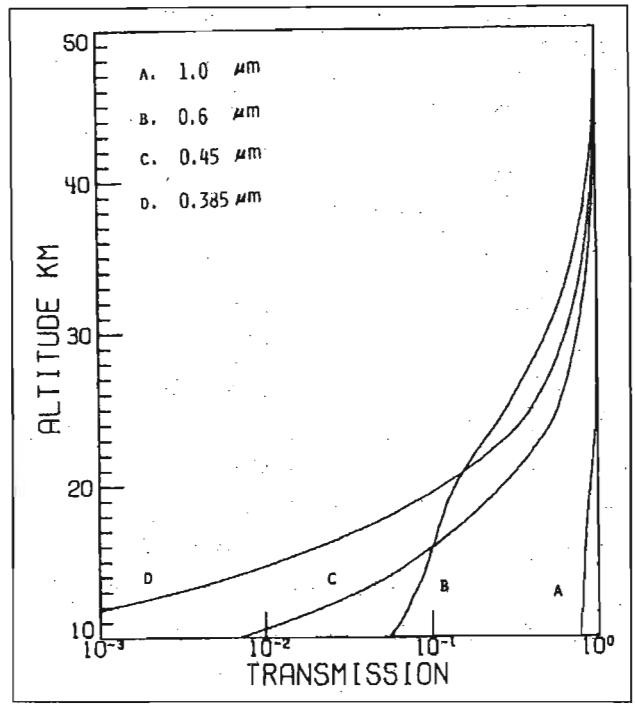

Figure 7.5: Tangent altitude vs atmospheric transmission measurements by SAGE II at four wavelengths for solar extinction geometry.

7.5 Calculation of LIDAR extinction coefficients

The LIDAR equation (equation (2.15)) as given in section (2.8) of Chapter 2 is

$$S(z) = S_o \cdot Q \cdot \frac{A}{(z - z_L)^2} \cdot \left(\frac{c \cdot \tau}{2}\right) \cdot \beta(z) \cdot \exp\left[-2 \int_{z_L}^{z} \sigma(z')\, dz'\right] \qquad (7.5)$$

where each term has been defined previously in section (2.8) of Chapter 2.

In equation (6.1) the extinction term is written as an integral over the two-way path from the LIDAR to the scattering volume.

In analysing the LIDAR data it is often convenient to use the backscatter ratio R(z) (Russell et al. 1979) which is defined as the ratio of the total backscatter coefficient to the molecular backscatter coefficient:

$$R(z) = \frac{\beta_m(z) + \beta_a(z)}{\beta_m(z)} \tag{7.6}$$

where $\beta_a(z)$ and $\beta_m(z)$ are the aerosol and molecular backscattering coefficients respectively.

The Klett inversion method (Klett 1981; Klett 1985) has been used to solve the LIDAR equation to obtain the total volume extinction coefficient $\sigma(z)$. The method reduces the LIDAR equation to a Bernoulli differential equation which is convergent for $z \leq z_{ref}$ where z_{ref} is a reference altitude chosen above the aerosol layer where the particle content is negligible. The determination of the total volume extinction coefficient $\beta(z)$ from equation (6.1) requires quantitative knowledge of a relationship between $\sigma(z)$ and $\beta(z)$ usually expressed as a ratio called the backscatter phase function $\varpi(z) = \frac{\beta(z)}{\sigma(z)}$. This ratio represents contribution from Rayleigh scattering by molecules ϖ_m and scattering by aerosols ϖ_a:

$$\varpi_m(z) = \frac{\beta_m(z)}{\sigma_m(z)} \tag{7.7}$$

$$\varpi_a(z) = \frac{\beta_a(z)}{\sigma_a(z)} \tag{7.8}$$

where ϖ_m is the Rayleigh backscatter phase function for molecular scattering and is equal to $\frac{3}{8\pi} \approx 0.119$ sr^{-1} (Chazette *et al.* 1995) and $\varpi_a(z)$ is the aerosol backscatter phase function which depends on the size distribution and refractive index of the aerosols, and can therefore vary with altitude. The backscatter phase function for aerosols may lie in the range 0.013 sr^{-1} to 0.030 sr^{-1}. This interval has been deduced from SAGE II data (Ackerman *et al.* 1989) and Mie scattering theory. Table (7.2) shows a comparison of the values of the aerosol backscatter phase functions following the El Chichon and Mount Pinatubo eruptions calculated by several workers using LIDAR (Thomas *et al.* 1987; Jäger and Hofmann 1991; Chazette *et al.* 1995), SAGE II satellite data (Ackerman *et al.* 1989) and radiosonde measurements (Deshler *et al.* 1993). As shown in table (7.2), the values of the aerosol backscatter phase function are large following major volcanic eruptions. This increase in the aerosol backscatter phase function is due to large injection of dust and sulphurous gases such as sulphur dioxide in the stratosphere.

Year	1983	1984/1985	1991 to 1993
Chazette et al. (1995)	0.025 sr^{-1}	0.016 sr^{-1}	0.025 sr^{-1}
using LIDAR			
Jäger and	0.017 $sr^{-1}$to	0.024 sr^{-1}	
Hofmann (1991) using LIDAR	0.045 sr^{-1}		
Ackerman et al. (1989)		0.013 $sr^{-1}$to	
using SAGE II		0.025 sr^{-1}	
Deshler et al. (1993)			0.015 sr^{-1}at 17 km
using balloon measurements			0.026 sr^{-1}at 19 km
			0.015 sr^{-1}at 23 km

Table 7.2: Values of the aerosol backscatter phase function following the El Chichon and Mount Pinatubo eruptions obtained using LIDAR, SAGE II and balloon measurements.

ϖ_m has been computed using the CIRA-1986 model. The determination of the backscatter phase function due to aerosols ϖ_a from the LIDAR measurements requires several assumptions. First, ϖ_a is assumed to remain constant with altitude. This assumption has been shown by Chazette *et al.*(1995) to be representative of the altitude range where the backscatter coefficient is maximum and the values of ϖ_a obtained are in agreement with other in situ and LIDAR measurements. Secondly, it is assumed that the scattering ratio R(z) (equation (7.6)) remains close to 1.00 at and above the reference altitude, z_{ref}.

The value of ϖ_a in the stratosphere following major volcanic eruption is large but decreases during the post-volcanic period. For example, during the period following the El Chichon eruption in 1983, reported average value of ϕ_a using LIDAR data at Observatoire de Haute-Provence in Southern France (Chazette *et al.* 1995) is 0.023 $\pm$ 0.003 sr^{-1} but decreases to 0.016 $\pm$ 0.004 sr^{-1} during the years 1984 to 1985. For background aerosols which are

located around 20 km (Junge 1961) ϖ_a has an estimated value of 0.018 sr^{-1}.

Due to biomass and large scale sugar-cane burning which occurs from June to October over the Kwazulu-Natal coast and also the large concentration of chemical industries in the south of Durban, we consider the stratosphere above Durban to be loaded in aerosol. For the present study, we estimate that a value of $\varpi_a = 0.020$ sr^{-1} will be suitable for the altitude range of the LIDAR measurement (20 km $\leq z \leq$ 60 km). In the Klett inversion method, z_{ref} is chosen to be 40 km as we assume there will be no aerosol present at and above this height. We also assume that the scattering at and above 40 km is only due to air molecules and R(z) $\approx$ 1.

The uncertainties in the determination of the total volume backscatter coefficient $\beta(z)$ arise from the following causes:

(1) statistical fluctuations of the measured LIDAR signal which are associated with random detection processes,

(2) the presence of aerosol particles at and above the reference altitude z_{ref} and the subsequent uncertainty in the value of R(z_{ref}),

(3) the uncertainty in the phase function ϖ_a and its altitude dependence.

The first uncertainty in the statistical fluctuations of the measured LIDAR signal can be reduced by averaging all the LIDAR raw data during the acquisition period which is 4 to 5 hours. This leads to a statistical uncertainty of less than 2.5 % (Chazette *et al.* 1995). The next two uncertainties are reduced when z_{ref} is approached in the Klett inversion algorithm. z_{ref} is chosen as high as possible so as to minimise the uncertainty due to low aerosol loading at higher altitude. The total uncertainty associated with all the three causes is less than 7 % when the signal-to-noise ratio is significant

above 40 km (Chazette *et al.* 1995).

7.6 Comparison of LIDAR/SAGE II Extinction profiles

The comparisons of SAGE II extinction profiles with those obtained from ground-based LIDARs (Ackerman *et al.* 1989; Parameswaran *et al.* 1991; Bencherif 1996), from an airborne LIDAR (Osborn *et al.* 1989), and from a balloon-borne dustsonde (Northam *et al.* 1974; Osborn *et al.* 1989) have been done mostly for middle and high latitudes. Few comparisons have been made for subtropical latitude (e.g. Durban), mainly because of the sparsity of ground-based LIDAR data. Indeed, most ground-based LIDARs are found in the Northern hemisphere as compare to a few LIDAR stations in the Southern hemisphere.

It should be noted that the SAGE II instrument scans the sun horizontally (see fig. (7.4)) during both spacecraft sunrise and sunset through an optical path of a few hundred kilometres whereas LIDAR samples the atmosphere vertically and therefore the measurements are localised. The LIDAR data are temporally integrated over a few hours. The other difference in the two methods is that they use different wavelengths to probe the atmosphere ($\lambda_{\mathrm{SAGE}} = 525$ nm, $\lambda_{\mathrm{LIDAR}} = 532$ nm). From the LIDAR data base of 1999, three days were selected when the subsatellite ERBS line of sight grazes the location of Durban according to the following criteria:

(i) less than 10^0 in latitude and longitude between the LIDAR location (Durban) and the tangent to the earth surface which aligns the satellite with

the sun,

(ii) less than 24 hours in the time between the two measurements.

The sunset data of SAGE II were chosen as LIDAR measurements were made at night on cloud-free skies. Table (7.3) below shows a comparison of the time of measurement and location of SAGE II with those of the LIDAR. The distance d of the subsatellite from Durban is also given for each date.

LIDAR	SAGE II		Position of	Distance
Date	Date	ΔTime	SAGE II	(km)
8 June 1999	8 June 1999		24.8^0S 38.4^0E	d=930
From 16h29 to	04h09 UT	-12h20		
21h56 UT				
7 July 1999			29.4^0S 25.9^0E	d=496
From 16h24 to	15h27 UT	-1 h		
20h28 UT				
8 July 1999	8 July 1999	-3 h	23.0^0S 27.9^0E	d=825
From 18h50 to	15h33 UT			
23h03 UT				

Table 7.3: Comparison of the temporal and spatial parameters of the LIDAR and SAGE II measurements. The last column values are the distances of the satellite from Durban.

We have plotted the average LIDAR and average SAGE II extinction profiles computed for the above 3 coincident days (fig.(7.6)). Between 15 and 22 km, the averaged values of the extinction coefficient obtained are lower than those calculated from LIDAR. The observed discrepancies are due to:

(i) the measurement technique of SAGE II which scans the atmosphere between the earth and the sun horizontally,

(ii) large variability of aerosols in the the troposphere of Durban as the latter is under the influence of biomass burning (including sugar-cane burning)

and industrial pollution-most of the chemical industries are located south of Durban.

(iii) the assumption that the backscattering phase function due to aerosol (ϖ_a) is constant at and above the reference atmosphere (z_{ref}) which is not always true.

Between 22 and 37 km the agreement between LIDAR and SAGE II is excellent. It seems that the backscatter phase function used for aerosol $\varpi_a = 0.02$ sr^{-1} in the determination of the LIDAR extinction coefficient is consistent with SAGE II. This comparison suggests that the values obtained for the two experiments are representative of the extinction profile for the latitude 30^0S. It is also a good indication of the quality of the Durban LIDAR data.

We now consider a coincident date for the LIDAR/SAGE II measurements. Fig.(7.7) shows a comparison of LIDAR/SAGE II extinction coefficients for July 8th 1999. The latter date is chosen as the overlap between the two extinction profiles is excellent compare to the other two dates (June 8th and July 7th 1999). Below 20 km the LIDAR extinction coefficients are higher than those of SAGE II. This could be explained by the measurement technique of the LIDAR compare to SAGE II. The LIDAR being localised, samples the atmosphere vertically above Durban whereas SAGE II is scanning the atmosphere horizontally through a few hundred km corresponding to an average horizontal value for the extinction coefficient.

Both SAGE II and LIDAR extinction profiles indicate a peak around 20 km. This could be due to a stratified layer of background aerosol usually situated in the stratosphere around 20 km (Junge, 1961). Between 20 and

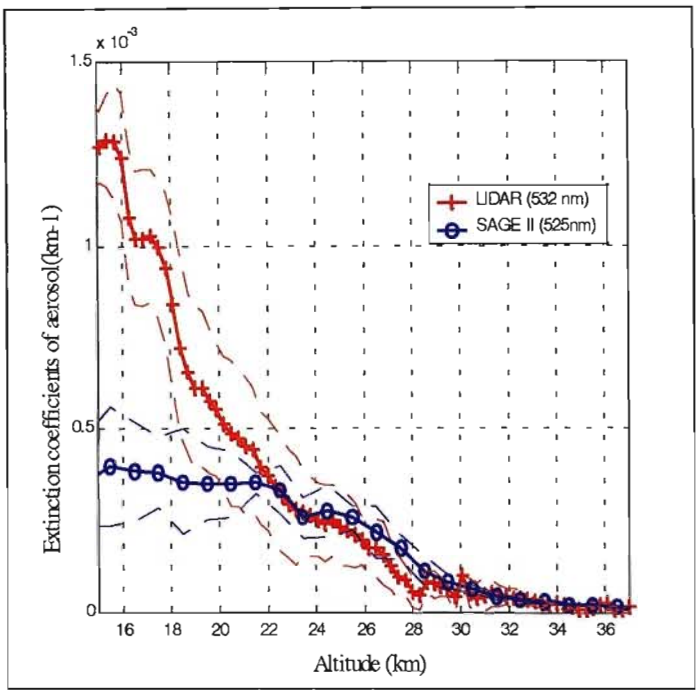

Figure 7.6: Average aerosol extinction profile (solid lines) obtained from LIDAR and SAGE II. The dashed lines indicate the corresponding standard deviations.

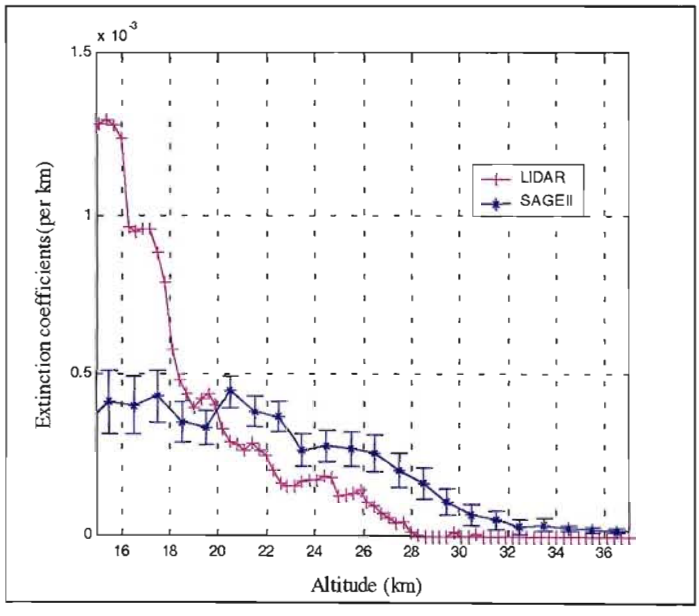

Figure 7.7: Aerosol extinction profiles obtained from LIDAR and SAGE II for July 8 1999. The distance of the subsatellite from Durban is 825 km.

26 km, several other peaks are detected on the LIDAR profile which are not present on the SAGE II profile. This is because the LIDAR has a better spatial resolution of 150 m compared to SAGE II which has a resolution of 1 km. Three such peaks can be clearly seen in fig.(7.7) at 21.4, 24.4 and 25.9 km respectively. Judging from the values of their extinction coefficients (2.8×10^{-4} km^{-1}, 1.8×10^{-4} km^{-1} and 1.4×10^{-4} km^{-1} respectively), they represent minor aerosol layers. The LIDAR Mie ratio profile is another way of showing the presence of aerosol in the atmosphere. The LIDAR Mie ratio is obtained from equation (7.6) by solving equation (6.1) for the backscattering coefficient due to aerosol ($\beta_a(z)$) using the Klett inversion method. From the backscatter phase function of aerosol ϖ_a= 0.02 sr^{-1} chosen, the value of $\beta_a(z)$ is estimated. Equation (7.6) can also be written as

$$R(z) = 1 + \frac{\beta_a(z)}{\beta_m(z)} \tag{7.9}$$

Equation (7.9) indicates that if $R(z)$ exceeds 1, aerosols are present in the atmosphere.

Fig.(7.8) shows the Mie ratio profile for July 8th 1999. The peaks detected in the fig.(7.7) are also found in the Mie ratio profile.

Equation (7.6) indicates that if $R(z)$ exceeds 1, aerosols are present in the atmosphere.

Fig.(7.8) shows a general decrease in Mie-scattering ratio values with height. Above 34 km, the Mie scattering ratio approaches 1.00. In this altitude range the atmosphere can be considered to be purely molecular (no aerosol). The large Mie-ratio values for the altitude range $15 \leq z \leq 26$ km indicate that the upper troposphere above Durban is loaded with aerosol.

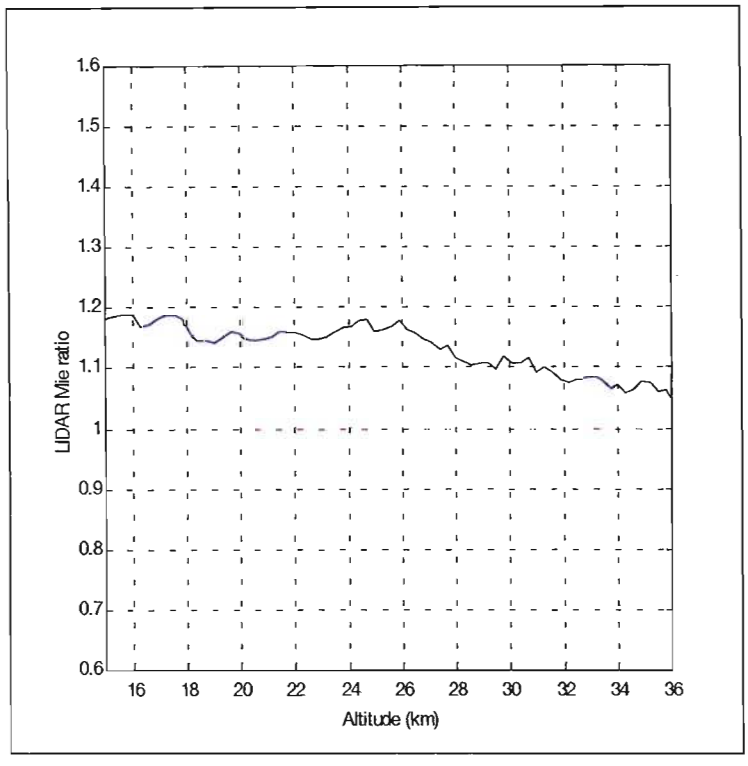

Figure 7.8: Profile of LIDAR Mie-scattering ratio for July 8 1999.

7.7 Validation of the LIDAR temperature profiles

Average monthly LIDAR temperature profiles are computed between 20 and 60 km. The LIDAR data consists of a total of 137 nights from April 1999 to December 2000, corresponding to a total of 514 hours of observation. The validation of the LIDAR temperature profiles is done in three steps:

(1) a comparison of the average monthly LIDAR temperature profiles with the average monthly South African Weather Service (SAWS) radiosonde temperature measurement for the lower stratosphere, 20 □ z □ 27 km,

(2) a comparison of the average monthly LIDAR temperatures with the

average monthly European Centre for Medium range Weather Forecast (ECMWF) temperatures for the altitude range $20 \leq z \leq 42$ km and

(3) a comparison of the average monthly LIDAR temperature profiles with the climatological model CIRA-1986 temperatures for the stratosphere and mesosphere, $20 \leq z \leq 60$ km.

The comparisons with the average monthly SAWS radiosonde temperatures are done for the year 1999. Due to only one night of LIDAR data for the months of October and December (rainy weather conditions in Durban), the comparisons for these two months are done for coincident dates with the SAWS data viz. October 30 1999 and December 14 1999.

Before proceeding with the validation, we describe briefly in the next section the SAWS radiosonde data, CIRA-1986 climatological model and the ECMWF temperature.

7.7.1 SAWS radiosonde data

The SAWS launches twice a day (01:00 a.m. and 12:30 p.m. South African local time) balloon radiosondes at Durban International Airport. The data consists of the station number (68588 for Durban), the year, month and day, the time, the pressure (in hPa), the temperature (in millidegrees Celsius), the relative humidity (expressed as a percentage), dew point temperature (in millidegrees Celsius), altitude (in metres), wind direction (in degrees) and wind speed (in m/s). For our purpose, we have worked with the temperature (converted in K) and the altitude (converted to km) from the early morning (1:00 a.m.) data as this corresponds closely to the time of the running of the LIDAR.

7.7.2 The CIRA-1986 climatological model

The COSPAR International Reference Atmosphere (CIRA)-1986 climatological model is a collection of experimental measurements and results from theoretical models. It is based mainly on nadir infrared soundings from the Selective Chopper Radiometer (SCR) experiment on board NIMBUS-6 from 1973 to 1974 and from the Pressure Modulated Radiometer (PMR) experiment on NIMBUS-7 from 1975 to 1978. These two experiments yield temperature profiles between 20 and 80 km (Barnett and Corney 1985). Together with tropospheric measurements carried out between 1958 and 1973 (Oort 1983), they give climatological monthly averages between 0 and 80 km with a global coverage from 80 ^{0}S to 58 ^{0}N. For altitudes in the thermosphere between 80 and 120 km, results from the empirical model MSIS-83 have been used to complete the CIRA-1986 model. The data base has been compiled (Fleming *et al.* 1985) to yield monthly average climatological temperatures between 0 and 120 km with a global coverage.

7.7.3 The ECMWF data

The European Centre for Medium range Weather Forecast (ECMWF) data is based on a numerical model for predicting the weather for the medium range (2 daysto 2 weeks). We have used the stratospheric temperature data for Durban at different pressure levels from 1 mb (48.4 km) to 1000 mb (0.10 km). The temperature data is obtained at four different times: 00h00, 06h00, 12h00 and 18h00. For our purpose, ECMWF temperatures corresponding to the time 00h00 have been extracted as LIDAR data acquisition is carried out

at night.

7.8 Comparison of LIDAR temperature profile with SAWS radiosonde temperature

The comparison between the monthly average LIDAR and monthly average SAWS radiosonde measurements are shown in figs.(7.9)-(7.13) from April 1999 to December 1999. For the months of October and December 1999, we have compared the LIDAR temperature profiles for 30 October 1999 (fig.(7.12) (a)) and 14 December 1999 (fig.(7.13)). No other LIDAR data are available for these two months as rainy weather conditions were prevailing.

As shown in the figures, in the overlap zone the two measurements are in quite good agreement. The LIDAR and radiosonde average profiles indicate that the temperature values obtained with LIDAR and sounding balloon of the SAWS are relatively similar. They did not exceed 5 K ($\Delta M = |M_{LIDAR}$-$M_{SAWS}| \leq 5$ K, where M denotes temperature) which can be considered as reasonable, taking into account the possible influence of stratospheric aerosols, and the great variability of the temperature in the winter stratosphere. The measurement comparisons are limited to the lower stratotosphere ($20 \leq z \leq$ 28 km) as the balloon usually bursts around 29-30 km. There is a decrease in the standard deviation of the LIDAR temperature profile above 50 km for July 1999 (fig.(7.10) (b)). This is due to the fact the maximum heights attained by the LIDAR the measurements done for the month of July 1999 (15 nights) range between 50 and 55 km. Hence the standard deviation of the

average LIDAR temperature profile for July will be squashed for height below 55 km. Some caution has to be observed when interpreting the standard deviation above 50 km for the average July LIDAR temperature profile.

In conclusion, we can say that for the lower stratosphere ($20 \leq z \leq 28$ km), the agreement between the average monthly LIDAR temperature and the average monthly SAWS temperature profiles are quite good. If the lower stratosphere is loaded with aerosol, the LIDAR temperature will be overestimated and will be slightly higher than the SAWS temperature.

7.9 Comparison of average monthly LIDAR temperature profiles with average monthly ECMWF temperature profiles

The average monthly LIDAR temperature profile is compared with the average monthly ECMWF temperature profile over the altitude range 20 and 48 km for the years 1999 and 2000. The results are shown in figs.(7.14)-(7.18).

As can be seen from the figures, the agreement between LIDAR and ECMWF is good below 30 km. Above 30 km the LIDAR temperature profiles are warmer for the months of April to July. For the month of July, we have separated the results into July 1999 and July 2000 average LIDAR profiles. The LIDAR temperature profile is consistently higher in July 2000 than any other LIDAR profiles of the year 1999 and 2000. Indeed in July 2000 (see fig.(7.16)) at a height of 43.5 km, the LIDAR temperature is 260 K compare to ECMWF temperature which is 249 K at the same height. This clearly shows a minor warming of the stratosphere. The stratopause height and the

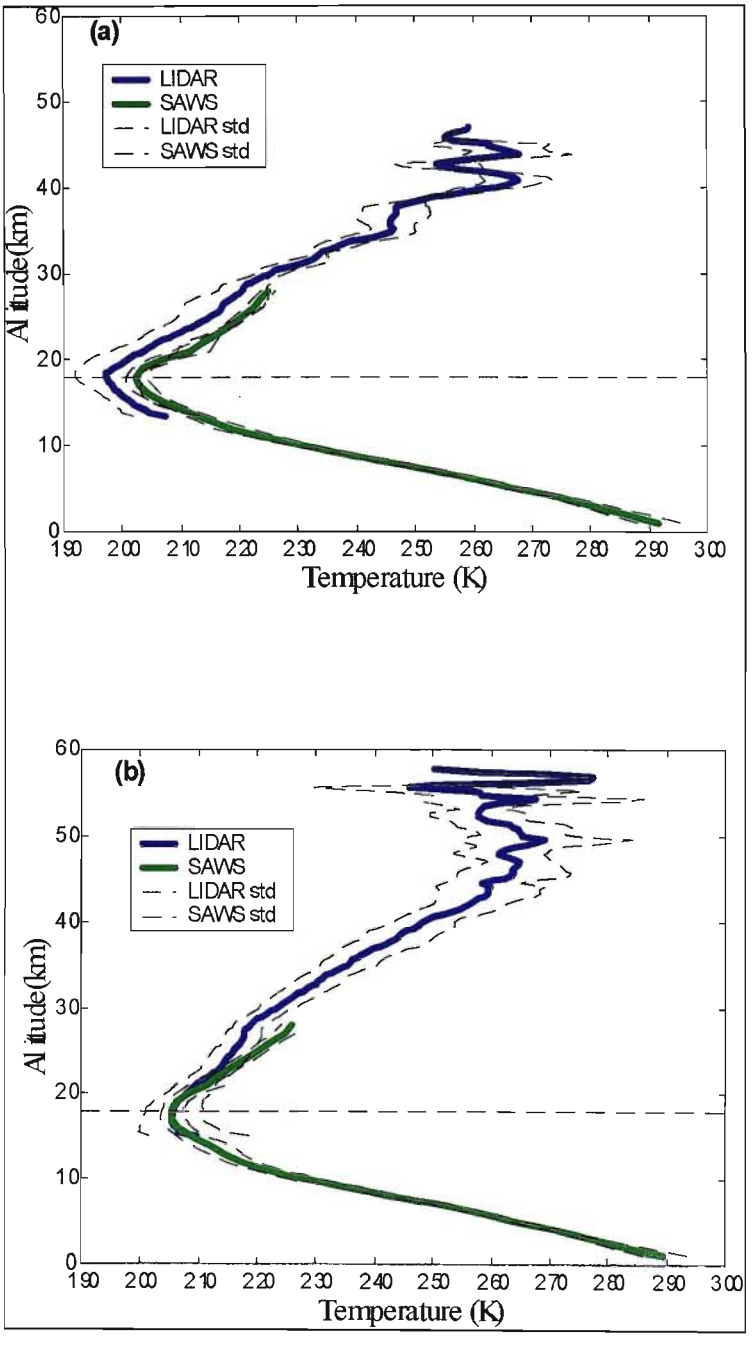

Figure 7.9: Comparison of average monthly LIDAR temperature profile with average monthly SAWS radiosonde temperature profile for the months of (a) April (b) May 1999. The LIDAR profile was averaged over 3 nights in April and 11 nights in May. The horizontal dashed line is the tropopause height.

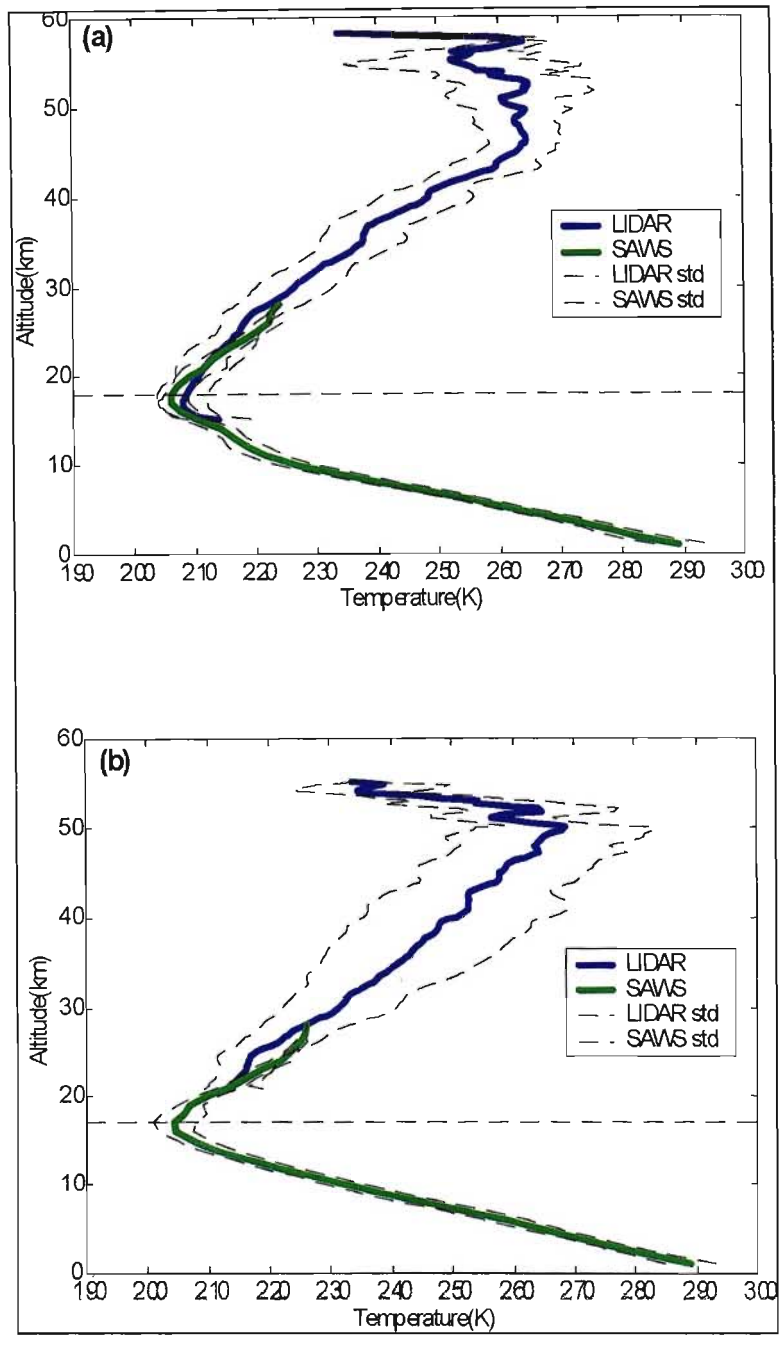

Figure 7.10: Comparison of average monthly LIDAR temperature profile with average monthly SAWS radiosonde temperature profile for the months of (a) June (b) July 1999. The LIDAR profile was averaged over 15 nights in June and 15 nights in July. The horizontal dashed line is the tropopause height.

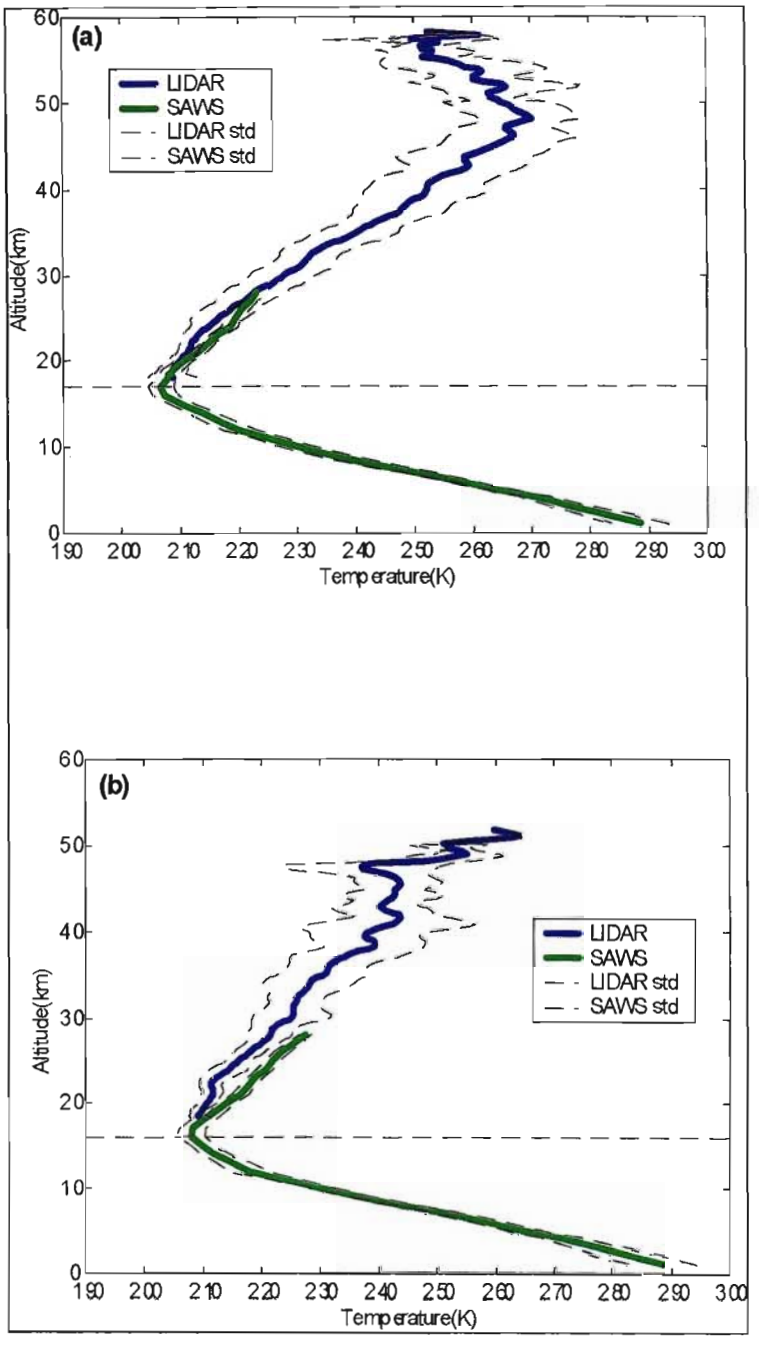

Figure 7.11: Comparison of average monthly LIDAR temperature profile with average monthly SAWS radiosonde temperature profile for the months of (a) August (b) September 1999. The LIDAR profile was averaged over 11 nights in August and 7 nights in September. The horizontal dashed line is the tropopause height.

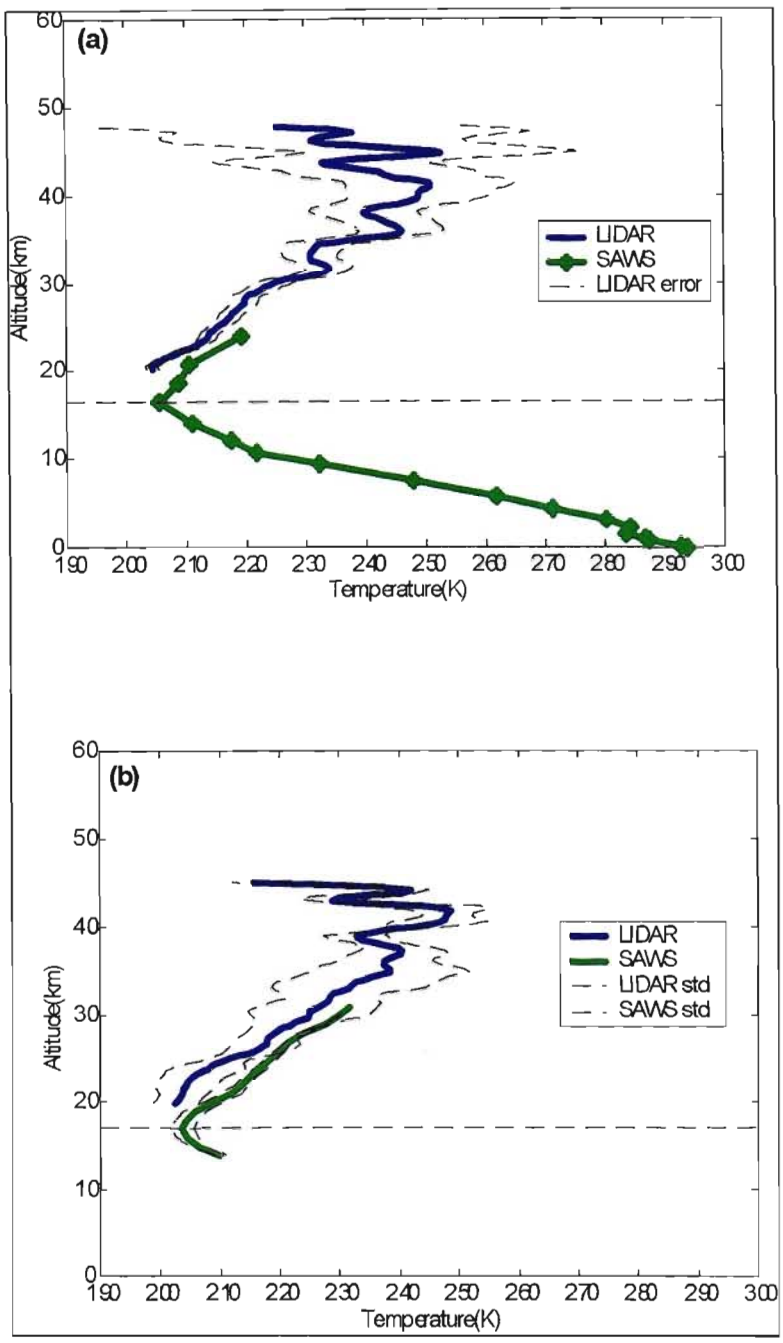

Figure 7.12: (a) Comparison of LIDAR temperature profile with SAWS radiosonde temperature profile for 30 October 1999. Due to rainy weather conditions in October, there is only one night of LIDAR data. (b) Comparison of average monthly LIDAR temperature profile with average monthly SAWS temperature profile for the month of Nov 1999. The LIDAR profile was averaged over 3 nights in Nov. The horizontal dashed line is the tropopause height.

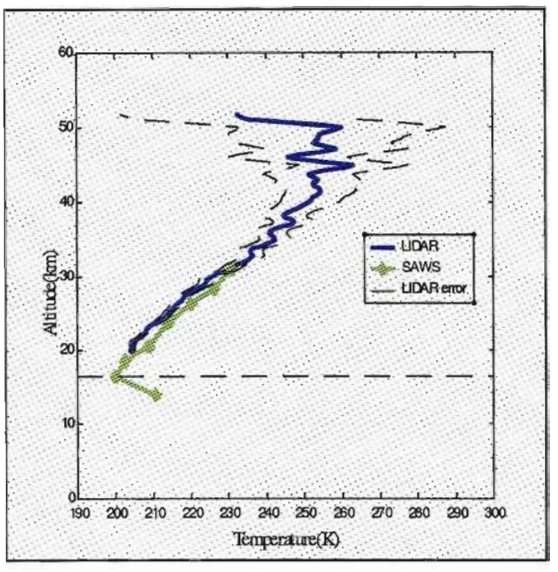

Figure 7.13: Comparison of LIDAR temperature profile with SAWS radiosonde temperature profile for 14 December 1999. Due to rainy weather conditions in Durban, there is only one night of LIDAR data in December. The horizontal dashed line is the tropopause height.

temperature vary during this event.

For the summer period (September to December) the LIDAR temperature profiles are slightly colder than the ECMWF temperature profiles especially above 35 km. It should be noted due to rainy weather conditions in October and December 2000, there is no LIDAR data for these two months. Results in 1999 have been shown (figs.(7.17) and (7.18)). The LIDAR temperature profile for the month of July is averaged separately over the year 1999 and 2000 and is shown in figs.(7.15) (b) and (7.16) (a) respectively. The reason for doing this is that the wave-like structures seen on the average July 2000 LIDAR profile are more pronounced compare to those on the average LIDAR June 1999. It has been felt necessary to separate the two profiles in order to preserve the information they carry.

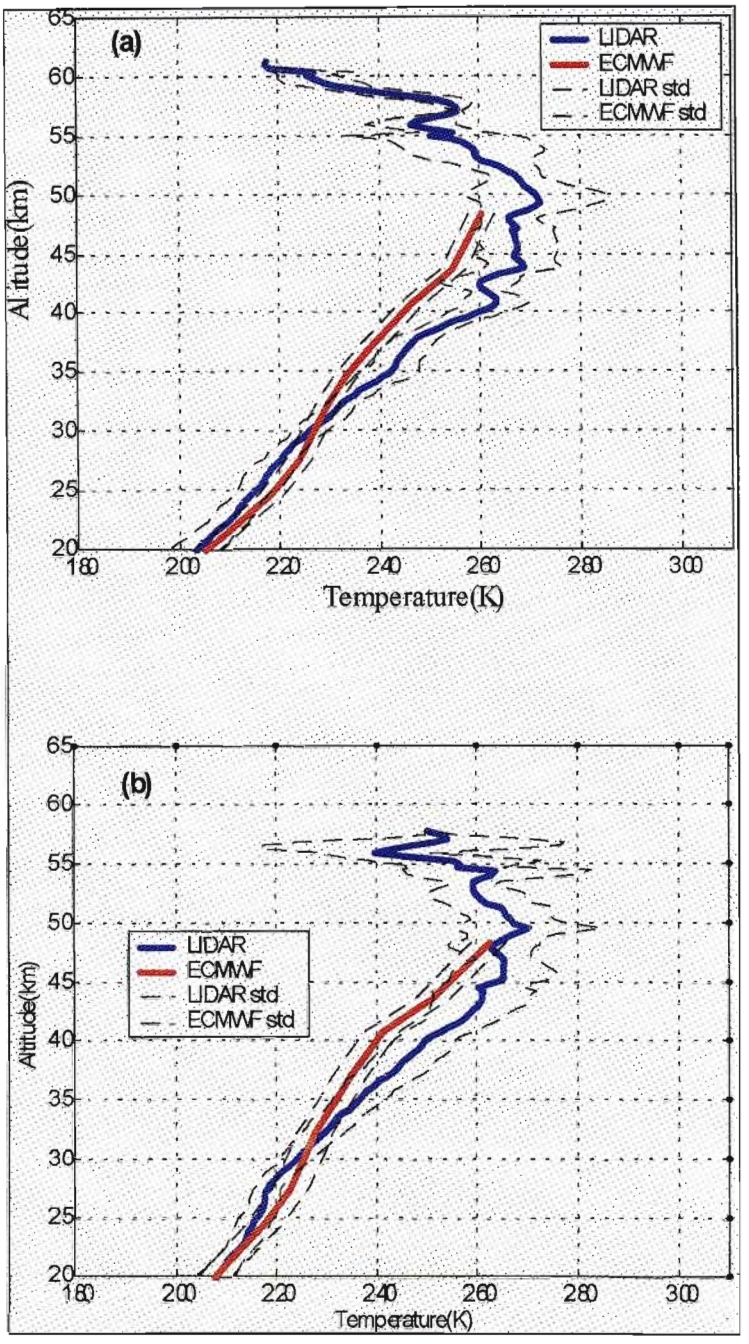

Figure 7.14: Comparison of the average monthly LIDAR temperature profile with average monthly ECMWF temperature profile for the months of (a) April 1999/2000 (b) May 1999/2000. The LIDAR profile was averaged over 7 nights in April and 12 nights in May.

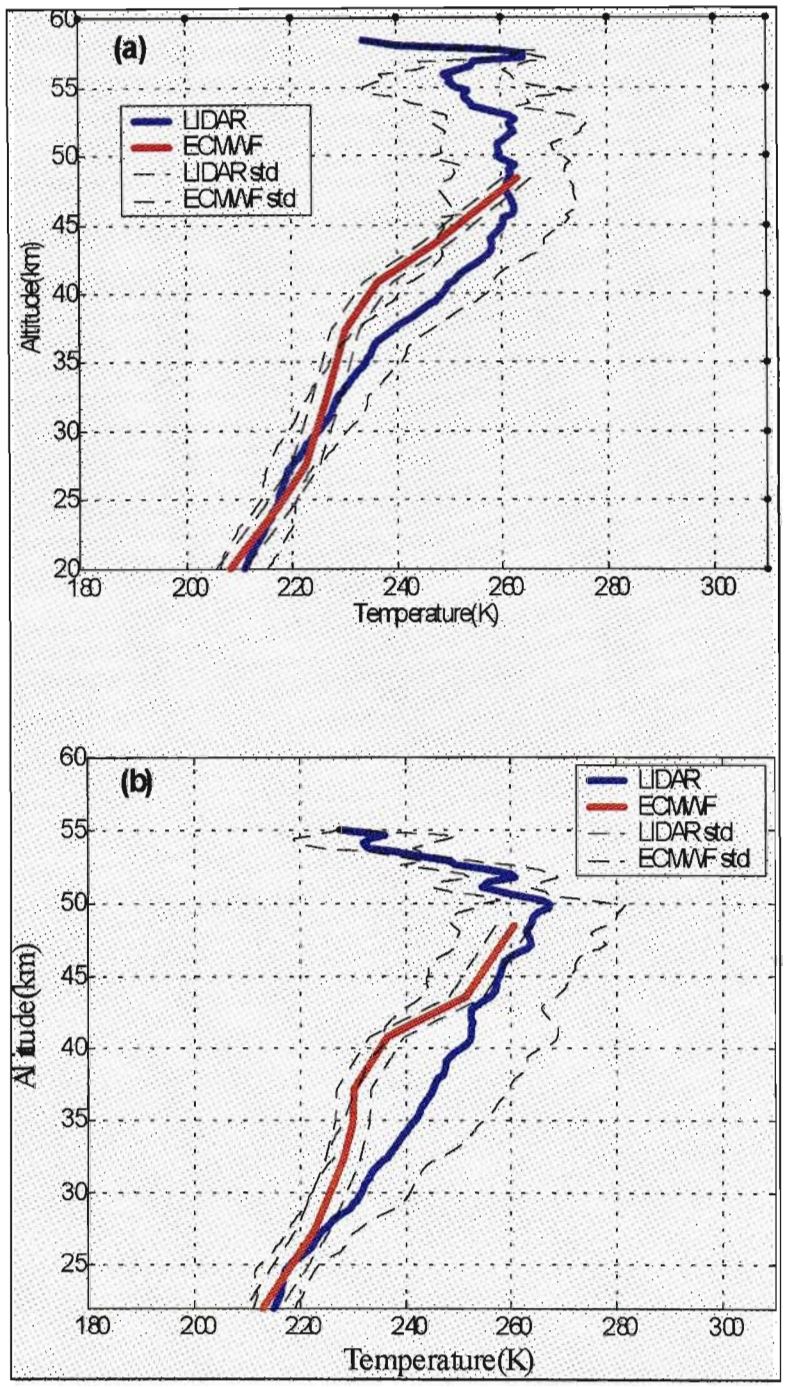

Figure 7.15: Comparison of the average monthly LIDAR temperature profile with average monthly ECMWF temperature profile for the months of (a) June 1999/2000 (b) July 1999. The LIDAR profile was averaged over 30 nights in June and 12 nights in July.

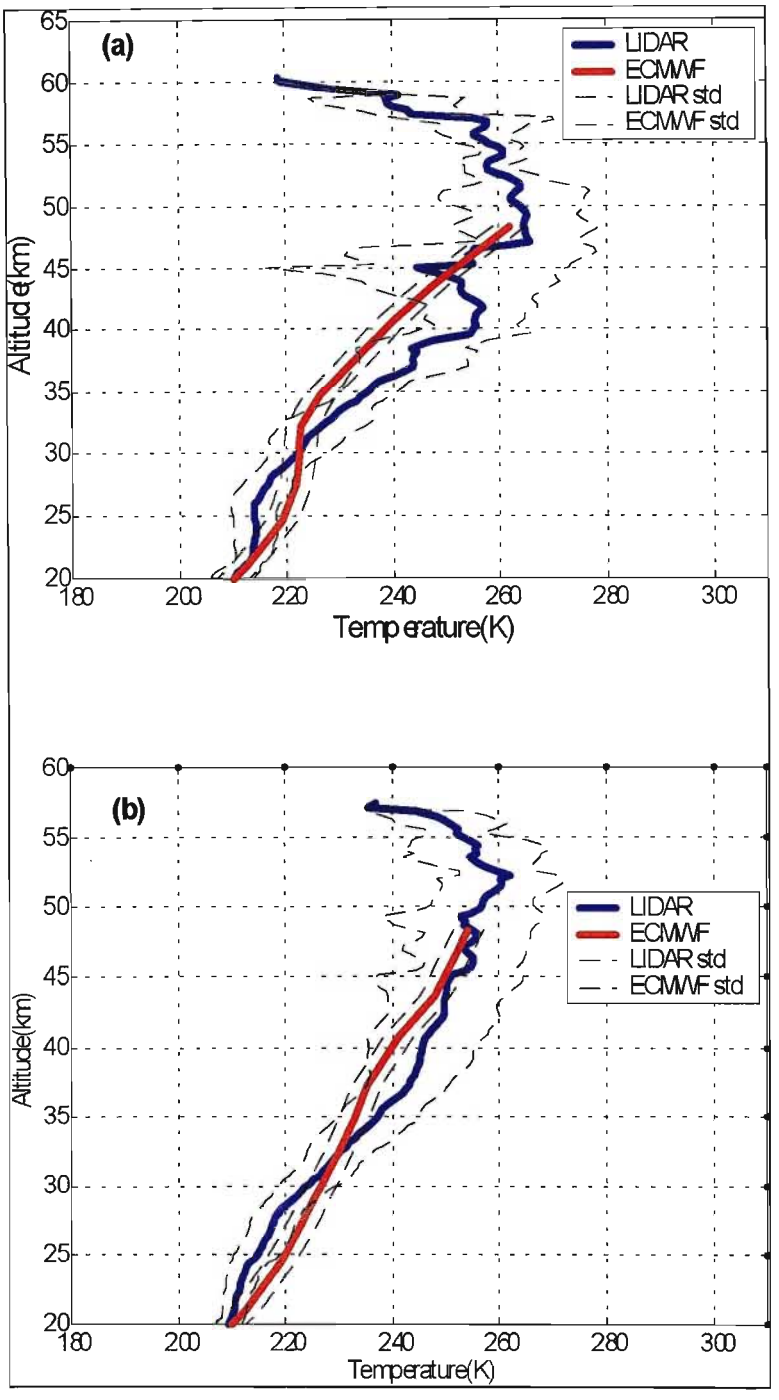

Figure 7.16: LIDAR temperature profile with average monthly ECMWF temperature profile for the months of (a) July 2000 (b) August 1999/2000. The LIDAR profile in (a) was averaged over 12 nights in July and in (b) the LIDAR profile was averaged over 23 nights in August.

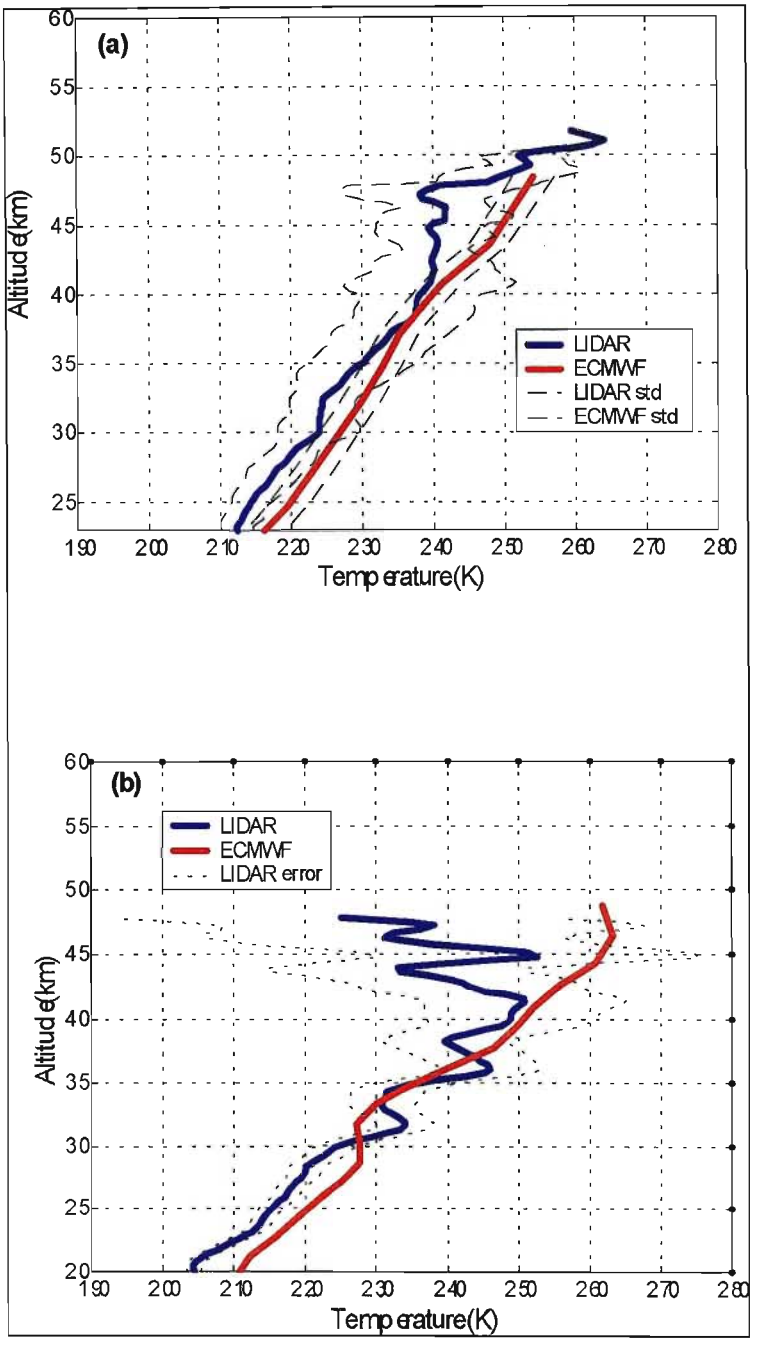

Figure 7.24: (a) Comparison of the average monthly LIDAR temperature profile with average monthly ECMWF temperature profile for the month of Sept 1999/2000. The LIDAR profile was averaged over 11 nights in Sept (b) Comparison of the LIDAR temperature profile with ECMWF temperature profile for 30 Oct 1999. Due to rainy weather conditions in Oct, there is only 1 LIDAR data.

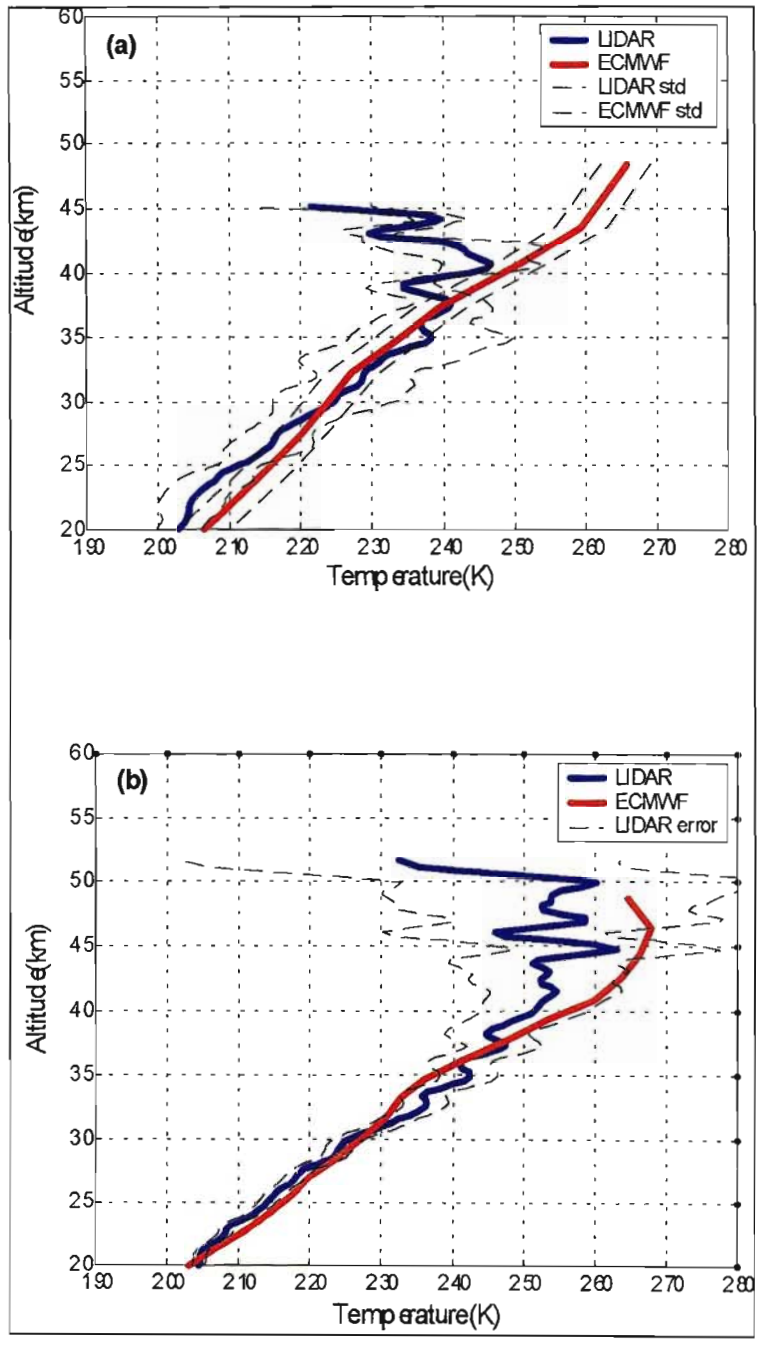

Figure 7.8: (a) Comparison of the average monthly LIDAR temperature profile with average monthly ECMWF temperature profile for the month of Nov. The LIDAR profile was averaged over 4 nights in Nov 1999/2000 (b) Comparison of the LIDAR temperature profile with ECMWF temperature profile for 14 Dec 1999. Due to rainy weather conditions in Dec, there is only 1 LIDAR data.

7.10 Comparison of average monthly LIDAR temperature profiles with CIRA-1986

Average monthly LIDAR temperature profiles measured over two years (1999 and 2000) are compared with the CIRA-1986 climatological model. The results are shown in figs.(7.19)-(7.23) from April to December in the altitude range 20 to 60 km.

It can be seen from all the profiles that between 20 and 30 km, LIDAR temperature profiles are colder than the model. The winter months (April to August) are characterised by minor stratospheric warming events, a good example of which is observed on the April and May profile where temperature as high as 272 K was observed at 50 km. An interesting feature which is observed on the July profile is the lowering of the stratopause height to $\approx$ 44 km compare to $\approx$ 49 km on the model. The stratopause height returns to the model value on the August profile. The June LIDAR temperature profile shows that the temperature is approximately constant between 47 and 49 km. Temperatures observed in summer (September, October, November and December) also show some variations with height and are lower than the model. For example, the LIDAR temperature profile for the month of November shows a temperature of 262 K at 45 km compare to 272 K for the model. Please note that the average LIDAR temperature profiles for July 1999 and 2000 have been separated. The reason for doing this is that the the wave-like structures seen above 40 km on the average profile of July 2000 are more pronounced than in July 1999 average profile. By separating the two profiles valuable information on the profile are preserved.

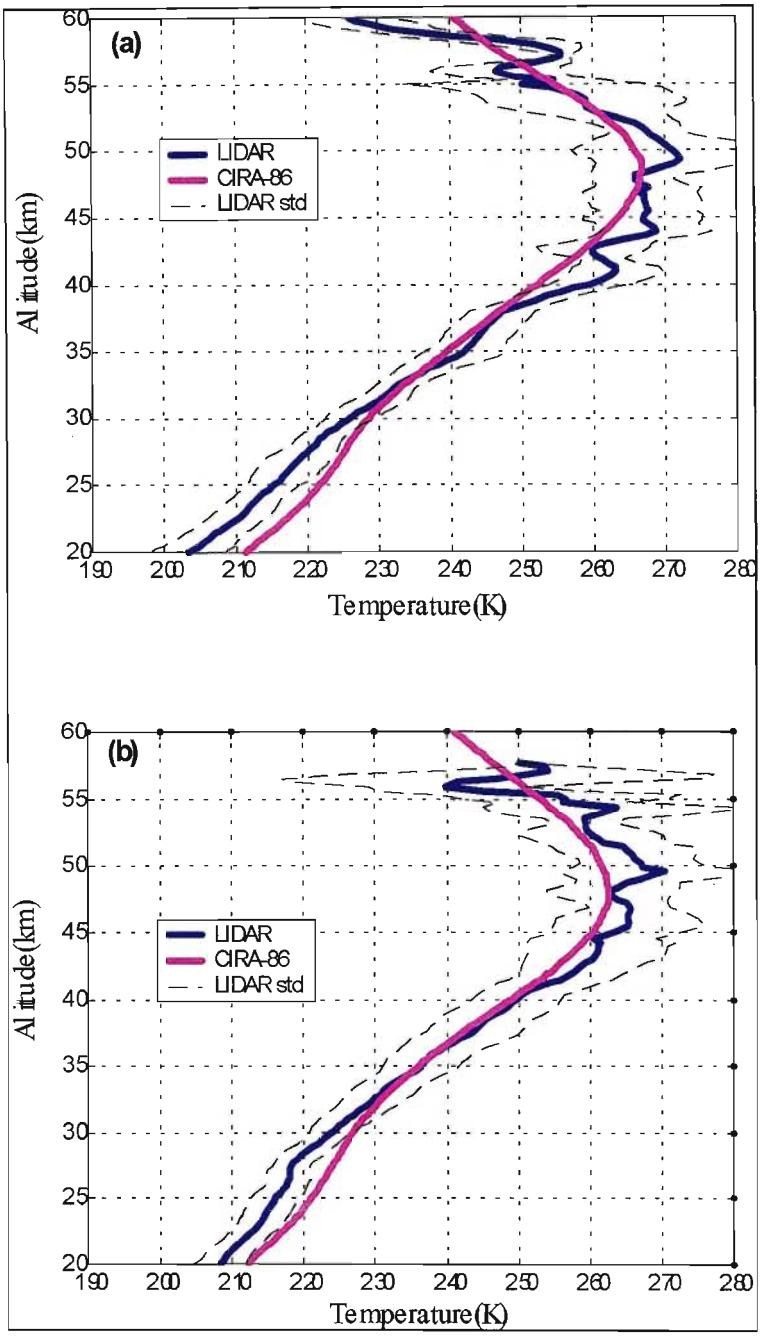

Figure 7.12: Comparison of the average monthly LIDAR temperature profile with average monthly CIRA-86 temperature profile for the months of (a) April 1999/2000 (b) May 1999/2000. The LIDAR profile was averaged over 7 nights in April and 12 nights in May.

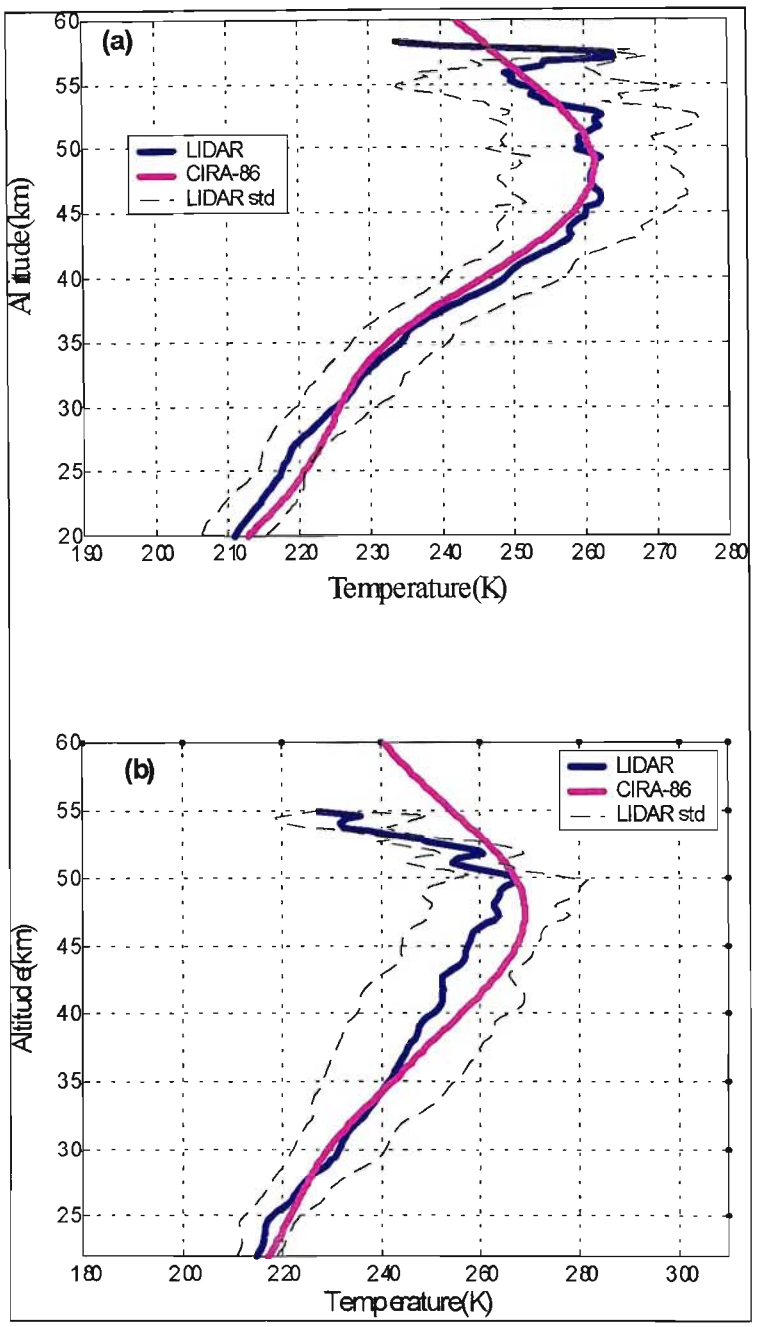

Figure 7.26: Comparison of the average monthly LIDAR temperature profile with CIRA-86 temperature profile for the months of (a) June 1999/2000 (b) July 1999. The LIDAR profile was averaged over 30 nights in June and 12 nights in July.

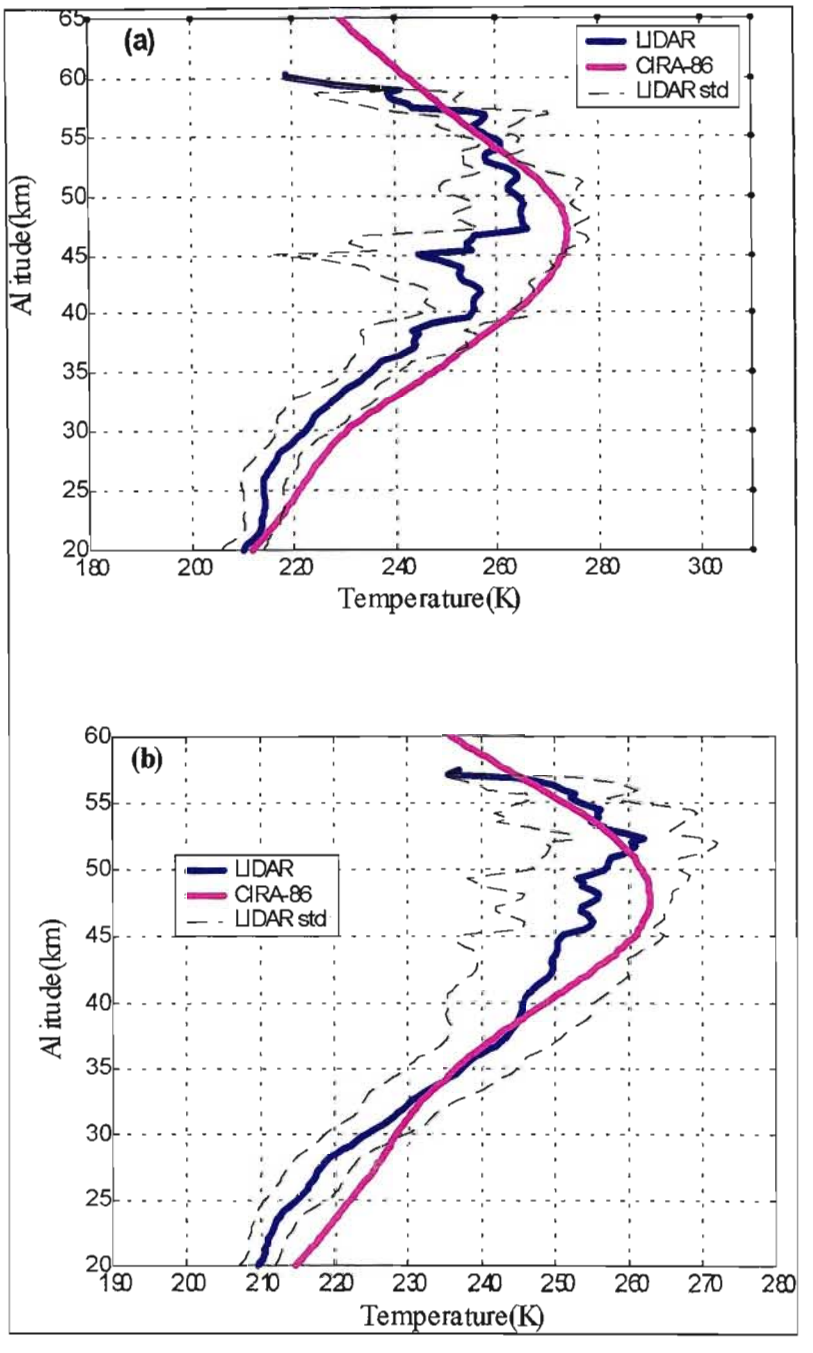

Figure 7.24: Comparison of the average monthly LIDAR temperature profile with CIRA-1986 temperature profile for the months of (a) July 2000 (b) August 1999/2000. The LIDAR profile was averaged over 12 nights in July and 23 nights in August.

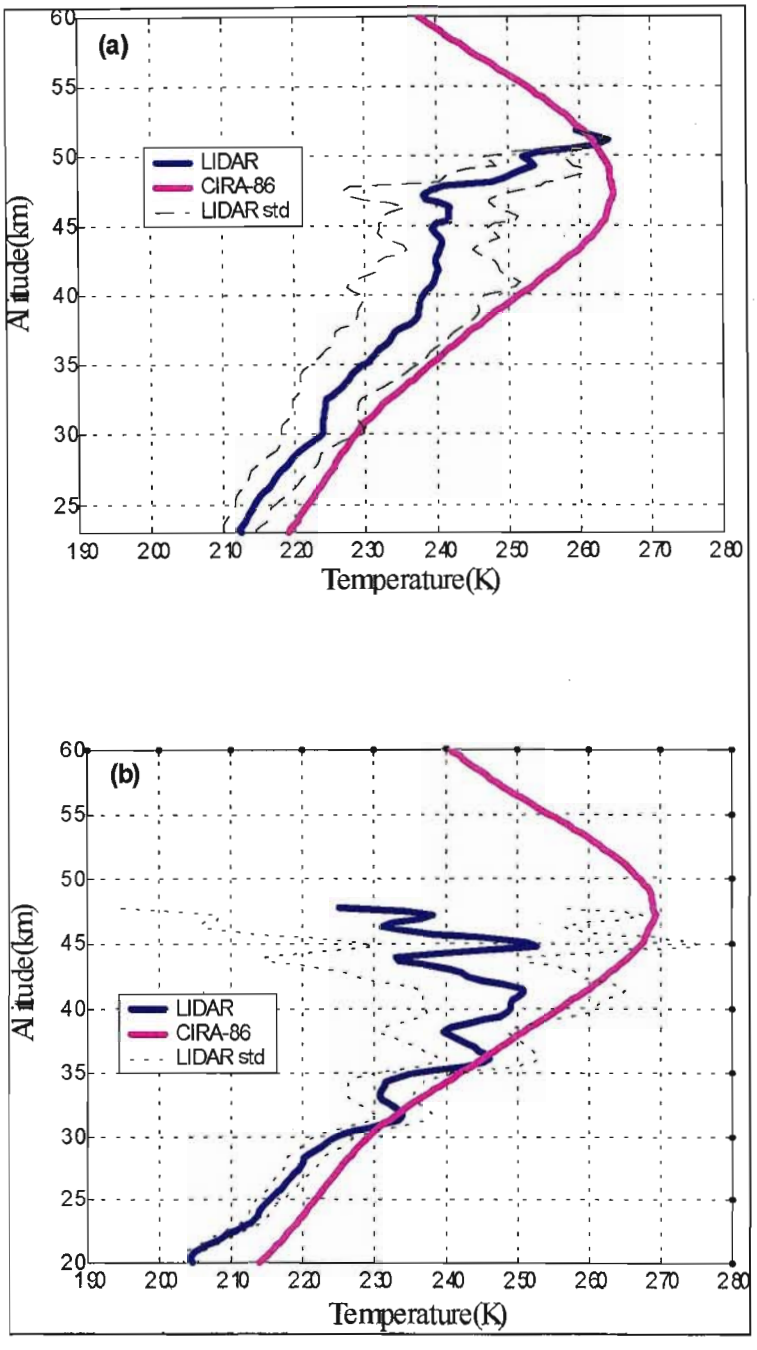

Figure 7.23: (a) Comparison of the average monthly LIDAR temperature profile with CIRA-1986 temperature profile for the months of Sept 1999/2000. The LIDAR profile was averaged over 11 nights in Sept (b) Comparison of the LIDAR temperature profile with the CIRA-86 temperature profile for 30 Oct 1999. Due to cloudy and rainy weather conditions, there is no LIDAR data in Oct 2000.

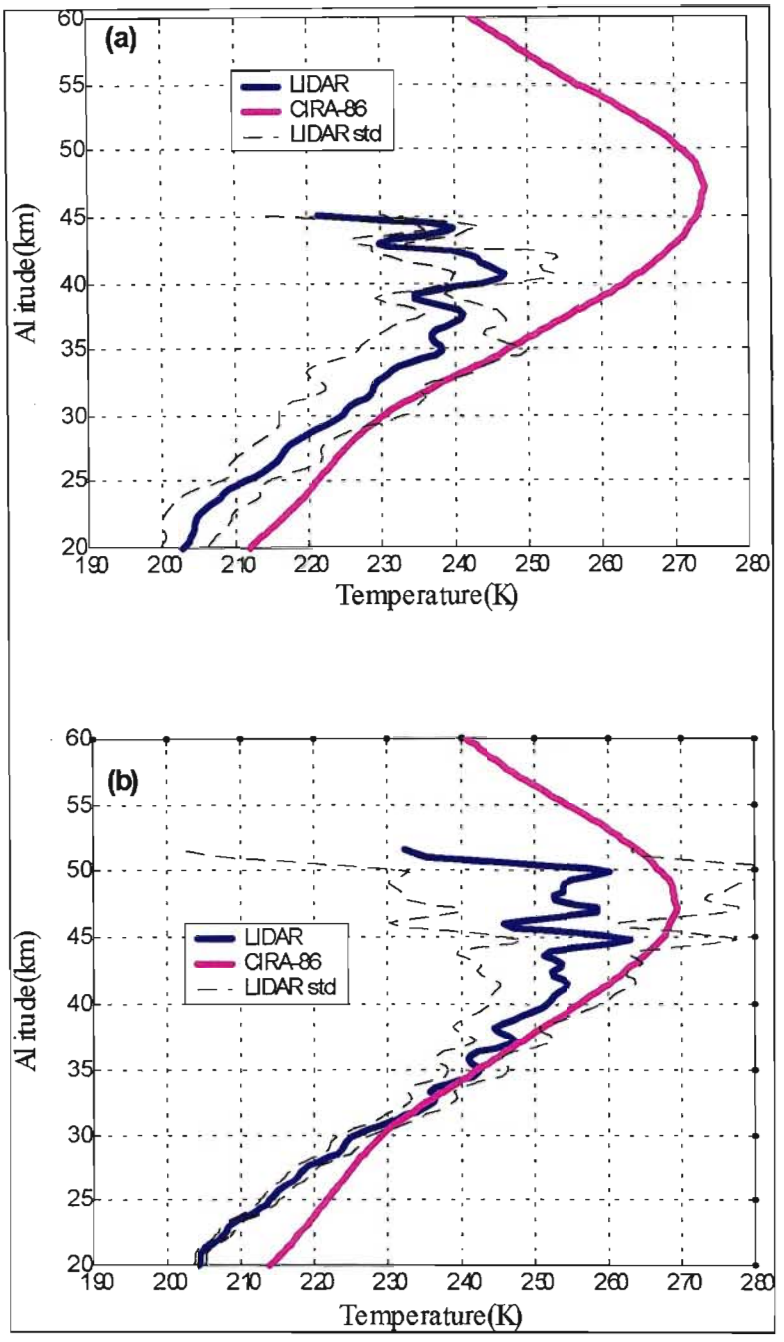

Figure 7.23: (a) Comparison of monthly LIDAR temperature profile with CIRA-86 model for the month of Nov. The LIDAR profile was averaged over 4 nights in Nov 1999/2000 (b) Comparison of the LIDAR temperature profile with the CIRA-86 temperature profile for 14 Dec 1999. Due to cloudy and rainy weather conditions, there is no LIDAR data in Dec 2000.

7.11 Discussion

7.11.1 LIDAR/SAWS comparison

The agreement between LIDAR and radiosonde temperatures of SAWS is usually good when radiosonde data reach altitudes above 20 km, and the two profiles appear easily joinable even when the balloon data stop at about 28 km. The ageement is particularly good for the months May, June, July, August and September 1999. The average LIDAR temperature profiles during these months do not exceed 5 K ($\Delta M = |M_{LIDAR}\text{-}M_{SAWS}| \leq 5$ K, where M denotes temperature) which can be considered as reasonable, taking into account the possible influence of stratospheric aerosols, and the great variability of the temperature in the winter stratosphere. It should be noted that the LIDAR vertical resolution at 150 m is better than the radiosonde vertical resolution. Because of the lack of radiosonde data from the ground, the SAWS profiles for the months of November and December start from 14 km. On each figure, the tropopause was identified around 17 km.

7.11.2 LIDAR/ECMWF comparison

First, it should be noted that the vertical resolution of the LIDAR is 300 m better than ECMWF which is of the order of km. The observed temperature differences between LIDAR/ECMWF may be the result of minor stratospheric warmings occuring during the winter period (from April to August). The winter warmings are amongst the large disturbances, which perturb the thermal structure of the stratosphere. These disturbances are associated with the vertical propagation of planetary waves, thus coupling

the troposphere and the stratosphere. The propagation of planetary waves is governed by the westward circulation associated with the winter polar vortex (Schoeberl 1978; Labitzke 1981). The planetary wave activity occuring in winter can be explained by the reversal of the zonal wind in the stratosphere as shown by the contour plot of the ECMWF zonal wind data (figs.(7.24) - (7.25)).

The 1999/2000 winter months (April to August) show a minor warming between 40 and 55 km in the upper stratosphere. Part of the observed variations may be attributed to relatively fast transient phenomena such as gravity waves. Some features of the LIDAR temperature profiles may be related to the dynamical evolution of the stratosphere. Naujokat *et al.* (1995) reported a detailed description of the evolution of the dynamical circulation in the middle atmosphere during winter 1994-1995 for the northern hemisphere where several minor warming events took place. Between 20 and 45 km the LIDAR temperature was higher for the month of July, reaching 260 K at 43.5 km compared to ECMWF temperature 249 K at the same height. A minor stratospheric warming took place between 35 and 45 km for the months of April to August.

For the summer period (September to December) the LIDAR temperature profiles are slightly colder than the ECMWF temperature profiles especially above 35 km. In summer the planetary wave activity in the stratosphere is less compared to winter and therefore the LIDAR temperature profiles are less perturbed.

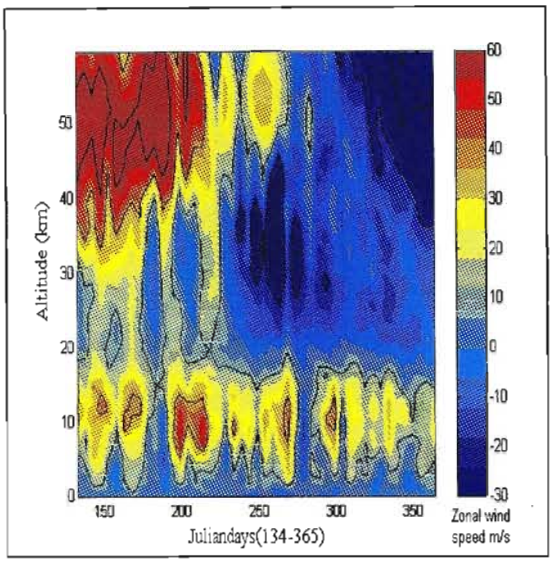

Figure 7.24: Time altitude ECMWF zonal wind cross-section 1999. The data was available from beginning of winter, May 14 to Dec 31 1999.

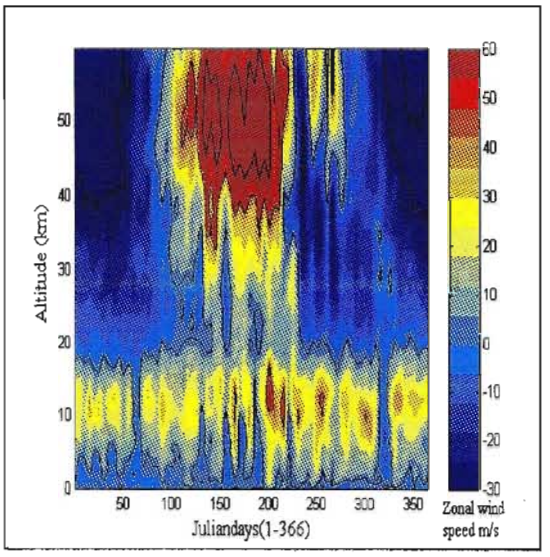

Figure 7.25: Time altitude ECMWF zonal wind cross-section for the year 2000.

7.11.3 LIDAR/CIRA-86 comparison

In the stratosphere between 20 and 35 km, LIDAR temperatures are lower than the CIRA-86 model with $|M_{CIRA}-M_{LIDAR}| \leq 6$ K. This may be the result of a possible minimum in the solar flux during the observation period. Another reason could be that the CIRA-86 model is quite old as it is based on data collected above 20 km on board NIMBUS 6 and 7 from 1973 to 1978 (see section 7.7.2). There is therefore a difference of more than 20 years between the LIDAR measurements and the data used for the CIRA-86 model. Furthermore, from 1973 to 2000 the composition of the lower stratosphere may have changed due to increasing CO_2 and decreasing O_3 leading to a cooling of the lower stratosphere.

Between 35 and 60 km during the winter months (April to August), LIDAR temperatures are warmer than the model with $|M_{LIDAR}-M_{CIRA}| \leq 7$ K. This could be explained by a minor stratospheric warming which took place during the winter period and disappeared during summer. Very interesting features have been observed in the LIDAR profile of July 2000 (see fig.(7.21) (a)). First, during the warming event a lowering of the stratopause is observed in the July 2000 profile. The stratopause height is located at 42 km compared to 49 km on the model. Furthermore, the LIDAR temperature remains constant at 265 K between 48 and 49 km - an unusual feature not found by the model. The large standard deviation in the LIDAR temperatures above 45 km on all the LIDAR profiles is due to the weak signal-to-noise ratio in the LIDAR return. The decrease of the standard deviation on some of the LIDAR profiles especially above 50 km is attributed to the fact that

the maximum altitude for which temperature could be measured is not the same for all nights. The temperature points at the top of the profile for the nights will tend to be squashed during the averaging process and this will lead to a "compressed" standard deviation. However, this is only an artefact and should not be taken as the actual error at the top of the average LIDAR temperature profile.

The winter temperature profiles show increased variabilty in the stratosphere compared with the summer profiles. These can be attributed to the vertical propagation of planetary waves which occur mostly in winter (Hauchecorne and Chanin 1982; Jenkins *et al.* 1987; Marenco *et al.* 1997). The precision of measurement in the stratosphere was sufficient to permit the detection of these waves. The existence of such perturbations in the stratosphere observed by the Durban LIDAR despite its low latitude (29.8^0S), can be explained by the position of the stratospheric polar vortex which is generally centred close to Durban in July (Labitzke 1980). Indeed, during the winter season, the zonal wind in the stratosphere is mainly from the west, the planetary waves of the troposphere penetrate the stratosphere, and even into the mesosphere (Labitzke 1981). As shown in figs.(7.24) and (7.25), large reversal of zonal winds with values from 50 to 60 ms^{-1} occurs in the stratosphere. These changes in the zonal wind direction and speed also lead to a warming of the stratosphere (Naujokat *et al.* 1995). These results show that the stratosphere above Durban is continously perturbed during winter due to two major phenomena:

(i) minor warming of the stratosphere which is influenced by the stratospheric polar vortex centred close to the location of Durban in July. The

LIDAR temperature profiles resulted from these warmings have vertical wavelengths of 5 to 7 km in the upper stratosphere (40-50 km) (see fig.(7.21) (a) on page 171).

(ii) propagation of planetary waves generated in the troposphere and entering the stratosphere and mesosphere. The propagation of these waves is facilitated by the westward circulation associated with the winter polar vortex.

In the Southern Hemisphere, these warmings rarely exceed a few kelvin and occur mainly after midwinter, but in the Northern Hemisphere at the stratopause, polar temperature sometimes rises by more than 50 K accompanying planetary waves whose amplitude on the temperature profiles is about 100 K. Events of this magnitude are described as major stratospheric warmings. Major warmings occur on average once per year, and each seems very different from others (Barnett 1980).

The appearance of a major warming in the upper stratosphere depends not only on the characteristics of the planetary wave present such as their amplitude and phase but also on the zonal wind circulation arising from the stratospheric polar vortex which, in winter, reaches its maximum and is close to the latitude of Durban (see fig.(7.27)) where the RHS of the figure refers to the zonal mean wind for Jul 1976 in the Southern hemisphere.

During summer the warm polar anticyclone is at its peak in the stratosphere. Together with the warm anticyclone, easterly winds prevail in the summer stratosphere (compare fig.(7.26), fig.(7.27)) which prohibit the propagation of planetary waves. The Southern summer stratosphere is warmer than the Northern summer stratosphere (Barnett 1974) because of the dif-

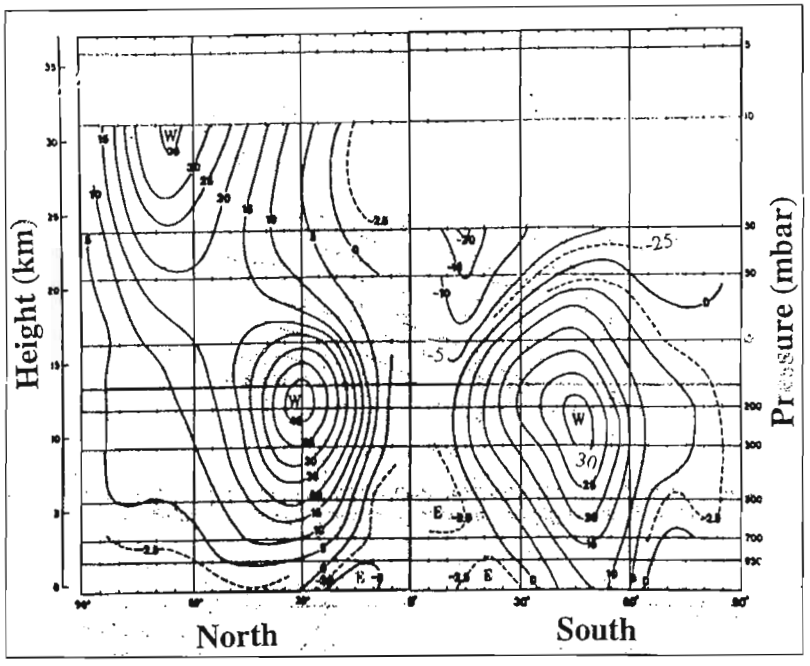

Figure 7.26: Vertical meridional section of zonal wind (in m/s) for January 1976 (from Knittel, 1976).

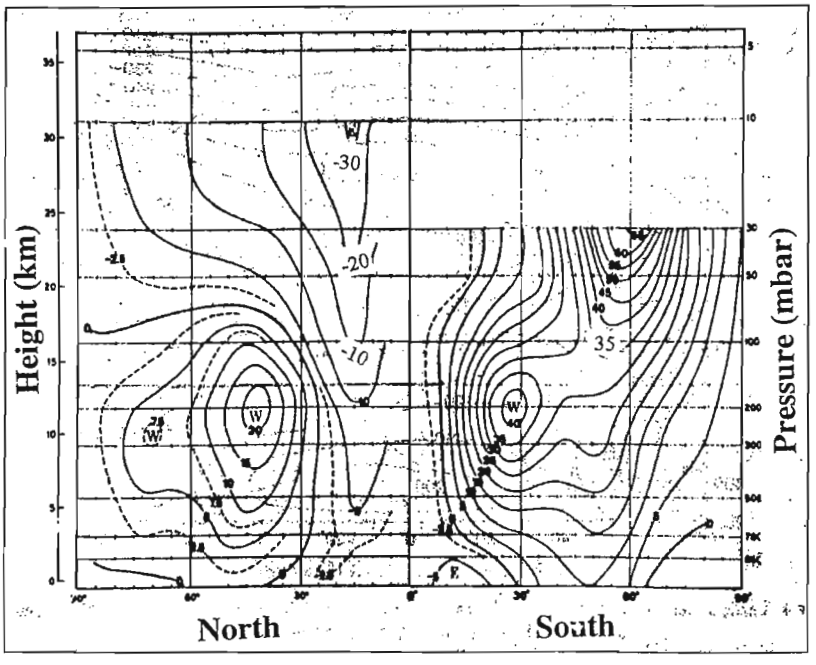

Figure 7.27: Vertical meridional section of zonal mean winds (in m/s) for July 1976 (from Knittel, 1976).

ference in the ozone distribution in the Southern and Northern hemispheres and hence the Southern hemisphere has different solar heating compare to the Northern hemisphere. Furthermore, the ellipticity of the Earth's orbit produces a 6 % modulation of the solar input (Barnett 1974).

The September to December LIDAR temperature profiles are colder than the CIRA-86 model especially between 35 and 50 km. The observed differences between the model and the LIDAR may be due to the fact that measurement temperatures of CIRA-1986 are quite old. In fact the CIRA-1986 temperatures are more than 20 years older and during this time the stratospheric concentration of gases may have changed. Also, due to rainy weather conditions in summer, there is insufficient LIDAR data to make a good correlation with the model.

7.12 Summary

The comparison between LIDAR and SAGE II extinction coefficients show several aerosol layers in the lower stratosphere above Durban. On June 11 1999 both LIDAR and SAGE II detected an aerosol layer between 29 km and 31 km. Probably, the same layer is also detected on August 20 1999 where both SAGE II and LIDAR show a peak at $\approx$ 30.5 km. However, below 29 km the correlation between LIDAR and SAGE II extinction profiles is poor. This can be explained by the variability of the vertical distribution of aerosols as detected by LIDAR and also by the geometry of the SAGE II measurements.

The comparisons between average monthly LIDAR temperature profiles with the CIRA-1986 model and average monthly ECMWF temperature profiles are fairly good between 20 and 30 km. Above 30 km LIDAR tem-

peratures are warmer than the model and ECMWF temperatures especially during winter. This can be attributed to stratospheric warming and the large planetary wave activity in winter. The LIDAR temperature profiles are slightly colder in summer compared with the model and ECMWF temperatures. This is because in summer the LIDAR temperature profiles are not perturbed by planetary waves whose activities are reduced. Furthermore, the weak zonal wind speeds in summer inhibit the propagation of these waves in the stratosphere above Durban (see figs.(7.24) and (7.25)).

The agreement between LIDAR and radiosonde temperatures of SAWS is usually good especially when radiosonde data reach altitudes above 20 km. The average LIDAR temperature profiles for the months May, June, July, August and September 1999 are reasonably good taking into account the possible influence of stratospheric aerosols, and the great variability of the temperature in the winter stratosphere.

Chapter 8

Preliminary study of atmospheric gravity waves using the new LIDAR

8.1 Introduction

We are all familiar with the concept of a wave. Generally speaking, a wave is characterised by a perturbation (oscillatory in nature) of physical parameters of the medium, with respect to its equilibrium position. For example, a sugar cube dropped into a cup of tea generates waves that travel radially outwards from the point of impact; everyday at the seashore we observe a continuous panorama of incoming waves which grow in height and eventually break against the shore. These are examples of wave motion in a fluid. There are two important properties that they have in common:

(1) Energy is being propagated from one point to another,

(2) The disturbance travels through the medium without giving the medium as a whole any permanent displacement.

The atmosphere is capable of sustaining a large number of wave phenomena. In the next section we classify the various types of atmospheric waves.

8.2 Atmospheric waves

Lower atmospheric waves can be broken up into three classes:

- waves that propagate horizontally and are composed of vertical displacements (vertical transverse waves), for example gravity waves.
- waves that propagate horizontally with horizontal displacements perpendicular to the propagation direction (horizontal transverse waves), for example Rossby waves.
- waves whose displacements are in the same direction as the propagation (longitudinal), for example sound or acoustic waves.

The basic features of these waves are shown in fig.(8.1). Atmospheric wave motion may be thought of as a combination of all these types of waves. These waves (shown in fig.(8.1)) exist in the form of small perturbations on a steady background state of the atmosphere. In the linear approximation, small disturbances with different amplitudes, wavelengths and frequencies can be superimposed without interacting. One wave can penetrate straight through another without producing any noticeable effect. However, as the wave progresses it may either become attenuated or actually grow in amplitude.

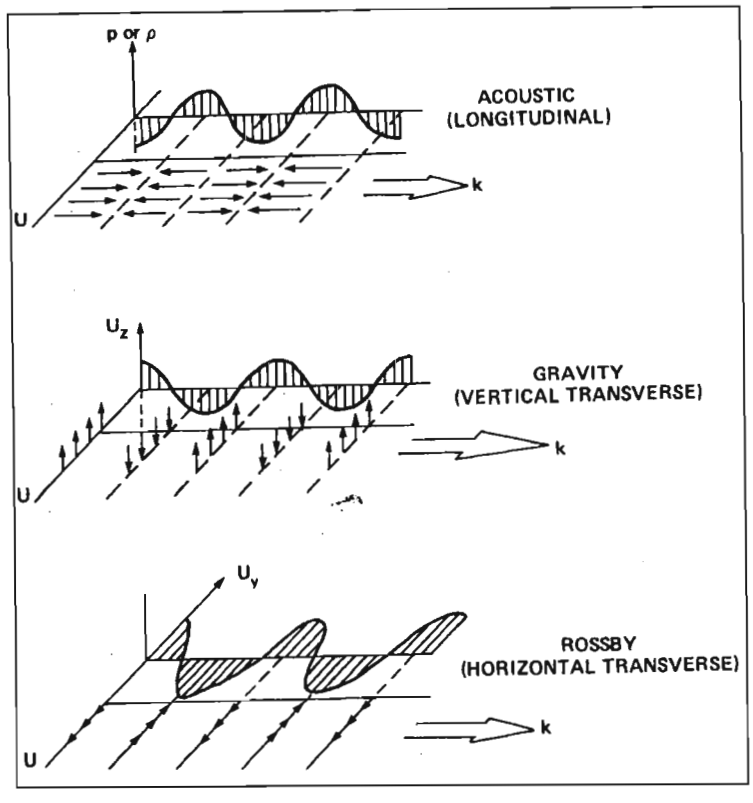

Figure 8.1: The three main types of atmospheric waves. $\overline{k} = \frac{2 \cdot \pi}{\lambda} \hat{\imath}$ is the the propagation vector ; p is the pressure of the atmosphere and ρ is the density of the atmosphere; U_x, U_y and U_z are the velocity components in the x, y and z directions respectively.

The most familiar of atmospheric waves is the sound or acoustic wave which plays a vital role in the field of communication. Acoustic waves are longitudinal, formed by a balance between the fluid's compressibility and inertia. The latter is related to the force by Newton's second law of motion. In a homogeneous stationary fluid, in the absence of an external force (gravitational, magnetic, etc.), acoustic waves are the only type of waves that can exist. We use the method of linearisation to derive the fundamental quantities associated with the propagation of atmospheric waves. In order to illustrate this method, we begin with the propagation of sound waves in

the atmosphere (Appendix C, section C.5).

The earth's atmosphere is under hydrostatic pressure balance which means that the vertical pressure gradient balances the downward gravitational force. There is, therefore, a distinct decrease in density with altitude, which is generally referred to as a density stratification, due in fact to a smooth variation in density rather than a layered one. Fig. (8.2) shows the variation of density with altitude for the U.S. Standard Atmosphere from an altitude of 0 km to 20 km.

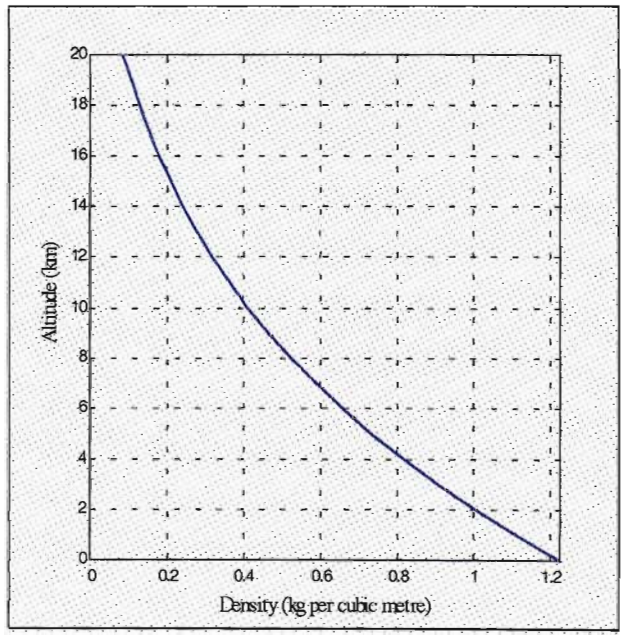

Figure 8.2: The distribution of density with height in the atmosphere (the data is from the U.S. Standard Atmosphere, 1962).

The decrease of density with height shown in fig. (8.2) indicates in fact that the atmosphere is gravitationally stable. When the force of gravity and the magnitude of the stabilising restoring force introduced by the atmospheric density gradient become comparable with compressibity forces, the

resulting waves are called acoustic gravity waves. These waves are no longer purely longitudinal (except when they propagate vertically) because gravity produces a component of the air particle motion tranverse to the propagation direction. A mathematical analysis of the propagation of gravity waves in the atmosphere using the method of perturbation or linearisation is given in Appendix C, section C.8.

There also exist long waves that are governed by the curvature of the earth and its rotation. The latitudinal variation of the Coriolis force acts as an external force field which results in horizontally transverse waves with wavelengths thousands of kilometres long. These waves are known as Rossby waves or planetary waves; they provide a meteorologically useful theoretical framework for the description of the pressure distribution associated with moving wave-like high-pressure and low-pressure systems.

Rossby waves have a phase velocity that always points to the west and is often directed in the opposite direction to the background wind. Thus, the planetary wave concept is primarily of meteorological interest in regions of prevailing westerlies. Appendix C, section C.10 gives a detailed mathematical treatment of the propagation of Rossby waves in the atmosphere.

Table (8.1) shows the principal atmospheric waves and some typical periods.

Waves propagating in the earth's atmosphere are both anisotropic and dispersive. This is a consequence of the existence of a preferred direction of the geophysically important forces such as gravity and Coriolis.

Wave	Period
Acoustic	$<$ 270 seconds
Gravity	270 seconds-3 hours
Atmospheric tides	$\frac{24}{m}$ hours (m = 1,2,...)
Rossby	$>$ 12 hours

Table 8.1: Principle atmospheric waves and their periods.

If the phase speed of the waves, $\frac{\omega}{k}$, is functionally dependent on the wavelength (or the wavenumber k), the wave is said to be dispersive. In the atmosphere, dispersion arises because of the "bounce" or Brunt-Väisälä frequency N(z) which is defined as

$$N^2 = -\frac{g}{\varrho_0} \cdot \frac{\partial \varrho_0}{\partial z} \tag{8.1}$$

where ϱ_0 is the density of a parcel of air under hydrostatic equilibrium.

The dispersion of atmospheric waves is structural in origin and is connected to the internal resonant frequencies that the atmosphere possesses. For gravity waves, the resonant frequency is the Brunt-Väisälä frequency (derived in section C.7.1 of Appendix C).

In the next section we discuss in more detail atmospheric gravity waves.

8.3 Atmospheric gravity waves

8.3.1 Mechanism and generation of atmospheric gravity waves

Atmospheric gravity waves occur when the dominant motion in the atmosphere is due to the restoring force of density gradients. It has been recog-

nised for a long time that atmospheric gravity waves are important in meteorology (Haurwitz 1951). The deformation of rockets' smoke trails in the troposphere provides evidence of the existence of these waves at low altitudes (Naito 1966). Clear air turbulence can also be caused by atmospheric gravity waves. In the presence of large wind shears, it is possible for the atmospheric gravity waves in these shear layers to become unstable (Bretherton 1969). The amplified atmospheric gravity waves eventually break down under the action of an instability (called the Kelvin-Helmholtz instability) and form zones of turbulence. At lower heights similar unstable waves become visible in the form of billow clouds.

An observation of a special case of a stationary atmpospheric gravity wave is to be found in the formation of lee waves downwind of the Drakensberg mountains in stably stratified air (fig. (8.3) below). As shown in fig. (8.3), when the wind blows over the mountain top a discontinuous vortex is formed called a rotor which perturbs the lower atmosphere. The gravity waves thus formed are carried vertically up by the current of air in which they are formed.

The amplitude of atmospheric gravity wave can increase up to 2 km until the wave becomes a rotor. The two conditions that govern their speed of translation are as follows:

(1) if the depth z, of a discontinuity between adjacent layers exceed $\frac{1}{40}$ of the wavelength of the wave, then the speed v of the wave is given by the "deep water" expression:

$$v = v_w \pm \left(\frac{g \cdot \lambda}{2\pi}\right)^{\frac{1}{2}} \tag{8.2}$$

where v_w is the wind speed, g is the acceleration due to gravity and λ is the

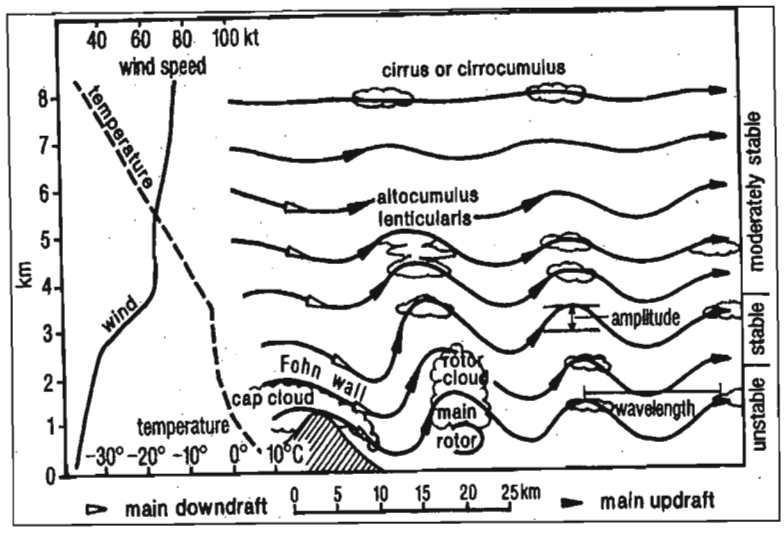

Figure 8.3: Types of lenticular clouds produced by airflow across mountains with the occurrence of appropriate wind and temperature profiles (after Ernst, 1976).

wavelength.

(2) when the atmospheric gravity waves are formed in shallow flows, i.e. $z < \frac{\lambda}{40}$, then we have the "shallow water" form:

$$v = v_w \pm (g \cdot z)^{\frac{1}{2}} \tag{8.3}$$

Atmospheric gravity waves are often associated with wave clouds, the exact form of which depends on the variations of wind speed and temperature with height. An example of a lenticular cloud formed over Kwazulu-Natal, South Africa, is shown in fig. (8.4).

Atmospheric gravity waves are mainly generated in the troposphere where dynamical phenomena influence their occurrences. There are numerous ways in which atmospheric gravity waves are generated. The most simple one as mentioned above is the formation of Lee waves downwind of mountains. Other systems that can generate gravity waves in the atmosphere are cold

Figure 8.4: Example of lenticular cloud formed over Kwazulu-Natal (Preston-Whyte and Tyson, 1997).

fronts, cyclones, convective systems and wind shears.

From this research, it can be hypothesised that penetrative convection is probably one of the most important sources of atmospheric gravity waves. It occurs when a convectively unstable region is capped by an overlying inversion. Typical situations are an unstable daytime boundary layer below an inversion layer and convection in clouds penetrating from the troposphere into the stably stratified stratosphere. Penetrative convection could also be the process by which gravity waves are generated during nuclear bomb tests in the atmosphere (Beer 1975).

Shear instability in particular in the polar and the subtropical jet streams generate Kelvin-Helmholtz waves and also vertically propagating atmospheric gravity waves (Klostermeyer and Ruester 1980).

In Durban the major sources of atmospheric gravity waves are Lee waves downwind of the Drakensburg mountains, cold fronts and shear instability due to subtropical jet streams, especially in the month of July around 12 km

altitude.

8.3.2 Amplitude of atmospheric gravity waves

Atmospheric gravity waves have amplitudes which grow upwards as $\varrho^{-\frac{1}{2}}$, where ϱ is the density of the atmosphere. This increase in amplitude is a direct consequence of conservation of energy. If the amplitude of the atmospheric gravity wave is represented by ψ then the kinetic energy is given by $\frac{1}{2} \cdot \varrho \cdot \psi^2$ which remains constant (assuming constant wavelength).

The density $\varrho\,(z)$ of the atmosphere varies exponentially with altitude and is related to the scale height H_s by the expression

$$\varrho(z) = \varrho_0 \exp\left(-\frac{z}{H_s}\right) \tag{8.4}$$

where ϱ_0 is the density of the atmosphere at the ground and is taken to be 1.225 kg m^{-3}; H_s is given by $\frac{U_R \cdot M}{W_m \cdot g}$ where U_R is the molar gas constant, W_m is the mean molecular mass of the atmosphere, g is the acceleration due to gravity and M is the thermodynamic temperature of the atmosphere.

Altitude (km)	Pressure (hPa)	Density (kg m^{-3})
0	1013.2	1.225
6	472.2	0.6601
11	227.0	0.3648
20	55.3	0.0889
50	0.8	0.0010
90	0.002	0.000003

Table 8.2: Selected values of density and pressure from the U.S. Standard Atmosphere (1962).

Selected values of the density and pressure from the U.S. Standard Atmosphere (1962) are given in table (8.2).

Along with the density profile (fig. (8.2)), the pressure also decreases exponentially with height. Fig. (8.5) shows the variation of pressure with height from 0 to 20 km. The data is from the U.S. Standard Atmosphere, 1962.

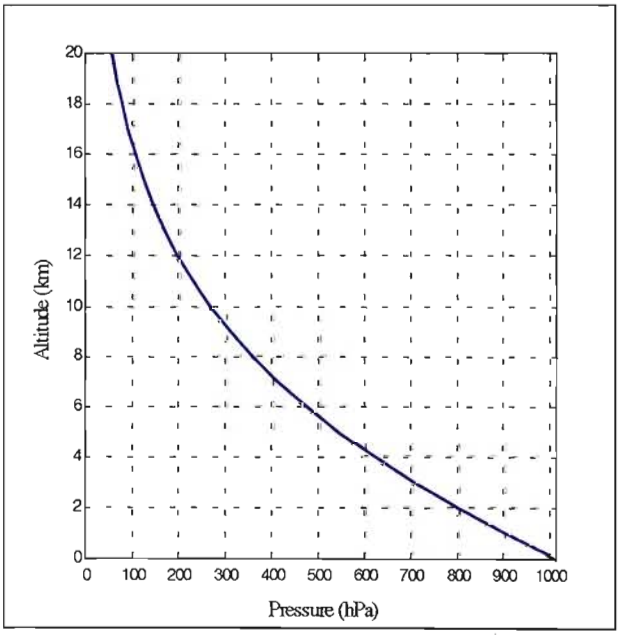

Figure 8.5: The distribution of pressure with height in the atmosphere (U.S. Standard Atmosphere, (1962)).

8.4 Atmospheric gravity waves observations using the new LIDAR

8.4.1 Methodology

The method adopted for the analysis of atmospheric gravity waves is similar to that employed by several researchers such as Wilson *et al.* (1990), Whiteway *et al.*(1994) and Souprayen *et al.* (1993). This consists of dividing the LIDAR-derived temperature profiles into two altitude domains:

1. the lower stratosphere from 20 to 30 km,
2. the upper stratosphere from 30 to 45 km.

High resolution measurements are employed for gravity wave studies. The raw LIDAR data (photon counts) are first temporally integrated over half an hour. LIDAR temperatures are then derived with a vertical resolution of 300 m. The analysis is best done with LIDAR data acquisition periods of at least 4 hours. As this is a preliminary study, we will consider the LIDAR data obtained for the nights of 28 and 29 May 2001 each representing 5 hours of data. The data are temporally integrated over half an hour so as to obtain 11 derived-LIDAR temperature profiles. Together with the average LIDAR temperature profiles, this adds up to a total of 12 LIDAR temperature profiles.

The analysis is done in 5 discrete steps:

1. Calculation of the temperature trend for the night (The temperature trend for the night is the filtered LIDAR temperature profile over the night).
2. Determination of the temperature fluctuations.
3. Correction of the boundary effects on the tempearture fluctuations.

4. Calculation of power spectral density.

5. Noise estimation in the power spectral density plots.

We will now describe each step separately.

8.4.2 Calculation of the temperature trend for the night

The atmospheric variance due to planetary and large period waves is first extracted from the LIDAR temperature profile integrated over the whole night of acquisition. The LIDAR temperature for the night is filtered using a low-pass Butterworth filter, of order 3. The Butterworth filter is a standard filter used in digital signal processing and can be applied for high-pass and band-pass filtering as well. The resulting temperature obtained after filtering is the temperature trend (M_{trend}) for the night.

8.4.3 Determination of the temperature fluctuations

It is important to note that due to the propagation of gravity wave in the atmosphere, it is of more relevance to consider fluctuations in relative density or temperature rather than fluctuations in pressure. This is because pressure variations on a vertical scale (fig. (8.5)) are much lower than the atmospheric density scale ($H_s \cdot \varrho$), where H_s is the atmospheric scale height defined as $H_s = \frac{U_R \cdot M}{W_m \cdot g}$ (U_R is the molar gas constant, M is the absolute temperature, W_m is the relative molecular mass of the atmosphere, g is the acceleration due to gravity), ϱ is the density of the atmosphere.

For each half-hour integrated temperature profile, between heights of 20

and 45 km, we calculate the following quantity:

$$\mathrm{M}'(\mathrm{z}) = \frac{\mathrm{M}_{LIDAR}(\mathrm{z}) - \mathrm{M}_{trend}(\mathrm{z})}{\mathrm{M}_{trend}(\mathrm{z})} \tag{8.5}$$

where $\mathrm{M}_{LIDAR}(\mathrm{z})$ is the half-hour integrated LIDAR temperature profile and $\mathrm{M}_{trend}(\mathrm{z})$ is the estimated temperature trend.

The resulting quantity $\mathrm{T}'(\mathrm{z})$ obtained is the temperature fluctuation between 20 and 45 km.

The temporal characteristics of the temperature fluctuations can be deduced from successive profiles of the temperature fluctuations which give the apparent frequency ι of the wave.

In fact, it is not possible to directly estimate from ground-based measurements, the intrinsic frequency $\omega(z)$ of the wave in the reference frame of the mean flow, as it depends on the average wind speed, the horizontal wave number, and the relative direction of propagation of the wave with respect to the mean flow. The intrinsic (or Doppler-shifted) frequency $\epsilon(z)$ of the wave is given by

$$\epsilon(\mathrm{z}) = \iota - \overline{k}_x \cdot \overline{\mathrm{u}}(\mathrm{z}) \tag{8.6}$$

where $\overline{k}_x$ is the wave number in the x direction and $\overline{\mathrm{u}}$ is the mean wind velocity.

8.4.4 Correction of boundary effects on the temperature fluctuations

In order to reduce boundary effects, we subtract a linear trend from $M'(z)$ which passes through the first and last points of the interval:

$$X'(z) = M'(z) - \left[\left(\frac{M'(z_b) - M'(z_a)}{z_b - z_a}\right) \cdot z + \text{costant}\right] \tag{8.7}$$

where z_a and z_b are the boundary values for the interval and the constant $= M'(z_b) - \left(\frac{M'(z_b) - M'(z_a)}{z_b - z_a}\right)$. The quantity $X'(z)$ is the corrected relative temperature fluctuations.

8.4.5 Calculation of the power spectral density

Spectral analysis as a function of vertical wave number is calculated on the two altitude ranges, viz. the lower stratosphere (20 to 30 km) and the upper stratosphere (30 to 45 km). The time evolution of the temperature fluctuations are described by a two-dimensional spectral analysis as a function of vertical wave number and apparent frequency. This is achieved by applying a frequency Fourier transform to X´(z), giving a qualitative insight into the temporal characteristics of the fluctuations. The mean spectrum for the night is obtained by averaging all the spectra resulting from the half hour integration time of the signal for the same night.

The 2-D spectrum shows the phase evolution of the successive Fourier transforms of the relative temperature fluctuations with vertical wave number. The zero frequency term in the 2-D spectrum represents the power

spectrum of the fluctuations with periods longer than the measurement duration.

8.4.6 Noise estimation in the 2-D spectra

It has been verified that the noise of the LIDAR signal due to the uncertainty on the photon counting has a white spectral response (Wilson *et al.* 1991). The white noise level is evaluated in the high wave number region of the mean power spectral density (where the signal-to-noise ratio is low), i.e. for vertical wavelengths smaller than 1 km and is subtracted from the rest of the spectra.

The relative uncertainty on the resulting power spectrum density can be estimated from

$$\frac{\Delta(\mathrm{P}_{sd}(\mathrm{k}) - \mathrm{W})}{\mathrm{P}_{sd}(\mathrm{k}) - \mathrm{W}} = \frac{1}{\mathrm{n}_s^{\frac{1}{2}}} \cdot \frac{\mathrm{P}_{sd}(\mathrm{k})}{\mathrm{P}_{sd}(\mathrm{k}) - \mathrm{W}} \tag{8.8}$$

where $\mathrm{P}_{sd}(\mathrm{k})$ is the power spectrum density of the raw data, W is the white noise level and n_s is the total number of spectra over which the average power spectrum has been obtained.

In the next section, we derive the power spectral density of relative temperature fluctuations as a function of vertical wave number in the case of saturated gravity waves. This will be used later to illustrate that saturation of gravity waves does indeed occur in the upper stratosphere.

8.4.7 Potential energy and power spectral density of saturated atmospheric gravity waves

The temperature fluctuations are associated with vertical displacements of the atmospheric fluid and therefore are related to the available potential energy of the fluctuations.

Assuming adiabatic conditions, the vertical displacement $\zeta(z)$ of an atmospheric fluid is related to the relative temperature perturbation according to the equation (Fritts 1984):

$$\zeta(z) = \frac{g}{\mathrm{N}^2} \cdot \frac{M'(z)}{M_{Trend}(z)} \tag{8.9}$$

where N is the Brunt-Väisälä frequency and g is the acceleration due to gravity (taken to be 9.81 ms^{-2}).

The Brunt-Väisälä frequency which is a measure of the static stability of the atmosphere, can be deduced from the temperature trend (M_{Trend}) for the night according to the equation (LeBlond and Mysak 1980):

$$\mathrm{N}^2(\mathrm{z}) = \frac{g}{\langle \mathrm{M}_{Trend}(z) \rangle} \left(\frac{\partial \langle \mathrm{M}_{Trend}(z) \rangle}{\partial z} + \frac{g}{C_p} \right) \tag{8.10}$$

where C_p is the specific heat capacity of air at constant pressure taken to be 1005 J / kg / K (assume to be constant for the altitude range between 20 and 45 km) and z is the altitude.

Using equation (8.9) the available potential energy per unit mass, PE for the vertical displacement ζ of an air mass is given by

$$\mathrm{PE} = \frac{1}{2} \cdot \mathrm{N}^2(\mathrm{z}) \cdot \langle \zeta^2 \rangle = \frac{1}{2} \cdot \mathrm{N}^2(\mathrm{z}) \cdot \langle \left(\frac{g}{\mathrm{N}^2(\mathrm{z})} \cdot \frac{\mathrm{M}'}{\mathrm{M}_{Trend}} \right)^2 \rangle \tag{8.11}$$

Equation (8.11) shows that the potential energy per unit mass can be estimated by integrating the power spectral density obtained from the Fourier transform of the corrected relative temperature fluctuations X' (see subsection 8.4.4), between the wavelength 1 and 10 km.

In order to obtain the vertical displacement of the air mass, a new quantity X'' is defined using the Brunt-Väisälä static stability profile $N^2(z)$ and X':

$$X'' = \frac{g}{N^2} \cdot X' \tag{8.12}$$

The quantity X'' is useful since it indicates the vertical displacement of air mass.

Assuming that the saturation of the atmospheric gravity waves results only from convective instabilities, Dewan and Good (1986), Smith *et al.* (1987) and Sidi *et al.* (1988) have shown that the power spectral density P^s_{sd} of the relative temperature fluctuations as a function of vertical wave number of a saturated wave field reduces to

$$P^s_{sd}\,(\overline{k_z}) = \eta \cdot \frac{N^4}{g^2 \cdot k_z^2} \tag{8.13}$$

where η is a proportionality factor ranging between $\frac{1}{2}$ and $\frac{1}{20}$, depending on the spectral width of the saturated wave field. Here $\overline{k_z}$ is the vertical wave number. The superscript s denotes saturation. It is interesting to note that equation (8.13) does not depend on the frequency distribution of the waves because of the assumption that convective instabilities provide the sole saturation mechanisms. Using these equations, we now present some results in the next section.

8.4.8 Results and discussions

We consider results obtained for the LIDAR measurements of May 28 and 29 2001. These nights have been chosen on the basis of high signal-to-noise ratio and large wave amplitudes.

Nightly mean temperature profiles

Figs. (8.6) and (8.7) show the LIDAR temperature profile for 28 and 29 May 2001, respectively. Above 45 km wave-like structures are clearly visible. These planetary waves perturb the atmospheric fluid as they propagate vertically up in the atmosphere. Owing to the excellent vertical resolution (150 m), a LIDAR can detect these waves in contrast to satellite measurements where the vertical resolution is low (for example for SAGE II, the resolution is 1 km). The waves depicted on the LIDAR temperature profile in fact represents a superposition of several waves of different periodicities. In this study, we will restrict ourselves to atmospheric gravity waves.

Figs. (8.8) and (8.9) show the half an hour time evolution of the temperature profiles (shown in blue) of 28 and 29 May together with the average LIDAR temperature profile for the night (shown in magenta). Above 30 km shorter time and length scale wavelike temperature perturbations are observed. These are interpreted as atmospheric gravity waves. Between 35 and 45 km on the successive hour temperature profiles of 28 May (fig. (8.8)), large amplitude gravity wave can be seen propagating to the upper stratosphere. The wave amplitudes are such as to induce convective instability.

Another interesting way of representing the half hour evolutions of the

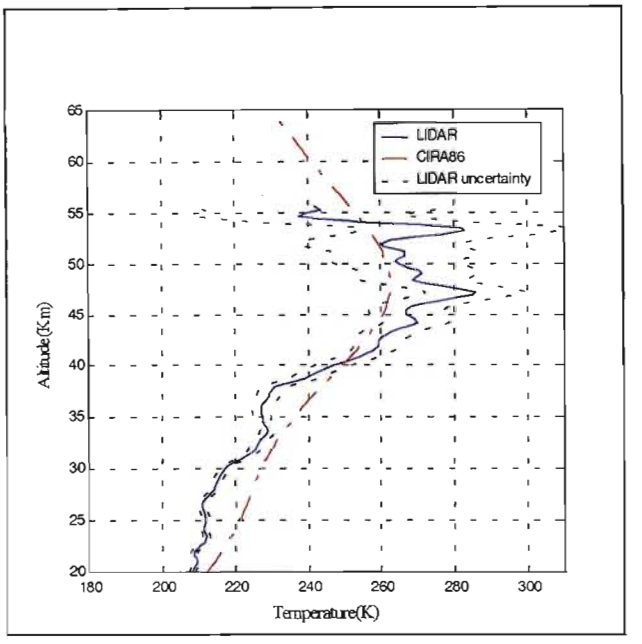

Figure 8.6: Average LIDAR temperature profile for May 28 2001 (5 hours of data).

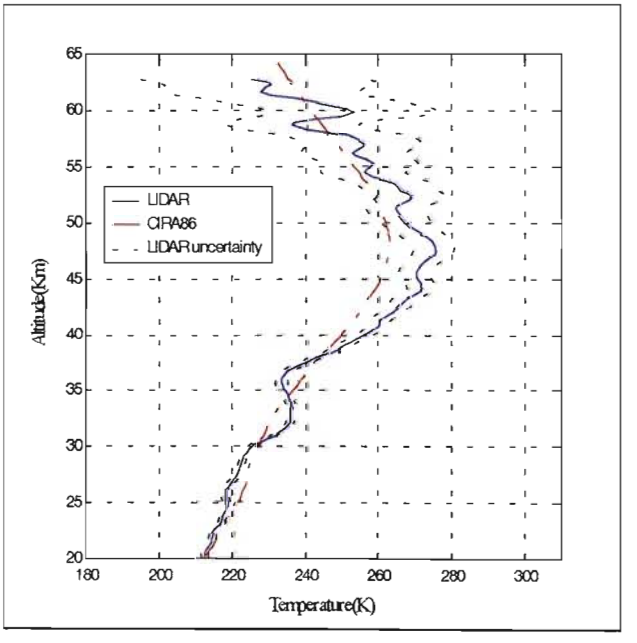

Figure 8.7: LIDAR temperature profile for May 29 2001 (5 hours acquisition).

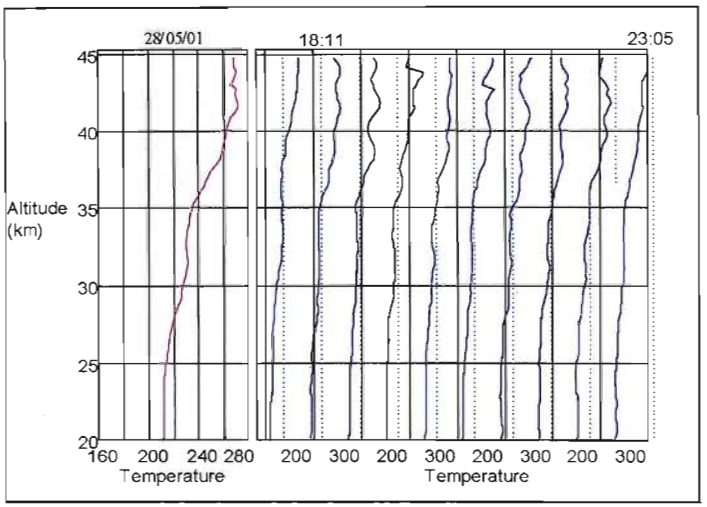

Figure 8.8: Sequence of $\frac{1}{2}$ hour temperature profiles between the heights of 20 km and 45 km for the night of 28 May 2001. The left hand figure is the average LIDAR temperature profile for the night.

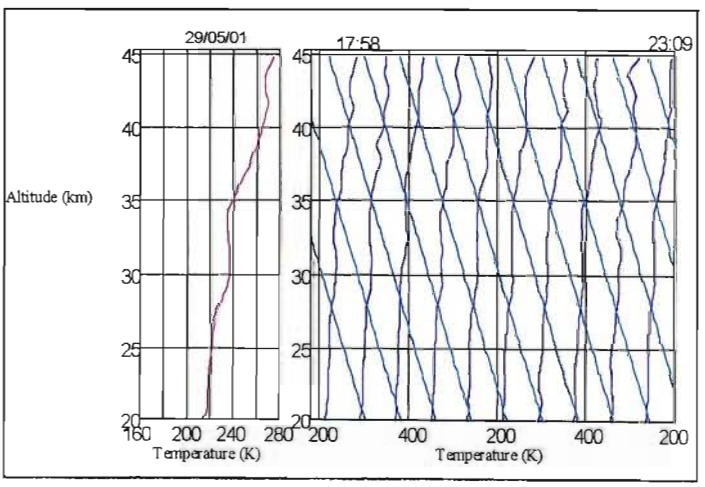

Figure 8.9: Sequence of $\frac{1}{2}$ hour temperature profiles between the heights of 20 and 45 km for the night of 29 May 2001. The left hand figure is the average LIDAR temperature profile for the night. The blue lines correspond to an adiabatic lapse rate (-9.8 K/km).

LIDAR temperature profiles are shown in figs. (8.10) and (8.11) which display the contour plot of the half hour smoothed LIDAR temperatures for the two nights.

Figs. (8.12) and (8.13) show the superimposed plots of the average LIDAR temperature and the temperature trend for the respective night. The temperature trend for the night is used to calculate the Brunt-Väisälä frequency which is used to estimate the available potential energy of the gravity wave (see section 8.4.7).

Temperature fluctuations and convective instabilty

Atmospheric gravity waves are best observed in profiles of relative temperature perturbations, obtained as explained above. Figs. (8.14) and (8.15) show the contour plots of the relative temperature fuctuations for 28 and 29 May respectively. A random superposition of vertical wavelengths less than 10 km is generally observed. However, on a few occasions such as on 28 May, there was a distinct dominant vertical wavelength. The temperature perturbations have amplitudes large enough to induce adiabatic lapse rates. For a dry atmosphere, the adiabatic lapse rate (ALR) defined as $-\frac{g}{C_p}$ (where g is the acceleration due to gravity) and C_p the specific heat capacity at constant pressure with a value 1005 J $kg^{-1}K^{-1}$), is estimated to be

$$\begin{aligned} ALR &= -\frac{9.81}{1005} \\ &= -0.00976 \text{ K m}^{-1} \\ &= -9.76 \text{ K km}^{-1}. \end{aligned}$$

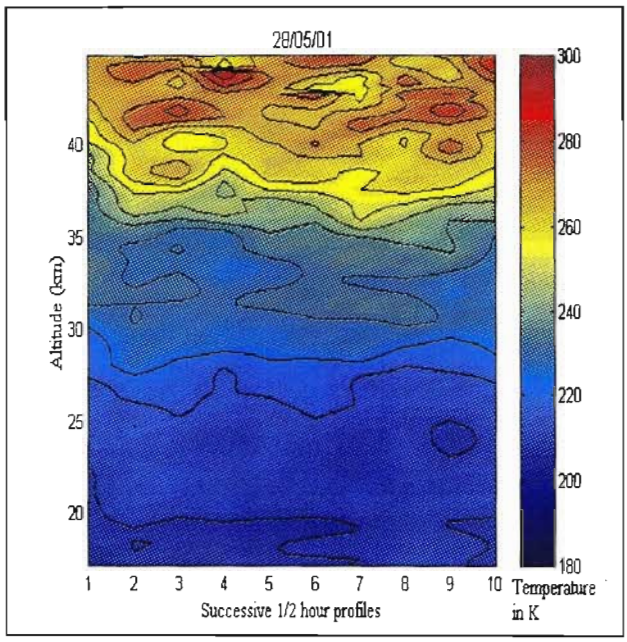

Figure 8.10: Contour plot of the temperature evolution over the night of 28 May 2001. The half hour temperatures have been smoothed.

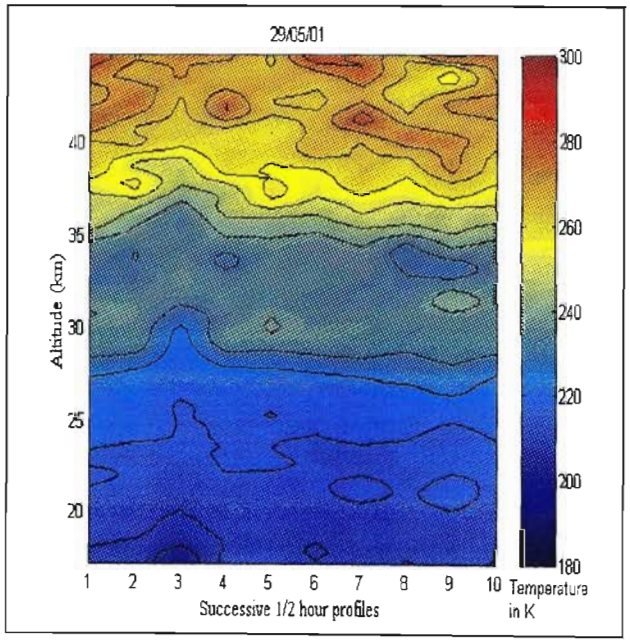

Figure 8.11: Contour plot of the temperature evolution over the night of 29 May 2001. The half hour temperatures have been smoothed.

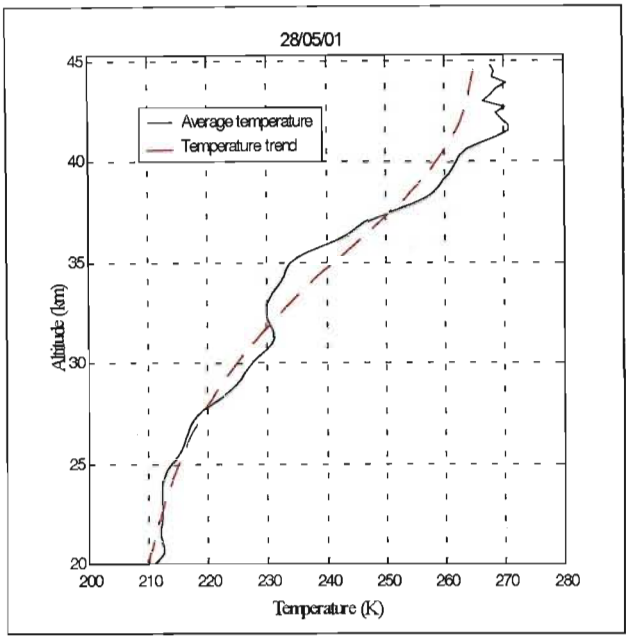

Figure 8.12: Superimposed plots of the average LIDAR temperature and the temperature trend for the night of 28 May 2001.

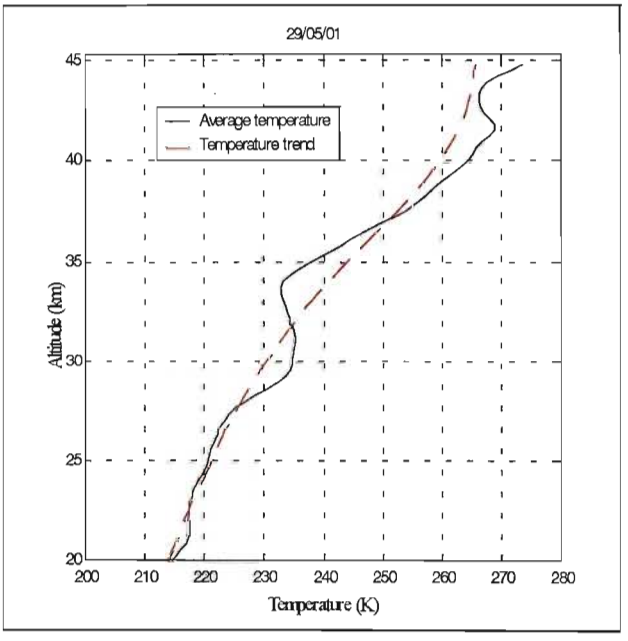

Figure 8.13: Superimposed plots of the average LIDAR temperature and the temperature trend for the night of 29 May 2001.

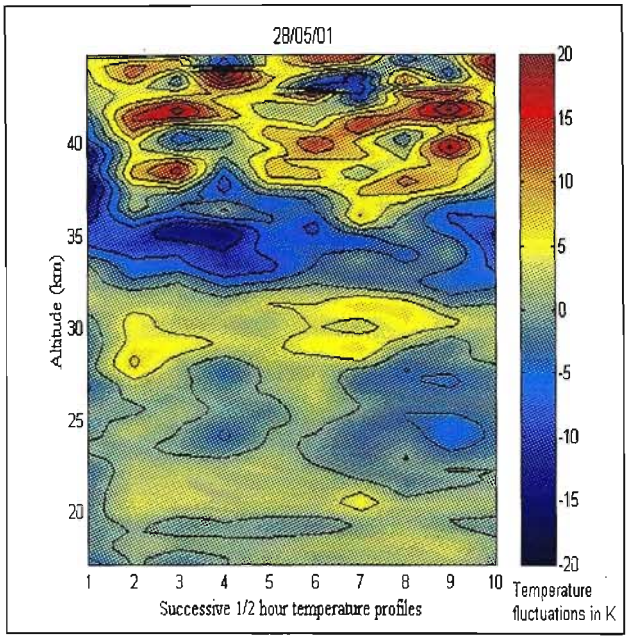

Figure 8.14: Temperature fluctuations evolution over the night of 28 May 2001.

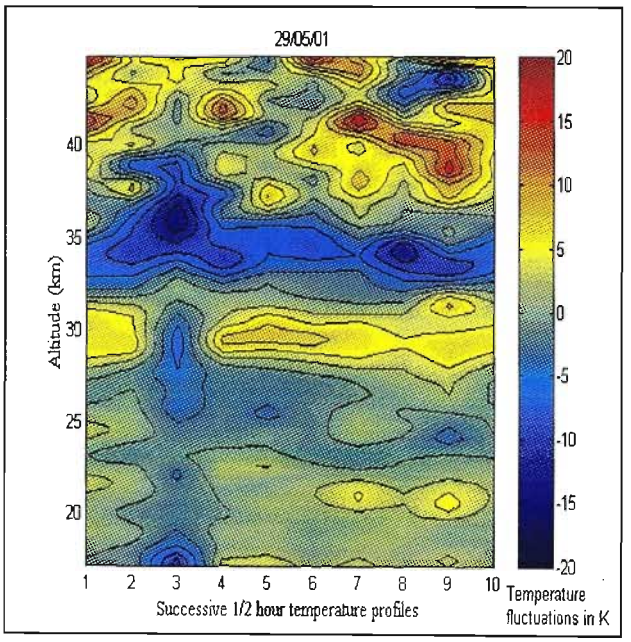

Figure 8.15: Temperature fluctuations evolution over the night of 29 May 2001.

These convective unstable layers are sometimes observed to persist for hours. This occurs as a result of shorter wavelengths at lower altitudes and longer wavelengths above. This is because the gravity waves as they propagate upward into the stratosphere and mesosphere, their wavenumber, amplitude as well as their available potential energy increase with altitude (Holton 1982, 1983) until they reach a point where the amplitude shows no significant growth with altitude. At this point, the wave field is saturated and the wave energy is strongly dissipated - a result known as convective instability.

For non-dissipative linear gravity wave propagation, the induced temperature perturbations will grow with altitude z, in response to diminishing density, in proportion to $\exp\left(\frac{z}{2H_s}\right)$ (refer to section 8.3.2).

At 210 K the density scale height H_s for the region of our observations is

$$\begin{aligned} H_s &= \frac{U_R \cdot M}{W_m \cdot g} \\ &= \frac{(8.31)\cdot(210)}{(28.8)\cdot(9.81)} \text{ km} \\ &\approx 6.2 \text{ km.} \end{aligned}$$

Vertical wavenumber power spectral density and potential energy of atmospheric gravity wave

The nightly mean vertical wavenumber power spectral densities, computed over the altitude intervals 20 - 30 km and 30 - 45 km, are shown in fig. (8.16) for May 28 and fig. (8.17) for May 29, respectively. Also shown as dotted lines in figs. (8.16) and (8.17) is the saturation limit of the gravity wave

computed using the linear instability "saturated" spectral model proposed by Dewan and Good (1986) and extended by Smith *et al.* (1987).

Considering a superposition of atmospheric gravity waves with induced temperature gradients limited by convective instability, the power spectral density for these waves will reach a saturation limit given by $\frac{N^2}{10 \cdot m^3}$ where m is the vertical wave number and N is the Brunt-Väisälä frequency. Vertical growth of spectral density at a given wavenumber, within a broad spectrum, will cease (saturate) at this convective instability limit, shown as dotted lines in figs. (8.16) and (8.17).

The spectra of 28 and 29 May show that all the wave modes present are below the convective instability limit. The power spectral density is increasing as one moves from the troposphere to the stratosphere. Growth with altitude occurs at the smaller wavenumbers, corresponding to wavelengths greater than about 5 km, where the spectral density magnitude is far below the convective instability limit in the range 20 - 30 km. The power spectral density plots for both dates show that in the altitude range 30 - 45 km the vertical spectra seem to increase for smaller wave numbers (longer wavelengths) whereas for the altitude range 20 - 30 km the larger wave numbers (for both dates, the spectra for the portion 30 - 45 km of the stratosphere seem to increase for smaller wave numbers (longer wavelengths) whereas for the altitude range 20 - 30 km the larger wave numbers (smaller wavelengths) predominate.

The quantity N^2 given in equation (8.10) is a measure of the static stability of the atmosphere. Figs. (8.18) and (8.19) show the static stability

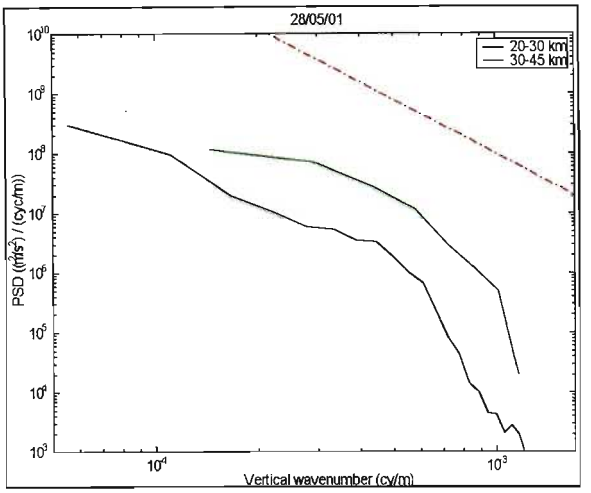

Figure 8.16: Power spectral density plot of the relative temperature fluctuations. The dashed line shows the saturation limit computed using linear instability model.

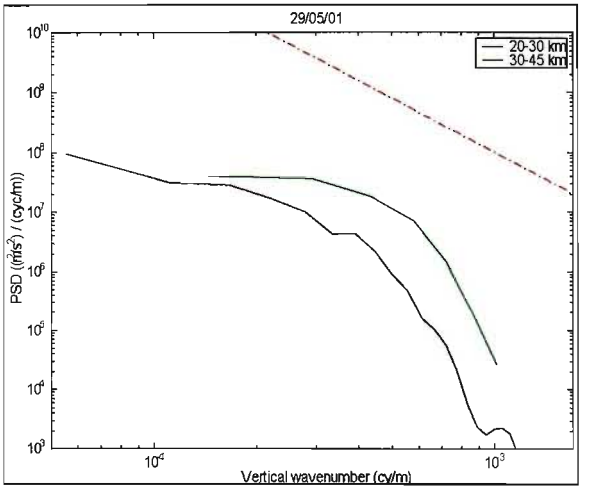

Figure 8.17: Power spectral density plot of the relative temperature fluctuations. The dashed line shows the saturation limit computed using linear instability model.

(N^2) profiles for May 28 and 29 respectively obtained using equation (8.10). These profiles show that between 30 and 38 km, N^2 reaches a maximum of about 5×10^{-5} s^{-2} on both dates which implies that for this altitude range the stratosphere is statically more stable.

The quantity N^2 is in fact related to the Brunt-Väisälä frequency N, refer to Appendix C, section C.7.1 for the derivation. If $N^2 > 0$, a parcel of air will oscillate about its original height with frequency N.

A rough estimate of the Brunt-Väisälä frequency N in terms of the scale height H_s is given by

$$N \approx \sqrt{\frac{g}{H_s}} \tag{8.14}$$

For the region of our observation, $H_s = 6200$m, then N is

$$\begin{aligned} N &\approx \sqrt{\frac{9.81}{6200}} \text{ per sec} \\ &= 0.04 \text{ per sec.} \end{aligned}$$

Therefore,

$$\text{period} = 2.6 \text{ mins.}$$

Coming back to figs. (8.16) and (8.17), the average potential energies per unit mass available for the two altitude ranges (20-30 km and 30-45 km) have been obtained by integrating the corresponding power spectral density plots between the wavelengths 1 and 10 km and multiplying by 0.5 and the average value of N^2 for the corresponding altitude range (refer to equation (8.11)). The average potential energies for the altitude ranges 20-30 km and 30-45 km are shown in table (8.3).

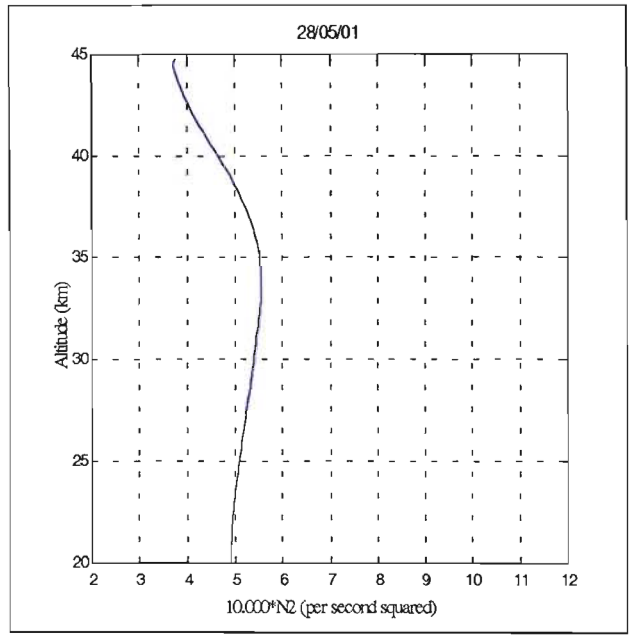

Figure 8.18: The average profile of the static stability of the atmosphere, N^2, for the night of 28 May 2001. The values of the x-axis have been multiplied by 10000 so as to obtain an enlarged profile.

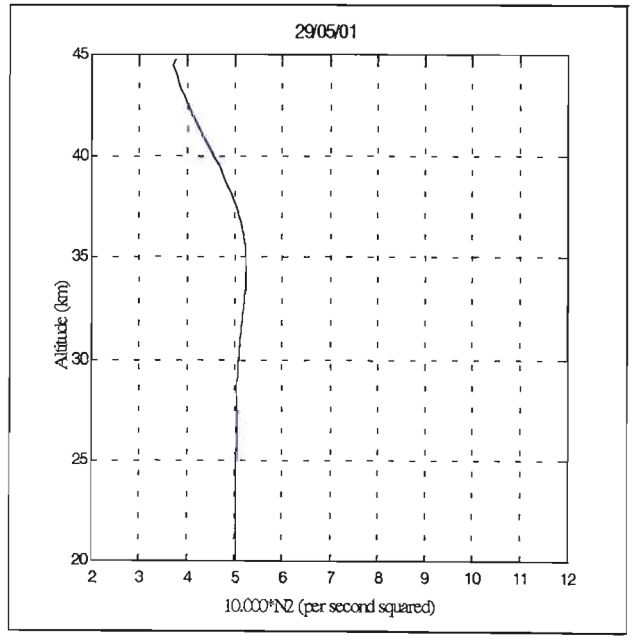

Figure 8.19: The average profile of the static stability of the atmosphere, N^2, for the night of 29 May 2001. The values of the x-axis have been multiplied by 10000 so as to obtain an enlarged profile.

Date	28/05/01	29/05/01
Potential energy for 20-30 km (J/kg)	65	61
Potential energy for 30-45 km (J/kg)	235	109

Table 8.3: Values of average potential energy per unit mass for the lower and upper stratosphere.

As indicated in the table, the average potential energy per unit mass increases from the lower stratosphere to the upper stratosphere. This is in accordance with equation (8.11) since at higher altitude the temperature fluctuations are larger and hence the potential energy is consequently larger.

8.5 Summary

The average LIDAR temperature profiles of May 28 and 29 show large wave-like structures above 20 km. These large temperature perturbations are caused by the upward propagation of atmospheric gravity waves. The available potential energy of these waves are computed using the power spectral method for two altitude domains: lower stratosphere (from 20 to 30 km) and upper stratosphere (from 30 to 45 km). The results show that the available potential energy increases with altitude. Plots of the vertical wave number power spectral density for May 28 and 29 show that the wave modes are below the convective instability limit. For both dates, the vertical power spectra for the altitude range 30-45 km increase for smaller wave number whereas for the altitude range 20-30 km, the larger wave numbers predominate. A larger data base of LIDAR acqusition is required in order to quantify the gravity wave activity above Durban.

Chapter 9

Conclusions

When I first started this doctoral study, the only atmospheric LIDAR that existed at the University of Natal in Durban was an old, outdated and slow, dye laser driven LIDAR. In parallel with this study, a new LIDAR system was assembled by a visiting French team from France and Reunion Island. However, when the team departed, after a relatively short visit, a great deal of improvement and maintenance work still had to be done. The new LIDAR became operational in April 1999 and from then on the arduous task of validating the LIDAR temperature profiles in comparison with the South African Weather Service (SAWS), European Centre for Medium range Weather Forcast (ECMWF) and CIRA-86 temperatures was undertaken. This validation was successful in that agreement between the various LIDAR temperature profiles (to within 5 K) was obtained.

Having validated the system, it became possible to study extinction coefficients due to aerosols as well as planetary waves in the stratosphere. The aerosol extinction coefficients obtained from the Durban LIDAR were compared for three days which were the only coincident days for the Stratospheric Aerosol and Gas Experiment (SAGE) II. It was found that in comparison

with SAGE II, the LIDAR extinction coefficient profiles were higher for the upper troposphere and nearly the same in the lower stratosphere.

The average monthly LIDAR temperature profiles of Durban show increased variability in the stratosphere, especially during winter. This can be attributed to the vertical propagation of planetary waves which originate in the troposphere (Hauchecorne and Chanin, 1982; Jenkins *et al.*, 1987; Marenco *et al.*, 1997). The propagation of these waves into the stratosphere is allowed due to large reversal of zonal winds which occur in the stratosphere during winter.

An improvement of the LIDAR instrument which was carried out towards the end of the doctoral thesis was the installation of a lower atmosphere channel. This was tested and operated in parallel with the high altitude channel to obtain aerosol extinction profiles from 15 to 37 km. As an integral part of this thesis, these profiles were validated using SAGE II aerosol extinction measurements. The result shows that the lower atmosphere of Durban is predominantly loaded with aerosols from biomass and sugar-cane burning and the presence of inversion layers in the troposphere (Cosijn and Tyson, 1996) which trap the aerosols and prevent their vertical dispersion.

The experimental investigations have also provided the researcher with opportunities to gain first-hand experience with the running, maintaining and reconditioning of the old and new LIDAR system. Some of this expertise has been conveyed to Natal 2nd year engineering students through demonstrations and training as part of their B.Sc. engineering degree and also to visiting honours and masters students from Reunion Island. This doctoral thesis represents the culmination of efforts in observing the atmosphere

above Durban at night time with the LIDAR system over extended periods of 4-6 hours and thereafter analysing and synthesising the resultant data. One of the shortcomings of this research was the scarcity of comparative LIDAR observational data in the latitude belt around 30 ^{0}S in the Southern Hemisphere.

In conclusion, it should be mentioned that as a result of the successful operation of the LIDAR (high and low altitude channels), our Reunion Island partners have now installed in Durban a more powerful laser system: 6.5 W, 30 Hz Spectra Physics Neodemium:Yttrium Aluminium Garnet (Nd:YAG) laser. They also seriously envisage expanding the system with 4 extra channels of acquisition. This Franco-South African cooperation will no doubt upgrade the Durban LIDAR system to world standards in terms of acquisitions of temperature and relative density for the lower and upper atmosphere, aerosols and ozone in the lower atmosphere.

References

Ackerman M., C. Brogniez, B. S. Diallo , G. Fiocco, P. Gobbi, M. Herman, M. Jager, J. Lenoble, C. Lippens, G. Megie, J. Pelon, R. Reiter, and R. Santer, European validation of SAGE II aerosol profiles, *J.* Geophys. Res. **94**, 8399 (1989).

Allain J. Y., High Energy Pulsed dye Lasers For Atmospheric Sounding, *A*ppl. Opt. **18**, 289 (1979).

Aoki Y. and M. Suzuki Image Property Of Gas Lens, *IEEE Trans. on microwave theory and Technique.* **15**, 2 (1967).

Balin Yu S., V. V. Burkov, I. V. Znamenskii, V. E. Zuev, V. I. Efimkin, V. S. Il'ichevskii, V. E. Mel'nikov, I. V. Samokhvalov, V. N. Sobolev, and A. A. Tikhominov AbstractsXV International Laser Radar Conference, Tomsk, USSR (1990).

Barnett J. J. The mean meridional temperature behaviour of the stratosphere from November 1970 to November 1971 derived from measurements by the Selective Chopper Radiometer on Nimbus IV, *Q. J. R. Met. Soc.* **100**, 505 (1974).

Barnett J. J., Satellite measurements of middle atmosphere temperature structure, *Phil. Trans. R. Soc. Lond.* **A 296**, 41 (1980).

Barnett J. J., and M. Corney, Middle atmosphere reference model derived from satellite data, *Handbook for Map* **16**, editors K. Labitzke, J. Barnett, B. Edwards, Urbana, IL, 47 (1985).

Barteneva O. D., Temperature profiles on Stratospheric Aerosol, *Bull. Acad. Sci. USSR* **1**, 852 (1960).

Beer T., Atmospheric Waves, *Adam Hilger Ltd*, Bristol (1975).

Bejan A., Convection Heat Transfer, *John Wiley and Sons*, New York (1984).

Bencherif H., Observations de l'activite dynamique dans la moyenne atmosphere, par sondage LIDAR, au-dessus du site de l'ile de la Reunion, Ph.D. thesis, University of Paris 6, Jussieu, 1996.

Berreman D. W., A lens or light guide using convectively distorted thermal gradients in gases, *Bell Syst. Tech J.* **43**, 1469 (1964).

Born M. and E. Wolf, Electromagnetic Theory Interference and Diffraction of Light, *Principles of optics*, Pergamon, New York, 1965.

Bretherton F. P., Waves and turbulance in stably stratified fluids, *Radio Sci.* **4**, 1279 (1969).

Buccellato R., P. F. Cunningham, M. M. Michaelis, and A. Prause, Comparative electron density measurements for the refractive fringe diagnostic and Nomarski interferometry, *Las. and Par. Beams* **10,**, 697 (1992).

Buccellato R., N. Lisi and, M. M. Michaelis, Colliding Shock Lens, *Opt. Comm.* **101**, 350 (1993b).

Carswell A.I., Lidar measurement of atmosphere, *Can. J. Phys.* **61**, 378 (1983).

Cazalet R. S., P. F. Cunningham, M. M. Michaelis, M. Notcutt, and J. A. Waltham, Demonstration of optical phase conjugation by stimulated Brillouin scattering using a gas lens, *Meas. Sci. Tech.* **1**, 147 (1990).

Chazette P., C. David, J. Lefrere, S. Godin, J. Pelon, and G. Megie, Comparative lidar Study of the optical geometrical and dynamic properties of stratospheric post volcanic aerosols, folowing the eruptions of El Chichon and Mount Pinatubo, *J. Geophys. Res.* **100**, 23195 (1995).

Chu W. P., M. P. McCormick, J. Lenoble, C. Brogniez and P. J. Pruvost, SAGE II Inversion Algorithm, *Geophys. Res.* **94**, 8339 (1989).

Collis R. T. H., and P. B. Russell, *Laser Monitoring of the atmosphere: Topics in Applied Physics*, **14** , 71-151, Springer-Verlag, Berlin, FRG, 1976.

Cosijn C. and P. D. Tyson, Stable discontinuities in the atmosphere over South Africa, *S. Afr. Geogr. J.* **92**, 381 (1996).

Deirmendjian D., Notes on Laser Detection Of Atmospheric Dust Layers, *J. Geophys. Res.* **70**, 743 (1965).

Deshler T. B., B. J. Johnson, and W. R. Rozier, Balloonborne measurements of Pinatubo aerosol during 1991 and 1992 at 41 N: Vertical profiles, size distribution, and volatility, *Geophys. Res. Lett.* **20**, 1435 (1993).

Dewan E. M. and R. E. Good, Saturation and the "universal" spectrum for vertical profiles of horizontal scalar winds in the Atmosphere, *J. Geophys. Res.* **91**, 2742 (1986).

Elterman L., The measurement of stratospheric density distribution with the searchlight technique, *J. Geophys. Res.* **56**, 509 (1951).

Elterman L., A series of stratospheric temperature profiles obtained with the searchlight technique, *J. Geophys. Res.* **58**, 519 (1953).

Ernst J. A., SMS-1 night-time infra-red imagery of low-level mountain waves, *Mon. Wea. Rev.* **104**, 207 (1976).

European Space Agency, Bulletin **106** (2001).

Fenn R. W., Correlation between Atmospheric Backscattering and Meteorological Visual Range, *Appl. Opt.* **5**, 293 (1966).

Fiocco G. and G. Grams, Observations of the Aerosol Layer at 20 km by Optical Radar, *J. Atmos. Sc.* **21**, 323 (1964).

Fiocco G. and G. Colombo, Optical Radar Results and Meteoric Fragmentation, *J. Geophys. Res.* **69**, 1795 (1964).

Fiocco G. and L. D. Smullin, Detection of Scattering Layers in the Upper Atmosphere (60-140 km) by Optical Radar, *Nature* **199**, 1275 (1963).

Fleming E. L., S. Chandra, M. R. Schoeberl, and J. J. Barnett, Monthly mean global climatology of temperature, wind geopotential height, and pressure for 0-120 km, *NASA TM-100697*, NASA Scientific and technical information facility, Linthicum, MD 21240 (1985).

Fredriksson K., B. Galle, K. Nystrom, and S. Svanberg, Mobile lidar system for environmental probing, *Appl. Opt.* **24**, 4181 (1981).

Friedland S. S., J. Katzenstein, and M. M. Zatzick, Pulsed Searchlighting the Atmosphere, *J. Geophys. Res.* **61**, 415 (1956).

Fritts D. C., Gravity Wave Saturation in the Middle Atmosphere: A new review of theory and observation, *Rev. Geophys. and Space Phys.* **22**, 275 (1984).

Gaubau G., Optical Relations for Coherent Wave Beams in Electromagnetic Theory and Antennas, E. C. Jordan, Ed. Pergamon, New York, 907, (1963).

Gloge D., Deformation of gas lenses by gravity, *Bell Syst. Techn. J.* **46**, 357 (1967).

Hake R.D., Jr., D. E. Arnold, D. W. Jackson, W. E. Evans, B. P. Ficklin and R. A. Long, Dye Laser Observation at Nighttime Atomic Sodium Layer, *J. Geophys. Res.* **77**, 6839 (1972).

Handbook of Geophysics and Space Environments, edited by Valley S.L., *McGraw-Hill Book Company*, 7 (1965).

Hardesty R. H., R. J. Keeler, M. J. Post, and R. A. Richter, Returns from calibrated targets and aerosol, *Appl. Opt.* **20**, 3763 (1981).

Harwood R. S., The temperature structure of the Southern Hemisphere stratosphere, August-October 1971, *Q. J. R. Met. Soc.* **101**, 75 (1975).

Hauchecorne A. and M. L. Chanin, Density and Temperature Profiles Obtained by LIDAR Systems between 35 and 70 km, *Geophys. Res. Let.* **7**, 565 (1980).

Hauchecorne A. and M. L. Chanin, A mid-latitude ground-based LIDAR study of stratospheric warmings and planetary wave propagation, *J. Atmos. Terr. Phys.* **44**, 577 (1982).

Hauchecorne A., M. L. Chanin, P. Keckhut and D. Nedeljkovic, LIDAR monitoring of the temperature in the middle and lower atmosphere, *Appl. Phys.* **B55**, 29 (1992).

Haurwitz B., The perturbation equations in meteorology, in "Compendium of Meteorology", *Am. Metereo. Soc.*, Boston, Mass. (1951).

Hirono M., M. Fujiwara, O. Uchino and T. Itabe, Observation Of Stratospheric Aerosol Layers by Optical Radar, *Can J. Chem,* **52**, 1560 (1974).

Hirota I., Equatorial Waves in the Upper Stratosphere and Mesosphere in Relation to the Semiannual Oscillation of the Zonal Wind, *J. Atmos. Sci.,* **35**, 714 (1978).

Hofmann D. J. and J. M. Rosen, On the background stratospheric aerosol layer, *J. Geophys. Res.* **38**, 168 (1981).

Hulburt E. O., Observations of a searchlight beam to an altitude of 28 km, *J. Opt. Soc. Amer.* **27**, 337 (1937).

Iga K. and Y. Suematsu, Experimental Studies on the Limitation of Focusing Power of Hyperbolic-Type Gas Lens, *Jap. J. Appl. Phys* **8**, 255 (1969).

Iwasaka Y. and K. Isono, Lidar Observation Of The Stratosphere Aerosol, *J. Atmos. Terr. Phys.* **39**, 117 (1977).

Jager H. and D. J. Hofmann, Mid-latitude lidar backscatter to mass, area and extinction conversion model based on in situ aerosol measurements from 1980 to 1987, *Appl. Opt.* **30**, 127 (1991).

Jenkins D. B., D. P. Wareing, L. Thomas and G. Vaughan, Upper stratospheric and mesospheric temperatures derived from LIDAR observations at Aberystwyth, *J. Atmos. Terr. Phys.* **59**, 287 (1987).

Johnson E. A., R. C. Meyer, R. E. Hopkins and W. H. Mock, Temperature profile obtain from a lidar system, *J. Opt. Soc. Amer.* **29**, 512 (1939).

Junge C. E. and J. E. Manson, Stratospheric Aerosol Studies, *J. Geophys. Res.* **66**, 2163 (1961).

Junge C. E., C. W. Chagnon, and J. E. Manson, Stratospheric Aerosols, *J. Met.* **18**, 81 (1961).

Junge C. E., Sulphur in the Atmosphere, *J. Geophys. Res.* **68**, 3975 (1963).

Justice C. O., J. D. Kendall, P. R. Dowty, and R. J. Scholes, Establishment of a lidar system, *J. Geophys. Res.* **101** 23851 (1996).

Kaiser P., Measured Beam Deformations in a Guide made of Tubular Gas Lenses, *Bell Syst. Techn. J.* **47**, 179 (1968).

Keckhut P., M. L. Chanin and A. Hauchecorne, Stratosphere temperature measurement using Raman LIDAR, *Appl. Opt.* **29**, 5182 (1990)

Keckhut P. and A. Hauchecorne, A critical review on the data base aquired for a long term surveillance of the middle atmosphere by French Rayleigh Lidars, *J. Atmos. Oceanic Technol.* **10**, 850 (1993).

Kent G.S., B. R. Clemesha and R. W. Wright, High altitude atmospheric scattering of light from a laser beam, *J. Atmos. Terr. Phys.* **29**, 169 (1967).

Kent G.P and W. H. Wright, A review of laser radar measurements of atmospheric properties, *J. Atmos. Terr. Phys.* **32**, 917 (1970).

Kent G. S., C. R. Trepte, K. M. Skeens and D. M. Winker, LITE and SAGE II measurements of aerosols in the Southern Hemisphere upper troposphere, *J. Geophys. Res.* **103**, 19111 (1998).

Klett J.D., Stable analytical inversion solution for processing lidar returns, *Appl. Opt.* **20**, 211 (1981).

Klett J.D., Lidar inversion with variable backscatter/extinction ratios, *Appl. Opt.* **24**, 1 (1985).

Klostermeyer J. and Ruester, Radar Observation and Model Computation of a Jet Stream Generated Kelvin-Helmholtz Instability, *J. Geophys. Res.* **85**, 2841 (1980).

Kogelnik H. and T. Li, Laser beams and resonators, *Appl. Opt.* **5**, 1550 (1966).

Kuppen M., The establishment of a ground-based Lidar system, M.Sc. thesis, Universty of Natal, 1992.

Kuppen M., On the interaction of the Laser beams with Air with specific references to refraction and scattering, Ph.D. thesis, University of Natal, 1996.

Labitzke K., Climatology of the stratosphere and mesosphere, *Phil. Trans. R. Soc. Lond.* **A 296**, 7 (1980).

Labitzke K., Stratospheric Mesospheric Midwinter Disturbances, *J. Geophys. Res.* **86**, 9665 (1981).

LeBlond P. H. and L. A. Mysak, Waves in the Ocean, *Elsevier Scientific Publishing Company*, Amsterdam (1980).

Lefrere J. and C. Pelon Survey of the post Mt. St.Helens stratospheric aerosol at Haute-Provence Obsevatory, *App. Opt.* **7**, A70 (1981).

Leovy C. and P. J. Webster Stratospheric Lond Waves: Comparison of Thermal Structurein the Northern and Southern Hemispheres, *J.Atmos.Sci.* **33**, 1624 (1976).

Lisi N., R. Buccelato and M. M. Michaelis, Optical quality and temperature profile of a spinning pipe gas lens, *Opt. Laser. Tech.* **26**, 25 (1994).

Lutz H., E. Armandillo and, B. Battrick, ESA Laser Sounding from Space Report of the European Space Agency Technology Working Group on Space Laser Sounding and Ranging, *ESA* **SP-1108**, 1 (1989).

Maiman T.H., Stimulated Optical Radiation in Ruby, *Nature* **187**, 493 (1960).

Marcuse D., Antennas and Propagation, Theory of a thermal gradient gas lens, *IEEE Trans in Microwave Theory and Technique* **13**, 734 (1965).

Marcuse D., Light Transmission Optics, van Nostrand Reinhold, New York, 2nd edition (1982).

Marenco F., A. diSarra, M. Cacciani, G. Fiocco and, D. Fua, Thermal structure of the winter middle atmosphere observed by LIDAR at Thule, Greenland, during 1993-1994, *J. Atm. Sol. Terr. Phys.* **59**, 2151 (1997).

Martynenko O. G. and N. I. Lemesh, Light Guides with Thermohydrodynamic Gas Lenses, *Il Nuovo Cimento* **5D**, 225 (1985).

McClatchey R. A., J. E. Fenn, A. Selby, F. E. Volz, and J. S. Garing, Optical Properties of the Atmosphere *Air Force Cambridge Research Laboratories* **71-0279** (1971).

McClung F. J. and Hellwarth R. W., Giant Optical Pulsations from Ruby, *J. Appl. Phys.* **33**, 828 (1962).

McMaster L. R., Stratospheric aerosol and gas experiment (SAGE II), paper presented at Sixth Conference on Atmospheric Radiation, *Am. Meteorol. Soc.*, Williamsburg, Va. (1986).

Measures R. M., Laser Remote Sensing Fundamentals and Applications, John Wiley and Sons (1984).

Michaelis M. M., M. Notcutt, and P. F. Cunningham, Drilling Gas Lens Focused Laser, *Opt. Comm.*, **59**, 369 (1986).

Michaelis M. M.,P. F. Cunningham, R. S. Cazalet, J. A. Waltham, and M. Notcutt, Gas lens Application, *Las. Par. Beams* **9**, 442 (1991a).

Michaelis M. M., C. A. Dempers, M. Kosch, A. Prause, M. Notcutt, P. F. Cunningham, and J. A. Waltham, A gas-lens telescope, *Nature* **353**, 547 (1991b).

Naito K., Internal gravity shear waves in the troposphere, *Can. J. Phys.* **44**, 2259 (1966).

NASA Laser Atmospheric Wind Sounder (LAWS) Instrument Panel Report, NASA, *TM86129* **11g** (1987).

Naujokat B., K. Labitzke, R. Lenshow, B. Rajewski, M. Wiesner, and R. C. Wohlfahrt, The stratospheric winter 1994/95: A cold winter with a strong minor warming, *Beilage zur Berliner Wetterkarte* **81**, Institut fur Meteorologie der Freien Universitat Berlin (1995).

Northam G. B., J. M. Rosen, S. H. Melfi, T. J. Pepin, M. P. McCormick , D. J. Hofmann, and W. H. Fuller, Jr., Dustsonde and lidar measurements of stratospheric aerosols: a comparison, *Appl. Opt.* **13**, 2416 (1974).

Notcutt M., M. M. Michaelis, P. F. Cunnningam and J. A. Waltham, Spinning pipe gas lens *Opt. Las. Tech.* **20**, 243 (1988).

Oort A. H., Global atmospheric circulation statistics 1958-1983, *NOAA Professional paper* **14**, National Oceanic and Atmospheric Administration, 180 (1983).

Osborn M. T., J. M. Rosen, M. P. McCormick, P. H. Wang, J. M. Livingston, and T. J. Swissler, Sage II Aerosol Correlative Observations: Profile Measurements, *J. Geophys. Res.* **94**, 8353 (1989).

Otis G. and R. Tremblay, Lensing effect in helical TEC lasers, *Can. J. Phys.* **52**, 257 (1974).

Parameswaran K., K. O. Rose, B. V. Krishna Murthy, M. T. Osborn, and L. R. McMaster, Comparison of aerosol extinction profiles from LIDAR and SAGE II data at a tropical station, *J. Geophys. Res.* **96**, 10861 (1991).

Pelon J., Distribution verticale de l'ozone dans la troposphere et la stratosphere: Etude experimentale par teledetection laser et application aux echanges troposphere-stratosphere, Ph.D. thesis, University of Paris 6 Jussieu, 1985.

Phipps C. R., G. Albrecht, H. Friedman, D. Gavel, E. V. George, J. Murray, C. Ho, W. Priedhorsky, M. M. Michaelis and J. P. Reilly, ORION: Clearing near-Earth space debris using a 20 kW, 530 nm, Earth-based, repetitively-pulsed laser, *Las. Par.Beams* **14**, 1 (1996).

Pillay Y., R. D. Diab, and F. Sokolic, Ozone maxima off the east coast of South African: the role of biomass burning, *S. Afr. J. Sci.* **91**, 609 (1995).

Preston-Whyte R. A. and P. D. Tyson, The atmosphere and weather of Southern Africa, *Oxford University Press*, Cape Town (1997).

Ridenour L. N., Radiation laboratory series, Radar System Engineering, *McGraw-Hill*, New York (1947).

Rosen J.M., Vertical Distribution of Dust to 30 Km, *J. Geophys. Res.* **69**, 4673 (1961).

Russell P. B., J. Swissler, and M. P. McCormick, Methodology for error analysis and simulation of LIDAR aerosol measurements, *Appl. Opt.* **18**, 3783 (1979).

Schoeberl M. R., Stratospheric warmings: observations and theory, *Geophys. Space Phys.* **16**, 521 (1978).

Schwiesow R. L. and L. Lading, Temperature Profiling By Rayleigh Scattering, *Appl. Opt.* **20**, 1972 (1981).

Sidi C., J. Lefrere, F. Dalaudier, and J. Barat An improved Atmospheric bouyancy wave spectrum model, *J. Geophys. Res.* **93**, 774 (1988).

Siegert A. J., L. N. Ridenour, and M. H. Johnson, Radar System Engineering, *Boston Technology Lithography*, Massachusetts (1963).

Smith S. A., D. C. Fritts, and T. E. VanZandt, Evidence for a saturated spectrum of atmospheric gravity waves, *J. Atmos. Sci.* **44**, 1404 (1987).

Stolarski R. S., P. Bloomfield, R. D. McPeters, and J. R. Herman, Total ozone trends deduced from Nimbus-7 TOMS data, *Geophys. Res. Lett.* **18**, 1015 (1991).

Souprayen C., Climatologie des ondes de gravite dans l'atmosphere moyenne: contribution a leur parametrisation dans les modeles numeriques, Ph.D. thesis, University of Paris-6 Jussieu, 1993.

Spinhurne J. D., M. Z. Hansen, and L. O. Cauhil, Cloud top remote sensing by airbone LIDAR, *Appl. Opt.* **21**, 1564 (1982).

Steier W.H., Measurements on a Thermal Gradient Gas Lens, *IEEE Trans.* **MTT-13**, 740 (1965).

Stolarski R.S., Total ozone trends deduced from Nimburst Toms data, *Geophys. Res. Let.* **18**, 1015 (1991).

Synge E.H., A method of investigating the higher atmosphere, *Phil. Mag.* **9**, 1014 (1930).

Thomas L., D. B. Jenkins, D. P. Wareing, G. Vaughan, and M. Farrington, Lidar observation of stratosheric aerosols associated with the El Chichon eruption, *Ann. Geophys.* **5**, 47 (1987).

Twomey S. and H. B. Howell, The Relative Merit of White and Monochromatic Light for the Determination of Visibility by Backscattering Measurements, *Appl. Opt.* **4**, 501 (1965).

Van de Hulst H.C., Light scattering by small particles, *John Wiley and Sons*, New York (1957).

Waltham J. A., P. F. Cunningham, M. Notcutt, and M. M. Michaelis, Ion flow charecteristics from laser-produced plasmas, *J. Phys.* **22**, 766 (1989).

Weinman J. A., Effects Of Multiple Scattering On Light Pulses Reflected By Turbid Atmospheres, *J. Atmos. Sci.* **33**, 1763 (1976).

Whiteway J. A. and A. I. Carswell, Rayleigh Lidar Observation of Thermal Structure and Gravity Wave Activity in the High Arctic during a Stratospheric Warming, *J. Atmos. sci.* **51**, 21 (1994).

Wilson R., A. Hauchecorne and M. L. Chanin, Gravity Spectra in the Middle Atmosphere As observed by Rayleigh Lidar, *Geophys. Res. Let.* **17**, 1585 (1990).

Wilson R., A. Hauchecorne and M. L. Chanin, Gravity waves in the middle atmosphere observed by Rayleigh LIDAR *J. Geophys. Res.,* **96-D3**, 5153 (1991).

Winker D. M., R. H. Couch and M. P. McCormick, An overview of LITE: NASA's Lidar In-space Technology Experiment, *Proc. IEEE* **84**, 164 (1996).

World Meteorological Organisation, International ozone assessment, World Meteorological Organisation, Global Ozone research and monitoring project, *report* **20**, Washington D.C., U.S.A. (1989).

World Meteorological Organisation, Scientific assessment of ozone depletion, World Meteorological Organisation, Global Ozone Research and Monitoring Project, *report* **25**, Geneva, Switzerland (1991).

Wulfmeyer V., A. Brewer, A. Weickmann, R. Richter, J. Vanandel, J. Howell, C. Grund, M. Hardesty, and P. Hildebrand NCAR NOAA high-resolutin Doppler LIDAR for wind measurements and its potential for water-vapour differential absorption LIDAR, *Book of Abstracts* **2**, Fourth International Symposium on Tropospheric Profiling, Snowmass, Colorado, U.S.A., 341 (1998).

Appendix A

Fortran Programme for Determining Extinction Coefficients

A.1 Introduction

This programme calculates the extinction coefficients for the old LIDAR in the altitude range needed using the Klett inversion method. It requires three inputs:

(1) The raw data,

(2) The lower altitude limit and,

(3) The upper altitude limit.

A.2 Source code

```
C ************************************************************
C
C     Program KlettInversion
C     Language: Fortran
```

```
C     Function: To calculate the extinction coefficients
C               in the altitude range 20 km-30 km
C
C
C
C ************************************************************
C
      Program Klett_Inv
C
      Parameter (n=667)
      Real Alt(n),count(n),height(n),den(n),sig(n),diff(n)
      Real sigdiff(n),lvalue(n),integrand(n),sigma(n),num(n)
      Real r0,rm,h,hei,lsig
      External lsig
      Integer m,l,i,j,k
C
      write(6,*) ' LIDAR EXTINCTION COEFFICIENTS'
      Open(10,File='')
      Do 10 i=1,n
       read(10,*) Alt(i),count(i)
10    continue
      write(6,*)' Enter the lower limit of the altitude in km'
      read(5,*) r0
      If(r0.lt.20. .or. r0.gt.30.) then
       write(6,*)' Error in lower limit'
      Else
       Do 20 i=1,n
```

```
        diff(i)=Alt(i)-r0
        If (diff(i).le.0.05) then
          h=Alt(i)
          k=i
        end if
20      continue
        i=k
      End if
C
30    write(6,*)' Enter the upper limit of the altitude in km'
      read(5,*) rm
      If(rm.lt.20. .or. rm.gt.30.)then
       write(6,*)' Error in the upper limit of the altitude'
      Else
       do 40 j=1,n
        diff(j)=Alt(j)-rm
        If(diff(j).le.0.05) then
          hei=Alt(j)
          m=j
        end if
40      continue
        j=m
      End if
C
      Do 50 l=i,j
       sig(l)=count(l)
       height(l)=Alt(l)
```

```
50    continue
C
      Do 60 l=i,j
       lvalue(l) = lsig(height(l),sig(l))
60    continue
C
      Do 70 l=i,j
       sigdiff(l)=Exp(lvalue(l)-lvalue(j))
70    continue
C     Evaluation of integrand
      Do 90 l=i,j
        Integrand(l) = 0
        Do 80 m = l,j
          Integrand(l)=Integrand(l)+0.15*sigdiff(m)
80      continue
90    continue
C     Evaluation of denominator
      Do 100 l=i,j
       den(l)=1.0+2.0*Integrand(l)
100   continue
C     Evaluation of numerator
      Do 110 l=i,j
       num(l)=sigdiff(l)
110   continue
C     Evaluation of attenuation coefficients
      Do 120 l=i,j
       sigma(l)=num(l)/den(l)
```

```
120   continue
C
      Do 130 l=i,j
       write(6,*)' Attenuation coefficients for the range are',sigma(l)
130   continue
C
      Close(unit=10)
      End
C     Converting lidar data to a logarithmic variable
C
      Real Function lsig(r,s)
      Real r,s
        lsig=log(r**2*s)
      Return
      end
```

Appendix B

Programme listing of LIDARtemp.m

B.1 Introduction

This MATLAB programme calculates the temperature, relative denstity, Mie-scattering ratio and the extinction coefficients due to aerosols from the new LIDAR raw data.

B.2 Source code

```
disp('************************************************');
disp('           MAIN PROGRAMME for the retrieval of   ');
disp(' TEMPERATURE, PRESSURE AND RELATIVE DENSITY      ');
disp('              from the Rayleigh LIDAR signal     ');
disp('************************************************');

clear all

%Treatment for the lower and upper atmosphere channels A
```

```
%and B

an=menu('Choice of the year','1. 1999','2. 2000');
if an == 1
    vb=questdlg('Only channel A can be treated');
end
nbv = menu('No of channels','1. RAYLEIGH A',...
'2. RAYLEIGH A/B(Both channels)','3. VOIE B');
nbc = menu('No of bins','1. 512','2. 1024');
B_S = menu('Noise/signal ratio','1.10%','2.15%',...
'3.20%','4.25%','5.30%');
cm = menu('Choice of climatological model',
'1. CIRA-86','2. ECMWF',
'3. Superposition of the two models');

if nbc == 1
   ind = 1;
   ncan = 512;   % No of bins
   Dz    = .300; % Vertical resolution in km
   nmax = 334;   % Maximum altitude attained 100.2 km
else
   ind = 0;
   ncan = 1024;  % No of bins
   Dz = .150;    % Vertical resolution in km
   nmax = 667;   % Maximum altitude attained 100.05 km
end
```

```
%--------READING of the raw LIDAR data------------

if (an == 1) & (nbv ==1)
   [date,month,sig1,sig2,noofshots,starting_time,...,
finishing_time] = journalier(ind);
else

     ButtonName=questdlg('Which channels do you
want to treat?', ...
                         'Genie Question', ...
                         'Channel A','Channel A/B',
'Channel B');

           switch ButtonName,
            case 'Channel A',
               graff = 1;
   [date,month,sig1,sig2,noofshots] = journalier1(ind);

       case 'Channel A/B',
        graff = 1;
   [date,month,sig1,sig2,noofshots] = journalier2(ind);

       case 'Channel B',
        graff = 1;
   [date,month,sig1,sig2,noofshots] = journalier3(ind);

     end % switch
  end
```

```
if cm ==1
   model='CIRA-86';
end
if cm==2
   model='ECMWF';
end

%-----------------------------------------------------

zsite = .100;  % Altitude of Durban above sea level
kb = 1.380662e-23; % Boltzman constant (J/K)
alt = zsite+[0:Dz:(ncan-1)*Dz]; %LIDAR altitude vector(in km)

% LOADING of altitude, temperature, density and
%       pressure from CIRA86-model

clim  = cira(month,Dz);% Reading of data from the
%CIRA-1986 model

Zclim = clim(:,1);    % Altitude

Tclim = clim(:,2);    % Temperature (K)

Dclim = clim(:,3);    % Concentration of air
%molecules (molec./m3)


Pclim = clim(:,4); % Pressure (hPascal)

nclim = length(Zclim);    % Dimension of the model
```

```
load ozone.run; zo = ozone(:,1);
o3 = ozone(:,2);%Loading of ozone data

Oclim = interp1(zo,o3,alt(2:334));
 % Interpolation of ozone data(molec./m3)

graf = 0;      % Plotting of graphs from
%  the CIRA-86 model data
if (graf == 1)
figure;
subplot 141
fin=length(Zclim);
plot(Tclim,Zclim)
title('Temperature(K)')
axis([160 280 0 100])
subplot 142
plot(Oclim,Zclim(2:fin))
title('Ozone')
subplot 143
semilogx(Dclim,Zclim)
title('Density')
subplot 144
plot(Pclim(33:nclim),Zclim(33:nclim))
title('Pressure')
end
```

```
%-------------------------------------------------------------------------
%_____________________LOADING of ECMWF data_____________________________

[P1,P,T1,T2,Pecm,Tecm,Decm,necm,njour]=ecmwf(date,Pclim,...,
Tclim,nclim,zsite,Dz);
graff = 0; % Plotting of ECMWF AND CIRA-86 data
if (graff == 1)
figure
plot(Tclim,Zclim,Tecm,Zclim,'--')
legend('CIRA','ECMWF')
title(strcat(date,': THEORETICAL TEMPERATURES'))
ylabel('Altitude(km)')
xlabel('Temperature(K)')
grid
figure
plot(log(P),Zclim)
grid

end

%---LOADING of radiosonde temperatures from the SAWS---
date = strcat(date(1:2),date(4:5),date(7:8));
index = 0;
if index == 1
   clim3 = functio2(date,Dz);
 %Reading of radiosonde data
```

```
   Zclim3 = clim3(:,1); % Altitude(km)

   Tclim3 = clim3(:,2); % Temperature(K)
end
%-------------------------------------------------------

%--------------- LOADING of ECMWF data--

extract3;  % Reading of ECMWF data

%_________CORRECTIONS made on the LIDAR signal__

%-----------SKY NOISE-------------------------------
%      (The corrected signal = sigc1 or sigc2)

disp(' ');
disp('----------------------');
disp('Calculation of the sky noise');
if B_S == 1
   b_s = 10.0/100.0;
end
if B_S == 2
   b_s = 15.0/100.0;
end
if B_S == 3
   b_s = 20.0/100.0;
end
if B_S == 4
```

```
   b_s = 25.0/100.0;
end
if B_S == 5
   b_s = 30.0/100.0;
end
disp(['Ratio noise/signal :' blanks(1) num2str(b_s)]);

if (nbv == 1)|(nbv == 2)

   [Cztop1,Cfdc1,Csigc1,Cninf] = fdc4(sig1,ncan,Dclim,alt,...,
noofshots,nbv,nbc,0,b_s); % Correction of the signal from the
%  sky noise with respect to the CIRA-86 model

   Cnsup1 = fix((Cztop1-zsite)/Dz);

   [Eztop1,Efdc1,Esigc1,Eninf] = fdc4(sig1,ncan,Decm,alt,...,
nbtirs,nbv,nbc,0,b_s); % Correction of the signal from the
%                sky noise with respect to the ECMWF model
   Ensup1=fix((Eztop1-zsite)/Dz);

end
if (nbv == 3)|(nbv == 2)

   [Cztop2,Cfdc2,Csigc2] = fdc(sig2,ncan,Dclim,alt,...,
nbtirs,nbv,nbc,1,b_s); %Correction of the signal from the sky noise
   Cnsup2 = fix((Cztop2-zsite)/Dz);
   [Eztop2,Efdc2,Esigc2] = fdc4(sig2,ncan,Decm,alt,...,
nbtirs,nbv,nbc,1,b_s); % Correction of the signal from the sky noise
```

```
end

%-----------------------------------------------------

if cm == 1
 if (nbv == 1)
   figure; %Plotting of the LIDAR raw data signal
   semilogx(sig1,alt,Cfdc1,alt,'--',Csigc1,alt)
   grid on
   legend('Signal','noise','signal - noise')

   titre = strcat('LIDAR raw data for the night of',date);
   axis([1E-5 200 0 120])
   xlabel('Number of photons (/per shot/microsec)')

   ylabel('Altitude (km)')

 end

 if (nbv == 2)

   figure;
   semilogx(sig1,alt,Cfdc1,alt,'--',Csigc1,alt,...,
sig2,alt,Cfdc2,alt,'--',Csigc2,alt)
   legend('sig1','fdc1','sig1 - fdc1','sig2',...,
'fdc2','sig2 - fdc2')
   axis([1E-6 200 0 120])
   xlabel('No of photons (/shot/microsec)')
   ylabel('Altitude (km)')
```

```
 end

 if (nbv == 3)

   figure;
   semilogx(sig2,alt,Cfdc2,alt,'--',Csigc2,alt)
   legend('sig2','fdc2','sig2 - fdc2')
   axis([1E-6 200 0 120])
   grid;
   xlabel('No of photons (/shot/microsec)')
   ylabel('Altitude (km)')

 end
end
if cm == 2
 if (nbv == 1)
   figure;
   semilogx(sig1,alt,Efdc1,alt,'--',Esigc1,alt)
   grid on
   legend('sig1','fdc1','sig1 - fdc1')
   title('Raw data for the night of',date);
   axis([1E-5 200 0 120])
   xlabel('No of photons (/shot/ microsec)')
   ylabel('Altitude (km)')

 end
```

```
 if (nbv == 2)

   figure;
   semilogx(sig1,alt,Efdc1,alt,'--',Esigc1,alt,...,
sig2,alt,Efdc2,alt,'--',Esigc2,alt)
   legend('sig1','fdc1','sig1 - fdc1','sig2',...,
'fdc2','sig2 - fdc2')
  axis([1E-6 200 0 120])
  xlabel('nbr of photons (/shot/microsec')
   ylabel('Altitude (km)')

 end

 if (nbv == 3)

   figure;
   semilogx(sig2,alt,Efdc2,alt,'--',Esigc2,alt)
   legend('sig2','fdc2','sig2 - fdc2')
   axis([1E-6 200 0 120])
   grid;
   xlabel('No of photons (/shot/microsec)')
   ylabel('Altitude (km)')

 end
end


%--CORRECTION of the signal from the non-
```

```
%            linearity of the photomultiplier----

disp('----------------------');
disp('Elctronic shutters applied at:60 microsec');
disp('----------------------');
disp('Correction of the signal due to')
disp('non-linearity of the photomultiplier');

if (nbv == 1)|(nbv == 2)
    for i = 1:length(alt)
       if Csigc1(i+1)-Csigc1(i) < 0
          k = i;
       end
    end
   [Emax1,Ei1] = max(Esigc1(length(alt)));
%Ei1, index of the maximum of the vector Esigc1

   if nbc == 1

      depart = 30;
 %Electronic shutter at 60 microsec (9 km)

   else
       depart = 60;
   end

   if (Ci1 < depart)
      Ci1 = depart;
```

```
   end

   if (Ei1 < depart)
      Ei1 = depart;
   end

[Csgl1,Cs1_lin,Cdebut1] = lin(Csigc1,ncan,k);
 % Correction of non-linearity of the
% photomultiplier from channel A

[Esgl1,Es1_lin,Edebut1] = lin(Esigc1,ncan,Ei1);
% Correction of non-linearity of the
% photomultiplier from channel A

    if nbc == 1
       CAltDebutLin_A = Cdebut1*0.3+0.100;
 % Converting bins in km

       EAltDebutLin_A = Edebut1*0.3+0.100;
% Converting bins in km


    else
       CAltDebutLin_A = Cdebut1*0.15+0.100;
 % Converting bins in km

       EAltDebutLin_A = Edebut1*0.15+0.100;
 % Converting bins in km

    end
```

```
end
if (nbv == 2)|(nbv == 3)
   [Cmax2,Ci2] = max(Csigc2);
   [Csgl2,Cs2_lin,Cdebut2] = lin(Csigc2,ncan,Ci2);
 % Correction of non-linearity of the
% photomultiplier from channel B
   [Emax2,Ei2] = max(Esigc2);
   [Esgl2,Es2_lin,Edebut2] = lin(Esigc2,ncan,Ei2);
 % Correction of non-linearity of the
% photomultiplier from channel B

   CAltDebutLin_B = Cdebut2*0.3+0.1;
   Cdebut2;
   EAltDebutLin_B = Edebut2*0.3+0.1;
   Edebut2;

end
%------------------------

%___First combination of the signals of channels A and B
%___before correcting for the atmospheric transmission.
%   The combined signal is used for the Klett inversion to
%___obtain the extinction coefficients for the new LIDAR.

if (nbv == 2)
   [Caltracinfk,Caltracsupk] = altrac2(alt,Csigc1,Csigc2,...,
```

```
Cfdc2,ncan,Cdebut1);
   [Csklett,Csklett_lin] = raccord_mod(Csgl1,Csgl2,ncan,...,
Cdebut2,ncan,Caltracinfk,Caltracsupk,Cs1_lin,Cs2_lin);
   [Ealtracinfk,Ealtracsupk] = altrac2(alt,Esigc1,Esigc2,...,
Efdc2,ncan,Edebut1);
   [Esklett,Esklett_lin] = raccord_mod(Esgl1,Esgl2,ncan,...,
Edebut2,ncan,Ealtracinfk,Ealtracsupk,Es1_lin,Es2_lin);

end

%--CALCULATION of the statistical error of the density---
%----The statistical error of the density is calculated
% ----from the signal which has not been corrected from the
% atmospheric transmission.

disp('----------------------');
disp('Calculation of the statistical error of the density');
if (nbv == 1)

Cerror_d = erreur_stat(alt,nbtirs,nbv,Csgl1,...,
Csgl1,Cfdc1,0,0,Cdebut1);
Eerror_d = erreur_stat(alt,nbtirs,nbv,Esgl1,Esgl1,...,
Efdc1,0,0,Edebut1);

end

if (nbv == 2)
   [Caltracinf,Caltracsup] = altrac2(alt,Csigc1,...,
```

```
Csigc2,Cfdc2,ncan,Cdebut1);
   Cerror_d = erreur_stat(alt,nbtirs,nbv,Csgl1,...,
Csgl2,Cfdc1,Caltracinf,Caltracsup,Cdebut2);
   [Ealtracinf,Ealtracsup] = altrac2(alt,Esigc1,...,
Esigc2,Efdc2,ncan,Edebut1);
   Eerror_d = erreur_stat(alt,nbtirs,nbv,Esgl1,...,
Esgl2,Efdc1,Ealtracinf,Ealtracsup,Edebut2);

end
if (nbv == 3)
   Cerror_d = erreur_stat(alt,nbtirs,nbv,Csgl2,...,
Csgl2,Cfdc2,0,0,Cdebut2);
   Eerror_d = erreur_stat(alt,nbtirs,nbv,Esgl2,...,
Esgl2,Efdc2,0,0,Edebut2);

end
%-- CORRECTION of the signal due to
% the transmission of the atmosphere---------

if (nbv == 1)|(nbv == 2)

[Csignal1,Csignal1_lin] = trans(alt,Csgl1,Cs1_lin,...,
Pclim,Cdebut1,Cnsup1);
[Esignal1,Esignal1_lin] = trans(alt,Esgl1,Es1_lin,...,
Pecm,Edebut1,Ensup1);

end
```

```
if (nbv == 3)

   [Csignal2,Csignal2_lin] = trans(alt,Csgl2,Cs2_lin,...,
Pclim,Cdebut2,Cnsup2);
   [Esignal2,Esignal2_lin] = trans(alt,Esgl2,Es2_lin,...,
Pecm,Edebut2,Ensup2);

end

if (nbv == 2)
   [Csignal2,Csignal2_lin] = trans(alt,Csgl2,Cs2_lin,...,
Pclim,Cdebut2,Cnsup1);
   [Esignal2,Esignal2_lin] = trans(alt,Esgl2,Es2_lin,...,
Pecm,Edebut2,Ensup1);

end
%Second combination of the signals from channel A and B
% correcting from the transmission ---------------

if (nbv == 1)
   Csg_lin = Csignal1_lin;  % for one channel
   Csignal=Csignal1;

   Caltninf=Cninf*0.3+0.10;
%Altitude at which the PMT is not saturated

   Esg_lin = Esignal1_lin;  % for one channel
```

```
   Esignal=Esignal1;

   Ealtninf=Eninf*0.3+0.10;
% Altitude at which the PMT is not saturated

end

if (nbv == 2)

   if (Caltracinf<=Cdebut2*0.3+0.10)
      disp('Problem to combine the signals')
      pause;
   end
   if (Ealtracinf<=Edebut2*0.3+0.10)
      disp('Problem to combine the signals')
      pause;
   end

   [Csignal,Csg_lin] = raccord_mod(Csignal1,Csignal2,ncan,...,
Cdebut2,Cnsup1,Caltracinf,Caltracsup,Csignal1_lin,Csignal2_lin);
   [Esignal,Esg_lin] = raccord_mod(Esignal1,Esignal2,ncan,...,
Edebut2,Ensup1,Ealtracinf,Ealtracsup,Esignal1_lin,Esignal2_lin);

%-------------------------------------------------------------

end
```

```
%---CALCULATIONS of the temperature, density and pressure
%    and their associated statistical errors ----------

if (nbv == 1)
   [Caltnorm,Ctempf,Cninff,Cnsupf,CD_statf,CPf,CPf_err,...,
Cpr_statN,Cpr_dlinN,CDf,CDf_lin,CDf_err,CTf_stat,...,
CTf_lin,CTf_mod,CTf_err,Cd_rel] = param_mod(nbc,Cdebut1,...,
Cnsup1,ncan,Csignal,Pclim,Dclim,Cerror_d,Csg_lin,nbv,alt);

  [Ealtnorm,Etempf,Eninff,Ensupf,ED_statf,EPf,EPf_err,...,
Epr_statN,Epr_dlinN,EDf,EDf_lin,EDf_err,ETf_stat,...,
ETf_lin,ETf_mod,ETf_err,Ed_rel] = param_mod(nbc,Edebut1,...,
Ensup1,ncan,Esignal,Pecm,Decm,Eerror_d,Esg_lin,nbv,alt);

end
if (nbv == 2)
   [Caltnorm,Ctempf,Cninff,Cnsupf,CD_statf,CPf,...,
CPf_err,Cpr_statN,Cpr_dlinN,CDf,CDf_lin,CDf_err,...,
CTf_stat,CTf_lin,CTf_mod,...,
CTf_err,Cd_rel] = param_mod(nbc,Cdebut2,...,
Cnsup1,ncan,Csignal,Pclim,Dclim,Cerror_d,Csg_lin,nbv,alt);

  [Ealtnorm,Etempf,Eninff,Ensupf,ED_statf,EPf,...,
EPf_err,Epr_statN,Epr_dlinN,EDf,EDf_lin,EDf_err,...,
ETf_stat,ETf_lin,ETf_mod,ETf_err,Ed_rel] = param_mod(nbc,...,
Edebut2,Ensup1,ncan,Esignal,Pecm,Decm,Eerror_d,Esg_lin,nbv,alt);
```

```
end

% Statistical errors on the density profiles

if (nbv == 1)|(nbv == 2)
   for k = Cninff:Cnsupf
      Cd_rel_err(k) = CDf_err(k)/Dclim(k);
      Cd_relplus(k) = Cd_rel(k) + Cd_rel_err(k);
      Cd_relmoins(k)= Cd_rel(k) - Cd_rel_err(k);
   end
   for k = Eninff:Ensupf
      Ed_rel_err(k) = EDf_err(k)/Decm(k);
      Ed_relplus(k) = Ed_rel(k) + Ed_rel_err(k);
      Ed_relmoins(k)= Ed_rel(k) - Ed_rel_err(k);
   end

end
%---KLETT INVERSION  as applied to the new LIDAR----
inversion=0;
if (inversion==0)
   disp('Klett inversion');
 if cm == 1

   if (nbv == 1)

   [Csrayleigh,CRaybeta,CRayalpha,CRayratio]=
rayleigh2(532*1e-9,Dclim,Cdebut1,alt);
```

```
   [ref,Crapdc,CNrapdc,CMiealpha] =
klett(Cdebut1,Csgl1,ncan,alt,300,...,
CRayalpha,CRaybeta,CRayratio);

      figure
      plot(Crapdc(Cdebut1:length(Crapdc)),...,
alt(Cdebut1:length(Crapdc)));
      Cdebut2 = length(Crapdc);
      axis([0.9 1.25 5 50])
      grid
      ylabel('Altitude (km)')
      xlabel('Mie scattering ratio')
      zref=num2str(ref);
      titr=strcat('The reference height at which'
'the atmosphere is assumed to be purely '
'molecular is taken at (with CIRA-86 as model) :',zref,' km');
      title(titr)
   end
   if (nbv == 2)

     [Csrayleigh,CRaybeta,CRayalpha,CRayratio] =
rayleigh2(532*1e-9,Dclim,Cdebut2,alt);

     [ref,Crapdc,CNrapdc] =
klett(Cdebut2,Csklett,ncan,alt,300,...,
CRayalpha,CRaybeta,CRayratio);
     figure
```

```
     plot(Crapdc(Cdebut2:length(Crapdc)),...,
alt(Cdebut2:length(Crapdc)));
     axis([0.9 1.25 5 50])
     grid
     ylabel('Altitude (km)')
     xlabel('Mie scattering ratio')
     zref=num2str(ref);
     titr=strcat('The reference height at which the'
'atmosphere is assumed to be purely molecular'
'is taken at (with CIRA-86 as model) :',zref,' km');
     title(titr)

  end
  if (nbv == 3)

     [Csrayleigh,CRaybeta,CRayalpha,CRayratio] =
rayleigh2(532*1e-9,...,
Dclim,Cdebut2,alt);
     [ref,Crapdc,CNrapdc] = klett (Cdebut2,Csgl2,ncan,alt,...,
300,CRayalpha,CRaybeta,CRayratio);
     figure
     plot(Crapdc(Cdebut2:length(Crapdc)),...,
alt(Cdebut2:length(Crapdc)));
     %debut2 = length(rapdc);
     axis([0.9 1.25 5 50])
     grid;
```

```
     ylabel('Altitude (km)')
     xlabel('Mie scattering ratio')
     zref=num2str(ref);
     titr=strcat('The reference height at which the'
'atmosphere is assumed to be purely molecular'
'is taken at (with CIRA-86 as model) :',zref,' km');
     title(titr)
  end
end
 if cm == 2

   if (nbv == 1)

      [Esrayleigh,ERaybeta,ERayalpha,ERayratio]=
 rayleigh2(532*1e-9,Decm,Edebut1,alt);

      [ref,Erapdc,ENrapdc,EMiealpha]=
klett (Edebut1,Esgl1,ncan,alt,300,ERayalpha,...,
ERaybeta,ERayratio);

      figure
      plot(Erapdc(Edebut1:length(Erapdc)),...,
alt(Edebut1:length(Erapdc)));
      Edebut2 = length(Erapdc);
      axis([0.9 1.25 5 50])
      grid
      ylabel('Altitude (km)')
```

```
      xlabel('Mie scattering ratio')
      zref=num2str(ref);
      titr=strcat('The reference at which the '
atmosphere is assumed to be purely molecular'
'is taken at (with ECMWF as model) :',zref,' km');
      title(titr)

      figure
      plot(alt(Edebut1:length(Erapdc)),...,
EMiealpha(Edebut1:length(Erapdc)));
      Edebut2 = length(Erapdc);
      axis([10 35 0 2.5e-3])
      grid
      ylabel('Extinction coefficients(per km)')
      xlabel('Altitude (km)')
      zref=num2str(ref);
      titr=strcat('The reference at which the'
 'atmosphere is assumed to be purely molecular'
 'is taken at (with ECMWF as model) :',zref,' km');
      title(titr)

   end
   if (nbv == 2)

     [Esrayleigh,ERaybeta,ERayalpha,ERayratio]=
 rayleigh2(532*1e-9,Decm,Edebut2,alt);
```

```
      [ref,Erapdc,ENrapdc]=
klett(Edebut2,Esklett,ncan,alt,...,
300,ERayalpha,ERaybeta,ERayratio);
      figure
      plot(Erapdc(Edebut2:length(Erapdc)),...,
alt(Edebut2:length(Erapdc)));
      %debut2 = length(rapdc);
      axis([0.9 1.25 5 50])
      grid
      ylabel('Altitude (km)')
      xlabel('Mie scattering ratio')
      zref=num2str(ref);
      titr=strcat('The reference at which the '
'atmosphere is assumed to be purely molecular'
'is taken at (with ECMWF as model) :',zref,' km');
      title(titr)

   end
   if (nbv == 3)

      [Esrayleigh,ERaybeta,ERayalpha,ERayratio]=
 rayleigh2(532*1e-9,Decm,Edebut2,alt);
      [ref,Erapdc,ENrapdc]=
 klett (Edebut2,Esgl2,ncan,alt,300,ERayalpha,...,
ERaybeta,ERayratio);
      figure
```

```
     plot(Erapdc(Edebut2:length(Erapdc)),...,
alt(Edebut2:length(Erapdc)));
     %debut2 = length(rapdc);
     axis([0.9 1.25 5 50])
     grid;
     ylabel('Altitude (km)')
     xlabel('Mie scattering ratio')
     zref=num2str(ref);
     titr=strcat('The reference at which the '
'atmosphere is assumed to be purely molecular'
'is taken at (with ECMWF as model) :',zref,' km');
     title(titr)
  end
 end

end
%---------GRAPHICAL RESULTS----------
disp('Display of the graphical results');
graph = 0;
if graph == 0
 if cm == 1
  if (nbv == 1)|(nbv == 2)
   figure
   semilogx(sig1,alt,Csigc1,alt,'r',Cfdc1,alt,'g--')
   grid on
   legend('sig1','coorected signalA','skynoiseA')
```

```
   title(strcat('RAW SIGNAL (',date,')'));

   figure
   plot(Ctempf(Cninff:Cnsupf),alt(Cninff:Cnsupf),...,
Tclim,Zclim,'r-.');
   grid on
   legend('LIDAR','CIRA86')
   hold on
   plot(Ctempf(Cninff:Cnsupf)-CTf_err(Cninff:Cnsupf),...,
alt(Cninff:Cnsupf),'k--',...,
Ctempf(Cninff:Cnsupf)+CTf_err(Cninff:Cnsupf),...,
alt(Cninff:Cnsupf),'k--')
   axis([180 310 0 65])
   title(strcat('LIDAR TEMPERATURE (',date,')'));
   xlabel('Temperature(K)');
   ylabel('Altitude(Km)');
   figure
   grid
   subplot 121
   plot(Cd_rel(Cninff:Cnsupf),alt(Cninff:Cnsupf),...,
Cd_relplus(Cninff:Cnsupf),alt(Cninff:Cnsupf),'k--',...,
Cd_relmoins(Cninff:Cnsupf),alt(Cninff:Cnsupf),'k--')
   y = 1:length(alt);
   y = y./y;
   hold on
   plot(y,alt,'r:')
```

```
   axis([0.8 1.4 0 65])
   grid;
   title(strcat('RELATIVE DENSITY(',date,')'));
   ylabel('Altitude(Km)')
   subplot 122
   plot(Crapdc(Cdebut1:length(Crapdc)),...,
alt(Cdebut1:length(Crapdc)));
   Cdebut2 = length(Crapdc);
   axis([0.8 1.4 0 65])
   grid;
   ylabel('Altitude (km)')
   xlabel('Mie scattering ratio')
   zref=num2str(ref);
   titr=strcat('The reference at which the'
'atmosphere is assumed to be purely'
'molecular is taken at (with CIRA-86 as model):',zref,' km');
   title(titr)

   figure
   plot(alt(Cdebut1:length(CMiealpha)),...,
CMiealpha(Cdebut1:length(CMiealpha)));
   grid
   ylabel('Extinction coefficients(per km)')
   xlabel('Altitude (km)')
   zref=num2str(ref);
```

```
  end
  if (nbv == 3)
     figure
     semilogx(sig2,alt,Csigc2,alt,'r',Cfdc2,alt,'g--')
     grid on
     legend('sigB','correctedsigB','skynoiseB')
     title(strcat('RAW SIGNAL (',date,')'));

   figure
   grid
   subplot 121
   Cerror_d = erreur_stat(alt,nbtirs,nbv,Csgl2,...,
Csgl2,Cfdc2,0,0,Cdebut2);
   plot(Cerror_d(Cdebut2:length(Crapdc)),...,
alt(Cdebut2:length(Crapdc)));
   y = 1:length(alt);
   y = y./y;
   hold on
   plot(y,alt,'r:')
   axis([0.8 1.4 0 65])
   grid;
   title(strcat('RELATIVE DENSITY (',date,')'));
   ylabel('Altitude(Km)')
   subplot 122
   plot(Crapdc(Cdebut2:length(Crapdc)),...,
alt(Cdebut2:length(Crapdc)));
```

```
%   Cdebut2 = length(Crapdc);
    axis([0.8 1.4 0 65])
    grid;
    ylabel('Altitude (km)')
    xlabel('Mie scattering ratio')
    zref=num2str(ref);
    titr=strcat('The reference at which the'
'atmosphere is assumed to be purely '
'molecular is taken at (with CIRA-86 as model) :',zref,' km');
    title(titr)
   end
end
 if cm == 2
  if (nbv == 1)|(nbv == 2)
   figure
   semilogx(sig1,alt,Esigc1,alt,'r',Efdc1,alt,'g--')
   grid
   legend('sigA','correctedsigA','skynoiseA')
   title(strcat('RAW SIGNAL (',date,')'));

   figure
   plot(Etempf(Eninff:Ensupf),alt(Eninff:Ensupf),...,
Tecm,Zclim,'r-.');
   grid
   legend('LIDAR','ECMWF')
   hold on
```

```
   plot(Etempf(Eninff:Ensupf)-ETf_err(Eninff:Ensupf),...,
alt(Eninff:Ensupf),'k--',...,
Etempf(Eninff:Ensupf)+ETf_err(Eninff:Ensupf),...,
alt(Eninff:Ensupf),'k--')
   axis([180 310 0 65])
   title(strcat('TEMPERATURE (',date,')'));
   xlabel('Temperature(K)');
   ylabel('Altitude(Km)');
   figure
   grid
   subplot 121
   plot(Ed_rel(Eninff:Ensupf),alt(Eninff:Ensupf),...,
Ed_relplus(Eninff:Ensupf),alt(Eninff:Ensupf),...,
'k--',Ed_relmoins(Eninff:Ensupf),alt(Eninff:Ensupf),'k--')
   y = 1:length(alt);
   y = y./y;
   hold on
   plot(y,alt,'r:')
   axis([0.8 1.4 0 65])
   grid;
   title(strcat('RELATIVE DENSITY with ECMWF '
'as model (',date,')'));
   ylabel('Altitude(Km)')
   subplot 122
   plot(Erapdc(Edebut1:length(Erapdc)),...,
```

```
alt(Edebut1:length(Erapdc)));
   Edebut2 = length(Erapdc);
   axis([0.8 1.4 0 65])
   grid;
   ylabel('Altitude (km)')
   xlabel('Mie scattering ratio')
   zref=num2str(ref);
   titr=strcat('The reference at which the '
'atmosphere is assumed to be purely molecular '
'is taken at (with ECMWF as model) :',zref,' km');
   title(titr)
  end
end
if cm == 3
  if (nbv == 1)|(nbv == 2)
   figure
   grid
   plot(Ctempf(Cninff:Cnsupf),alt(Cninff:Cnsupf),...,
Etempf(Eninff:Ensupf),alt(Eninff:Ensupf),'--')
   legend('CIRA','ECMWF')
   hold on
   axis([180 310 0 60])
   title(strcat('TEMPERATURE (',date,')'));
   xlabel('Temperature(K)');
   ylabel('Altitude(Km)');
   figure
```

```
   grid
   plot(Cd_rel(Cninff:Cnsupf),alt(Cninff:Cnsupf),...,
Cd_relplus(Cninff:Cnsupf),alt(Cninff:Cnsupf),'k--',...,
Cd_relmoins(Cninff:Cnsupf),alt(Cninff:Cnsupf),'k--',...,
Ed_rel(Eninff:Ensupf),alt(Eninff:Ensupf),...,
Ed_relplus(Eninff:Ensupf),alt(Eninff:Ensupf),...,
'r--',Ed_relmoins(Eninff:Ensupf),alt(Eninff:Ensupf),'r--')
   legend('CIRA','ECMWF')

   y = 1:length(alt);
   y = y./y;
   hold on
   plot(y,alt,'r:')
   axis([0.8 1.4 0 60])
   title(strcat('RELATIVE DENSITY (',date,')'));
   ylabel('Altitude(Km)')

  end
 end

end
if graph  == 1
   figure
   grid
   plot(tempf(ninff:nsupf),alt(ninff:nsupf),'k',...,
Tclim,Zclim,'r-.');
   hold on
```

```
   plot(Tclim3,Zclim3,'b*-');
   axis([180 310 0 60])
  % axis([160 280 9.7 25]);
   xlabel('temperature(Kelvin)');
   ylabel('altitude(Km)');
   legend('LIDAR','CIRA','SAWB');
   hold on
   plot(tempf(ninff:nsupf)-Tf_err(ninff:nsupf),...,
alt(ninff:nsupf),'--k',tempf(ninff:nsupf)+Tf_err(ninff:nsupf),...,
alt(ninff:nsupf),'--k')
   title(strcat('TEMPERATURE (',date,')'));

end

end
```

Appendix C

Basic equations of fluid dynamics

C.1 Continuity equation

Consider a compressible fluid volume $d\tau$ of density ϱ moving with velocity $\overline{u}$. Conservation of matter requires (see fig. (C.1)).

$\frac{\partial}{\partial t}\int_{vol} \varrho \, d\tau = -\int_{s} \varrho\overline{u} \cdot d\overline{s} = -\int_{vol} \overline{\nabla} \cdot(\varrho\overline{u})$, by Green's theorem and therefore

$$\int_{vol}\left(\frac{\partial \varrho}{\partial t} + \overline{\nabla} \cdot(\varrho\overline{u})\right) d\tau = 0$$

$$\Longrightarrow \boxed{\frac{\partial \varrho}{\partial t} + \overline{\nabla} \cdot (\varrho\overline{u}) = 0} \qquad \text{(C.1)}$$

which is the continuity equation.

Now, $\frac{\partial \varrho}{\partial t} + \overline{\nabla} \cdot (\varrho\overline{u}) = \underbrace{\frac{\partial \varrho}{\partial t} + \overline{u} \cdot \overline{\nabla}\varrho}_{} + \varrho \, \overline{\nabla} \cdot \overline{u} = 0$

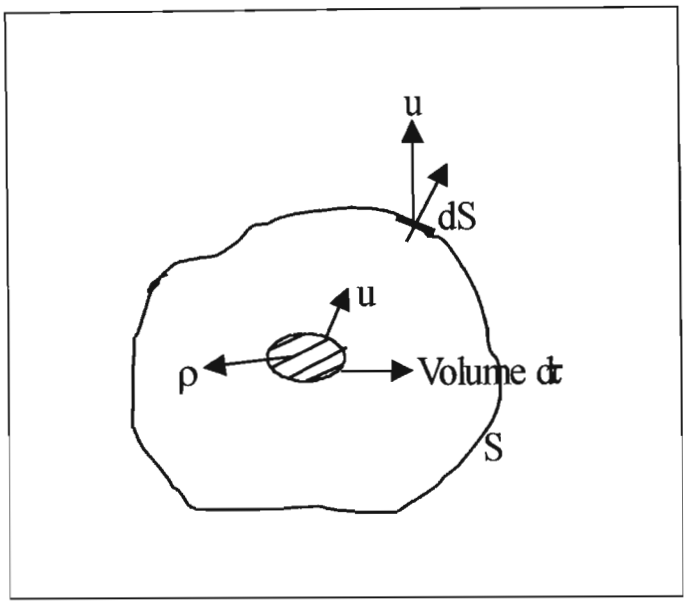

Figure C.1: Diagram to illustrate Green's theorem. The vectors u and S are shown in magnitudes only.

$$\frac{D\varrho}{Dt} + \varrho\, \overline{\nabla} \cdot \overline{u} \; = 0,$$

where $\dfrac{D}{Dt} = \dfrac{\partial}{\partial t} + \overline{u} \cdot \overline{\nabla}$ is the convective or total derivative.

C.2 Meaning of the convective derivative $\dfrac{D}{Dt}$

Let $\phi\,(x, y, z, t)$ be any fluid quantity (e.g. velocity, density, pressure, etc). Consider a small displacement of the fluid form $\overline{r}$ to $\overline{r} + \delta\overline{r}$ in a time interval δt (fig.(C.2)). The change of the fluid quantity with respect to space and time can be written as:

$$\phi(\overline{r} + \delta\overline{r}, t + \delta t) - \phi(\overline{r}, t) \tag{C.2}$$

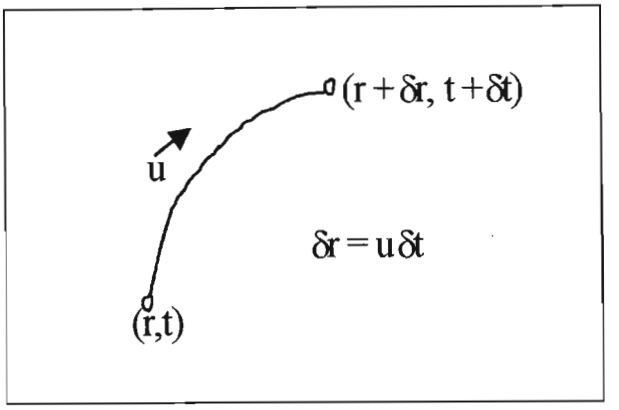

Figure C.2: Diagram to illustrate the meaning of the convective derivative. Vectors u and r are shown in magnitudes only.

Dividing equation by δt and taking the limit as δt tends to zero, we have

$$\underset{\delta t \to 0}{Limit} \frac{[\phi(\overline{r}+\delta\overline{r}, t+\delta t) - \phi(\overline{r}, t)]}{\delta t}$$

$$= \frac{\left[\delta x \frac{\delta\phi}{\delta x} + \delta y \frac{\delta\phi}{\delta y} + \delta z \frac{\delta\phi}{\delta z} + \delta t \frac{\delta\phi}{\delta t}\right]}{\delta t}$$

$$= u_x \frac{\delta\phi}{\delta x} + u_y \frac{\delta\phi}{\delta y} + u_z \frac{\delta\phi}{\delta z} + \frac{\delta\phi}{\delta t} = \left(\frac{\partial}{\partial t} + \overline{u} \cdot \overline{\nabla}\right)\phi = \frac{D\phi}{Dt}.$$

Thus $\dfrac{D\phi}{Dt}$ measures the rate of change of ϕ following a fluid particle.

C.3 Equation of Motion

$$\varrho \frac{D\overline{u}}{Dt} = -\overline{\nabla} p_r + \varrho \cdot \overline{F}_{ext} + \text{Viscous stresses} \tag{C.3}$$

where ϱ is the density of the fluid, $\overline{u}$ is the velocity of the fluid, p_r is the pressure exerted on the fluid and $\overline{F}_{ext}$ is the external force acting on the fluid.

The $\overline{F}_{ext}$ can be gravitational force and will have the form $\overline{F}_{ext} = -\dfrac{G \cdot M \cdot \varrho}{r^2}\hat{r} =$

$-g$, say.

Equation (C.3) can also be written as a conservation of momentum,

$$\varrho\left(\frac{\partial \overline{u}}{\partial t} + \overline{u} \cdot \nabla \overline{u}\right) = \frac{\partial}{\partial t}\left(\varrho \overline{u}\right) + \overline{u}\frac{\partial \varrho}{\partial t} + \varrho \overline{u} \cdot \overline{\nabla . u} = \frac{\partial}{\partial t}\left(\varrho \overline{u}\right) + \overline{u}\left(\overline{\nabla} \cdot \varrho \overline{u}\right) +$$

$\varrho \overline{u} \cdot \overline{\nabla . u}$

$$= \frac{\partial}{\partial t}\left(\varrho \overline{u}_i\right) + \frac{\partial G_{ij}}{\partial x_{ij}} = -\frac{\partial p_{r\,i}}{\partial x_i} + \varrho \overline{F}_i + \text{Viscous stresses}$$

where $G_{ij} = \varrho u^2 \delta_{ij} + \varrho \overline{u}_i \overline{u}_j$.

The equation of motion can be written as

$$\frac{\partial}{\partial t}\left(\varrho \overline{u}_i\right) = -\frac{\partial}{\partial x_j}\left(\left(p_r + \varrho u^2\right) \cdot \delta_{ij} + \varrho \overline{u_i} \cdot \overline{u_j}\right) + \varrho \overline{F}_{ext} + \text{Viscous stresses} \tag{C.4}$$

The term on the LHS is the momentum density $(\overline{M_d})$ and the first term on the RHS is the momentum flux density $(\overline{J})$. In terms of the momentum density $\overline{M}_d$ and flux $\overline{J}$, equation (C.4) becomes

$$\frac{\partial \overline{M}}{\partial t} = -\nabla \overline{J} + \varrho \overline{F}_{ext} + \text{Viscous stresses , where } \overline{M_d} = \varrho \overline{u}_i.$$

C.4 Energy equation

Energy density $E = \varrho\left(\frac{1}{2}u^2 + e\right)$,where e = internal energy $= \dfrac{p_r}{\varrho\,(\gamma - 1)}$,

where $\gamma = \dfrac{C_p}{C_v}$.

Energy flux $\overline{Q} = \varrho\overline{u}\left(\frac{1}{2}u^2 + \text{enthalpy}\right)$. The enthalpy is

$$\begin{aligned} &= e + \frac{p_r}{\varrho} \\ &= \frac{\gamma}{(\gamma - 1)}\frac{p_r}{\varrho} \text{ (for an ideal gas).} \end{aligned}$$

Hence conservation of energy reads

$$\boxed{\frac{\partial E}{\partial t} + \overline{\nabla}\cdot\,\overline{Q} = \varrho\overline{u}\cdot\overline{F}_{ext}} \tag{C.5}$$

The dissipationless form of equation (C.5) implies that the flow is adiabatic, i.e.

$$\frac{D}{Dt}\left(\frac{p_r}{\varrho^\gamma}\right) = 0. \tag{C.6}$$

$\dfrac{p_r}{\rho^\gamma}$ is a constant following the flow (stream line)

This can also be written as

$$\frac{Dp_r}{Dt} = c^2\frac{D\varrho}{Dt}, \tag{C.7}$$

where $c^2 = \dfrac{\gamma p_r}{\varrho}$.

This follows from energy conservation :

$$\frac{\partial}{\partial t}\varrho\left(\frac{1}{2}u^2 + \frac{p_r}{(\gamma-1)\,\varrho}\right) + \overline{\nabla}\left[\varrho\overline{u}\left(\frac{1}{2}u^2 + \frac{\gamma}{\gamma-1}\frac{p_r}{\varrho}\right)\right] = \varrho\overline{u}_i \cdot g \qquad \text{(C.8)}$$

along with momentum equation : $\varrho\left(\dfrac{\partial \overline{u}}{\partial t} + \overline{u}\cdot\overline{\nabla}\overline{u}\right) = -\overline{\nabla}\cdot p_r - \varrho\cdot g,$

and the continuity equation : $\dfrac{\partial \varrho}{\partial t} + \overline{\nabla}\,(\varrho\cdot\overline{u}) = 0,$

Equation (C.8) can be rewritten as

$$\varrho\overline{u}\cdot\frac{\partial\overline{u}}{\partial t} + \tfrac{1}{2}\cdot u^2\cdot\frac{\partial\varrho}{\partial t} + \frac{1}{\gamma-1}\frac{\partial p_r}{\partial t} + \left(\tfrac{1}{2}u^2 + \frac{\gamma}{\gamma-1}\frac{p_r}{\varrho}\right)\left(\frac{-\partial\varrho}{\partial t}\right) + \varrho\overline{u}\cdot\overline{\nabla}\left(\tfrac{1}{2}u^2 + \frac{\gamma}{\gamma-1}\frac{p_r}{\varrho}\right)$$

$= \varrho\overline{u}\cdot g$, from which equation(C.6) follows.

C.5 1-Dimensional Sound Wave

Consider motion to be along the x-axis only. We further assume that the motion is adiabatic with no friction. The procedure we follow is we linearize the equations about uniform background state:

$\varrho_o, p_o, \overline{u_o} = 0$, where ϱ_o is the density, p_o is the pressure and $\overline{u_o}$ is the velocity along the x-axis of the background. We now introduce small perturbations ϱ_1, p_1,$\overline{u_1}$and neglecting quadratic and product terms,

we have $\varrho = \varrho_o + \varrho_1$, $p = p_o + p_1$, $\overline{u} = 0 + \overline{u_1}$.

Using the continuity equation, we have $\frac{\partial}{\partial t}(\varrho_o + \varrho_1) + \frac{\partial}{\partial x}((\varrho_o + \varrho_1)\overline{u_1})$

which linearises to

$$\frac{\partial \varrho_1}{\partial t} + \varrho_o \frac{\partial \overline{u_1}}{\partial x} = 0 \tag{C.9}$$

The equation of motion becomes

$$\varrho_o \frac{\partial \overline{u_1}}{\partial t} = -\frac{\partial p_1}{\partial x} \tag{C.10}$$

Using equation (C.7) for adiabatic flow, we have

$$\frac{\partial p_1}{\partial t} = c_o^2 \frac{\partial \varrho_1}{\partial t} \text{ where } c_o^2 = \frac{\gamma \cdot p_o}{\varrho_o} = \gamma \cdot R \cdot M_o, \tag{C.11}$$

where M_o is the temperature of the flow.

Do $\frac{\partial}{\partial t}$ of equation (C.10) and use equation (C.11) to eliminate p_1, we have

$$\frac{\partial^2 \overline{u_1}}{\partial t^2} = c_o^2 \cdot \frac{\partial^2 \overline{u_1}}{\partial x^2} \tag{C.12}$$

This the classical one-dimensional sound wave equation showing that compressional disturbances propagate at the speed of sound $c_o = \sqrt{\gamma \cdot R \cdot M_o}$.

C.6 3-D Sound wave

The three-dimensional wave equation is

$$\frac{\partial^2 \varrho^1}{\partial t^2} = c_o^2 \nabla^2 \varrho^1 \tag{C.13}$$

where $\nabla^2 \equiv \frac{\partial^2}{\partial x^2} + \frac{\partial^2}{\partial y^2} + \frac{\partial^2}{\partial z^2}$ and $\varrho^1 = \varrho_x + \varrho_y + \varrho_z$is the three dimensional density of a wave particle.

We seek plane wave solutions of the form $\varrho^1 = A \exp i(\omega t - \overline{k} \cdot \bar{r}\ )$, where ω is the angular frequency and $\overline{k}$ is the wave number vector, then the wave equation is satisfied if

$$v^2 = c_o^2(k_x^2 + k_y^2 + k_z^2) = c_o^2 k^2 \tag{C.14}$$

where $k^2 = k_x^2 + k_y^2 + k_z^2$.

This is the dispersion equation for three-dimensional sound waves. At a fixed frequency ω, equation (C.14) is a sphere of radius $\frac{\omega}{c_o}$ in k- space (fig.(C.3)).

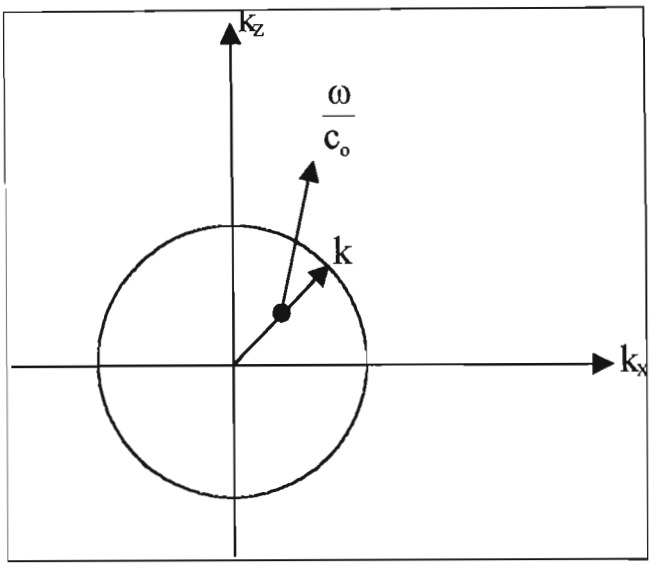

Figure C.3: Dispersion of sound waves in k-space at fixed frequency ω.

C.7 Atmospheric gravity waves

We have seen that for a sound wave, inertia is essentially balanced by pressure gradient and is "longitudinal" i.e. compressive, with motions parallel to the wave direction. In contrast to a sound wave, in a gravity wave inertia is balanced by a combination of the pressure gradient $(-\nabla p_r)$ and the bouyancy force. In this case, the wave is transverse-shearing with the motion perpendicular to wave vector $\overline{k}$.

C.7.1 The bounce frequency (Brunt-Vaïsälä) of the atmosphere

Consider a parcel of air of density ϱ_o at a height z in the atmosphere.

Hydrostatic equilibrium requires pressure gradient balances the gravitational weight of the atmosphere:

$$\frac{dp_o}{dz} = -\varrho_o g \tag{C.15}$$

where p_o is the pressure of the air and is equal to $\rho_o \cdot U_R \cdot M_o$ (R is the molar gas constant and M_o is the temperature of the atmosphere), assuming ideal gas.

Let the parcel of air be displaced adiabatically upward to a height $z+h$. At the height $z+h$,the parcel of air has a different density from its surroundings but is at the same pressure p_o.

The change in density of the parcel of air during an adiabatic process is

$$\delta\varrho = \frac{\delta p_r}{c_o^2} = -\frac{h \cdot \varrho_o \cdot g}{c_o^2} \tag{C.16}$$

where $c_o^2 = \dfrac{\gamma \cdot p_o}{\varrho_o}$ and $\gamma = \dfrac{C_p}{C_v}$.

Hence the difference in density between the displaced parcel and its surrounding is

$$-\frac{h \cdot \varrho_o \cdot g}{c_o^2} - h.(\frac{d\varrho_o}{dz}) = -h \cdot (\frac{d\varrho_o}{dz} + \frac{\varrho_o \cdot g}{c_o^2}) \tag{C.17}$$

Hence the equation of motion for the parcel of air is

$$\frac{d^2h}{dt^2} = -\frac{g \cdot h}{\varrho_o}\left(\frac{d\varrho_o}{dz} + \frac{\varrho_o \cdot g}{c_o^2}\right) \tag{C.18}$$

which is of the form

$$\frac{d^2h}{dt^2} = -N^2 \cdot h$$

where $N^2 = \frac{-g}{\varrho_o}\left(\frac{d\varrho_o}{dz} + \frac{\varrho_o g}{c_o^2}\right)$.

If $N^2 > 0$, the parcel of air will oscillate about its original height with frequency N known as the Brunt-Vaïsälä frequency.

To a first approximation,

$$N^2 \approx -\frac{g}{\varrho_o} \cdot \frac{d\varrho_o}{dz} \tag{C.19}$$

The scale height H_s is given by

$$\frac{1}{H_s} = -\frac{1}{\varrho_o} \cdot \frac{d\varrho_o}{dz} \tag{C.20}$$

Substituting equation (C.19) in equation (C.20), we have

$$N = \sqrt{\frac{g}{H_s}}. \tag{C.21}$$

As an illustration, the Brunt-Vaïsälä frequency at a scale height of 10 km in the Earth atmosphere, assuming $g \approx 10$ ms^{-2}, is given by

$$N = \sqrt{\frac{10}{10000}} \approx 0.0316 \text{ s}^{-1}$$

with a corresponding period of the motion

$$\begin{aligned} &= \frac{2 \cdot \pi}{N} \\ &= \frac{2 \cdot \pi}{0.0316} \text{ s} \\ &\approx 200 \text{ s} \\ &\approx 3 \text{ mins} \end{aligned}$$

For period < 3 mins, sound waves (higher frequencies) are propagated in the atmosphere, whereas for period > 3 mins, atmospheric gravity waves (lower frequencies) are propagated.

C.8 Derivation of the dispersion equation for atmospheric gravity wave propagating in the atmosphere

Consider perturbations about background states ϱ_o, p_o, $\overline{u_o} = 0$ (stationary atmosphere). The background states are in hydrostatic equilibrium (equation (C.15)).

We now allow a small perturbation on the background states such that $\varrho = \varrho_o + \varrho'$, $\overline{u} = (\overline{u}, 0, \overline{\mathrm{w}})$ and $p_r = p_o + p'_r$. Using the continuity equation (equation(C.1)), we have

$$\frac{\partial \varrho'}{\partial t} + \frac{\partial}{\partial x}(\varrho_o \cdot \overline{u}) + \frac{\partial}{\partial z}(\varrho_o \cdot \overline{\mathrm{w}}) = 0 \tag{C.22}$$

where all quadratic terms have been neglected and the motion is confined to the z-x plane only.

Similarly, the equation of motion (equation (C.3)) becomes (assuming no viscous stresses),

$$\varrho\left(\frac{\partial}{\partial t} + \overline{u} \cdot \nabla\right)\overline{u} = -\nabla p_r - \varrho \cdot g \tag{C.23}$$

This linearises to

$$(\varrho_o + \varrho')(\frac{\partial \overline{u}}{\partial t}) = -\nabla(p_o + p'_r) - (\varrho_o + \varrho') \cdot g \tag{C.24}$$

The z-component of equation (C.24) is

$$\frac{\partial(\varrho_o \overline{\mathrm{w}})}{\partial t} = -\frac{\partial p'_r}{\partial z} - \varrho' g \tag{C.25a}$$

The x-component of equation (C.24) is

$$\varrho_o \frac{\partial \overline{u}}{\partial t} = -\frac{\partial p_r'}{\partial x} \tag{C.26}$$

If there is no dissipation, the motions are adiabatic,

$$\frac{Dp_r}{Dt} = c^2 \cdot \frac{D\varrho}{Dt} \tag{C.27}$$

where $c^2 = \dfrac{\gamma \cdot p_r}{\varrho}$.

Equation (C.27) becomes

$$p_r \left(\frac{\partial}{\partial t} + \overline{u} \cdot \nabla \right) = c^2 \left(\frac{\partial}{\partial t} + \nabla \right) \varrho$$

$$\left(\frac{\partial}{\partial t} + \overline{u}\frac{\partial}{\partial x} + \overline{\mathrm{w}}\frac{\partial}{\partial z} \right) \left(p_o + p_r' \right) = \left(c_o^2 + c'^2 \right) \left(\frac{\partial}{\partial t} + \overline{u}\frac{\partial}{\partial x} + \overline{\mathrm{w}}\frac{\partial}{\partial z} \right) \left(\varrho_o + \varrho' \right) \tag{C.28}$$

Linearising equation (C.28),

$$\frac{1}{c_o^2} \left(\frac{\partial p_r'}{\partial t} + \overline{\mathrm{w}}\frac{\partial p_o}{\partial z} \right) = \left(\frac{\partial \varrho'}{\partial t} + \overline{\mathrm{w}}\frac{\partial \varrho_o}{\partial z} \right)$$

$$\frac{\partial \varrho'}{\partial t} = \overline{\mathrm{w}} \left(\frac{1}{c_o^2}\frac{\partial p_o}{\partial z} - \frac{\partial \varrho_o}{\partial z} \right) + \frac{1}{c_o^2}\frac{\partial p_r'}{\partial t} \tag{C.29}$$

The terms between brackets on the RHS of equation (C.29) can be written as

$$\begin{aligned} \frac{1}{c_o^2}\frac{\partial p_o}{\partial z} - \frac{\partial \varrho_o}{\partial z} &= \frac{1}{c_o^2} \cdot (-\varrho_o \cdot g) - \frac{\partial \varrho_o}{\partial z} \\ &= -\frac{\varrho_o}{g} \left(\frac{g^2}{c_o^2} + \frac{g}{\varrho_o} \cdot \frac{\partial \varrho_o}{\partial z} \right) \\ &= -\frac{\varrho_o}{g} \cdot N^2 \end{aligned}$$

where $\frac{\partial p_o}{\partial z} = -\varrho_o \cdot g$ and $-\frac{N^2}{g} = \frac{1}{\varrho_o} \cdot \frac{\partial \varrho_o}{\partial z} + \frac{g}{c_o^2}$.

Therefore, substituting in equation (C.29), we have

$$\frac{\partial \varrho'}{\partial t} = -\frac{\varrho_o}{g} \cdot N^2 \cdot \overline{\mathrm{w}} + \frac{1}{c_o^2}\frac{\partial p_r'}{\partial t} \tag{C.30}$$

We use the Boussinesq approximation in which for motion in a stratified incompressible fluid, only the density perturbation term in the gravity term of equation (C.25a) is important.

Do $\frac{\partial}{\partial t}$ of equation (C.25a),

$$\frac{\partial^2}{\partial t^2}(\varrho_o \overline{\mathrm{w}}) = -\frac{\partial^2 p_r'}{\partial z \partial t} - g \cdot \frac{\partial \varrho'}{\partial t} \tag{C.31}$$

Substituting equation (C.29) in equation (C.30) and using Boussinesq approximation which states that all density variations other than the buoyancy force where ϱ' is multiplied by g are ignored.

$$\begin{aligned}
\frac{\partial^2}{\partial t^2}(\varrho_o \overline{\mathrm{w}}) &= -\frac{\partial^2 p_r'}{\partial z \partial t} - g \cdot (-\frac{\varrho_o}{g} \cdot N^2 \cdot \overline{\mathrm{w}} + \frac{1}{c_o^2}\frac{\partial p_r'}{\partial t}) \\
&= -\frac{\partial^2 p_r'}{\partial z \partial t} - g \cdot (-\frac{\varrho_o}{g} \cdot N^2 \cdot \overline{\mathrm{w}}), \text{ By Boussinesq approximation}
\end{aligned}$$

After simplification,

$$(\frac{\partial^2}{\partial t^2} + N^2)(\varrho_o \overline{\mathrm{w}}) = -\frac{\partial^2 p_r'}{\partial z \partial t} \tag{C.32}$$

By equation (C.26),

$$\varrho_o \frac{\partial \overline{u}}{\partial t} = -\frac{\partial p'_r}{\partial x} \tag{C.33}$$

$$\frac{\partial}{\partial t}(\varrho_o \overline{u}) = -\frac{\partial p'_r}{\partial x}$$

Recall the continuity equation,

$$\frac{\partial \varrho'}{\partial t} + \frac{\partial}{\partial x}(\varrho_o \overline{u}) + \frac{\partial}{\partial z}(\varrho_o \overline{\mathrm{w}}) = 0$$

which in the Boussinesq approximation (the first term is ignored) approximates to

$$\frac{\partial}{\partial x}(\varrho_o \overline{u}) + \frac{\partial}{\partial z}(\varrho_o \overline{\mathrm{w}}) = 0 \tag{C.34}$$

Do $\frac{\partial}{\partial x}$ of equation (C.33) and use equation (C.34) to eliminate u to yield

$$\frac{\partial}{\partial t}(\frac{\partial}{\partial z}(\varrho_o \overline{\mathrm{w}})) = \frac{\partial^2 p'_r}{\partial x^2} \tag{C.35}$$

Equations (C.32) and (C.35) are two coupled partial differential equations for $\varrho_o \mathrm{w}$ and p'_r.

Do $\frac{\partial^2}{\partial z \partial t}$ of equation(C.35) and $\frac{\partial^2}{\partial x^2}$ of equation (C.32) (this operation eliminates p'_r),

$$\frac{\partial^2}{\partial z \partial t}(\frac{\partial^2}{\partial t \partial z}(\varrho_o \overline{\mathrm{w}})) = \frac{\partial^2}{\partial x^2}(\frac{\partial^2}{\partial t^2} + N^2)(\varrho_o \overline{\mathrm{w}})$$

$$(\frac{\partial^2}{\partial t^2}\frac{\partial^2}{\partial z^2})(\varrho_o\overline{\mathrm{w}}) = \frac{\partial^2}{\partial x^2}(\frac{\partial^2}{\partial t^2} + N^2)(\varrho_o\overline{\mathrm{w}}) \tag{C.36}$$

Equation (C.36) can be rewritten as

$$\frac{\partial^2}{\partial t^2}(\frac{\partial^2}{\partial x^2} + \frac{\partial^2}{\partial z^2})(\varrho_o\overline{\mathrm{w}}) = N^2\frac{\partial^2}{\partial x^2}(\varrho_o\overline{\mathrm{w}}) \tag{C.37}$$

Equation (C.37) is the gravity wave equation. It displays dispersive and anisotropic characteristics through the appearence of N^2 and the Laplacean $\frac{\partial^2}{\partial x^2} + \frac{\partial^2}{\partial z^2}$.

Seeking plane wave solutions,

$\varrho_o\overline{\mathrm{w}} \equiv \mathrm{v} = q = A\exp i(\upsilon t - k_x x - k_z z)$, of equation (C.37) yields the following dispersion equation

$$\frac{k_z^2}{k_x^2} = (\frac{N^2}{\upsilon^2} - 1) \tag{C.38}$$

If we have retained a $y-$variation then equation (C.38) becomes

$$\frac{k_z^2}{k_x^2 + k_y^2} = (\frac{N^2}{\upsilon^2} - 1) \tag{C.39}$$

For a given frequency $\upsilon < N$ (RHS of equation (C.39) is positive), equation(C.39) is a cone in k-space (fig.(C.4)).

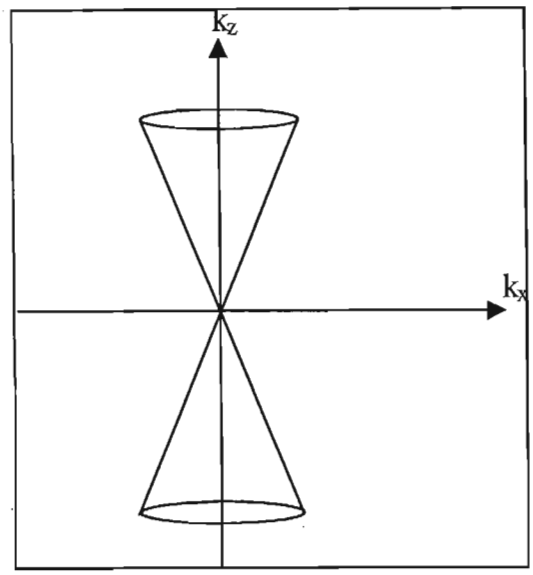

Figure C.4: Dispersion of gravity wave in k-space.

C.9 The Effect of rotating frame of reference on the equation of motion

The equation of motion in a rotating frame contains additional inertial terms namely, Coriolis and centrifugal accelerations:

$$\varrho(\frac{D\overline{\mathrm{v}}}{Dt} + 2\,\overline{\upsilon} \times \overline{\mathrm{v}} + \overline{\upsilon} \times (\overline{\upsilon} \times \overline{r})) = -\nabla p_r + \varrho g \qquad \text{(C.40)}$$

where ϱ is the density of an element of fluid, $\overline{\mathrm{v}}$ is the velocity component in the y-direction, $\overline{\upsilon}$ is the angular velocity of a rotating axis fixed to the earth's surface, $\overline{r}$ is the radius vector and p_r is the pressure of the fluid element.

The second and third terms on the LHS are the Coriolis and the centrifugal terms respectively.

In "geostrophic" motion, the Coriolis force balances the pressure gradient:

$$2\,\overline{\upsilon} \times \overline{\mathrm{v}} = -\frac{\nabla p_r}{\varrho}$$

C.10 Derivation of the Rossby-wave equation on β-plane

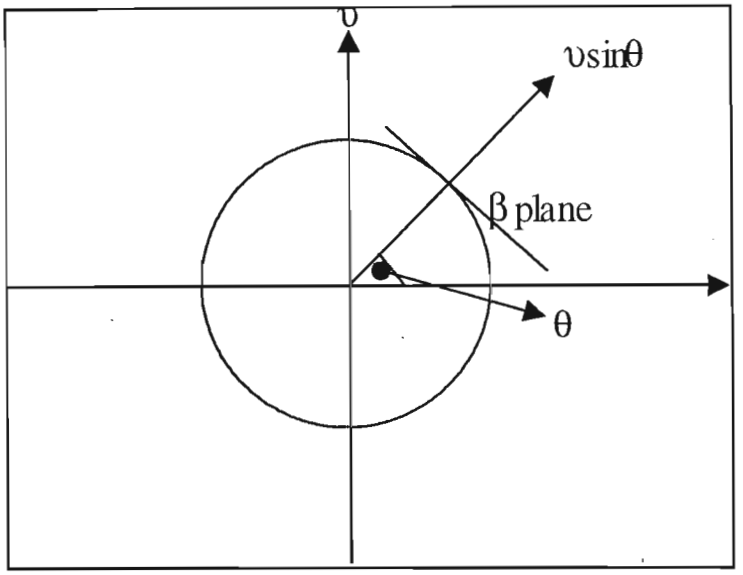

Figure C.5: Simple geometry of the earth to calculate the y-component of the angular velocity υ of the earth.

Construct a plane tangential to the earth's surface at a given latitude θ (fig.(C.5)).

The vertical component of the angular velocity of a rotating axis fixed to the earth's surface, $\overline{\upsilon}$, is

$$2\ \upsilon_z = 2\ \upsilon \sin\theta \doteqdot 2\ \upsilon \sin(\theta + \delta\theta) = 2\ \upsilon(\sin\theta + \cos\theta\ \delta\theta)$$

But $B\delta\theta = y = 2\ \upsilon(\sin\theta + \cos\theta\ \frac{y}{B})$, where B is the radius of the earth.

Thus $\frac{\partial}{\partial y}(2\ \upsilon_y) = \frac{2\ \upsilon \cos\theta}{B} = \beta.$

Consider wave perturbations in this geometry for incompressible flow and the velocity field $= (\overline{u}, \overline{\mathrm{v}}, o)$ (no vertical motion).

The equation of continuity (equation (C.1)) becomes:

$$\frac{\partial \overline{u}}{\partial x} + \frac{\partial \overline{\mathrm{v}}}{\partial y} = 0 \tag{C.41}$$

The x-component of the equation of motion (equation (C.40)) is

$$\frac{\partial \overline{u}}{\partial t} - 2\, \upsilon_z \overline{\mathrm{v}} = -\frac{1}{\varrho}\frac{\partial p_r}{\partial x} \tag{C.42}$$

The y-component is

$$\frac{\partial \overline{\mathrm{v}}}{\partial t} + 2\, \upsilon_z \overline{u} = -\frac{1}{\varrho}\frac{\partial p_r}{\partial y} \tag{C.43}$$

Also,

$$2\, \upsilon_z = 2\, \upsilon \sin\theta + \beta y$$

Do $\dfrac{\partial}{\partial y}$ of equation (C.41) $-$ $\dfrac{\partial}{\partial x}$ of equation (C.42) to eliminate the pressure gradient,

$$\frac{\partial}{\partial y}\left(\frac{\partial \overline{u}}{\partial t} - 2\, \upsilon_z \overline{\mathrm{v}}\right) - \frac{\partial}{\partial x}\left(\frac{\partial \overline{\mathrm{v}}}{\partial t} + 2\, \upsilon_z \overline{u}\right) = 0$$

$$\frac{\partial}{\partial t}\left(\frac{\partial \overline{u}}{\partial y} - \frac{\partial \overline{\mathrm{v}}}{\partial x}\right) - 2\, \upsilon_z \left(\frac{\partial \overline{\mathrm{v}}}{\partial y} + \frac{\partial \overline{u}}{\partial x}\right) + \overline{\mathrm{v}}\beta = 0 \tag{C.44}$$

where $\beta = \dfrac{2\,\upsilon}{a}\cos\theta$

By equation (C.41), the second term between brackets of equation (C.44) vanishes and we have

$$\frac{\partial}{\partial t}\left(\frac{\partial \overline{u}}{\partial y} - \frac{\partial \overline{\mathrm{v}}}{\partial x}\right) + \overline{\mathrm{v}}\beta = 0 \tag{C.45}$$

Do $\frac{\partial}{\partial x}$ of equation (C.45) and use equation (C.41) to eliminate $\overline{u}$, to obtain

$$\frac{\partial}{\partial t}(\frac{\partial^2 \overline{\mathrm{v}}}{\partial x^2} + \frac{\partial^2 \overline{\mathrm{v}}}{\partial y^2}) = \beta \frac{\partial \overline{\mathrm{v}}}{\partial x} \tag{C.46}$$

This is the Rossby wave equation.

For plave wave solutions, $\mathrm{v} \equiv A \exp i(\upsilon t - k_x x - k_y z)$, we obtain the dispersion equation

$$k_x^2 + k_y^2 - \beta \frac{k_x}{\upsilon} = 0$$

or,

$$(k_x - \frac{\beta}{2\upsilon})^2 + k_y^2 = (\frac{\beta}{2\upsilon})^2 \tag{C.47}$$

Equation (C.47) is the dispersion equation for Rossby waves in the (k_x,k_y) plane. At a fixed υ, equation (C.47) is a circle of radius $\frac{\beta}{\upsilon}$ whose centre is displaced $\frac{\beta}{\upsilon}$ units along the k_x axis.

Appendix D

Effects of aperture and obstruction of the receiver telescope

The analysis which follows is due to Halldorsson and Langerholc (1978). For a detailed treatment the reader should refer to their work.

Consider an infinitesimal source of size dA entering the telescope opening (fig.(D.1)). The source casts circular images of the telescope opening at radius R' and of the obstruction of radius b' onto the plane of the aperture which is placed at a distance x'_a from the focal plane.

The distance r' of their common centre from the axis can be obtained by considering the ray passing through the centre of the lens; using similar triangles,

$$\frac{r}{x} = \frac{r'}{f + x'_a}$$

$$\Longrightarrow r' = \frac{f + x'_a}{x} \cdot r \tag{D.1}$$

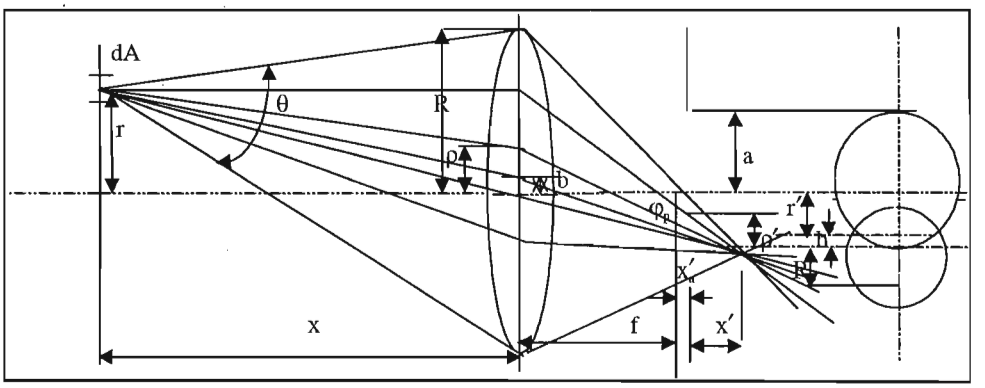

Figure D.1: Ray diagram for light from an infinitesimal source entering the receiver telescope.

The radius of the image cast by a circle of radius χ in the plane of the lens can be calculated by the similarity relation about the angle ϕ_p:

$$\frac{\rho}{f+x'} = \frac{\rho'}{|x'-x'_a|}$$

$$\Longrightarrow \rho' = \frac{|x'-x'_a|}{f+x'} \cdot \rho \tag{D.2}$$

Using $x' = \dfrac{f^2}{(x-f)}$, equation (D.2) can be written as

$$\rho' = \left| \frac{f}{x} - \frac{x'_a(x-f)}{x \cdot f} \right| \cdot \rho \tag{D.3}$$

In the case that the aperture is located in the focal plane ($x'_a = 0$), equations (D.1) and (D.3) simplify to

$$r' = \left(\frac{f}{x}\right) \cdot r \text{ and } \rho' = \left(\frac{f}{x}\right) \rho.$$

We now define $F \equiv 1 + \dfrac{x'_a}{f}$ and $\xi \equiv \left| F - \dfrac{x'_a \cdot x}{f^2} \right|$. The general relations become

$$r' = \frac{F \cdot f \cdot r}{x} \text{ , } \rho' = \frac{\xi \cdot f \cdot \rho}{x}.$$

Appendix E

Review of work done on Gas Lenses

As part of this doctoral study, work has also been done to investigate the concept of refraction by atmospheric gases as applied to gas lenses.

The study on gas lenses has been conducted within the experimental framework on scattering and refraction by atmospheric gases. Gas lenses were invented and developed at the Bell Systems Laboratories in the sixties and early seventies with the intention to create a device that could guide a laser beam over some distance. Potential applications were power transmission and optical communications. However, the former has not been implemented due to the relative inefficiency of lasers compared to transformers, and the latter due to the invention of high clarity optical fibre. These waveguides comprising spaced converging lenses were an option, but a costly one due to the power lost at each glass-air surface. Gas lenses provided a lossless solution, and hence the work done by the group at Bell was aimed at guiding pencil laser beams along horizontal paths.

The fact that solid state lenses are damaged when high power lasers

are used (power densities of order 10 GW cm^{-2}) offers a great opportunity for using gas lenses. Other obvious disadvantages of solid state lenses are their considerable cost and the expensive anti-reflection coatings they often require.

In the first paper published on the subject Berreman (1964), lenses of one meter in length and 6 mm in diameter were considered. These lenses used direct flow of gas and were heated to focus or guide a laser beam.

Marcuse (1965) showed that a thermal gradient gas lens approximates a thin lens since the two principle surfaces almost coincide. His thermal gradient gas lens worked on the principle of injecting a cool gas through a heated cylinder. The gas heats up near the walls of the cylinder and the heat penetrates radially into the gas creating a temperature gradient that in turn causes a density gradient. The gas density (and hence the refractive index) is larger at the center of the tube and decreases radially towards the wall. Marcuse (ibid) found an optimum gas velocity that yields not only the minimum focal length but also minimises lens distortions. The shape of the wavefront and other aberration were investigated experimentally by Steier (1965). He found that convection caused distortions in such lenses, with the effects more pronounced in carbon dioxide than air.

The distortion of the gas flow due to gravity and the corresponding effects on the focus were investigated by Gloge (1967). He showed that the optical centre of the lens is displaced downwards. The displacement varies as the fourth power of the tube diameter and the square of the gas pres-

sure. He found that if the tube diameter is greater than 1 cm, then for a one metre long lens the optical centre would be outside the lens. Despite these distortion effects, gas lenses could still find certain applications. Aoki and Suzuki (1967) used a gas lens as an objective lens in a telescope. It consisted of a heated metal tube through which cold air was sent by a micro fan. The air flow was kept laminar to avoid turbulence as this would distort the focus. They found that the optical quality of the image was improved for increasing wall temperature and air flow velocity up to a point where gas flow and heat convection fluctuations distort the image. In any case, the imaging quality of the gas lens was inferior to conventional glass lenses because of the aforementioned fluctuations and the small lens diameter.

Considerable work was also done on the properties of these lenses as waveguides when arranged in a confocal configuration. The propagation modes and beam distortion were investigated for straight and curved waveguides which were as long as 3 km (Kaiser 1968). In an attempt to improve these gas lenses, Kaiser (1968) made a slight modification to the gas lens design. He found that the optical quality of a thermal gas lens could be considerably improved if the heated gas was exhausted radially. He constructed a lens with outlets for the hot gas, with cool gas still pumped through as before. Imaging and waveguiding properties were improved with this design.

Iga and Suematsu (1969) built a hyperbolic type gas lens. This consisted of a heated and cooled pair of poles. They were convex in the direction of the heated pair and concave in the direction of the cooled pair. Their intention was also to use gas lenses to waveguide a laser beam. In fact, they found that

a chain of hyperbolic gas lenses could achieve stable beam transmission by alternately focusing the beam in the transverse direction and defocusing it in the other. However, there is a maximum temperature depending on the pole spacing above which the gas lens did not work. For transmission of beams without mode conversion, a quadratic distribution of gas temperature must be maintained.

Otis and Tremblay (1974) have observed a divergent gas lens effect in the cavity of a helical TEA laser. A thick diverging could be attributed to each turn of the helix. The index profile was parabolic for the first 2 μs after the excitation pulse, then it levelled off.

In 1985, a review paper was published by a member of a group at the Luykov Institute of Heat and Mass Transfer in Minsk, U.S.S.R. (Martynenko *et al.* 1985). This publication describes scientific studies on gas lenses between 1967 and 1972. The intention of this group was also to use gas lenses in transmission lines. Typical lenses were 25 mm in diameter, focusing beams at extremely long focal lengths 25 m. Although no mention is made of the focal spot quality, the Minsk group investigated a variety of lens designs and different flow configurations. In a circular gas lens, light beam focusing is performed in a heated horizontal tube. Gas motion is maintained by the free convection arising from the temperature difference in vertical tubes. In the central tube the gas, being heated by electric coils, goes upwards; in the side channels it is cooled and moves downwards. Other designs included a lens with twisted flow and a lens with a porous wall. Other constructions by this group were colliding streams of gas to produce

a lens shaped region of refractive index difference, and a 'hyperbolic' lens comprising sets of opposed cool and heated rods, through which the beam is passed. The Minsk group was the first to use a spinning pipe gas lens.

In the mid-eighties, the laser group at the University of Natal, Durban has been quite active in the development and applications of gas lenses. Michaelis *et al.* (1986) investigated the refractive effects of flames produced by different configurations of nozzles. The results were that flat oxy-acetylene flames are capable of focusing an aligned laser beam to a line focus. A heated vertical pipe was used to create a long focal length lens for laser beams of a few cm in diameter. This was used for drilling holes in metal sheets. However, aberrations due to overheating and turbulence affected the quality of the lens. The lens worked best when the burner was switched off and in the absence of any motion in the lab. One major difference of this lens is that no gas was injected into the pipe. Notcutt *et al.* (1988), working independently, succeeded in maintaining a continuous focus in a horizontal pipe by using a combination of gas jet and spinning pipe. They found that if the pipe was rotated at less than 1 Hz, the convection patterns were unaffected except for a slight tilt, but at higher speed of rotation of the pipe, momentary stable temperature gradients were created along the axis of the pipe.

These types of gas lenses were further developed and found to have some useful applications in laser physics. Waltham *et al.* (1989) used gas lenses to generate a laser produced plasma. Gas lenses are used for drilling and cutting metals (Michaelis *et al.* 1991a). A gas lens has also been used as an objective lens for a telescope (Michaelis *et al.* 1991b), when images of the

sun spots and moon were taken.

Cazalet *et al.* (1990) had observed a "bird wing" structure at the focus of horizontal gas lenses which had been removed by focusing a ruby laser into an SBS cell and reversed passing the reflected phase conjugate beam through the gas lens.

Properties of the spinning pipe gas lens were investigated by Lisi *et al.* (1994). They showed that a flat temperature distribution exists in the middle region of the pipe, while two regions of strong transverse thermal gradients were present near the edges of the pipe. They concluded that the optical quality of the lens would deteriorate as the optical aperture approached the pipe aperture, since rays would be refracted weakly at the walls of the pipe.

All the gas lenses discussed so far were continuous gas lenses. Michaelis *et al.* (1991a) proposed the use of pulsed gas lens as a solution to the optics problem in Inertial Confinement Fusion (ICF). The idea was pursued by Buccelato (1992) who carried out a series of experiments on a pulsed gas lens. It consisted of a system of generating converging shocks at high pressure which were instantaneously released into the atmosphere. This created a density gradient causing the laser beam to deflect. Buccelato *et al.* (1993b) further developed the colliding shock lens (CSL). They examined the gas lens effect achieved by colliding the shock waves. These shock waves, at suitable Mach number, collided in a nonlinear but orderly manner to create an axially symmetric cigar shaped expanding density distribution that can act as a graded index lens. Both focal length and effective diameter of the lens increased with

time.

The CSL has also been used as an intracavity Q-switch for ruby lasers (Lisi *et al.* 1994a).

Gas lenses have been proposed as focusing device for laser launch plants in a feasibility study on laser impulse space propulsion (Phipps *et al.* 1996).

E.1 Principles of thermal gradient gas lenses

E.1.1 The radial temperature distribution

The velocity and temperature profiles created in thermal gradient gas lenses (TGGLs) can be derived using the convection heat transfer theory. The relevant information has been taken from the works of Bejan (1984) and Marcuse (1982). The relevant equations involved are the Navier-Stokes equations. These are derived using the conservation of mass, momentum and energy (first law of thermodynamics).

In the case of the TGGL, pressure changes are negligible and we can assume zero internal heat generation, constant material properties and a steady-state condition. The Navier-Stokes equations under these conditions become

$$\nabla \mathrm{v} = 0 \tag{E.1}$$

$$\varrho(\mathrm{v}.\nabla)\mathrm{v} = \Xi\nabla^2\mathrm{v} + F_b \tag{E.2}$$

$$\varrho.C_{p_r}(\mathrm{v}.\nabla)M = \kappa_t\nabla^2 M \tag{E.3}$$

where

v is the velocity,

ϱ is the density,

Ξ is the viscosity,

C_{p_r} is the specific heat capacity at constant pressure,

M is the temperature,

κ_t is the thermal conductivity of the gas, and

F_b is a body force which is responsible for natural convection.

Equation (E.1) expresses the conservation of mass and it is assumed that under steady state condition, there will be no net mass flow into any volume element. The conservation of momentum (equation (E.2)) yields the acceleration of a volume element (LHS) due to the forces on this particular volume element originating from viscous friction (first term RHS) and external body forces. The remaining Navier-Stokes equation, the conservation of energy (equation (E.3)), equates the energy flow into a volume element due to convection (LHS) to energy losses caused by heat conduction (RHS).

Inside a uniformly heated laminar flow tube, the radial velocity ϑ will vanish at any point on the axis or parallel to the axis of the tube at sufficient distance from the tube orifice. Under these conditions, using the azimuthal symmetry of the problem and the conservation of mass (equation(E.1)), we find that the axial velocity $\overline{u}$ is only dependent on the radial distance r from the axis $\overline{u} = \overline{u}(r)$.

In cylindrical coordinates, the equation for conservation of energy be-

comes

$$\varrho.C_{p_r}.\overline{u}(r).\frac{\partial M}{\partial x} = \kappa_t(\frac{\partial^2 M}{\partial r^2} + \frac{1}{r}\frac{\partial M}{\partial r} + \frac{\partial^2 M}{\partial z^2}) \tag{E.4}$$

where x is the axial coordinate. The left hand side of equation (E.4) represents the axial convection, the first and second term on the right hand side represent the radial heat conduction and the third term the axial heat conduction (Bejan 1984). For average axial velocities V the axial conduction is negligible compared to the other effects. A scale analysis shows that the condition for this approximation is

$$\mathrm{V}.\phi_{\mathrm{tube}} \gg \frac{\kappa_t}{\varrho.C_{p_r}} \tag{E.5}$$

where ϕ_{tube} is the diameter of the tube. Hence equation (E.4) further reduces to

$$\varrho.C_{p_r}.\overline{u}(r).\frac{\partial M}{\partial z} = \kappa_t(\frac{\partial^2 M}{\partial r^2} + \frac{1}{r}\frac{\partial M}{\partial r}) \tag{E.6}$$

It has been shown (Bejan 1984) that $\dfrac{\partial M}{\partial z}$ is constant everywhere inside the tube. This condition holds for uniform wall heat flux in regions where the thermal diffusion has reached the axis.

In this case equation (E.6) takes the form

$$\overline{u}(r) = \text{constant} \cdot (\frac{\partial^2 M}{\partial r^2} + \frac{1}{r}\frac{\partial M}{\partial r}) \tag{E.7}$$

where all the other quantities have been absorbed in the constant.

According to equation (E.7), a uniform velocity profile $\overline{u}(r) =$ constant leads to a parabolic temperature profile which can be written in a normalized

form as

$$\frac{M(r) - M_{r=0}}{M_w - M_{r=0}} = \left(\frac{r}{r_{p_r}}\right)^2 \tag{E.8}$$

where r_{p_r} is the radius of the pipe, $M_w = M(r_{p_r})$ the wall temperature and $M_{r=0}$ the temperature on the tube axis.

With the temperature profile known, the refractive index profile can be calculated.

E.1.2 Radial Refractive Index Profile

The refractive index of an ideal gas at constant pressure varies with temperature. If μ is the refractive index at temperature M and μ_o is the refractive index at temeprature M_o then they are related as

$$\frac{\mu - 1}{\mu_o - 1} = \frac{M_o}{M} \tag{E.9}$$

Rearranging equation (E.9) we get

$$\mu - \mu_o = (\mu_o - 1)\frac{M_o - M}{M} \tag{E.10}$$

For small temperature changes $M - M_o \ll M_o$, equation (E.10) becomes

$$\mu - \mu_o = (\mu_o - 1) \cdot \frac{M_o - M}{M_o} \tag{E.11}$$

In the case of the TGGL with refractive index μ_w close to the inside of the tube walls, $\mu(r)$ at a distance r from the tube axis and $\mu_{r=0}$ on the axis, a normalized refractive index can be defined as

$$\frac{\mu_{r=0} - \mu(r)}{\mu_{r=0} - \mu_w} \tag{E.12}$$

Using equation (E.11) we get

$$\frac{\mu_{r=0} - \mu(r)}{\mu_{r=0} - \mu_w} = \frac{M(r) - M_{r=0}}{M_w - M_{r=0}} \tag{E.13}$$

This means that the normalized temperature and refractive index profiles are equal. We can therefore conclude from equation (E.13) that the refractive index profile is also parabolic.

The most common type of TGGL is the spinning pipe gas lens (SPGL). We will now consider the effect of spinning the pipe. The focal length of the SPGL is derived mathematically in appendix E.

E.2 Effect of spinning the pipe

TGGLs are long focal length and small aperture devices. The obvious difficulty that is encountered in scaling up the aperture while keeping the focal length short is the consequent increase of the temperature radial gradients. These larger gradients give rise to convection currents which impair or even destroy the action of the lens (Gloge 1967). Some improvement could be obtained by spinning the lens (Notcutt 1988).

When the pipe is spun, warm air is centrifuged out from the near wall region while cold air is sucked in down the tube axis from both ends of the pipe (Fig.(E.1)). Sudden and more rapid rotation distributes the warm air uniformly around the circumference, momentarily creating favourable temperature and density profiles. These density distributions were found to give a good but high f-number lens. However, warm air flowing out is prone to Rayleigh Taylor instabilities, which may, in our case generate turbulence and

gas mixing. For this reason it is important not to overheat the pipe.

E.3 Spinning Pipe Gas Lenses

E.3.1 Description of the Spinning Pipe Gas Lenses

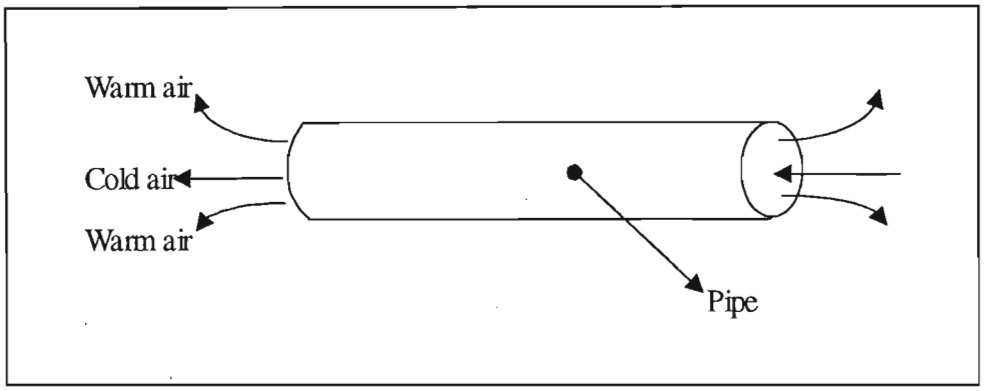

Figure E.1: Schematic view of the air flow inside a spinning pipe gas lens.

Two mechanically slightly different kinds of spinning pipe gas lenses (SPGLs) have been used. Both of them are of self-feeding type SPGLs. There are however some few requirements that must be observed on the pipe requirements:

(i) it must be straight within a good degree of accuracy in order to be vibration free when spun.

(ii) it must be made of a material which has a low thermal expansion to avoid deformations, since the latter will introduce vibrations when the pipe is spun.

Any vibration will destroy the steadiness of the gas flow and of the temperature profile, impairing the optical quality.

The older type gas lens, referred as SPGL1, consists of a 140 cm length stainless steel pipe with external diameter 40 mm. The tube has been wrapped with a standard heating tape. It is enclosed in a perspex casing to prevent wind from interfering with the operation of the gas lens. The pipe is mounted on ball bearings that allow rotation. It is spun by two standard sewing machine motors. Both the heater tape and the motors are powered by variacs. Electrical connection between the heater tape and the variac is achieved by a pair of carbon brushes. It is possible to vary independently both rotation speed and pipe temperature in order to optimise the performance. Typical values are 10 Hz[1] rotation frequency and the tube wall temperature up to 383 K. A focal length of about 8.0 m has been obtained.

The second SPGL, referred as SPGL2, is a pipe of exactly the same specifications, except for a smaller external diameter 35mm. The tube is made of thick wall cast iron and is driven by one pair of rollers at one end. The tube is spun by a standard sewing machine motor (belt drive). Heater tapes have been wrapped around the tube to provide a uniform heating of the tube. The pipe was secured by two G clamps on the stands so that there was less vibration when it spun. The focal length of SPGL 2 is about 6 m, 2 m less than SPGL1, when operated under the same conditions as SPGL1. However, if the pipe is heated at a lower temperature and spun at a higher speed, the focal length increases to 8.0 m. It should be noted that both SPGL 1 and SPGL 2 are varifocal lenses. The speed of rotation and temperature of the pipe are crucial in determining the focal length. Photographs of both gas

[1]The heat transfer rate depends on the relative rotational velocity of the gas and 10 Hz has experimentally been found to be optimal. At higher frequencies large scale turbulence sets in which degrades the optical quality.

lenses are shown in figs.(E.2) and (E.3). SPGL 1 and 2 are used as objective lenses of a camera to make photograph of the Sun spots as well as the maria on the Moon. The observations are described in section 9.9.

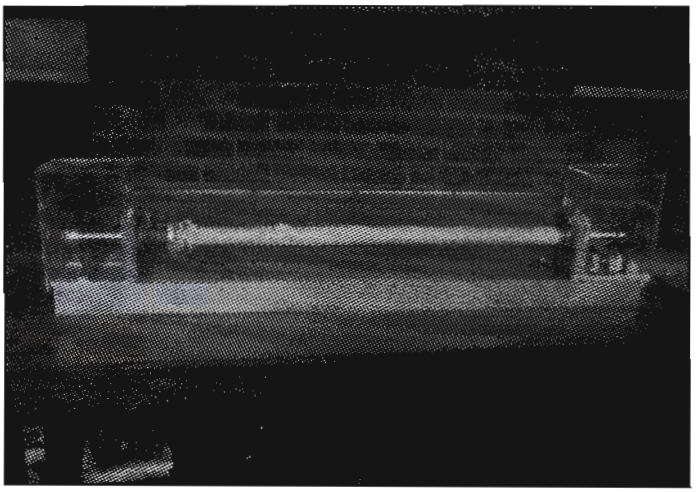

Figure E.2: Photograph of SPGL1.

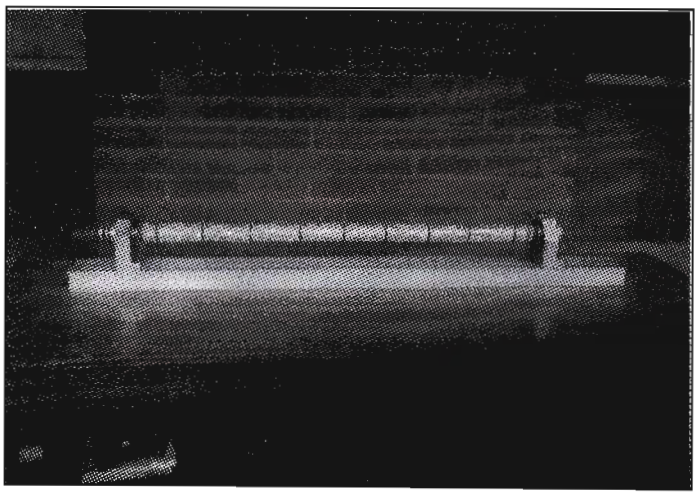

Figure E.3: Photograph of SPGL2.

E.4 Alignment Procedure

The SPGL is aligned with the tracker using a He-Ne laser as shown in fig.(E.4). The He-Ne is clamped at one end of the gas lens, at same height as the gas lens, so that the laser beam goes centrally through the pipe and strikes the mirror. Two cross-hairs are placed immediately after the SPGL. The cross-hairs are adjusted so that the laser beam passes through both of them. The tracker is then moved upward and sideways until the laser beam strikes the mirror at its centre. The tracker is inclined to the vertical at half the geographical latitude of Durban, which is 30^0 S. The SPGL is positioned in such a way that the focus of the gas lens lies inside a Wendy house which is located 9 m away from the SPGL.

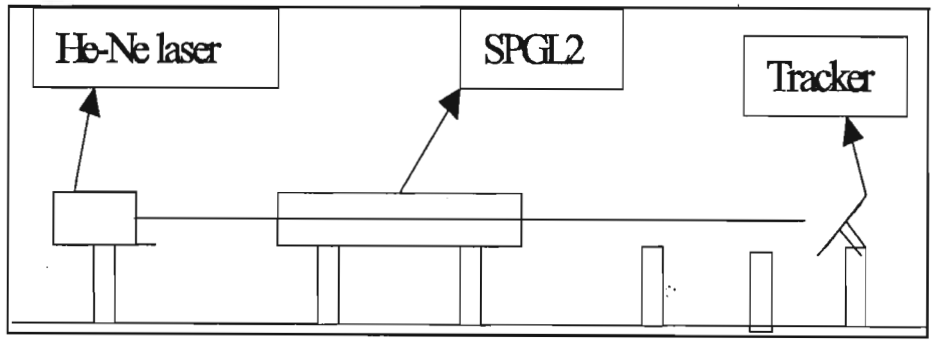

Figure E.4: Alignment of the SPGL.

E.5 The tracking system

The tracking system (referred as tracker in fig.(E.4)) was originally developed by the UND laser research group to compensate for the relative motion between the Earth and the observed planets. Fig.(E.5) shows a photograph of the tracker used. The tracker consists of a mirror mounted on a fork-like

support that rotates about an axis identical to the polar axis. The mirror can also be tilted about an axis perpendicular to the polar axis and hence acts as a declination axis. The rotations are achieved by stepper motors mounted behind the mirror. A gear ratio of 3000:1 has been fitted which allows smooth rotation of the mirror at an adjustable speed. Once the mirror is set to a star, it tracks automatically by rotation about a single axis, the polar axis. The tracker works quite well for short time tracking.

The tracking system is tilted from the vertical position at an angle equal to half the geographical latitude of Durban (taken to be 30^0S). This is achieved by tilting the tracker from the vertical at an angle 15^0.

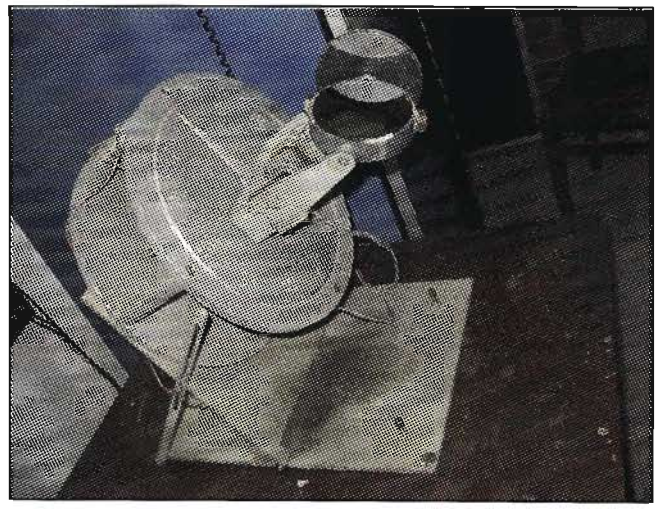

Figure E.5: The tracking system used in the SPGL experiment.

The tracker is positioned along the celestial pole with the mirror facing the south. From observations made with the SPGLs pointing due South, it is quite difficult to locate accurately the direction of the celestial pole due to the lack of a polar star and precision instruments. However, by comparing

the calculated and observed positions of the Sun during the day at a given time, an approximate location of the celestial pole can be found.

In order to make any astronomical observation, the mirror must be aligned with the gas lens (fixed horizontally) so that light reflected from it must pass through the optical axis of the lens. This requires precise alignment of the gas lens otherwise multiple reflections inside the pipe will occur which will distort the quality of the image. The alignment procedure is described below.

E.6 Experimental set up

Fig.(E.6) shows the experimental arrangement. The SPGL is positioned horizontally in front of the tracking system so that it faces south. The tracking system is found in front of the SPGL and is positioned in such a way that the mirror reflects light along the axis of the pipe. All observations are made inside a wendy house which is 9 m away from SPGL.

A horizontal stand between the tracker and the SPGL serves as a support for cross-wires for the alignment of the gas lens. The tracker is controlled remotely by means of a small joyce stick box. The variacs that powered the heating and spinning of the pipe are controlled from inside the Wendy house.

The SPGL, the tracking system and the Wendy house are located on the roof of the Desmond Clarence building which is five storeys high. They are arranged so that the Wendy house is north of the SPGL. Observations are made from the East to the West.

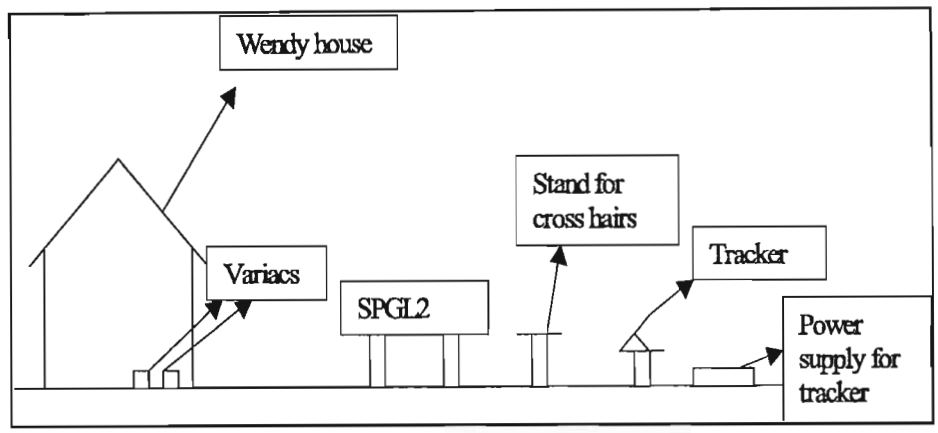

Figure E.6: Experimental arrangement of the SPGL.

E.7 Operation of the SPGL

Both SPGL 1 and SPGL 2 are spun at the same speed but heated at slightly different temperatures. SPGL1 was heated to 86 ^{0}C in order to have the focus inside the Wendy house whereas SPGL2 was heated at 60 ^{0}C. A thermocouple has been used to measure the temperature at the centre of the pipe. The advantage of this device is that it has a probe of length 20.5 cm that can be inserted easily inside the pipe to measure temperature at different points.

The SPGL is first preheated for some time before it is spun. During this time, the tracker is moved by means of the remote control to some star, example the sun, until the light passes centrally through the optical axis of the pipe. At night time, cross-hairs are used to align, for example the moon, in the centre of the pipe. The pipe is then spun at a suitable speed until a focus is obtained. The image formed by the SPGL is now magnified. In order to reduce the size of the magnified image by the SPGL, a 30 cm focal length convex lens is placed at 8 m from the centre of the SPGL, which is

about the focal length of the SPGL. The following calculation shows how the magnification of the image formed by the SPGL is reduced by the convex lens.

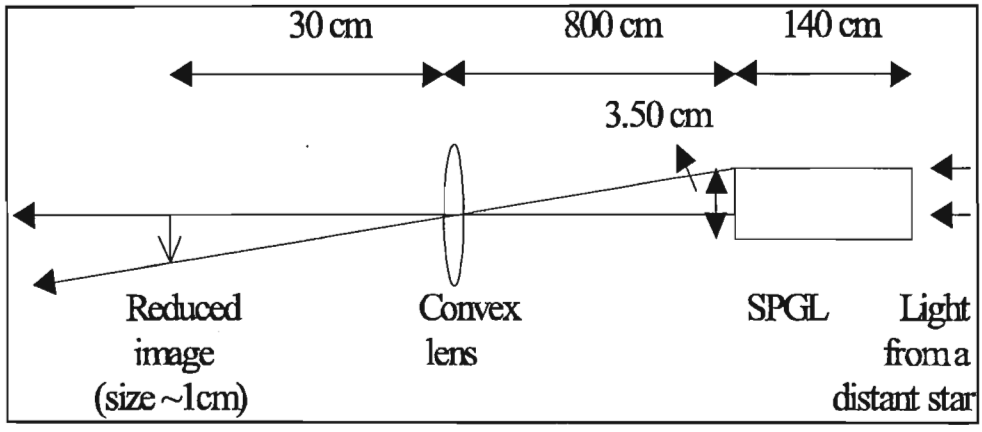

Figure E.7: Diagram showing calculation of field of view of SPGL. The scales are exaggerated.

Fig.(E.7) shows a simple sketch to calculate the magnification of the SPGL.

The magnification is given by

$$\begin{aligned} \text{magnification} &= \frac{\text{Image distance}}{\text{Object distance}} \\ &= \frac{800}{30} \\ &= 26.7 \end{aligned}$$

E.8 Observations

E.8.1 Sun spots

These are observed as dark spots which move across the surface of the Sun from west to east. The reason why the spots appear dark is that they are

1600 ^0C cooler than the surrounding solar surface. The sun spots usually show at intermediate solar latitudes and proceed towards the solar equator. The number of sunspots varies periodically over an 11-year cycle, driven by magnetic field fluctuations caused by convective energy flow from the Sun's core. Zeeman splitting of spectral lines indicates magnetic fields of up to 4 kG in sun spot regions. The magnetic field lines emanate perpendicular from the sun spots and spread into the space outside the sun in a manner similar to an electric field dipole. Sun spots often occur in pairs or groups of pairs of different polarity. They have diameters of up to 5×10^4 km and the average lifetime of an individual spot is a few days.

E.8.2 Experimental Procedure and Results

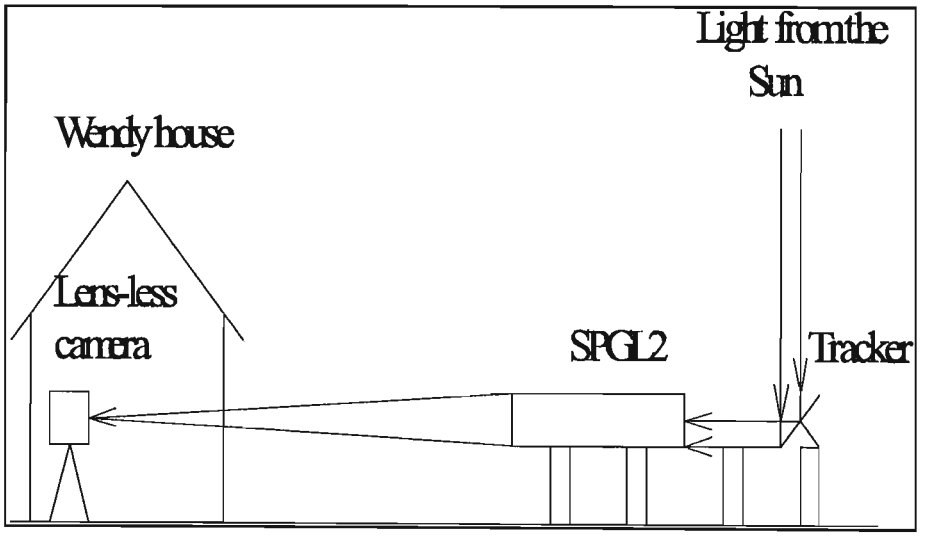

Figure E.8: Experimental set-up to capture image of the sun using a gas lens telescope.

The sun is first tracked so that light from it goes centrally through the tube of the SPGL 2. Meanwhile the pipe is heated to 60 ^{0}C, and the temper-

ature is measured with a thermocouple. When the pipe is allowed to spin, a clear image of the sun is obtained inside the wendy house. Fig.(E.8) shows the experimental set up. It should be noted that the SPGL focal length depends on the temperature and rotating speed of the pipe. The quality of the lens also fluctuates. An excellent focus may exist for three or four seconds. Then follows a second interval of degraded viewing. This is a typical behaviour for all thermal gradient gas lenses.

The SPGL forms an image of the sun about 8 m from the axial centre of the pipe which can be observed with a white screen inside the Wendy house. Due to the momentary focus of the SPGL, a degraded image of a sun spot can be seen below the solar equator (Fig.(E.9)). The exposure time of the camera was set to $\frac{1}{1000}s$ on 100 ASA film. The photograph was taken with the objective lens of the camera removed.

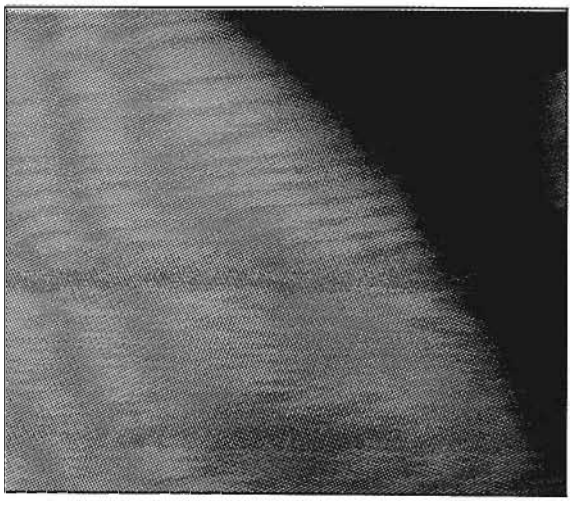

Figure E.9: Photograph of the sun taken with a gas lens telescope. A degraded image of a sun spot can be identified near the terminator of the sun.

E.8.3 The Moon

The moon has always fascinated mankind throughout the ages. By simply viewing with the naked eye, one can discern two major types of terrain: relatively bright highlands and darker plains. By the middle of the 17th century Galileo and other early astronomers made telescopic observations, noting an almost endless overlapping of craters. It has also been known for more than a century that the moon is less dense than the Earth. Although a certain amount of information was ascertained about the moon before the space age, this new era has revealed many secrets barely imaginable before that time. Current knowledge of the moon is greater than for any other solar system object except the Earth. This lends to a greater understanding of geologic processes and further appreciation of the complexity of terrestrial planets.

The moon is 384,403 km distant from the Earth. Its diameter is 3476 km. Both the rotation of the Moon and its revolution round the Earth takes 27 days, 7 hours, and 43 minutes. The dark, relatively lightly cratered *maria* cover about 16% of the lunar surface and are concentrated on the nearside of the moon, mostly within impact basins. This concentration may be explained by the fact the moon's centre of mass is offset from its geometric centre by about 2 km in the direction of the Earth, probably because the crust is thicker on the far side.

E.8.4 Experimental Procedure and Results

Fig.(E.10) shows the experimental set up used to capture the image of the full moon. The speed of rotation of the pipe is crucial to obtain a good focus.

In order to prevent any stray light from the Durban harbour from interfering with the moon light, a PVC pipe has been used to guide the moon light to the camera inside the Wendy house. The focal length of the gas lens is about 8.0 m.

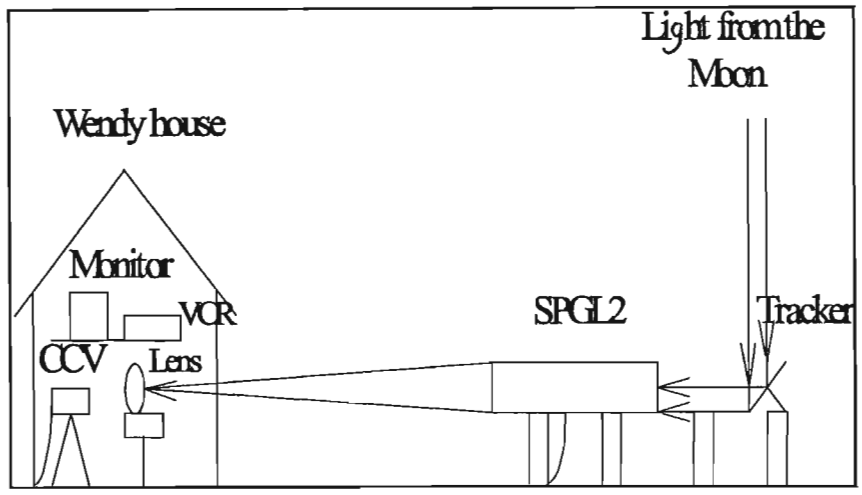

Figure E.10: Experimental set-up for observation of the Moon.

In order to enhance the quality of the image, a 30 cm focal length biconvex lens was placed at 8.30 m from the SPGL. A CCD camera was placed immediately after the biconvex lens. A camera lens with an adaptor was fitted to the CCD camera. The camera lens was set on infinity and its aperture wide open. The CCD camera was connected to a VCR and a monitor where the image was video-taped and later processed using a frame grabber. A magnified image of the full moon was obtained on the monitor. By moving the tracker, the whole moon could be viewed. Selected frames of the tape were "extracted" using a frame grabber. Photographs of the moon were then taken on the monitor using a 100 ASA film. The photographs were then compared with a lunar map to identify the *maria*. Fig.(E.11) shows photograph

of the moon as seen by a gas lens telescope. Some of the *maria* that can be identified are: *mare tranquilitatis, mare fecunditatis and mare nectaris.*

Figure E.11: Image of the moon as seen by a gas lens telescope.

E.9 Summary

Two spinning pipe gas lenses (SPGLs) are decribed and used to make astronomical observations of the moon and the sun spots. The SPGL is a varifocal length lens which depends on the temperature of the pipe and the rotation speed at which it is being spun.

The two SPGLs (SPGL 1 and SPGL 2) are operated at a rotation frequency of 10 Hz and heated up at a temperature of 383 K. The focal lengths obtained under these conditions are 8.0 m and 6.0 m respectively. The quality of the lenses fluctuates and momentarily an excellent focus can be obtained. The sun spot image obtained using SPGL 2 is not of good quality due to the fluctuation of the focus. On the other hand, a reasonably good image of the moon has been obtained with SPGL 1.

Appendix F

Calculation of the focal length of the spinning pipe gas lens

For paraxial rays, the optical path $d\Psi$ can be approximated by the path in the axial direction dx i.e. $d\Psi \approx dx$. The ray equation can be written in the form (Born and Wolf 1965)

$$\frac{d}{dx}\left(\mu\frac{dr}{dx}\right) = \nabla\mu \tag{F.1}$$

where μ is the refractive index of air and r is the distance along the radius of the spinning pipe gas lens (SPGL).

Expanding the left hand side of equation (F.1)

$$\frac{d}{dx}\left(\mu\frac{dr}{dx}\right) = \frac{d\mu}{dx}\frac{dr}{dx} + \mu\frac{d^2r}{dx^2} \tag{F.2}$$

In most gas lenses, the axial temperature gradient can be neglected.

The refractive index μ at the temperature M and the refractive index μ_o at the temperature M_o are related as

$$\frac{\mu - 1}{\mu_o - 1} = \frac{M_o}{M} \tag{F.3}$$

Using equation (F.3) the approximation $d\Psi \approx dx$ can be extended to the axial refractive index gradient.

Hence equation (F.2) further reduces to

$$\frac{d}{dx}\left(\mu \frac{dr}{dx}\right) = \mu \cdot \frac{d^2r}{dx^2} \tag{F.4}$$

Hence substituting in equation (F.1)

$$\frac{d^2r}{dx^2} = \frac{1}{\mu} \cdot \frac{\partial \mu}{\partial r} \tag{F.5}$$

The parabolic refractive index profile is given by

$$\frac{\mu_o - \mu_r}{\mu_o - \mu_w} = \left(\frac{r}{r_{p_r}}\right)^2, \tag{F.6}$$

where μ_w is the refractive index of the air at the wall of the pipe and r_{p_r} is the radius of the pipe.

Substituting equation (F.6) in equation (F.5) yields the differential equation

$$\frac{d^2r}{dx^2} + \frac{2 \cdot (\mu_o - \mu_w)}{\mu_r \cdot r_{p_r}^2} \cdot r = 0 \tag{F.7}$$

μ_r in this equation can be approximated by μ_o since it varies only marginally with r. On the other hand, the refractive index at the wall μ_w cannot be approximated by μ_r since the wall of the SPGL is at a higher temperature. We therefore have the following solution for a ray that enters the gas lens axially $\left(\left(\frac{dr}{dx}\right)_{x=0} = 0\right)$ at a distance $r_{x=0}$ from the cylinder axis:

$$r(z) = r_{x=0} \cos\left[\left(\frac{2(\mu_o - \mu_w)}{\mu_o r_{p_r}^2}\right)^{\frac{1}{2}} \cdot x\right] \tag{F.8}$$

If the refractive index outside the gas lens is not substantially different from the refractive index inside, the ray will leave the gas lens without undergoing refraction at a point given by $x = L$ and $r = r(L)$, where L is the length of the gas lens. From this point onwards the ray will proceed linearly in a direction according to $\frac{dr}{dx} = \left(\frac{dr}{dx}\right)_{x=L}$

The path outside the gas lens will thus be given by

$$r(x) = (L - x) \cdot r_{x=0} \cdot \sqrt{\Theta} \cdot \sin(L\sqrt{\Theta}) + r_{x=0} \cos(L\sqrt{\Theta}) \tag{F.9}$$

where $\Theta = \left(\frac{2\,(\mu_o - \mu_w)}{\mu_o \cdot r_{p_r}^2}\right)$

The beam crosses the axis at $x = f$ with $r(f) = 0$ where f is the focal length of the the SPGL.

From equation (F.9), we obtain

$$f = L + \frac{\cot\left(L\sqrt{\Theta}\right)}{\sqrt{\Theta}} \tag{F.10}$$

In the case of the SPGL, a simplified form for the focal length can be derived.

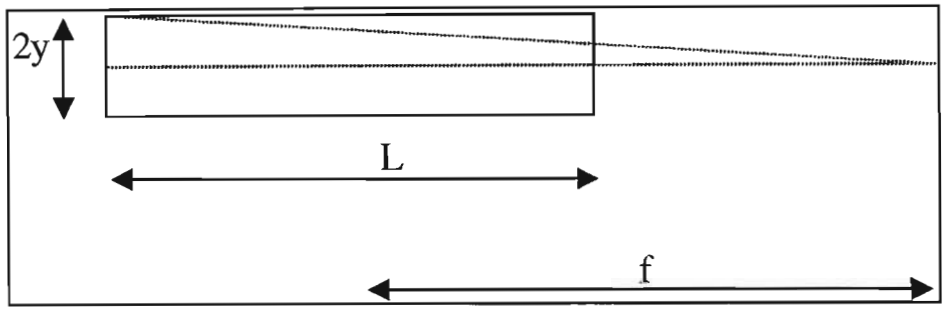

Figure F.1: Simple geometry to calculate the focal length of the SPGL.

Consider the geometry shown in fig.(F.1). The angle of deflection θ, of a paraxial ray is proportional to the length, L, of the tube and the refractive index gradient:

$$\theta = L \cdot \frac{\Delta\mu}{y} \tag{F.11}$$

where y is the diameter of the tube and μ is the refractive index of air in the tube.

The outer rays intersect the axis at a distance f such that $r = f \cdot \theta$ (fig. (F.1)) where θ is in radians and is small.

Using equation $\frac{\Delta\mu}{\Delta\mu_w} = \frac{\Delta M}{M_o}$ and equation (F.11) we have

$$f = \frac{r}{\theta} \tag{F.12}$$

$$= \frac{r \cdot r}{L \cdot \Delta\mu}$$

$$f = \frac{r^2}{L \cdot \Delta M} \cdot \frac{M_o}{\Delta\mu_w} \tag{F.13}$$

Equation (F.13) can be further simplified if the temperature at the centre of the pipe, M_o and the change in refractive index at the wall of the pipe, $\Delta\mu_w$ are known. Assuming the air at the centre of the pipe is at room temperature where M_o is taken to be 300 K. The refractive index of air differs from unity by the small amount $\Delta\mu_w \sim 10^{-4}$.

Therefore, $\frac{M_o}{\Delta\mu_w} \sim 10^6$. Then equation (F.13) becomes

$$f \approx 10^6 \cdot \frac{r^2}{L \cdot \Delta M} \tag{F.14}$$

First validation of stratospheric temperature profiles obtained by a Rayleigh LIDAR over Durban, South Africa

H. Bencherif[a], A. Moorgawa[b], B. Morel[a], M. Michaelis[b], J. Leveau[a], A. Hauchecorne[c], J. Porteneuve[c] and D. Faduilhe[a]

The first measurements of atmospheric temperature above a Durban site, obtained with a Rayleigh LIDAR system, are presented. The results were collected between 21 April and 30 June 1999. In order to validate the LIDAR measurements, they were compared with the daily observations of the South African Weather Bureau as well as the monthly averages calculated for the Durban site from the CIRA-86 climatological model. This general comparison is only possible for the lower section of the LIDAR profile (15–30 km) and gave satisfactory agreement between the different values (LIDAR, SAWB and CIRA-86): the discrepancies between the LIDAR measurements and the others did not exceed 5 K. For altitudes greater than 30 km, the LIDAR temperatures were consistently above those of the CIRA-86 model, within ±5 K. The observed middle-atmospheric temperature differences between the LIDAR and the CIRA-86 model could have been caused by the background stratospheric aerosols as well as by perturbations generated by wave propagation.

Background

LIDAR (acronym for LIght Detection and Ranging) can be used to probe the atmosphere optically. It is an instrument that, owing to the particular properties of the interaction between light and matter, yields an original contribution by measuring parameters that are inaccessible to other methods. It is able to measure the optical properties of dust and droplets, held in suspension in the atmosphere. LIDAR has higher precision and better vertical resolution than satellites and actually serves to calibrate them. As a remote sensing system, it is particularly well suited to the observation of physico-chemical parameters:[1]

- humidity and temperature soundings; localization of aerosols and their transport mechanism,
- the concentration of aerosols and particles in the atmosphere: Rayleigh-Mie LIDAR,
- wind and turbulence measurements: Doppler LIDAR,
- concentration of various gases: DIfferential Absorption Lidar (DIAL).

Moreover, the interpretation of LIDAR measurements allows one to study dynamic processes in the atmosphere such as planetary and gravity waves.[3,6,8]

In the southern hemisphere, unlike the northern, the study of the dynamics of the middle atmosphere by direct observation suffers from an extremely low density of measurement sites. The installation in April 1999 of a Rayleigh LIDAR at the Durban site is part of a bilateral research programme aimed at understanding the contribution of dynamic processes to the phenomena that drive meridional exchanges through the southern subtropical barrier. By exploiting simultaneous measurements (such as LIDAR measurements) undertaken as part of a coordinated campaign at Réunion (tropical latitude: 20°S) and Durban (subtropical latitude: 31°S), it should be possible to characterize the dynamic activity at both sites and determine its role in the horizontal transfers. The first phase of this research programme consists of a campaign to validate the new LIDAR installed at the Durban site. The results, presented here, will allow the first assessment of the influence of wave activity on the thermal structure of the middle atmosphere above Durban. After describing the basic principles of LIDAR measurement, we give a brief technical description of the LIDAR system. There follows a description of the inversion method used to obtain vertical temperature profiles. The LIDAR results obtained during the April–June 1999 period are then compared with climatological observations (CIRA[a]-1986) and daily balloon sonde records (SAWB[b]).

LIDAR principle and instrumentation

The basic LIDAR principle consists of transmitting a laser beam into the atmosphere and processing the return signal (for a review of the topic of optical scattering, see ref. 5). Depending on which parameters and which atmospheric components are to be measured, the wavelength can be fixed or variable. The return signal is concentrated by the telescope and then transmitted to one or several detectors.

The atmospheric LIDAR, installed on the Durban campus of the University of Natal in April 1999, is of the Rayleigh type. It consists of a transmitter (a pulsed laser), a receiver (biaxial telescopes), a photomultiplier (PM) and an acquisition system controlled by a central unit (Fig. 1). The laser is a pulsed Nd:YAG[c]. The emitted wavelength is λ_e = 532 nm, obtained by doubling the YAG fundamental frequency: λ_0 = 1064 nm. The pulse repetition frequency is 10 Hz and the laser energy is about 300 mJ per pulse. The laser characteristics are given in Table 1. Laser light is transmitted into the atmosphere after passing through a system of mirrors and a Galilean telescope. This factor 10 beam-expansion system also reduces the divergence of the emitted beam by the same amount.

The telescopic reception system consists of two 445-mm parabolic mirrors. As can be seen from Fig. 1, the mirrors are held inside two long tubes which protect them from luminous interference (see Table 1 for the telescope parameters). After collection by the telescope, photons are transmitted by optical

[a]Laboratoire de Physique de l'Atmosphère, Université de la Réunion, France.
E-mail: hassan.bencherif@univ-reunion.fr
[b]School of Pure and Applied Physics, University of Natal, Durban, 4041 South Africa.
E-mail: moorgawaa@scifs1.und.ac.za
[c]Service d'Aéronomie du CNRS, Paris, France.
E-mail: alain.hauchecorne@aerov.jussieu.fr

[a]COSPAR International Reference Atmosphere.
[b]South African Weather Bureau.
[c]Yttrium aluminium garnet.

Table 1. Durban LIDAR specifications.

Transmitter		Receiver		Data processing	
SpectraPhysics GCR-150		Newtonian telescope		Photon counting	
Wavelength	532 nm	Diameter	445 mm	Max. count rate	100 MHz
Repetition rate	10 Hz	Focal length	2000 mm	Vertical resolution	150 m
Average power	300 mJ/pulse	Axial telescope separation	50 cm	Total number of bins	1024
Beam divergence (full angle)	0.7 mrad	Filter bandwidths	1.0 nm	Photomultiplier tube	Hamamatsu
Pulse width	6–7 ns	Number of channels	1		R1477

fibres placed at the focal point of each mirror, to the detection box which contains a collimator, an interference filter, and a photomultiplier tube.

The interference filter is centred on the emission wavelength λ_e of the laser and its bandwidth is $\Delta\lambda = 1$ nm. Placed between the arrival point of the fibre and the PM, it eliminates a large proportion of the parasite signal. The PM is contained in a Peltier effect cooling system, which reduces the dark current by lowering the cathode temperature. After amplification, the LIDAR return signal is numerically integrated and recorded with a vertical resolution $\Delta z = 150$ m.

Temperature retrieval method

To measure the temperature in the middle atmosphere we make use of the theory of molecular Rayleigh diffusion. The LIDAR return signal $S(\lambda_e,z)$ from a layer of thickness Δz at an altitude z can be calculated from the following equation:

$$S(\lambda_e,z)=\kappa_0\cdot\frac{\beta_t(\lambda_e,z)}{(z-z_0)^2}\cdot\exp\left\{-2\int_{z_0}^{z}\alpha_t(\lambda_e,u)du\right\}\cdot\Delta z, \qquad (1)$$

where α_t is the total extinction coefficient, β_t is the total backscattering coefficient, z_0 is the altitude of the site, κ_0 is a calibration constant which takes into account the acquisition parameters,

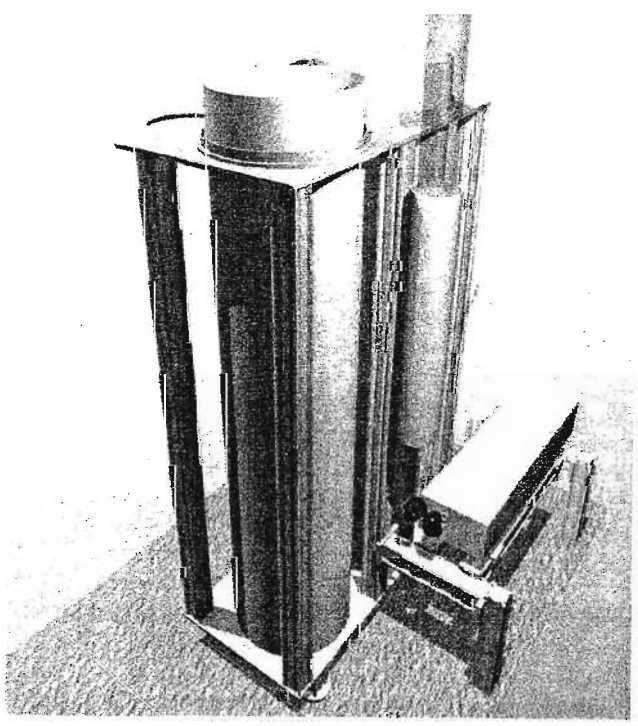

1. Schematic reconstruction of the transmission/reception system of urban Rayleigh LIDAR. The YAG laser is in the background on the the transmission telescope is the small tube on the right and the two reception telescopes are in the centre.

and u is an integration variable.

The intensity of the backscattered light depends on the components present in the atmosphere: mostly air molecules and aerosols. If we suppose that the observed layers are free of aerosols, the LIDAR signal is equal to the molecular density times a constant. Assuming a perfectly clean atmosphere, clear of aerosols, the vertical temperature profile can be directly deduced from the density profile if we treat the atmosphere as a perfect gas.[2] Knowing that the molecular backscattering coefficient β_m is proportional to the density of the atmosphere $n_m(z)$ $[\beta_m(z,\lambda_e)=n_m(z)\cdot\sigma_m(\lambda_e)]$, where σ_m is the Rayleigh backscatter cross-section, $n_m(z)$ can be obtained from Equation (1) following the expression

$$n_m(z)=\kappa_t\cdot S(\lambda_e,z)\cdot(z-z_0)^2\cdot T^2(z,z_\infty), \qquad (2)$$

where $T^2(z,z_\infty)$ is the atmospheric transmission coefficient between z and the top of the atmosphere z_∞, and

$$T(z_0,z)=\exp\left[-\int_{z_0}^{z}\alpha(\lambda,u)\cdot du\right].$$

This retrieval method depends on the aerosol concentration in the layers probed by LIDAR, because particular contributions to the backscattered signal can be important. Indeed, because of their size the aerosol backscatter cross-section $\sigma_{aer}(\lambda_e)$ at a given wavelength is much greater than that of atmospheric molecules:

$$\sigma_{aer}(\lambda_e)\propto\lambda_e^{-\alpha},\ \text{for } 1\le\alpha\le 2 \text{ and } \sigma_m(\lambda_e)\propto\lambda_e^{-4}.$$

Particles present in the atmosphere contribute to an overestimation of the backscattered signal. This retrieval method is limited to layers where the aerosol contribution is negligible.

The calibration constant κ_t does not depend on altitude but its value cannot be determined absolutely, as it depends on the power of the laser pulses, on the quantum efficiency of the PM as well as the transmission coefficient of the receiver. κ_t is determined by assuming that for a layer centred on a reference altitude z_{ref} (= 40 km), the atmosphere behaves as a reference atmosphere, deduced for the corresponding site and altitude and for the appropriate month from the CIRA-86 model. One then obtains the relative density $n_r(z)$:

$$n_r(z)=\frac{n_m(z)}{n_{cira}(z_{ref})}=\frac{S(\lambda_e,z)\cdot(z-z_0)^2}{S(\lambda_e,z_{ref})\cdot(z_{ref}-z_0)^2}. \qquad (3)$$

Thus, by taking the atmosphere to be a perfect gas in hydrostatic equilibrium and by initializing the pressure measurement at the top of the profile with an external value, the temperature profile can be deduced through successive integration downwards.

As mentioned above, when aerosols are present, one overestimates the backscattered signal and consequently underestimates the corresponding temperature values. Figures 2(b) and (c) highlight the limits of temperature derivation using a Rayleigh LIDAR when the probed layers contain aerosols.

The temperature uncertainty depends on the initialization

procedure described above, whose contribution decreases rapidly with decreasing altitude (downward and iterative integration), and becomes negligible compared to the background sky noise.[7] Nevertheless, before interpreting the LIDAR signal, it is subjected to many numerical treatments with the objective of compensating for the exact number of photons backscattered by the atmosphere. This is because LIDAR measurements suffer from various types of noise and errors due to the method used or to the instrumentation, which affect the laser signal. One distinguishes two categories of noise:[7]

- noise that affects the lower part of the LIDAR profile:
  - that due to detector saturation caused by the high density of the lower layers,
  - optical alignment errors due to parallax and image defocusing of the backscattering volume,
  - errors in the correction of the transmission signal for ozone absorption and for aerosol extinction,
- noise that affects the upper part of the LIDAR profile:
  - background sky noise [BSN],
  - errors due to the initialization procedure at the top of the atmosphere with an externally determined value.

To minimize the errors that can arise with the LIDAR output at low altitude, we used an electronic shutter. This protected the photomultiplier from being saturated by strong backscatter from the lower layers of the atmosphere. This explains why the LIDAR raw data presented here are limited to altitudes above a lower limit z_0 (≈15 km). However, with the present configuration of the Durban LIDAR, other errors such as those due to focalization and to parallax are difficult to quantify. The only way to do this is to compare the LIDAR results with other measurements such as those of the radiosonde programme.

We note that the installation of a second acquisition channel specifically aligned for the observation of the lower layers would provide a means of optimizing the optical alignment of the existing channel and of minimizing the optical effects of focalization and parallax.

As to the errors occurring with the upper part of the LIDAR profile, the dominant factors are statistical errors due to photon counting and background sky noise. The latter is easy to evaluate. The backscattered photons arrive at the PM photo-cathode in a random manner governed by Poisson's statistical law. The standard deviation is then given by the square root of the incident signal.

$$\sigma_{S(z)} = \sqrt{S(z)}. \tag{4}$$

The uncertainty in the density $n(z)$ and therefore on the temperature $T(z)$ can thus be written as

$$\frac{\Delta n}{n} = \frac{\sigma_{S(z)}}{S(z)} = \frac{1}{\sqrt{S(z)}}. \tag{5}$$

This statistical error is reduced when the temporal and/or spatial resolution are degraded. Thus, all temperature profiles shown hereafter have been smoothed and sampled with a vertical resolution of $\Delta z = 1$ km.

The effect of the BSN increases rapidly with altitude, owing to the exponential decrease of atmospheric density and instrumental limitations with the dynamic range of the signal (over 4 orders of magnitude). The BSN parameter is estimated over altitude in the range $100 \leq z \leq 150$ km). The useful signal $[S_{LIDAR}(z) = S_{RAW}(z) - S_{NOISE}(z)]$ is the total number of backscattered photons from different atmospheric layers. This is estimated by taking into account the entire range of noise affecting the LIDAR measurement $[S_{NOISE}(z)]$. Plot (a) of Fig. 2 gives an example of

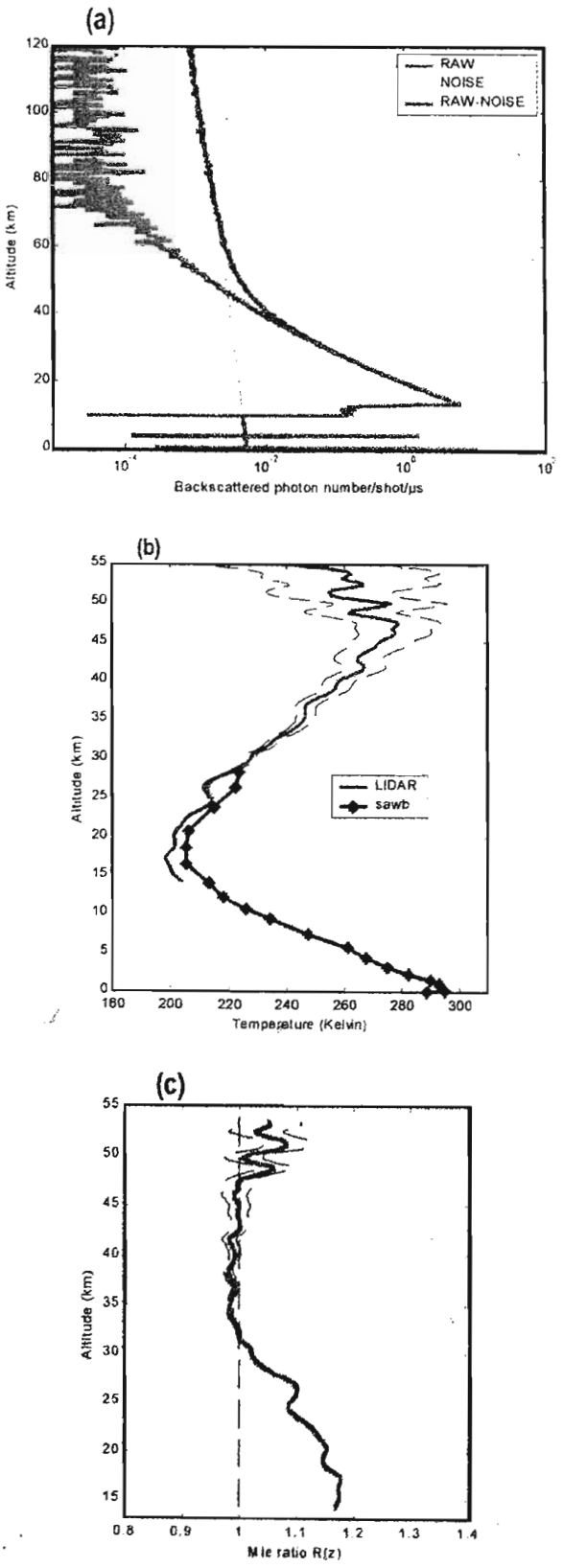

Fig. 2. (**a**) LIDAR measurement on 8 June 1999 (198 000 shots). The total noise (discontinuous green line) follows a parabolic parameter over the 100–150 km range of altitude. The useful signal (continuous red line) is that from which the total noise is subtracted. (**b**) LIDAR temperature profile for 8 June 1999 (continuous blue line). For comparison purposes, the June climatological profile and the SAWB radiosonde temperature measurement for the same day over Durban are superimposed. The discontinuous lines that frame the LIDAR profiles indicate the total measurement error. (**c**) the corresponding Mie ratio $R(z)$ profile, with $R(z) = \frac{\beta_t(\lambda_e, z)}{\beta_m(\lambda_e, z)} = 1 + \frac{\beta_{aer}(\lambda_e, z)}{\beta_m(\lambda_e, z)} \geq 1$.

LIDAR acquisition and of the noise contribution.

As mentioned above, temperature profiles are obtained from density profiles. Computation of the density profile requires pressure initialization at the top of the profile. To initialize the pressure profile, it is assumed that the values of this parameter at the top of profile are, on average, equal to those of a standard atmospheric model (CIRA-86). Taking into account the exponential decrease in atmospheric pressure with altitude, the uncertainty due to this initialization (which is estimated to be 15% at the initialization level) shows that this error rapidly becomes negligible with decreasing altitude.

The temperature obtained, even with this pressure initialization, can be considered as absolute and the estimated error is due mainly to the photon noise (BSN). The temperature profile showed ɔy (b) of Fig. 2 is a result of the retrieval ɱethod described above. In this case :he total error ΔT in temperature ncreases with height as follows:

- $\Delta T \leq 3$ Kelvin for $z \leq 35$ km,
- $\Delta T \leq 10$ Kelvin for $z \leq 45$ km,
- $\Delta T \leq 20$ Kelvin for $z \leq 50$ km.

⁻irst results and validation

This validation study is based on .IDAR measurements undertaken dur-ıg the first measurement campaign ·om 21 April to 30 June 1999, represent-ıg 28 LIDAR experiments or over 100 ɔurs of observation. The validation as carried out by comparing the .DAR data with the daily SAWB mea-:rements and the climatological infor-ation of the CIRA-86 model.

SAWB measurements are collected .ily by balloon radiosonde at the ırban site. The balloon can reach the atosphere and overlap over a rela-ely large altitude range ($15 \leq z \leq 27$ km) with the LIDAR. The ?A-86 climatology is a collection of experimental measure-nts and results from theoretical models. It is based mainly on lir infrared soundings, with the SCR[d] experiment on board nbus 6 from 1973 to 1974 and with the PMR[e] experiment on nbus 6 from 1975 to 1978. These two experiments yield tem-ature profiles between 20 and 80 km. Together with tropo-.ere measurements carried out between 1958 and 1973, they ɜ climatological monthly averages between 0 and 80 km for a ɔal coverage from 80°S to 58°N.[4]

⁹R–SAWB comparisons

ıe comparison between the LIDAR measurements and the /B radiosonde was carried out with data collected during the lation campaign. Figure 3 shows temperature profiles measured by the Durban SAWB radiosondes and the LIDAR on 11, 31 and 25 May, and on 11 June [see (a), (b), (c) and (d), respectively]. The measurement comparisons are limited to the lower stratosphere (balloon sondes rarely fly above 25–30 km). In the overlap zone the two measurements are in quite good agreement, although LIDAR measurements, unlike the sondes, are nocturnal.

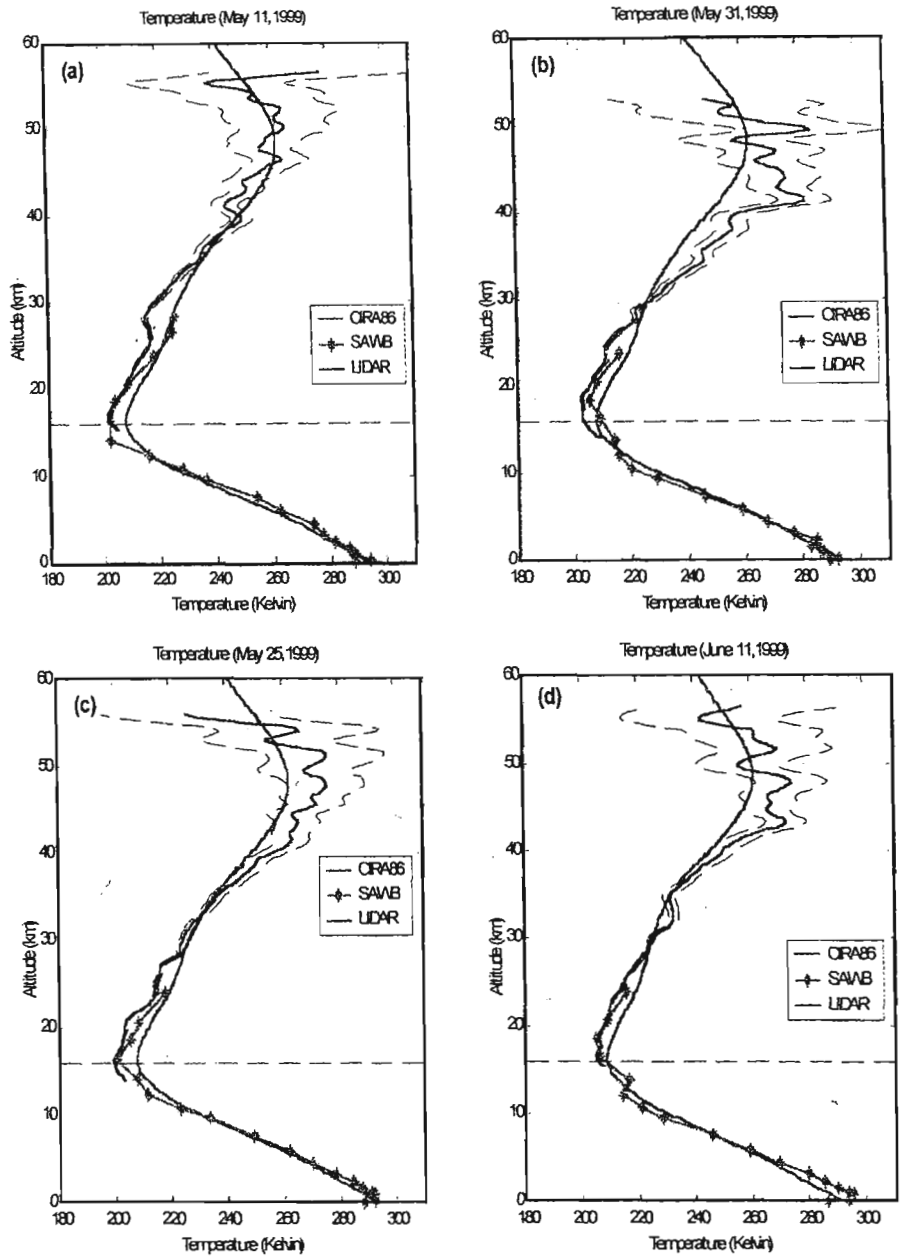

Fig. 3. Plots **(a)**, **(b)**, **(c)** and **(d)** represent, respectively, the LIDAR temperature profiles obtained for May 11, 25 and 31 and for June 11 (continuous blue lines) superimposed on the SAWB radiosonde profiles recorded on the same days over Durban. The dashed curves represent the LIDAR total uncertainty.

The LIDAR and radiosonde average profiles, computed using the entire set of LIDAR and SAWB measurements during the study period (28 measurements), indicate that temperature values obtained with LIDAR and sounding balloons of the SAWB were relatively similar (figure not shown). They did not exceed 5 K [$\Delta T = |T_{LIDAR} - T_{SAWB}| \leq 5$ K], which can be considered as reasonable, taking into account the possible influence of stratospheric aerosols, the fact that LIDAR and balloon measurements are not simultaneous, and the great variability of the temperature in the winter stratosphere.

Note that during the study period the upper limit of the tropo-

tive chopper radiometer.
ure modulated radiometer

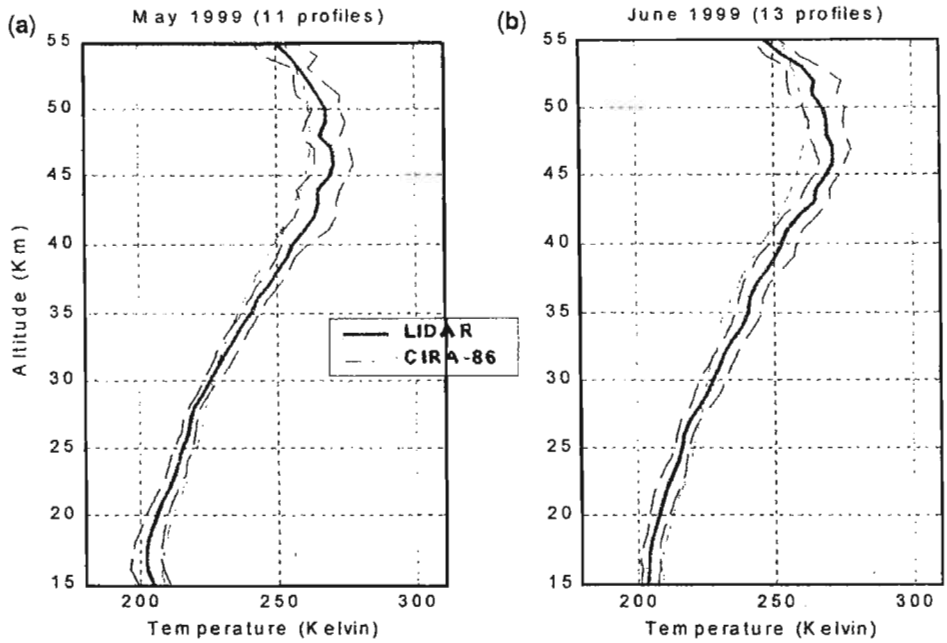

Fig. 4. Averaged monthly temperature profiles for (a) May and (b) June 1999, obtained with the LIDAR (continuous blue line). The standard deviation curves are also shown (dashed lines). The (red) dotted lines represent the CIRA model for the month.

sphere, called the tropopause, was localized at about 16 km (see Fig. 3).

Comparison of the Durban LIDAR and CIRA-86

This comparison was carried out over an altitude range from 15 to 55 km. The average monthly values for the LIDAR temperature were obtained for May (11 profiles) and June (13 profiles). They are superposed in Fig. 4 on the monthly climatological profiles calculated for the Durban site. For the lower stratosphere (up to 28–30 km), the LIDAR analysis agrees with the CIRA-86 climatology. LIDAR temperatures were systematically colder than the corresponding climatological values but not by more than 4–5 K. This could be due to the stratospheric aerosol effect on the return signal, which underestimates LIDAR temperatures. Between 30–32 km and the lower mesosphere (55 km), LIDAR temperatures differed slightly (within 5 K) from those of CIRA-86 climatology, and indicated a warmer stratopause (+8 K) at an altitude of about 46 km. Moreover, LIDAR temperature profiles showed much variability from day to day, as shown on Fig. 5. This could have been due to the atmospheric planetary waves propagating through the middle atmosphere.

The observed wavy structures in daily temperature profiles obtained by LIDAR (see Figs 3 and 5) are characteristic of atmospheric wave propagation. Note that the study period corresponded to the change of season from autumn to winter. In winter stratospheric temperatures are disrupted by the activity of atmospheric waves and notably gravity waves (for periods of some hours) and planetary waves (for periods from days to weeks). Those waves are generated mainly in the troposphere and propagate via westerly winds in winter in the middle atmosphere.[10]

Owing to its good temporal resolution, the LIDAR gives temperature profiles integrated over 2 to 5 hours and takes into account short-term perturbations of the atmosphere due to internal gravity waves.[9] Besides, these LIDAR observations seem to be consistent with theory because we observed that the amplitudes of oscillations due to gravity wave propagation increased quickly with height, because of the exponential decrease of atmospheric density with altitude (see Fig. 3). Moreover, as shown in Fig. 6, one notices, from the ECMWF[f] data, that during

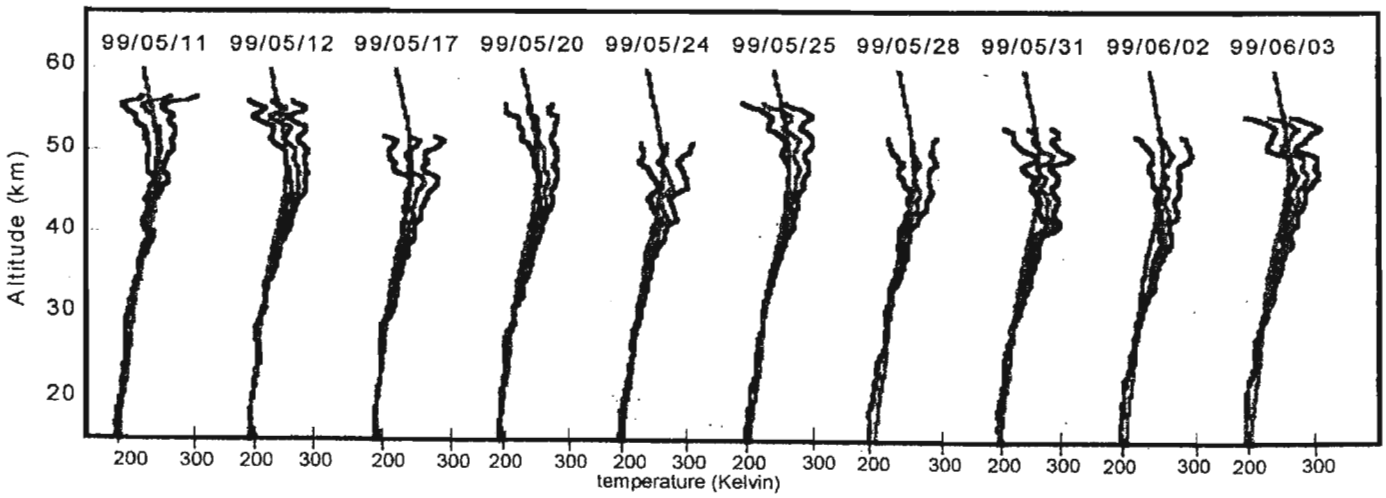

Fig. 5. An example of the evolution of the temperature profiles obtained with the LIDAR (continuous blue lines) for the 15–60 km altitude range. Each profile is framed by the temperature profiles at ±σ the total uncertainty (discontinuous lines).

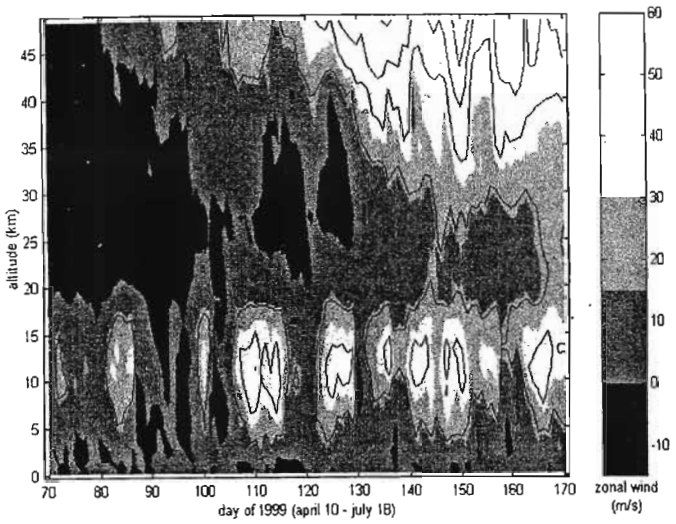

Fig. 6. Time-height zonal wind cross-section as derived from the ECMWF analyses including the study period (from 24 April to 30 June, which corresponds to the period from the 114th day to the 181st day of 1999).

the validation period stratospheric zonal wind direction changed. This is consistent with the observed day-to-day LIDAR variability and explains the temperature differences observed between LIDAR measurements and the CIRA-86 climatological values. A full study of wave activity observations by LIDAR over Durban, taking into account the entire dataset recorded during 1999, is being conducted.

Conclusion

In this study we present preliminary temperature measurements with the Durban LIDAR taken during the first validation campaign. Clearly, these initial results must await confirmation from a larger database.

The Durban LIDAR installation is the fruit of Franco-South African cooperation, which involved over two years of technical, logistical and scientific investment, and produced the first results in April 1999.

The measurements presented here show that the Durban LIDAR temperature measurements broadly agree with the CIRA-86 climatological model and with the SAWB daily radiosonde measurements. This correspondence, however, varies in accuracy according to altitude. For instance, as shown in Fig. 3, for altitudes between 15 and 27 km, the LIDAR temperatures were in good agreement with the SAWB daily profiles. However, the average LIDAR temperatures were systematically lower and the discrepancy ($|T_{LIDAR} - T_{SAWB}|$) decreased with altitude. This was also the case with the monthly averaged LIDAR temperatures as compared with the CIRA-86 climatological model, for the same altitude range (Fig. 4). This is easily explained in terms of a lower stratospheric layer of background aerosols known as the Junge layer. These aerosols and the resultant Mie scattering lead to an increase in the backscattered signal and a corresponding underestimate of the temperature.

The temperature discrepancy of 5 K between the quasi-simultaneous LIDAR–SAWB measurements indicates that the local stratosphere is not heavily loaded with aerosols.

For the upper altitudes (upper stratosphere and lower mesosphere), LIDAR temperatures were within 5 K of the CIRA–1986 climatology, and the measured LIDAR temperatures show great variability (Fig. 5), as expected for the middle atmosphere in winter. As explained above, part of the observed variations may be attributed to relatively fast transient phenomena like gravity waves and/or planetary waves.

The CIRA climatological model is constructed from a database of IR soundings carried out on the SCR and PMR experiments on Nimbus 6 and 7 between 1973 and 1978. The model does not account for either short-term atmospheric variation due to wave activity, nor for the evolution of the earth's atmosphere. Moreover, we recorded only a limited number of LIDAR measurements for the monthly profiles. This may explain the LIDAR–CIRA temperature discrepancies above 30 km.

We thank the French Ministry of Foreign Affairs and Co-operation, the South African Foundation for Research Development (now National Research Foundation) and the Regional Council of Réunion. We also thank the technical personnel of the Services d'Aéronomie of the CNRS and at the Laboratoire de Physique de l'Atmosphère at La Réunion University, who contributed to the realization of this project: G. Bain, J.M. Metzger and A. Theodon. We also thank the physics workshop of the University of Natal for their help in the maintenance and proper running of the LIDAR. Special thanks go to the officials of the South African Weather Bureau, who supplied us with the data obtained from their daily radiosonde measurements. We also thank J.D. Hey for advice.

Received 27 October 1999. Accepted 1 May 2000.

[1]European Centre for Medium Range Weather Forecasting.

1. Mégie G. (1979). Applications des lasers à l'étude de l'atmosphère. *Rev. de Physique Appliquée* **14**, 369–378.
2. Hauchecorne A. and Chanin M.L. (1980). Density and temperature profiles obtained by lidar between 35 and 70 km. *Geophys. Res. Lett.* **7**, 565–568.
3. Hauchecorne A. and Chanin M.L. (1982). Mid-latitude ground-based lidar study of stratospheric warming and planetary waves propagation. *J. Atmos. Terr. Phys* **44**, 577–583.
4. Barnett J. and Corney M. (1985). In *Middle Atmosphere Reference Model Derived from Satellite Data*, ed. K. Labitzke, Handbook for MAP, chap. 16, pp. 47–137. J.J. Barnett, B. Edwards, Urbana, IL.
5. Hey J.D. (1986). From Leonardo to the graser: light scattering in historical perspective. Part V: the fourth Baron Rayleigh. *S. Afr. J. Sci.* **82**, 356–360.
6. Wilson R., Hauchecorne A. and Chanin M.L. (1990). Gravity wave spectra in the middle atmosphere as observed by Rayleigh LIDAR. *Geophys. Res. Lett.* **17**, 1585–1588.
7. Keckhut P., Hauchecorne A. and Chanin M.L. (1993). A critical review of the database acquired for the long-term surveillance of the atmosphere by the French Rayleigh lidars. *J. Atmos. Oceanic Technol.* **10**, 850–867.
8. Bencherif H. (1996). *Observations de l'activité dynamique dans la moyenne atmosphère, par sondage LIDAR, au-dessus du site de l'île de la Réunion.* Doctorat de l'Université Paris-6.
9. Lindzen R.S. (1981). Turbulence and stress owing to gravity wave and tidal breakdown. *J. Geophys. Res.* **86**, 9707–9714.
10. Salby M.L. (1984). Survey of planetary scale travelling waves: the state of theory and observations. *Rev. Geophys.* **22**, 209–236.

The Durban Atmospheric LIDAR Program

A. Moorgawa, M. M. Michaelis, R. D. Diab, J. Anderson, M. Kuppen, A. R. Prause, E. Mckenzie
School of Physics, University of Natal, Durban, South Africa

J. Porteneuve
Service d'Aéronomie du CNRS, Paris, France

J. Leveau, H. Bencherif, B. Morel
Laboratoire de Physique de l'Atmosphère
Université de La Réunion, France

P. F. Cunningham
University of Namibia, Namibia

ABSTRACT

A brief description and use of two LIDAR (Acronym for LIght Detection And Ranging) systems in the measurements of atmospheric aerosols and vertical temperature profiles above Durban are presented. Early local aerosol profiles for low medium and high altitudes from the old LIDAR are shown. With the recent installation of the new LIDAR, vertical temperature measurements in the troposphere and stratosphere are made possible. A first validation of the new LIDAR has been carried out showing atmospheric wave activity above the Southern African continent for the first time.

It is envisaged in the future to correlate the results obtained with the new LIDAR, especially for the low altitude, with those of the old LIDAR. Plans are also going ahead to implement an additional channel on the new LIDAR which will measure ozone concentration in the troposphere.

Introduction

Although there is a great number of weather stations and atmospheric LIDARs in the Northern hemisphere, the Southern hemisphere is far less well endowed, especially on the African continent. But weather is a global phenomenon and no real understanding of the associated problems - global warming and stratospheric ozone depletion - can be complete without world coverage.

It is for this reason that the CNRS Centre d'Aéronomie, Jussieu, Paris has encouraged the creation of a sophisticated Laboratoire de Physique de l'Atmosphère on the Island of Reunion (21^0S) which in turn has helped Durban (30^0S) initiate an up to date atmospheric LIDAR program. With the two LIDARs working in parallel, it is possible to compare data from either side of the Southern sub-tropical barrier.

Prior to the installation of the French LIDAR system (the "new LIDAR") a rather simple system (the "old LIDAR") had been installed in 1991 on the roof of the University of Natal's Physics Department[1] to measure aerosols. Local aerosol profiles at low altitude depict stable layers in the troposphere[2]. These stable layers are believed to influence the local climate. In this article we will discuss old but never published LIDAR results going back almost a decade. Because of atmospheric evolution and the recent growth of industrialisation in Natal, these results though very fragmentary could be of historic interest.

With the installation of the new LIDAR in April 1999, vertical temperature and density measurements as well as aerosol concentration observation became possible both in the troposphere and in the stratosphere.

This installation was made possible thanks to a Franco-South African Co-operation agreement. It is hoped that it will be extended to enable ozone to be included in our results. Apart from world climatology this may be important for a more local reason: with reducing weather bureau budgets, the number of radiosonde launches has been dramatically cut. It should be possible, once the LIDAR is well established to obtain the same data as that gathered by the sondes at much reduced cost. The LIDAR is in fact capable of giving much more data (greater range of altitude) but obviously only when there is no complete cloud cover.

1. The old Durban LIDAR

The old Durban atmospheric LIDAR can be regarded as having served three purposes: together with the SAOZ experiments[3] it created for the first time a "climate of climatology" at the University of Natal (South Africa) where we now have well established environmental programs[4-5] and climatic activities. Secondly, its very existence allowed the little Durban group to join up with the French CNRS and the Laboratoire de Physique de l'Atmosphère (LPA), Reunion. And finally it gave the first crude LIDAR data for aerosol behaviour above Durban; this data has never been published except in three University theses[1, 6-7].

Fig(1) shows the old LIDAR receiver and transmitter configuration. The transmitter consists of a flashlamp-pumped dye laser manufactured by PHASE R. The dye used for the laser is Rhodamine 6G in a concentration of 0.5×10^{-4} moles/litre of methanol. This produces a series of pulses (pulse length 0.6 μs at FWHM) of wavelength 589 nm with a total energy of 0.8 J.

The receiver consists of a 1.56 m backsilvered parabolic searchlight mirror with a focal length of 654 mm. Collimating optics are positioned at the focus of the mirror. These consist of a microscope objective with a field of view of 79^0 followed by a variable aperture(1-10 mm). Two stacked 589 nm interference filters each with a bandwidth of 10 nm and 50 % transmission are placed in front of the collimating optics. These filters eliminate a large proportion of the background light.

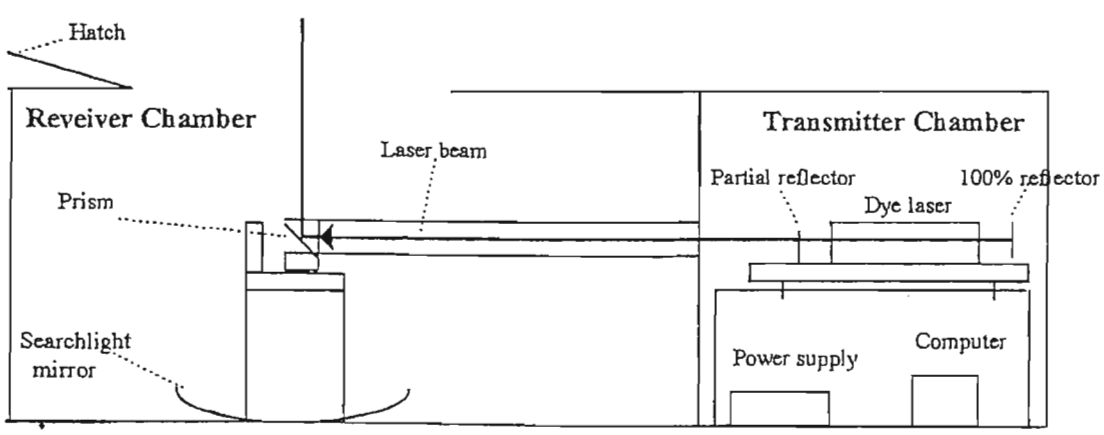

Figure 1: Receiver and transmitter configuration of the old LIDAR.

1 a. Old LIDAR results (1992 - 1994 Cunningham and Kuppen).

The old LIDAR was installed in 1991 but only gave useful results in late 1992. Fig 2 shows early cloud LIDAR traces of high altitude cirrus (12 km) and some lower cumulus (6 km). Fig 3 shows a medium height aerosol return at ≈ 18 km. Fig 4 is a successful attempt at obtaining a high altitude return: apart from a not unexpected aerosol return at ≈ 22 km, there is a strong signal at ≈ 60 km. This was seen again on the nights of 13th and 14th June, becomes weak on the 15th and has disappeared by the 19th (fig(5)) and remained absent for the next four nights (not shown).

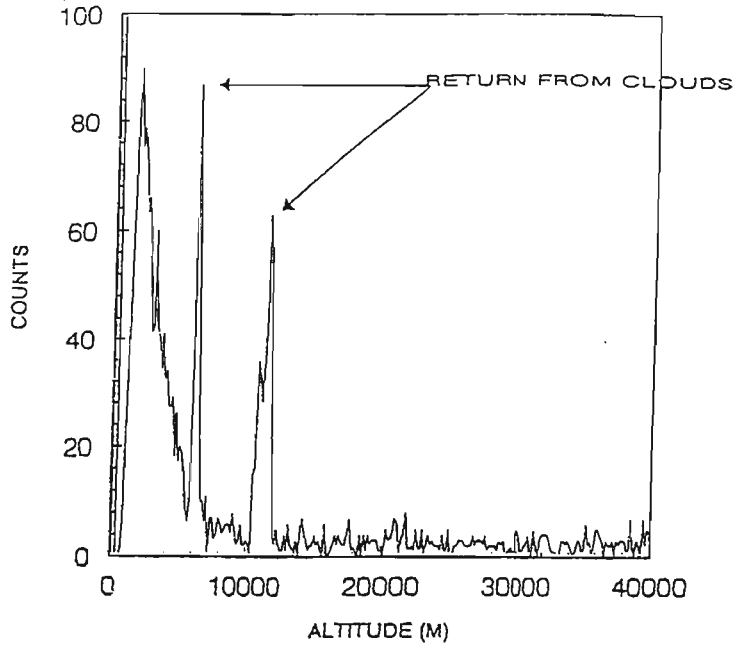

Figure 2: LIDAR return from two cloud layers.

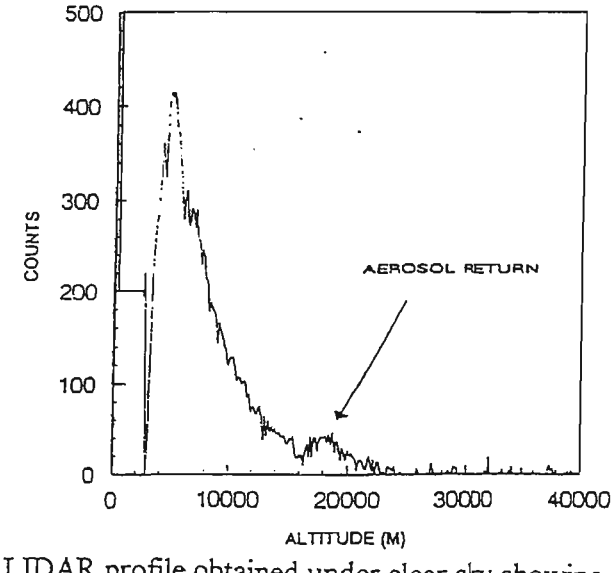

Figure 3: LIDAR profile obtained under clear sky showing aerosol return.

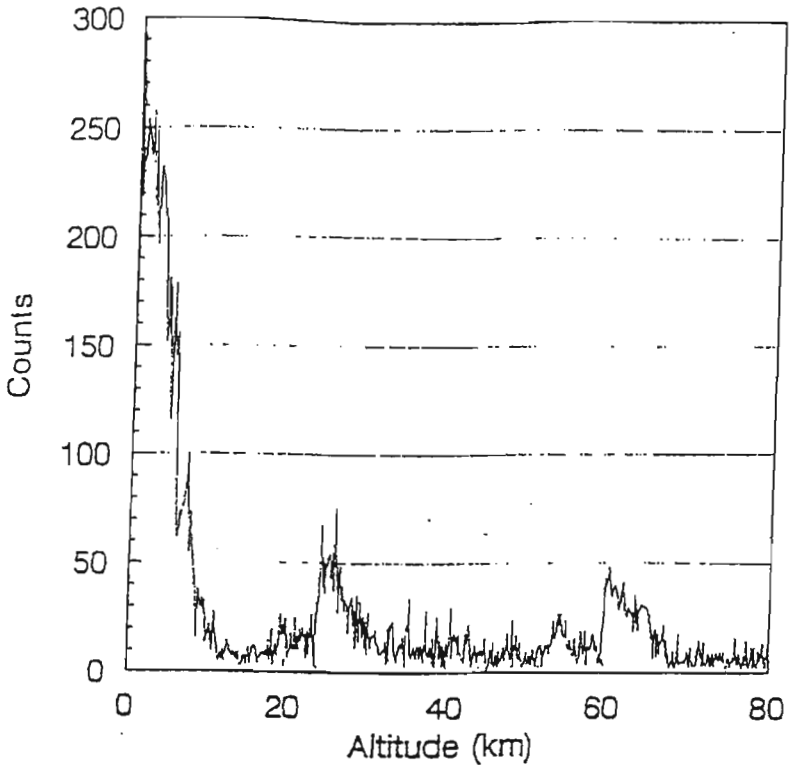

Figure 4: High altitude LIDAR return obtained under clear sky.

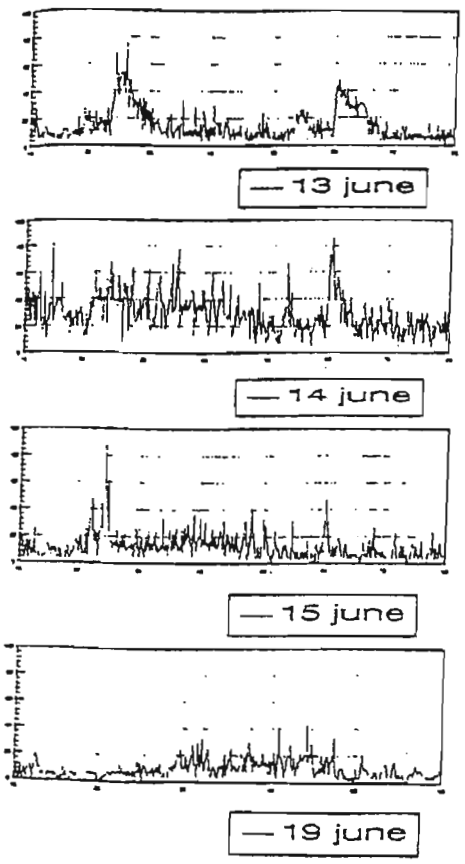

... for 4 days in June 1994

1 b. Old LIDAR results (1997 Moorgawa and Prause).

Between 1995 and 1996, the LIDAR was hardly ever used due to lack of funds and man power.

It should be noted that due to unfavourable weather conditions in Durban (lack of clear skies) and technical problems with the old LIDAR, it was not possible to run it on a day-to-day basis. Results obtained in the months of July, August, September and October 1997 are reported.

The results show important features in the low altitude (0-10 km) and mid altitude (10-35 km). These results are raw data as they are recorded by the data capturing system. The LIDAR was operated on clear nights only. It is important that the moon and clouds should not be present during data acquisition. The moonlight will saturate the photomultiplier (PM) so that LIDAR returns from high altitudes will not be detected.

Low altitude aerosols

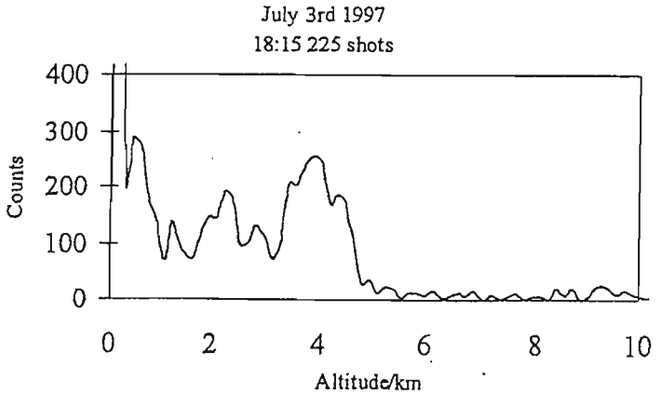

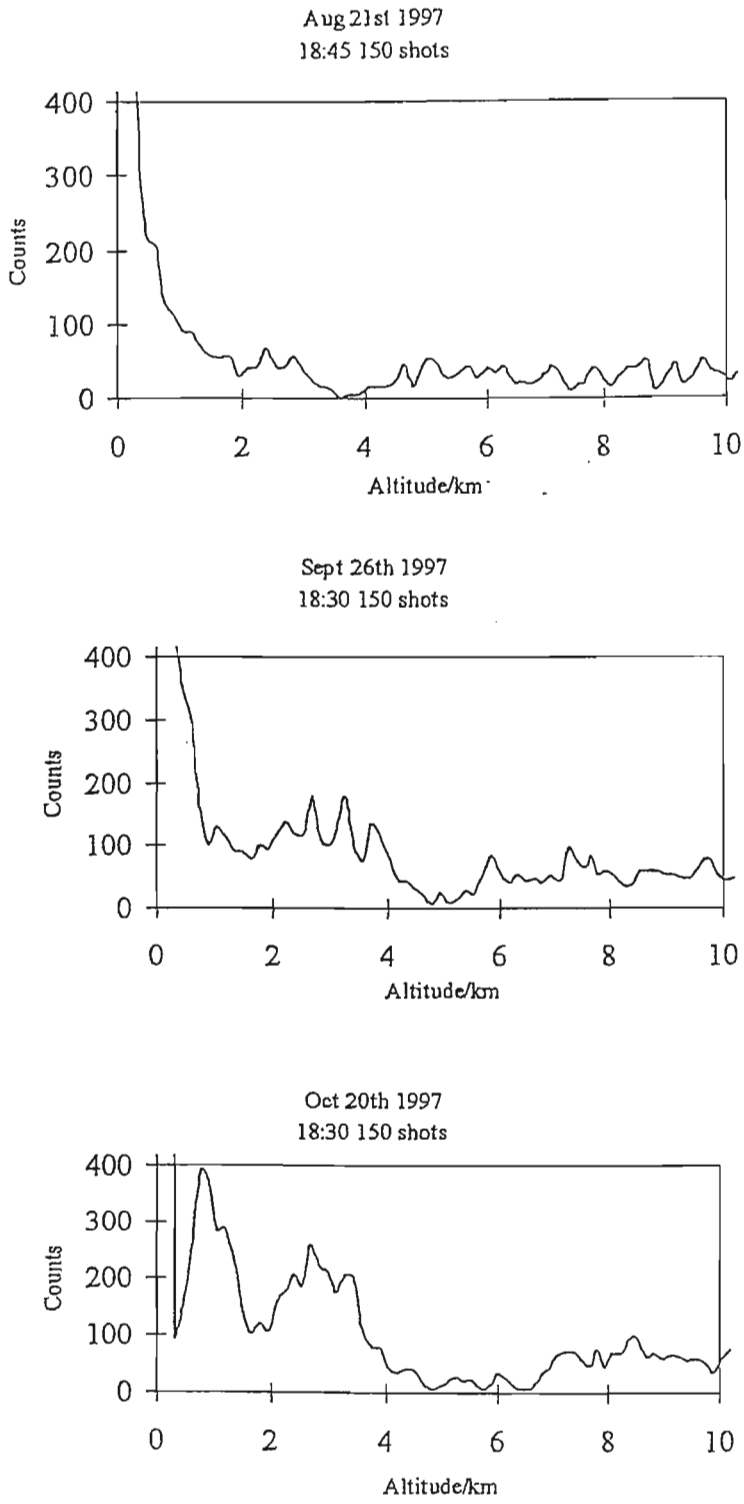

Figure 6 : Low altitude LIDAR profiles taken on July 3rd, August 21st, September 26th and October 20th 1997.

There seem to be three aerosol layers in the July 3rd profile around 1, 2 and 4 km respectively. One of the layers seems to disappear in the Aug 21st profile. The Sept 26th profile shows one layer around 3 km and probably two layers which have merged around 4 km. The Oct 20th profile shows two big layers around 1 and 3 km respectively.

Mid-altitude aerosols

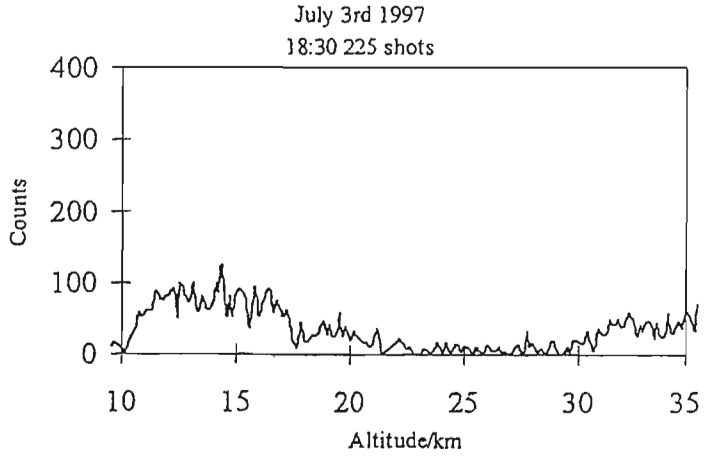

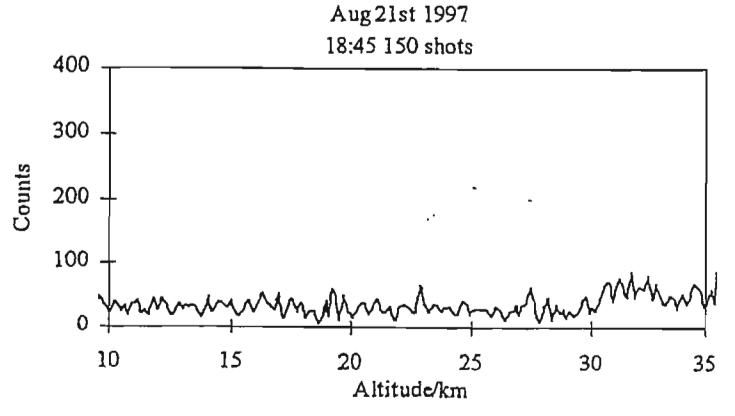

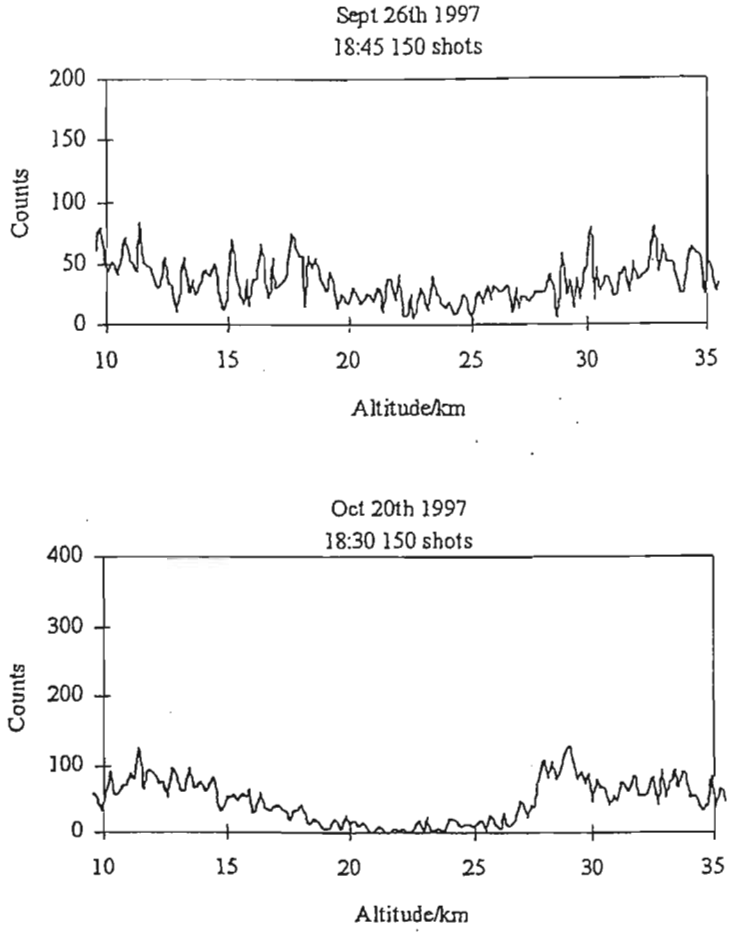

Figure 7: Mid-altitude LIDAR profiles taken on July 3rd, August 21st, September 26th and October 20th 1997.

Fig(7) shows the profiles obtained for the mid-altitude (10-35 km). There are two interesting points to note in these plots. First, the aerosol layer at $\approx$ 14 km (July 3rd profile) and the dramatic increase in the LIDAR return at $\approx$ 28 km as seen on the October 20th profile.

2. The new Durban LIDAR (1999 Franco-South African Co-operation).

The new LIDAR, installed in April 1999, is a more sophisticated system. Fig(8) shows the configuration of the new LIDAR system. The transmitter is a pulsed Nd:YAG laser. The emitted wavelength is λ_e = 532 nm obtained by frequency doubling the YAG fundamental: λ_0 = 1064 nm. The laser energy is about 300 mJ per pulse (pulse length ≈ 6-7 ns). The laser light is transmitted in the atmosphere after passing through a system of mirrors and a Galilean telescope.

The receiver system consists of two 445 mm parabolic mirrors. As shown in fig(8), the mirrors are held inside two long tubes which protect them from luminous interference. After collection by the telescope the photons are transmitted by optical fibres placed at the focal point of each mirror, to the detection box which contains a collimator, an interference filter and a PM tube.

An electronic acquisition system, controlled by a computer, counts and integrates the number of photons received.

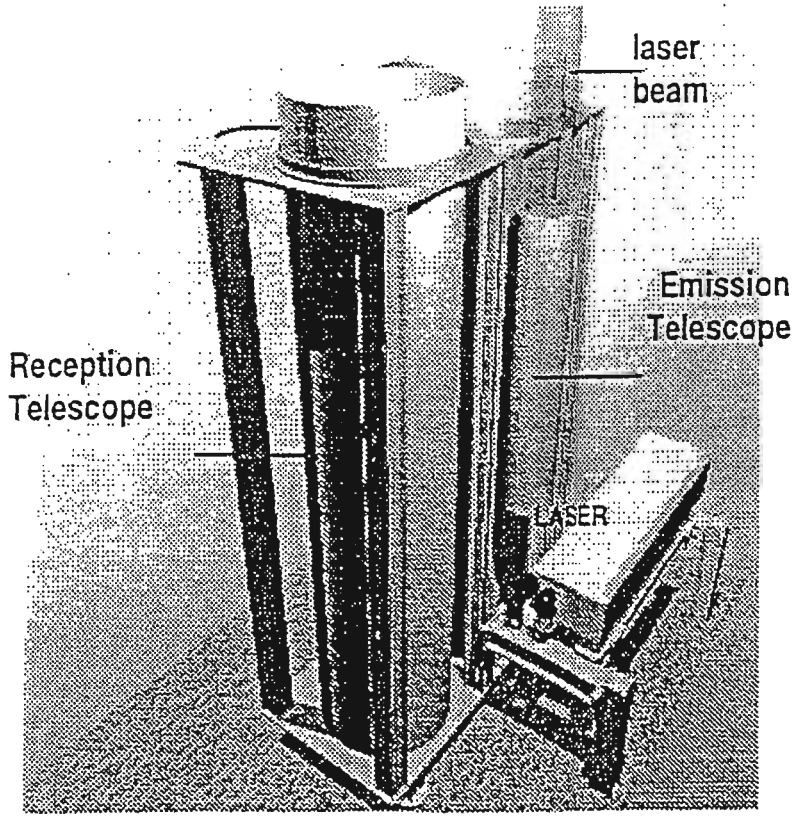

Fig 8: Receiver and transmitter configuration of the new LIDAR system.

Fig 9 shows a plot of the temperature profile obtained with the new LIDAR on June 8 1999. The South African Weather Bureau (SAWB) measurements and the climatological model CIRA-1986 are also shown. The SAWB measurements are collected daily by balloon radiosonde at Durban International Airport. The CIRA-1986 climatology is a collection of experimental measurements and results from theoretical models.

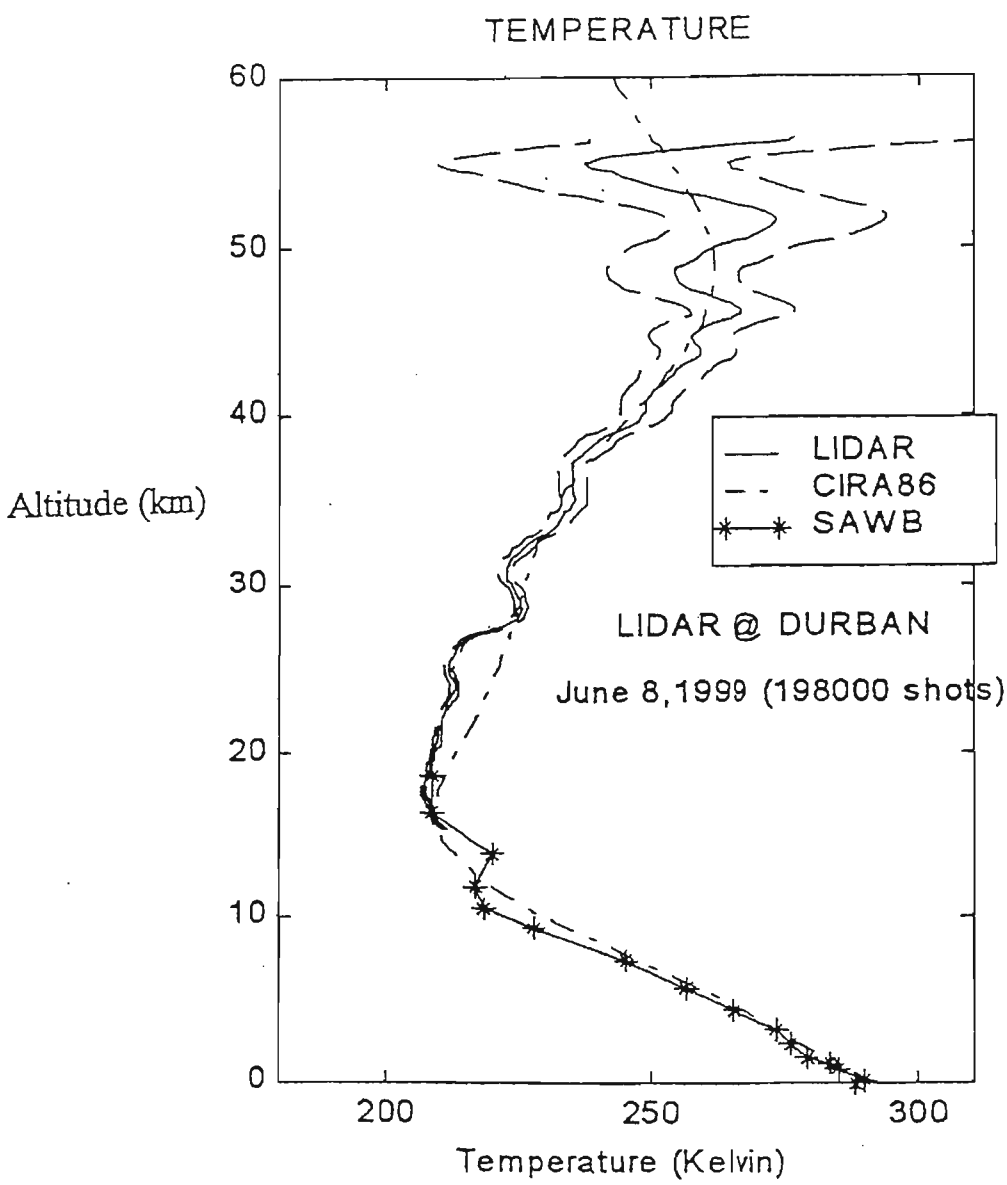

Fig 9: LIDAR temperature profile taken on June 8th 1999.

3. Discussions

The 60 km return shown in fig(4) is intriguing. Several groups working with flashlamp-pumped dye lasers[8-9] detected sodium layers between 70 and 100 km, through resonant scattering. 60 km seems a little low.

Three possible explanations which could account for the behaviour of the aerosols in the low altitude (as seen in the 1997 results) are:

(1) Over most of Southern Africa, layers of absolutely stable air occur preferentially at around 700 hPa (≈ 3 km), 500 hPa (≈ 5 km) and 300 hPa (≈ 9 km) as shown in fig(10)[2]. A fourth layer also occurs over the coast at around 850 hPa (≈ 1.5 km). All four layers have the effect of inhibiting vertical transfer of aerosols and trace gases and of trapping them in the intervening layers.
The profiles of fig(6) show that only two such layers have been detected - the 700 hPa and the 850 hPa layers.

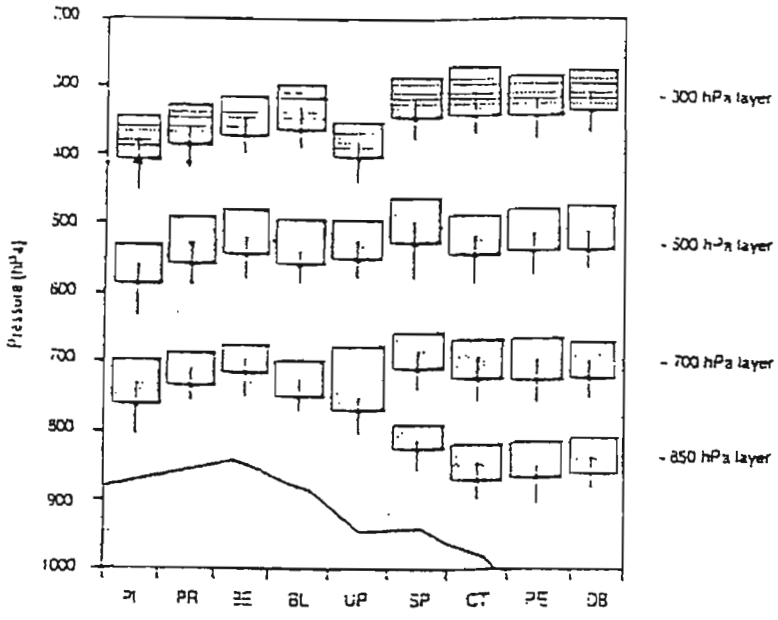

Figure 10: Mean annual spatial variation of absolutely stable layers at 850, 700, 500 and 300 hPa over South Africa. PI denotes Pietersburg, PR Pretoria, BE Bethlehem, BL Bloemfontein, UP Upington, SP Springbok, CT Cape Town, PE Port Elizabeth and DB Durban.

(2) Biomass burning occurs frequently in South Africa, either in the form of prescribed burns or wild fires[10]. The extent of these burns on the east coast of South Africa reaches its maximum in the winter season[11]. Thus the loading of the atmosphere with aerosols will be higher in winter.

(3) Sugar cane burning occurs in Natal between the beginning of June and the end of October. This will influence the loading of the atmosphere and the aerosol layers.

The mid-altitude LIDAR profiles show an increase in aerosol concentration around 14 km on July 3rd 1997(Fig(7)). There is reason to believe that this could originate from sugar cane burning. The upward tropospheric circulation has transported this layer to higher altitude. The 14 km aerosol layer seems to persist for the whole of July and increases in concentration towards the end of July. This is evidently due to the continuous loading of the atmosphere with sugar cane burning which started in the beginning of June and finishes around the end of October. At the same time mixing is also taking place but probably at a slower rate.

The second interesting feature that can be seen from fig(7) is perhaps the dramatic increase in the LIDAR return at 28 km (the October 20th profile). Kuppen[6] previously detected an aerosol layer at 25 km. This might be the same layer. The "28 km layer" was detected only in the month of October. The weather might have been ideal in October (low water vapour concentrations) which have resulted in strong LIDAR return from higher altitudes.

This layer is rather intriguing as aerosols have rarely been detected at such high altitude. In the past, Hirono et al[12] observed aerosol layers above 25 km and which are reported to be rather variable. Iwasaka and Isono[13] reported a dust layer above 24 km with a peak intensity at 27 km.

The temperature profile (fig(9)) obtained with the new LIDAR shows two interesting points. First, the upper limit of the troposphere, known as the tropopause, is localised around 12 km. Secondly, the oscillatory feature in the plot from 40 km to 55 km. This is due to the vertical propagation of gravity waves from the mid atmosphere to the stratosphere. The same phenomenon has been observed with LIDAR in the Northern hemisphere[14].

Conclusion

The LIDAR program is beginning to yield interesting results on the local atmosphere over the Southern African Eastern seaboard. We are presently studying the possibility of upgrading the system to measure ozone concentration in the troposphere.

References

1. Kuppen M., "The establishment of a ground-based LIDAR system", *M.Sc. thesis*, University of Natal, Durban, South Africa (1992).

2. Cosijn C. and Tyson P.D, "Stable Discontinuities in the atmosphere over South Africa", *South African Journal of Science*, 92, 381(1996).

3. Mravlag E, "Observations of total ozone at Durban", *1996 Spring Meeting der American Geophysical Union* , Baltimore, USA (1996).

4. Diab R. D., "Estimates of Air Pollution Potential over Southern Africa", *South African Journal of Science*, 73, 270 (1977).

5. Preston-Whyte R. A., Diab R. D., and Tyson P. D., "Towards an Inversion Climatology of Southern Africa: Part II, Non-Surface Inversions in the Lower Atmosphere", *South African Geographical Journal*, 59, 44 (1977).

6. Kuppen M., "On the interaction of Laser Beams with Air with specific reference to refraction and scattering", *Ph.D. thesis*, University of Natal, Durban, South Africa (1996).

7. Moorgawa A, "Applications of scattering and refraction by atmospheric gases", *M.Sc. thesis*, University of Natal, Durban, South Africa (1998).

8. Thomas L, Gibson A. J. and Battacharyya S. K., *Nature*, **263**, 115 (1976).

9. Megie G and Blamont J. E., *Planetary Space Science*, 25, 1039 (1977).

10. Rutherford M. E. and Westfall R. H., "Memorial Botanical Survey South Africa", **54**, *Government Printer*, Pretoria, South Africa (1986).

11. Pillay Y., Diab R. D., and Sokolic F., "Ozone maxima off the east coast of South Africa: the role of biomass burning", *South African Journal of Science*, 91, 609 (1995).

12. Hirono M., Fujiwara M., Uchino O., and Itabe T., *Canadian Journal of Chemistry*, 52, 1560 (1974).

13. Iwasaka Y. and Isono K., *Journal of Atmospheric Terrestrial Physics*, **39**, 117 (1977).

14. Hauchecorne A. and Chanin M. L., *Journal of Geophysical Research*, **88**, 3843 (1983).

Submitted to Journal of Atmospheric and Solar-Terrestrial Physics, December 2001. Accepted December 2002.

LIDAR observations of lower stratospheric aerosols over South Africa linked to large scale transport across the southern subtropical barrier

Bencherif, H., T. Portafaix, J.L. Baray, B. Morel, S. Baldy, and J. Leveau
Laboratoire de Physique de l'Atmosphère, Université de la Réunion, France

A. Hauchecorne, and P. Keckhut
Service d'Aéronomie du CNRS, Paris, France

A. Moorgawa and M.M. Michaelis
School of Pure and Applied Physics
University of Natal, Durban 4041, South Africa

R. Diab
School of Life and Environmental Sciences
University of Natal, Durban 4041, South Africa

corresponding author

Dr. Hassan BENCHERIF
Université de la Réunion
15, avenue R. Cassin, BP 7151
97715, St-Denis, cedex 9
Réunion Island, FRANCE

e-mail adress : hassan.bencherif@univ-reunion.fr

Fax number :
02 62 93 86 65 (*from France*)
+262 262 93 86 65 (*from abroad*)

Abstract

The study of the variability of stratospheric aerosols and the transfer between the different atmospheric regions improves our understanding of dynamical processes involved in isentropic exchanges that take place episodically in the lower stratosphere through the subtropical barrier. One useful approach consists in combining in situ ground-based and global measurements with numerical analyses. The present paper reports on a case study of a horizontal transfer evidenced first by Rayleigh-Mie LIDAR observations over Durban (29.9°S, 31.0°E, South Africa). Additional data from MeteoSat and SAGE-2 experiments, and from ECMWF meteorological analysis have been used in this study. Contour advection maps of potential vorticity from the MIMOSA model derived from ECMWF fields, were also used.

By the end of April, 1999, LIDAR observations showed that aerosol extinction, in the lower stratosphere, has increased significantly and abnormally in comparison with other LIDAR and SAGE-2 observations recorded for the period from April 20 to June 14, 1999. The dynamical context of this case study seems to exclude the possibility of a local influence of the subtropical jet stream or tropical convection, which could inject air masses enriched with tropospheric aerosols into the stratosphere. On the contrary, a high-resolution model based on PV advection calculations and ECMWF meteorological analyses shows that air masses are isentropically advected from the equatorial zone close to Brazil. They cross the southern barrier of the tropical reservoir due to laminae stretching and reach the southern subcontinent of Africa 5-6 days later.

Keywords

LIDAR, aerosols, isentropic transport, stratosphere, subtropical barrier, PV-contour advection

I- Introduction

Aerosols have been shown to have a significant influence on radiative forcing and hence temperature [Robock and Mao, 1992 ; Labitzke and McCormick, 1992 ; Kinninson et al., 1994]. Furthermore, a survey of aerosols from Mount Pinatubo indicated that aerosol loading has important chemical effects by enhancing heterogeneous reactions [Brasseur and Granier, 1992] and can modify ozone concentrations [Solomon et al., 1996 ; Roumeau et al., 2000]. Knowledge of mass exchange between different parts of the atmosphere is essential in understanding the transport and vertical and spatial distribution of aerosols. Eddy transport barriers separate the tropical stratospheric reservoir from the mid-latitude stratosphere [Holton et al., 1995; Haynes and Shuckburgh, 2000]. Steep aerosol and trace gas gradients clearly characterize the edges of that reservoir [Grant et al., 1996]. Sporadic disruptions of those barriers occur due to planetary wave breaking and the generation of eddies that enhance transport out of the tropics [Chen et al., 1994 ; Horinouchi et al., 2000]. Since tropospheric air enters the stratosphere mostly through the tropical tropopause, exchanges between the tropics and mid-latitudes have a large influence on the distribution of many long-lived stratospheric constituents.

The transport of aerosols from the tropics to mid-latitudes is well documented in a number of publications. Randel et al. [1993] using global maps obtained from satellite-borne instruments showed that aerosols can be transported through eddy mixing. Waugh et al. [1994] using meteorological data sets showed that aerosols can also be transported through isentropic advection. However, most dynamical studies and co-ordinated campaigns focus on the

northern hemisphere or on the southern polar region. In the southern hemisphere, dynamical processes are not similar to those studied or observed in the northern hemisphere. Besides, the height-latitude structure of dynamical fields and of disruption mechanisms controlling the release of material between the tropics and mid-latitudes, is still under study. One of the useful approaches consists in combining in situ ground-based and global measurements with numerical analysis.

We report here a case study of an observed tropical / extra-tropical aerosol loading event detected by LIDAR in the lower southern stratosphere. Analyses take advantage of the high vertical resolution of LIDAR profiles. Developments of large-scale "*tongues*" through the surf zone are simultaneously surveyed by the MIMOSA high resolution contour advection model based on ECMWF data sets and by water vapour infrared MeteoSat images.

II- LIDAR instrumentation, aerosol observations and comparisons with SAGE 2

II.1- South African LIDAR system

The present study has been undertaken using LIDAR observations obtained at Durban (*30.7°S, 31.0°E*), South Africa. The system was implemented on the campus of the University of Natal within the framework of a bi-lateral Franco-South African cooperation [Service d'Aéronomie of CNRS, Laboratoire de Physique de l'Atmosphère of Reunion Island University and University of Natal].

The LIDAR system operating at Durban is of the Rayleigh-Mie type. It uses a Nd:YAG pulsed laser with a repetition rate of 10 Hz and transmits in the green at *532 nm*. The receiver consists of two separate telescopic systems and two photomultiplier detectors. LIDAR observations are thus made through two

separate - but instrumentally identical – channels. One channel is allocated to probe the troposphere. It uses the return signal collected by the smallest telescope whose total receiving surface is about *0.03 m²*. The other channel has a total receiving surface of about *0.31 m²*, and its observation field is directed to receive photons back-scattered from stratospheric layers.

Assuming that the observed atmospheric layers behave as a perfect gas in hydrostatic equilibrium, aerosol and temperature profiles can be derived from the return signal backscattered by successive atmospheric layers in the local troposphere and stratosphere [Hauchecorne and Chanin, 1980 ; Chazette et al., 1995]. More information about the instrumental details and temperature profile retrieval method and validation are given by Bencherif et al. [2000]. The aerosol profiles are derived from the LIDAR equation using the Klett procedure [Klett, 1981, 1985] that gives a convergent solution to the total volumetric backscatter coefficient $\hat{a}(z)=\hat{a}_{aerosol}(z)+\hat{a}_{molecular}(z)$. The back-scatter ratio R(z) (total to molecular volume backscatter coefficient ratio) is then calculated from:

$$R(z)=\frac{\beta_{aerosol}(z)+\beta_{molecular}(z)}{\beta_{molecular}(z)}=1+\frac{\beta_{aerosol}(z)}{\beta_{molecular}(z)}\geq 1 \ .$$

Values of R(z) depend on the choice of Rayleigh parameters (molecular contribution) which should be as realistic as possible. For the present study, molecular parameters are computed on the basis of ECMWF daily fields. It allows a better determination of the molecular density profile than that of a climatological model [Keckhut et al., 1993].

Moreover, the determination of the total volumetric backscatter coefficient from the LIDAR equation requires quantitative knowledge of a relationship

between the aerosol extinction coefficient $\alpha_{aerosol}(z)$ and the aerosol backscatter coefficient $\beta_{aerosol}(z)$, usually the ratio $\frac{\alpha_{aerosol}(z)}{\beta_{aerosol}(z)}$ [Klett, 1981]. That ratio depends strongly on the size, shape and refractive index of the aerosols. Accounting for micro-physical properties of stratospheric aerosols, Wang et al. [1989] estimated the value of this ratio for particles to be 30 sr around 15 km, increasing with altitude up to 50 sr at 28 km. Here, the ratio of extinction to back-scattering coefficient of aerosols is considered to be 50 sr throughout the whole stratospheric altitude range. The Klett procedure also requires a boundary condition, i.e., the knowledge of $\beta_{aerosol}$ at a reference altitude z_{ref}, chosen above the aerosol layer : at and above this reference altitude, the particle content is negligible and scattering is only due to the molecular atmosphere, assuming that $R(z) = 1.0$. Typically, we choose $z_{ref} \approx 40$ km.

Uncertainties in the determination of the total volumetric backscatter coefficient β and in the aerosol extinction coefficient $\alpha_{aerosol}$ and in the back-scatter ratio R are due to three main causes : (1) statistical fluctuations of the measured signal associated with random detection processes, (2) the presence of particles at and above the chosen reference altitude and (3) the subsequent uncertainty on the value of $R(z_{ref})$, and the value of the ratio of extinction to back-scattering coefficient of aerosols and its altitude dependence. The resulting total uncertainty is less than 7%, with the signal being significant up to 40 km [Chazette et al., 1995].

The algorithm used here is similar to the one used to retrieve aerosol LIDAR optical properties from the NDSC primary stations of the Observatoire de Haute-Provence in Southern France [Chazette et al., 1995] and Dumont

d'Urville in Antarctica [David et al., 1998]. It has thus been tested within the framework of the NDSC comparison of the processing algorithms for stratospheric aerosols [Steinbrecht et al., 1996].

II.2 Data

The LIDAR data set used in this study consists of daily records of back-scattered photons obtained over Durban during the period from April 21 to June 14, 1999 (22 profiles). Daily LIDAR measurements are time-integrated over about *3.5 hours* on average.

In order to validate aerosol extinction profiles derived from LIDAR observations, we use the 5.99 version SAGE-2 (Stratospheric Aerosol and Gas Experiment) measurements. Indeed, the long life (since 1984) and the calibration-independent nature of the SAGE-2 instrument [McCormick, 1987 ; Thomason et al., 1997] make it well suited for observations of the long term variability of aerosols and for comparison with other instruments such as LIDARs. For the present work, SAGE-2 data are derived from the 525-nm wavelength channel and are selected depending on :

- the geographical position, i.e., a SAGE-2 profile is selected if its latitude and longitude correspond to the LIDAR position ±6° of latitude and ±10° of longitude,
- the time acquisition, i.e., a SAGE-2 profile is selected if it was recorded on the same day as one of the 22 LIDAR profiles ±12 hours.

Taking into account the duration of the study, the LIDAR dependency on meteorological conditions and the SAGE-2 operating mode [Chu et al., 1989] which is very different in comparison with the LIDAR's, we expect a very small

number of coincidences on the basis of the selection criteria mentioned above. Only one coincident SAGE-2 extinction profile has thus been selected. It was recorded on June 8, 1999, sunrise, at 24.8°S and 38.4°E. The corresponding LIDAR profile was recorded on the same day, at Durban, and was time integrated from 16:30 to 19:55 UTC.

In the local stratosphere, SAGE-2 and LIDAR aerosol extinction profiles, superposed on figure-1, show closely similar vertical distribution. Despite the fact that both profiles' error bars overlap in the whole studied altitude range, the observed discrepancy in the 17-20 km layer is mainly due to the operating modes : SAGE-2 measurements are obtained by looking through a horizontal path of a few hundred kilometres (solar occultation) and thus correspond to a horizontally averaged atmosphere, while LIDAR measurements are obtained vertically and are time-integrated over a few hours. It is also important to note that other parameters can contribute to the mentioned discrepancy, particularly : the difference in wavelength between SAGE-2 and LIDAR observations, and the validity of hypotheses used for the inversion of the LIDAR equation in particular height independence of the aerosols' extinction to the back-scatter ratio.

Knowing that all LIDAR profiles used in the present work have been retrieved using the same inversion method, this comparison, even though it is made with one coincidence, shows that the quality of aerosol profiles obtained by LIDAR over Durban is consistent. These observations can be used consequently for climatological studies as well as for the purpose of a case study, within the framework of co-ordinated campaigns or for validation and inter-comparisons.

III- Results

From the LIDAR data set described above, an averaged aerosol extinction profile has been derived (see the solid line with cross symbols showed on figure-2). As expected, note that extinction values of the stratospheric background aerosols decrease rapidly with increasing altitude up to the 28-30 km altitude range. Beyond that layer, which can be called the local stratospheric aerosol top layer, the observed atmosphere can be considered as typically molecular, i.e., free of aerosols.

Moreover taking into account the extinction mean values the daily LIDAR profiles distribution, illustrated by superposition of all LIDAR profiles on figure-2, highlights a high day-to-day variability of the observed stratospheric aerosols. This high variability can be associated with the zonal wind transitory regime in the stratosphere, as shown by Bencherif et al. [2000].

However, if one considers the 29th of April profile for stratospheric heights under 27 km, the observed extinction values are significantly higher than those of the mean profile and higher too than all other values from all LIDAR profiles. The aerosol increase observed on April 29 is therefore unusual and suggests that, by the end of April, 1999, aerosol extinction has increased significantly and abnormally in the lower stratosphere, as a result of an aerosol loading through a transport process.

For a discussion of the origin of the stratospheric aerosol loading observed over Durban two possible origins are investigated ; the first is related to vertical transport from the troposphere to the stratosphere, the second to horizontal transfer between the tropics and extra-tropics.

IV- Discussion on the origin of the aerosol loading over South Africa

IV.1- Dynamical characteristics of the stratospheric air mass over South Africa on April 29

Potential Vorticity (PV) contours for the 400 K potential temperature level, in the lower stratosphere, have been computed from ECMWF data for the whole studied period. ECMWF data used in this study are re-analysed data, with a horizontal resolution of 1 degree by 1 degree, 15 vertical levels between 1000 and 10 hPa, and with 4 fields per day. These data have already been used for tropospheric-stratospheric dynamical studies in the tropical southern hemisphere [Baray et al., 2000].

Figure-3a shows the latitude vs longitude PV field for the 400 K isentropic surface, averaged for the period April 18 to May 10, 1999, that corresponds to the aerosol loading event date ±10 days. The mean value of PV over the LIDAR site of Durban lies between 7 and 8 PVU. The PV field of April 29 is presented in figure-3b and shows a zone of low-PV ($2 \leq PV \leq 5$ PVU) lying between 25°S and 35°S and 20°E and 45°E. With the exception of the equatorial zone, the lowest PV values ($PV \leq 3$ PVU) appear around the 27°S and 39°E position. This low-PV air mass either has a local upper-tropospheric origin or has originated from long range isentropic quasi-horizontal transport.

IV.2- A local tropospheric origin ?

The dynamic mechanisms which can induce a transfer from the upper troposphere to the lower stratosphere are tropical convection and the jet-streams (polar and subtropical). An examination of the Meteosat image for 29 April (figure 4) shows that there was virtually no cloud cover over Durban on

29 April, thus precluding the possibility of locally strong convective activity capable of injecting an air mass enriched in tropospheric aerosols into the lower stratosphere.

Tropospheric jets/frontal systems are a very perturbed zone and can induce areas of convergence and subsidence, in association with horizontal and vertical ageostrophic circulations. They can result either in strong subsiding motions in tropopause folds, or in strong ascending motion, generally on the anticyclonic side near the entrance zone of the jet stream [Shapiro and Kennedy, 1981 ; Holton et al., 1995]. In our case study, the upper level front associated with the subtropical jet stream is clearly visible on the Meteosat image (figure 4) and is localised in the middle of the Atlantic Ocean, far from the south-western coast of Africa. Within the upper troposphere, winds over Durban are weak, and no PV signature is visible (ECMWF data, not shown). Hence we can conclude that the lower stratosphere over Durban has not been influenced by a local tropospheric source, either by convective activity or by the jet stream.

IV.3- A long-range equatorial origin ?

Having excluded the possibility of a short-range troposphere-stratosphere transport, we now consider the hypothesis of long-range horizontal transport.

In order to check for the origin of the aerosol increase, associated with a low-PV decrease, the high resolution advection MIMOSA model [Hauchecorne et al., 2001] has been used to produce a continuous evolution of PV fields for the period from 21 to 30 April. The non-conservative terms of the large scale field are taken into account using a relaxation toward the ECMWF

meteorological fields [Hauchecorne et al., 2001]. MIMOSA has been used for real time 5 day forecasts of the PV fields and has been found useful for the detection of sub-tropical and polar filaments and alert release in the frame of the METRO project (MEridional TRansport of Ozone in the lower stratosphere, a research project included in the European campaign THESEO [Heese et al., 2001]).

Four advected-PV maps, derived for the 400 K level from the MIMOSA model are presented in figure 5. A low-PV air mass of tropical origin (over the South American continent) stretches latitudinally in the form of a "*tongue*" towards the southern mid-latitudes. The tropical air mass was localised close to Brazil on 23 April (see figure 5a), and moved south-eastwards in the days thereafter. On 25 April, the forward edge of the event is positioned in the middle of the Atlantic Ocean around 30°S and has a south-easterly movement (see figure 5b). On 28 April, the forward edge is situated near the west coast of southern Africa, extending towards the north (figure 5c). The tropical low-PV filament has elongated and covers nearly all of South Africa by 29 and 30 April (figure 5d).

Moreover, kinematic back-trajectories calculated from ECMWF (not shown) are in a close agreement with the advection contour model, and show the same origin for the stratospheric air mass over Durban.

V. Discussion-conclusion

The central line of this work is the use of both LIDAR measurements and modelling in order to analyse an isentropic transport event through the southern subtropical barrier. We first focused on the use of aerosol profiles obtained by

LIDAR over Durban, South Africa. Because of their life expectancy, stratospheric aerosols provide a good tracer. Aerosols can thus be used to study stratospheric dynamics and notably to study transport from the tropical stratospheric reservoir to mid-latitudes. As reported by several authors [Trepte and Hitchman, 1992 ; McCormick and Viega, 1992], the tropical stratospheric reservoir has an air mass that is distinctly different from that in the mid-latitude stratosphere.

That is evidenced on figure 6, which shows a tropical and a subtropical height vs time cross-section of aerosol extinction as recorded by the 525-nm wavelength channel of the SAGE-2 experiment, from 1994 to 1999. Whatever the period of observation is, one can observe that aerosol distributions in the lower stratosphere are different in the tropical zone and the subtropics. During the period from April to June 1999 (indicated with two vertical heavy lines), a 2 km-layer with a maximum extinction value of ≈ 1.7 km^{-1} was evident in the tropical lower stratosphere ; while in the subtropical stratosphere the maximum extinction value only reached ≈ 0.6 km^{-1}. This indicates that the observed aerosol loading event over Durban can correspond to a transport process of air mass from tropics.

Examination of MIMOSA output PV-maps at 380 K and 420 K potential temperature levels (not shown) show almost the same filamentary development, as for the 400 K level (see figure 5), with the same trajectory and during the same period. The detected horizontal transport event in the lower stratosphere concerns several isentropic levels in the lower stratosphere, in agreement with LIDAR observations over the Durban site (see figure 2).

All these results, LIDAR observation together with SAGE-2 measurements, the PV-maps, and the MIMOSA model retrieval of filamentary structures derived from ECMWF fields, agree with each other supporting the hypotheses of a horizontal transport in the lower stratosphere of air mass from tropics towards the subtropics and mid-latitudes.

Moreover, it is well known that the winter stratosphere is disrupted by wave activity, chiefly gravity and planetary waves. These waves are mainly generated in the troposphere and propagate with the westerly winds in winter through the middle atmosphere. It is also known that horizontal air mass exchanges between the tropical stratospheric reservoir and mid-latitudes are episodic and take place through the subtropical barrier due to planetary wave breaking. Indeed, it is the large-scale Rossby waves in the westerlies that pull air masses and tracers from the tropics into mid-latitudes in the form of large-scale filaments through the surf zone [Leovy et al., 1985 ; McIntyre and Palmer, 1984].

Using the same LIDAR data base recorded over Durban during the same period as in the present study, Bencherif et al. [2000] have shown that the daily variability of the local thermal structure was getting large, as the zonal wind component was becoming westerly and Rossby waves could propagate upward. Furthermore, in recent years and mostly in the northern hemisphere, there has been much interest in understanding the effects of mixing barriers on either side of the tropical stratosphere. With regard to the latitudinal extent of the air mass transport, coupling of observations and modelling is therefore essential in studying large-scale events.

In order to understand and quantify the meridional exchange events through the southern subtropical barrier, we carry on monitoring the LIDAR over Durban, in parallel with similar observations over Reunion Island (20.8°S, 55.5°E).

Such ground-based atmospheric *in situ* experiments at tropical and subtropical latitudes, when combined with global observations of trace gases and with dynamical models such as MIMOSA and LOBADY, an analytical tool for localising the subtropical barrier [Portafaix et al., 2000], offer new possibilities for investigation of exchange processes through the southern subtropical barrier. The quantification of the effective diffusivity, air mass and tracer fluxes will further contribute to that understanding [Haynes and Shuckburgh, 2000 ; Hauchecorne at al., 2001].

Acknowledgement

The authors wish to acknowledge the South African Weather Service and ECMWF for providing meteorological data and the G.R.T.R. (University of Strasbourg, France) for providing the Meteosat data. We also want to thank the French Embassy at Pretoria , the National Research Foundation (South African agency), *le Ministère de l'Education Nationale de l'Enseignement Supérieur et de la Recherche*, *le Ministère des Affaires Etrangères et de la Coopération* and *le Conseil Général de la Réunion*, for their financial support.

References

Baray J.L., Daniel, V., Ancellet, G., Legras, B., 2000. Planetary scale tropopause folds in the southern subtropics, *Geophys. Res. Lett.*, **27**, 353-356.

Bencherif. H., Morel, B., Moorgawa, A., Michaelis, M.M., Leveau, J., Porteneuve, J., Hauchecorne, A., Faduilhe, D., 2000. Observation and first validation of stratospheric temperature profiles obtained by a Rayleigh-Mie LIDAR over Durban, South Africa, *South African Journal of Science*, **96**, 487-492.

Brasseur, G., Granier, C., 1992. Mount Pinatubo aerosols, chlorofluorocarbons and ozone depltion, *Science*, **257**, 1239-1242.

Chazette, P., David, C., Lefrère, J., Godin, S., Pelon, J., Mégie, G., 1995. Comparative LIDAR study of optical, geometrical, and dynamical propreties of stratospheric post-volcanic aerosols, following the eruptions of El-Chichon and Mount Pinatubo, *J. Geophys. Res.*, **100**, 23195-23207.

Chen, P., Holton, J.R., O'Neill, A., Swinbank, R., 1994. Isentropic mass exchange between the tropics and extratropics in the stratosphere, *J. Atmos.. Sci.*, **51**, 3006-3018.

Chu, W.P., McCormick, M.P., Lenoble, J., Brogniez, C., Pruvot, P., 1989. SAGE II inversion algorithm, *J. Geophys. Res.*, **94**, 8339-8351.

David, C., Bekki, S., Godin, S., Mégie, G., Chipperfield, M.P., 1998. Polar stratospheric clouds climatology over Dumont d'Urville Between 1989 and 1993 and the influence of volcanic aerosols on their formation, *J. Geophys. Res.*, **103**, 22163-22180.

Grant, W.B., Browell, E.V., Long, C.S., Stowe, L.L., Graiger, R.G., Lambert, A., 1996. Use of volcanic aerosols to study the tropical reservoir, *J. Geophys. Res.*, **101**, 3973-3988.

Hauchecorne, A., Godin, S., Marchand, M., Heese, B., Souprayen, C., 2001, Quantification of the transport of chemical constituents from the polar vortex to middle latitudes in the lower stratosphere using the high-resolution advection model MIMOSA and effective diffusivity, *J. Geophys. Res.*, in press.

Hauchecorne, A, Chanin, M.L., 1980. Density and temperature profiles obtained by LIDAR between 35 and 70 km, *Geophys. Res. Lett.*, **7**, 565-568.

Haynes, P., Shuckburgh, E., 2000. Effective diffusivity as a diagnostic of atmospheric transport, *J. Geophys. Res.*, **105**, 22777-22794.

Heese, B., Godin, S., Hauchecorne, A., 2001. Forcast and simulation of stratospheric ozone filaments : a validation of a high-resolution potential vorticity advection model by airborne ozone lidar measurements in winter 1998-1999, *J. Geophys. Res.*, 106, 20011-20024.

Holton, J.R., Haynes, P.H., McIntyre, M.E., Douglass, A.R., Rood, R.B., Pfister, L., 1995. Stratosphere-Troposphere Exchange, *Reviews of Geophysics*, **33**, 403-439.

Horinouchi, T., Sassi, F., Boville, B.A., 2000. Synoptic-scale Rossby waves and the geographic distribution of lateral transport routes between the tropics and extratropics in the lower stratosphere, *J. Geophys. Res.*, **105**, 26579-26592.

Keckhut, P., Hauchecorne, A., Chanin, M.L., 1993. A critical review of the database acquired for the long-term surveillance of the middle atmosphere by the french Rayleigh LIDARs, *J. Atmos. Ocean. Tech.*, **10**, 850-867.

Kinninson, D.E., Grant, K.E., Connell, P.S., Rotman, D.A., Wuebbles, D.J., 1994. The chemical and radiative effects of the Mount Pinatubo eruption, *J. Geophys. Res.*, **99**, 25705-25731.

Klett, J.D., 1985. LIDAR inversion with variable backscatter / extinction ratios, *Appl. Opt.*, **24**, 1638-1643.

Klett, J.D., 1981. Stable analytical inversion solution for processing LIDAR returns, *Appl. Opt.*, **20**, 211-220.

Labitzki, K., McCormick, M.P., 1992. Stratospheric temperature increases due to Pinatubo aerosols, *Geophys. Res. Lett.*, **19**, 207-210, 1992

Leovy, C.B., Sun, C.-R., Hitchman, M.H., Remsberg, E.E., Russel, J.M., Gordley, L.L., Gille, J.C., Lyjak, L.V., 1985. Transport of ozone in the middle stratosphere : evidence for planetary wave breaking, *J. Atmos. Sci.*, **42**, 230-244.

McCormick, M.P., Viega, R.E., 1992. SAGE II measurements of early Pinatubo aerosols, *Geophys. Res. Lett.*, 19, 155-158.

McCormick, M.P., 1987. SAGE II: an overview, *Adv. Space res.*, **7**, 219-226.

McIntyre, M.E., Palmer, T.N., 1984. The "surf zone" in the stratosphere, *J. Atmos. Terr. Phys.*, **46**, n° 9, 825-849.

Portafaix, T., Bencherif, H., Baldy, S., Godin, S., Hauchecorne, A., 2000. A case study of isentropic exchange through the southern dynamical barrier limiting the tropical stratosphere, *Proceedings of the SPARC 2000,* Mar del Plata, Argentina, November 6-10.

Randel, W.J., Gille, J.C., Lahoz, A.E., 1993, Stratospheric transport from tropics to middle latitudes by planetary wave mixing, *Nature*, **365**, 533-535.

Robock, A., Mao, J., 1992. Winter warming from large volcanic eruption, *Geophys. Res. Lett.*, **19**, 2405-2408.

Roumeau, S., Brémaud, P., Rivière, E., Baldy, S., Baray, J.L., 2000. Tropical cirrus clouds : a possible sink for ozone, *Geophys. Res. Lett.*, **27**, 2233-2236

Scientific Assessment of Ozone Depletion : 1994

Shapiro, M.A., Kennedy, P.J., 1981. Research aircraft measurements of jet stream geostrophic and ageostrophic winds, *J. Atmos. Sci.*, **38**, 2642-2652.

Solomon, S., Portmann, R.W., Garcia, R.R., Thomson, L.W., Poole, L.R., McCormick, M.P., 1996. The role of aerosol variations in antropogenic ozone depletion in northern mid-latitudes, *J. Geophys. Res.*, **101**, 6713-6727.

Steinbrecht, W., Jager, H., Adriani, A., di Donfrancesco, G., Barnes, J., Beyerle, G., Neuber, R., David, C., Godin, S., Donovan, D., Carswell, A. I., Gross, M., McGee, T., Masci, F., D'Altorio, A., Rizi, V., Visconti, G., McDermid, I. S., Megie, G., Mielke, A., Stein, B., Wedekind, C., Nagai, T., Uchino, O., Nakane, H., Osborn, M., Winker, D., 1996. NDSC Intercomparison of Stratospheric Aerosol Processing Algorithms, *Advances in Atmospheric Remote Sensing with LIDAR,* 501-504.

Thomason, L.W., Poole, L.R., Deshler, T., 1997. A global climatology of stratospheric aerosol surface area density deduced from Stratospheric Aerosol and Gas Experiment II measurements: 1984-1994, *J. Geophys. Res.*, **102**, 8967-8976.

Trepte, C.R., Hitchman M.H., 1992. Tropical stratospheric circulation deduced from satellite aerosol data, *Nature*, **355**, 626-628.

Wang, P.H., McCormick, M.P., Swissler, T.J., Osborn, M.T., Fuller, W.H., Yue, G.K., 1989. Interference of stratospheric aerosol composition and size distribution from SAGE II satellite measurement, , *J. Geophys. Res.*, **94**, 8435-8446.

Waugh, D.W., Plumb, R.A., 1994. Contour advection with surgery : a technique for investigating fine-scale structure in tracer transfer, *J. Atmos.. Sci.*, 51, 530-540.

FIGURE Captions

FIGURE 1 : Aerosol extinction profiles recorded by LIDAR over Durban from April 20 to June 14, 1999. The corresponding averaged profile is shown by the solid line with cross symbols (see legend).

FIGURE 2 : LIDAR and SAGE-2 aerosol extinction profiles recorded quasi-simultaneously, on June 08, 1999 (see legend). The vertical lines represent the SAGE-2 error bars. The LIDAR profile is framed by the aerosol extinction profiles at $\pm \sigma$ the total uncertainty.

FIGURE 3 : Potential Vorticity analyses derived from ECMWF fields, for the 400 K potential temperature level. **(a)** PV mean fields from April 18 to May 10th, 1999, and **(b)** PV field on April 29th, 1999.

FIGURE 4 : Water vapour and cloud distributions in the troposphere derived from MeteoSat satellite for April 29th, 1999.

FIGURE 5 : Advected-PV contours as obtained with the MIMOSA model for April **(a)** 23rd, **(b)** 25th, **(c)** 28th and **(d)** 30th, 1999.

FIGURE 6 : Time vs height cross-sections of aerosol extinction derived from SAGE-2 profiles obtained from the 525-nm wavelength channel, for the period from January 1994 to December 1999. The upper and lower plates present the 0°-15°S and 20°S-40°S latitudinal bands, respectively. The heavy red solid lines frame the period from April to June 1999.

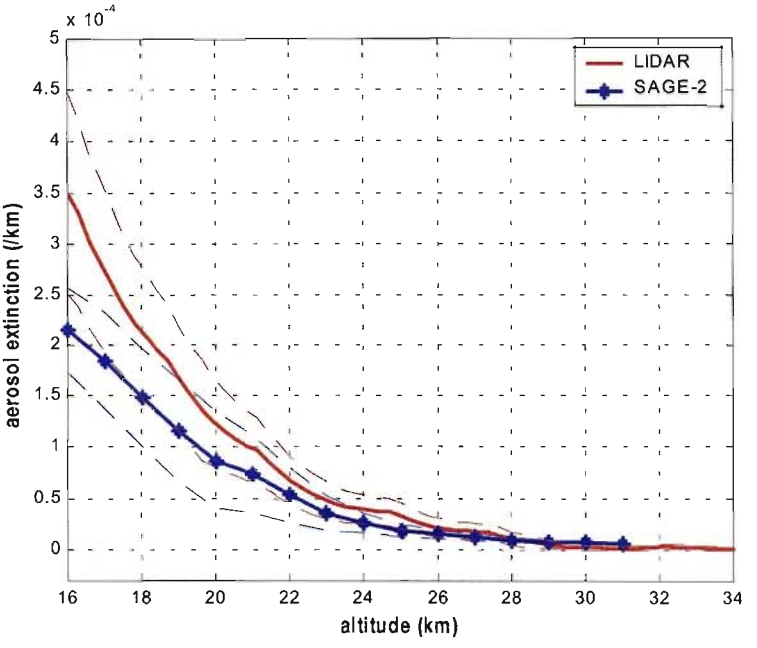
x 10^-4
5
4.5
4
3.5
3
2.5
2
1.5
1
0.5
0
aerosol extinction (/km)
16
18
20
22
24
26
28
30
32
34
altitude (km)
LIDAR
SAGE-2

Figure - 1

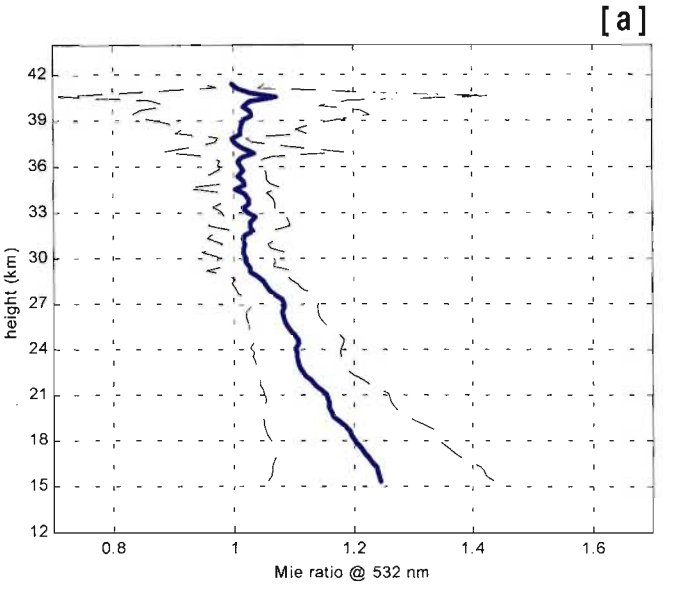
[a]
height (km)
42
39
36
33
30
27
24
21
18
15
12
0.8
1
1.2
1.4
1.6
Mie ratio @ 532 nm

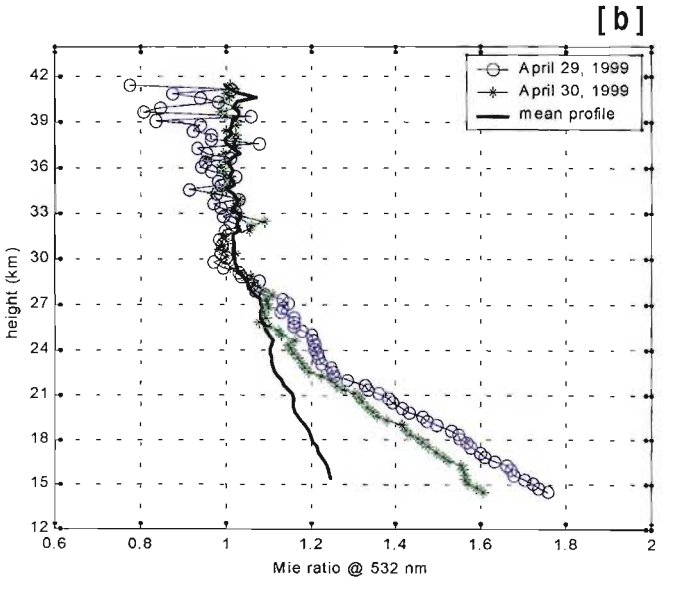
[b]
April 29, 1999
April 30, 1999
mean profile
height (km)
42
39
36
33
30
27
24
21
18
15
12
0.6
0.8
1
1.2
1.4
1.6
1.8
2
Mie ratio @ 532 nm

Figure - 2

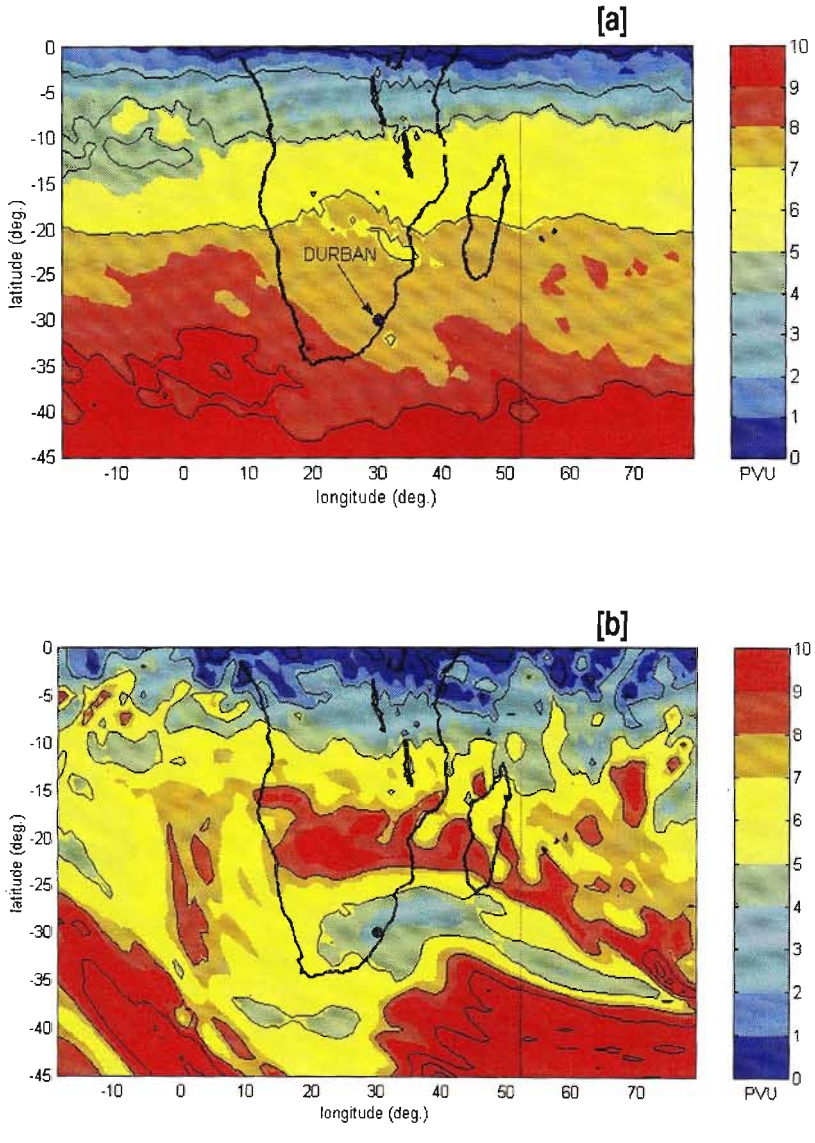
[a]
DURBAN
latitude (deg.)
longitude (deg.)
PVU
[b]
latitude (deg.)
longitude (deg.)
PVU

Figure - 3

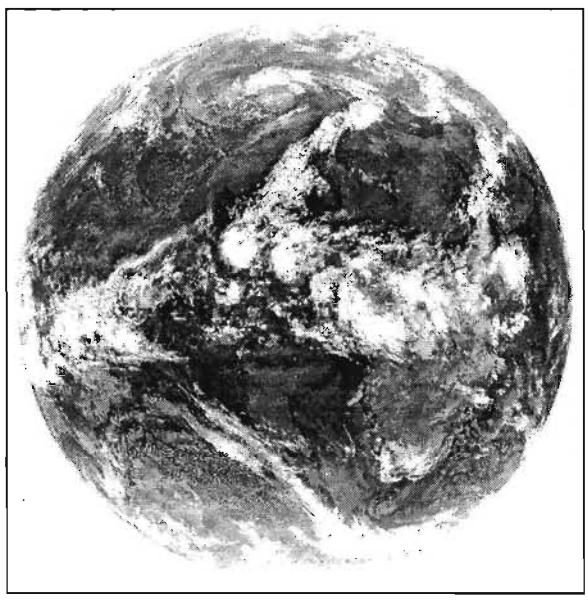

Figure - 4

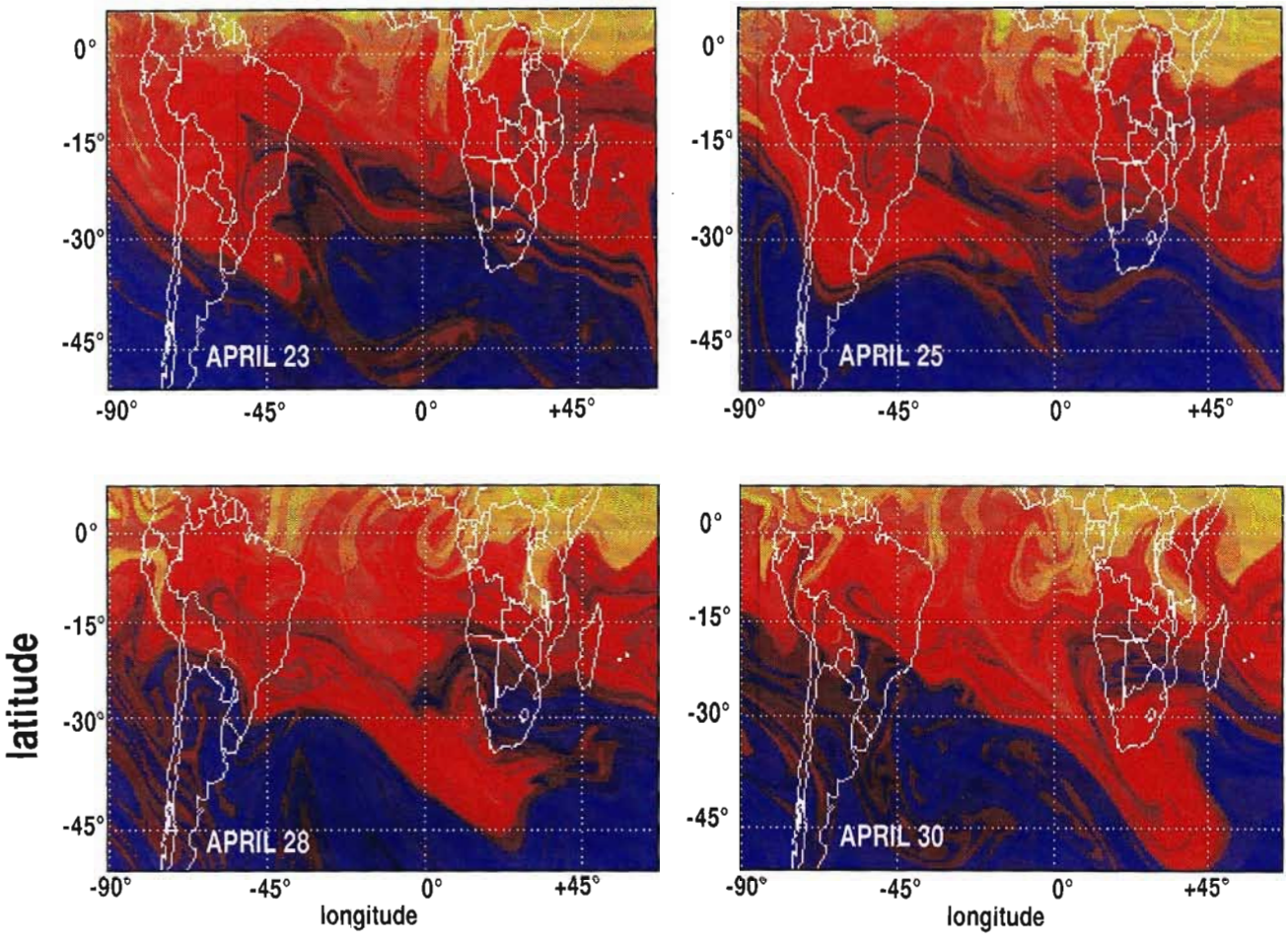
0°
-15°
-30°
-45°
APRIL 23
-90°
-45°
0°
+45°
APRIL 25
APRIL 28
APRIL 30
latitude
longitude

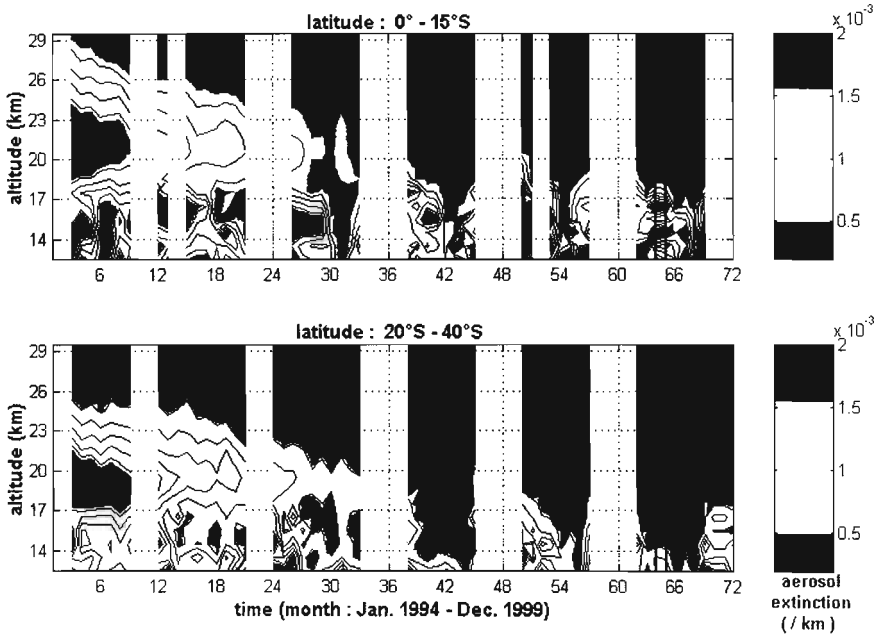
latitude : 0° - 15°S
altitude (km)
29
26
23
20
17
14
6
12
18
24
30
36
42
48
54
60
66
72
x 10^-3
2
1.5
1
0.5
latitude : 20°S - 40°S
altitude (km)
time (month : Jan. 1994 - Dec. 1999)
aerosol extinction (/ km)

Figure 6